Novel Donor-Acceptor Polymers for Solar Cells

Jagadeesh Babu Bodapati

Submitted to the
Institute of Graduate Studies and Research
in partial fulfillment of the requirements for the Degree of

Doctor of Philosophy
in
Chemistry

Eastern Mediterranean University
February 2011
Gazimağusa, North Cyprus

ABSTRACT

The process of photo conversion in most opto-electronic devices includes transfer of absorbed solar energy to convert it into either chemical or electrical energy. Perylene and naphthalene dyes are characteristic *n*-type conjugated organic materials and are very attractive with great potential applications in the photonic field as they possess high stabilities, absorption capacities, and light emitting properties.

The focus of this work is the synthesis, structure, photophysical, and electrochemical properties of oligomer dyes based on perylene and naphthalene chromophores, named, perylene-3,4,9,10-tetracarboxylic acid-Bis-(*N*,*N'*-Bis 2-[2-(2-{2-[2-(2-hydroxy-ethoxy)-ethoxy]-ethoxy}-ethoxy)-ethoxy]-ethylpolyimide (EOPPI), naphthalene-1,4,5,8-tetracarboxylic acid-Bis-(*N*,*N'*-Bis 2-[2-(2-{2-[2-(2-hydroxy-ethoxy)-ethoxy]-ethoxy}-ethoxy)-ethoxy]-ethylpolyimide (EONPI).

Additionally, two previously synthesized *n*-type materials based on the same chromophores were considered to explore the electrochemical properties concerning photovoltaic devices. The compounds are characterized in detail by studying their optical, photophysical, thermal and electrochemical properties using the techniques IR, GPC, UV-vis, Fluorescence, DSC, TGA and Cyclic, squarewave voltammetries.

Both oligomeric dyes exhibited attractive color tunability with different light-emitting properties. They possessed outstanding solubilities, molar absorption coefficients, thermal stabilities and electrochemical stabilities and reversibilities. The strong solvent dependent photophysical and electrochemical properties of EONPI, including the large shift of excimer emission maximum, makes the oligomer potential candidate for various photo sensing applications.

Keywords: Perylene, naphthalene, solar cell, photovoltaic, color tunability.

ÖZ

Birçok opto elektronik aygıtlarda foton dönüşümü süreci, absorblanan solar enerjinin kimyasal veya elektriksel enerjiye dönüşümünü içermektedir. N tipi yarıiletken özellikler sergileyen perilen ve naftalen boyaları yüksek kararlılık, absorblama yeteneği ve ışın yayma özellikleri nedeniyle, fotonik alanda çok ilgi uyandıran konjüge organik materyallerdir.

Tez kapsamında, perilen ve naftalen kromoforları esaslı iki oligomer, perilen-3,4,9,10-tetrakarboksilik asid-bis-(N,N'-bis 2-[2-(2-{2-[2-(2-hidroksi-etoksi)-etoksi]-etoksi}-etoksi)-etoksi]-etilpoliimid (EOPPI) ve naftalen-1,4,5,8-tetrakarboksilik asid-bis-(N,N'-bis 2-[2-(2-{2-[2-(2-hidroksi-etoksi)-etoksi]-etoksi}-etoksi)-etoksi]-etilpoliimidin (EONPI) sentezine, yapılarına, fotofiziksel ve elektrokimyasal özelliklerine odaklanılmıştır. Ayrıca, Daha önce sentezlenmiş olan benzer kromoforlar esaslı iki ayrı n-tipi materyalin elektokimyasal özellikleri fotovoltaik aygıtlarla ilgili olarak araştırılmıştır. Sentezlenen maddelerin optik, fotofiziksel, termal ve elektrokimyasal özellikleri IR, GPC, Uv-vis, emisyon, DSC, TGA ve CV ölçümleri ile detaylı araştırılarak tanımlanmıştır.

Her iki oligomerik boya da değişik ışık yayma özelliğinde olup ilgi çekici renk ayarlanılabilirlilik özelliği sergilemiştir. Olağanüstü çözünürlük, molar absorblama sabitleri, termal kararlılık ve tersinir elektrokimyasal kararlılık özelliklerine sahiptirler.

Kuvvetle çözgene bağlı fotofiziksel ve elektrokimyasal özellikler ve maksimum ekzimer emisyonunda büyük kayma sergileyen EONPI oligomeri değişik foto duyarlı uygulamalar için potansiyel bir adaydır.

Anahtar kelimeler: Perilen, naftalen, solar hücre, fotovoltaik, renk ayarlanabilirlilik.

To My Supervisor

ACKNOWLEDGMNTS

PREFACE

Every creature needs energy for survival. The picture where the bud blossoms to a beautiful flower explains the necessity and importance of energy. Obviously, we are facing an increase in energy demand day by day which resulted in an energy crisis. The scientists focused on development of alternative, renewable energy sources instead of depending solely on the dwindling natural energy resources. Sunlight, an inexhaustible and free cost energy supply, is an excellent source of energy which can be converted to different forms of energy. Among many technological methods defined, photovoltaic (PV) effect (conversion of light energy into electrical energy by a photovoltaic or solar cell) is a popular method for obtaining electrical energy. Again, there are several solar cells such as conventional silicon solar cells, organic-polymer solar cells, etc. constructed of. This thesis deals with synthesis of new donor/acceptor pairs which can be used in deriving organic solar cells.

The first chapter, Chapter 1, is an introductory chapter. It presents a brief introduction to solar cells and a small review on the previous works carried out on the solar cell devices that are made of some donor/acceptor pairs.

Chapter 2 discusses the theoretical background of solar cells, their working style, and some important chemistry concepts relating to solar cells.

Synthesis methods of various acceptors and their characterization are illustrated in Chapter 3. Data and calculations concerning synthesized compounds were shown in Chapter 4. Chapter 5 presents a detailed discussion of the results followed by concluding remarks that are summarized in Chapter 6.

TABLE OF CONTENTS

LIST OF TABLES

LIST OF FIGURES

xvii

LIST OF ILLUSTRATIONS

LIST OF SYMBOLS/ABBREVIATIONS

$\overset{\circ}{A}$	:	Armstrong
a	:	Mark-Houwink-Sakurada's constant
A	:	Absorption
A	:	Area of working electrode
A	:	Electron acceptor
AM	:	Air mass / air mass ratio
Anal.	:	Analytical
AU	:	Arbitrary unit
Avg.	:	Average
c	:	Concentration
calcd.	:	Calculated
^{13}C NMR	:	Carbon-13 nuclear magnetic resonance spectroscopy
CB	:	Conduction band
CC	:	Flash Column chromatography
CH	:	Chitosan
CHL	:	Chloroform
CT	:	Charge transfer
CV	:	Cyclic voltammetry
δ	:	Chemical shift
D	:	Diffusion Constant
D	:	Electron donor
Da	:	Dalton

DAEO	:	1-Azido-2-[2-(2-{2-[2-(2-azido-ethoxy)-ethoxy]-ethoxy}-ethoxy)-ethoxy]-ethane
DC	:	Dielectric constant
DC	:	Direct current
DCM	:	Dichloromethane
DMAc	:	Dimethylacetamide
DMAP	:	4-dimethylaminopyridine
DMF	:	N,N′-dimethylformamide
DMSO	:	Dimethyl sulfoxide
DNA	:	Deoxyribonucleic acid
DSC	:	Differential scanning calorimetry
DSSC	:	Dye sensitized solar cell
DTEO	:	1-Toulene-4-sulfonic acid 2-[2-(2-{2-[2-(2-toulene-4-sulfonic acid-ethoxy)-ethoxy]-ethoxy}-ethoxy)-ethoxy]-ethane
ε	:	Extinction coefficient
ε_{max}	:	Maximum Extinction coefficient/Molar absorptivity
$\varepsilon_A(\bar{v})$	:	Extinction coefficient of acceptor
eV	:	Electron volt
$E_{1/2}$	:	Half-wave potential
EA	:	Electron affinity
ECE	:	Energy conversion efficiency
E_g	:	Band gap energy
EI	:	Electron ionization
EODA	:	2-[2-(2-{2-[2-(2-amino-ethoxy)-ethoxy]-ethoxy}-ethoxy)-ethoxy]-ethylamine

EONPI	:	Naphthalene-1,4,5,8-tetracarboxylic acid-bis-(*N*,*N*′-bis 2-[2-(2-{2-[2-(2-hydroxy-ethoxy)-ethoxy]-ethoxy}-ethoxy)-ethoxy]-ethyl polyimide
E_{o-o}	:	Singlet energy (Excited state energy of 0-0 electronic transition) in eV
EOPPI	:	Perylene-3,4,9,10-tetracarboxylic acid-Bis-(*N*,*N*′-Bis 2-[2-(2-{2-[2-(2-hydroxy-ethoxy)-ethoxy]-ethoxy}-ethoxy)-ethoxy]-ethylpolyimide
E_{ox}	:	Oxidation potential
ΔE_p	:	Separation of peak potentials
E_{pa}	:	Anodic peak potential
E_{pc}	:	Cathodic peak potential
EQE	:	External quantum efficiency
Equn.	:	Equation
E_{red}	:	Reduction potential
E_s	:	Singlet energy (Excited state energy of 0-0 electronic transition) in kcal/mol
ET	:	Energy transfer
f	:	Oscillator strength
ff	:	Fill-factor
Fc	:	Ferrocene
$F_D(\bar{\nu})$	:	Normalized area of the fluorescence spectrum of donor
Fig.	:	Figure
FRET	:	Fluorescence resonance energy transfer
FT-IR	:	Fourier transform infrared spectroscopy

FU	:	Functional unit
ΔG	:	Gibbs free energy
ΔG_{ET}	:	Free energy change for electron transfer
ΔG_{EN}	:	Free energy change for energy transfer
GPC	:	Gel permeation chromatography
h	:	Hour
$h\nu$	:	Irradiation
^{1}H NMR	:	Proton nuclear magnetic resonance spectroscopy
HEG	:	Hexaethyleneglycol
HFIP	:	Hexafluoroisopropanol
HOMO	:	Highest occupied molecular orbital
HP-CH	:	N-(4-hydroxyphenyl)-3,4,9,10-perylenetetracarboxylic-3,4-anhydride-9,10-imide conjugated chitosan
i_p	:	Peak current
i_{pa}	:	Anodic peak current
i_{pc}	:	Cathodic peak current
I_{sc}	:	Short circuit current
I_0	:	Fluorescence intensity of donor in the absence of acceptor
$I_{1, 2, 3, etc}$	:	Fluorescence intensity of donor in the presence of acceptor
IP	:	Ionization potential
IR	:	Infrared spectrum/spectroscopy
ITO	:	Indium tin oxide
J	:	Coupling constant
J	:	Overlap integral between the fluorescence spectrum of donor and the molar absorption spectrum of acceptor

K	:	Orientation factor (for normally distributed molecules)
K	:	Mark-Houwink-Sakurada's constant
kcal	:	Kilocalorie
k_d	:	Rate constant of radiationless deactivation
kDa	:	kiloDaltons
k_f	:	Fluorescence rate constant
k_q	:	Rate constant for bimolecular fluorescence quenching
l	:	Path length
LED	:	Light emitting diode
LUMO	:	Lowest unoccupied molecular orbital
M	:	Molar concentration
M^+	:	Molecular ion peak
M_n	:	Number average molecular weight
M_w	:	Weight average molecular weight
M_v	:	Viscosity average molecular weight
max	:	Maximum
MHS	:	Mark-Houwink-Sakurada
MHz	:	Megahertz
min	:	Minute
min	:	Minimum
mmol	:	Millimole
mol	:	Mole
mp	:	Melting point
MPP	:	Maximum power point
MS	:	Mass spectrometry

mV	:	Millivolt
n	:	Refractive index
n	:	Number of electrons (in the reduction process)
N	:	Avogadro's number
$[\eta]$	:	Intrinsic viscosity
η_{sp}	:	Specific viscosity
η_{red}	:	Reduced viscosity
NDA	:	1,4,5,8-naphthalenetetracarboxylic dianhydride
NDI	:	Naphthalene diimide
NHE	:	Normal hydrogen electrode
NMP	:	*N*-methylpyrrolidinone
NMR	:	Nuclear magnetic resonance spectroscopy
NPI	:	Naphthalene polyimide
Φ_f	:	Fluorescence quantum yield
P_{max}	:	Maximum power
PDA	:	Perlyene 3,4,9,10-tetracarboxylic dianhydride
PDI	:	Perlylene diimide
PDI	:	Polydispersity index
PET	:	Photoinduced electron transfer
PI	:	Polyimide
PPI	:	Perylene polyimide
ppm	:	Parts per million
PV	:	Photovoltaic
Q	:	Quencher/Quenching factor
QD	:	Quantum dot

R_0	:	Critical transfer distance
RET	:	Resonance Energy Transfer
RT	:	Room temperature
SC	:	Solar cell
SC	:	Spin coating
SCE	:	Saturated calomel electrode
SHE	:	Standard hydrogen electrode
Std.	:	Standard
SWV	:	Square wave voltammetry
τ_0	:	Theoretical radiative lifetime
τ_f	:	Fluorescence lifetime
t	:	Time
TBAPF6	:	Tetrabutylammoniumhexafluorophosphate
TEA	:	Triethylamine
TEODA	:	4,7,10-trioxa-1,3-tridecanediamine
TEONPI	:	Poly[bis-*N*,*N'*-(3-(2-(2-(3-aminopropoxy)-ethoxy)-ethoxy)-propyl)-1,4,5,8-naphthalene imide]
TFAc	:	Trifluoroacetic acid
TGA	:	Thermogravimetric analysis
THF	:	Tetrahydrofuran
TsCl	:	4-Toulenesulfonyl Chloride
u	:	Unknown
μ	:	Micro
UV	:	Ultraviolet
UV-vis	:	Ultraviolet visible light absorption

ν	:	Scan rate
$\bar{\nu}$	:	Wavenumber
$\Delta\bar{\nu}_{1/2}$	:	Half-width (of the selected absorption)
$\bar{\nu}_{max}$	:	Maximum wavenumber/Mean frequency
V	:	Volt
VB	:	Valence band
V_{oc}	:	Open Circuit Voltage
vs.	:	Versus
λ	:	Wavelength
λ_{exc}	:	Excitation wavelength
λ_{em}	:	Emission wavelength
λ_{max}	:	Maximum wavelength

Chapter 1

INTRODUCTION

1.1 The Solar Cell

A solar cell (SC) or a photovoltaic (PV) cell is a device that converts solar energy into electrical energy directly by photovoltaic effect. The term, solar cell, sometimes is reserved for devices which specifically capture energy from sunlight, while the term, photovoltaic cell, is applied when the source of energy/light is unspecified.

At present, solar cells comprising an inorganic semiconductor such as mono- and multi-crystalline silicon are developed commercially and can be found in markets for small scale devices such as solar panels on roofs, pocket calculators, and water pumps. These conventional SCs can harvest up to as much as 24% of the incoming solar energy. The percentage is already passed to 25% and is close to the theoretically predicted upper limit of 30% [1]. The production of these SCs requires many energy intensive processes at very high temperatures and high vacuum conditions followed by numerous other steps leading to relatively high manufacturing costs. This illustrates the necessity of developing new technologies which allow low fabrication costs rather than higher conversion efficiencies of commercial silicon SCs. Organic solar cells made of organic semiconductors are one of the alternatives that accomplish the requirements [2].

1

1.2 Motivation

The importance of SCs is not only based on the depletion of natural energy sources but also related to their environmental effect. The high usage and combustion of fossil fuels caused in dwindling of energy sources and resulted in harmful effects on the delicate balance of nature. The plants are unable to absorb the huge extra amounts of CO_2 producing in the atmosphere caused the greenhouse effect. This again caused the global warming and the global mean surface temperature has increased by $0.3 - 0.6\ ^{o}C$ [3]. Because of these consequences, the renewable energy sources such as photovoltaic cells, hydroelectric, geothermal, wind-power, and biomass systems and their development as environmental clean energy sources is mandatory for the future of human.

Photovoltaic cells are one of the most effective and attractive renewable energy devices. Starting with the First-generation conventional silicon SCs, an intensive research was carried out and reached to the current, Fourth-generation nano-material based devices but did not reach cheap and efficient commercial architectures. Although significant progress was achieved, the research profile since two decades outlined the necessity of developing new materials in order to make the PVs more efficient and economic. The clear research picture on *p-* and *n-* type organic materials and corresponding outstanding organic/molecular devices definitely motivates the scientists towards the target of cheap and efficient devices.

1.3 Photovoltaic Focus on Perylene and Naphthalene Dyes

The mechanism of photovoltaic effect in organic PV device architectures explains the importance of *n*-type organic materials (discussed in Chapter 2). Conjugated *n*-type organic materials and their charge transfer kinetics, whose influence on exciton dissociation and charge extraction have profound impact on overall efficiency of an organic solar cell [2].

The earliest studies include fullerene and its derivatives which were widely used in bulk hetero junction PV devices as electron accepting *n*-type materials and recorded appreciable efficiency. Still, they are one of the promising materials in the device architecture of organic based polymer hetero junction SCs with recent figured out 7% power conversion efficiency [3].

Rylene dyes with extendable conjugation (Figure 1.1) are emerged as much more exciting and attracting candidates for the PV device architectures [4].

(a) naphthalenebis(dicarboximide)

(b)
n = 0 → a perylenebis (dicarboximide)
n = 1 → a terrylenebis (dicarboximide)
n = 2 → a quaterrylenebis (dicarboximide)
n = 3 → a pentarylenebis (dicarboximide)
n = 4 → a hexarylenebis (dicarboximide)
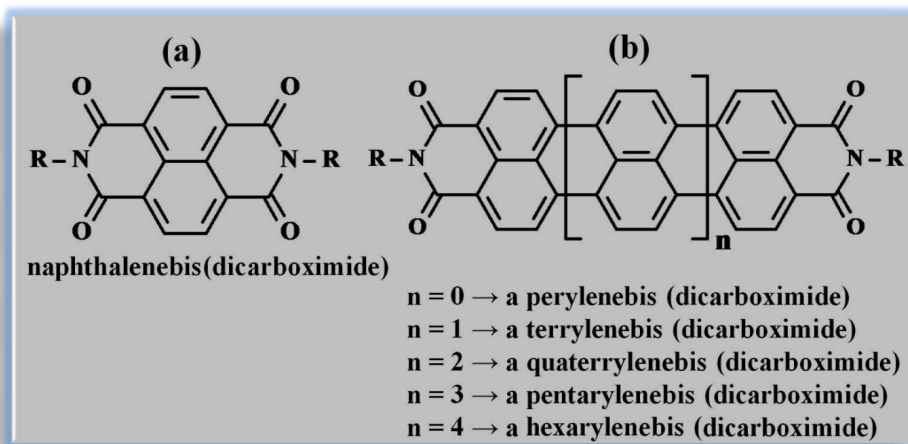
Figure 1.1: A General (a) Naphthalene Dye and (b) Higher Order Rylenes with

Extendable Aromatic Scaffold.

As a simple and effective conjugated molecular design with high stabilities, a versatile mono-, di-, oligo-, and poly- naphthalene and perylene dyes were investigated and characterized towards device applications.

A perspective on organic solar cell structure, characteristics, mechanisms, fabrication, and the materials phthalocyanines as *p*-type; perylene and naphthalene derivatives as *n*- type were presented by Wöhrle and Meissner in 1991 [2]. Four years later, Wöhrle and co-workers described their investigations of n/p-junction PV cells constructed by the vapor deposition of *n*-conductor perylene diimides and *p*-conductor phthalocyanines. The photovoltaic efficiencies achieved were <0.43% and 1.6% under white light of 100 mW cm^{-2}, illumination of 1 mW cm^{-2} respectively [5]. In their classical theory, Wöhrle and Meissner explained the cell structure and the necessity of strong absorption of solar energy by organic materials in the visible region of the spectrum [2]. Efficient conversion of solar energy thus requires highly colored organic materials with extended absorption ranges. This was achieved by Klaus Müllen et al., in 1997, reported several reasonably soluble perylene and rylene dyes with extended π-system and resulting long-wavelength absorbtion and fluorescence [6]. A broadly absorbing perylene dye for dye sensitized solar cells was also prepared [7]. Dynamic π-π stacked molecular assemblies that emit green to red colors were presented by Wang and co-authors [8]. Recently, a perylene- and naphthalene-based color tunable oligomeric diimides using flexible spacer were reported by Bodapati and Icil [9-10]. Starting with the approach of developing new materials possessing extended absoption and emission, a wide variety of perylene

4

and naphthalene derivatives not only with exciting optical properties but also with great stabilities were synthesized and reported [11-15]. This resulted in development of various opto-electronic and PV devices constructed of perylene and naphthalene derivatives in addition to the wide variety of applications. A review focused on OLEDs discuss in detail the role of perylene and naphthalene dyes in opto-electronic applications [16]. The reported (a) facile chromophoric oxidants, cyanated perylenedicarboximides, for organic photonics and electronics [17]; (b) various perylene bisimide dyes as versatile building blocks for functional supramolecular architectures [18]; (c) dendronized perylene diimide emitters for light emitting diodes [19]; (d) perylene-doped polymer nanotubes as fluorescence sensors [20]; (e) naphthalene- and perylene-based linkers for the stabilization of hairpin triplexes [21]; (f) naphthalene diimide derivatives as model compounds for molecular layer epitaxy [22]; (g) ambient stable- arylene diimide semiconductors with tuning orbital energitics [23]; (h) a fluorescent photochromic molecule composed of a fluorescent perylene- derivative and diarylethene [24] give some examples of such kind. Vapor-deposited thin-layer titanium dioxide and perylene- based solar cells were reported by Thelekkat and co-authors [25].

Pentacene/Perylene co-deposited SCs were fabricated and noted a power conversion efficiency of 0.54% [26]. Polymer-perylene diimide heterojunction solar cells were reported by Gregg, and et al, achieved 0.71% power conversion efficiency under 100 mW cm^{-2} [27]. Appreciable increment in power conversion efficiency (1.9%) using perylene pigments was reported by Nakamura and et al [28]. Some improved performance of perylene-based PV cells using polyisocyanopeptide arrays was reported recently [29]. Light-harvesting arrays comprised of (a) a porphyrin bearing

multiple perylene monimide pigments [30]; (b) self-assembling perylene diimide-appended hexaazatriphenylene [31]; (c) multichromophoric perylene molecular square were prepared and their photophysics were studied [32]. Dye sensitized solar cells based on (a) five different perylene molecules with different intramolecular charge-transfer characters [33]; and (b) electron-donating perylene tetracarboxylic acids were established [7]. The latter design reported an efficiency of 2.6% [7]. Several donor-acceptor based systems including perylene and naphthalene chromophores were prepared and various important processes concerning PVs such as charge transfer, energy transfer and related excited-state photodynamics were outlined [34-37].

A few reviews outlined the progress of organic/molecular photovoltaics/devices [38-43] and give a clear picture and better understanding on organic-photonics [44-50]. Some of them were aimed at possible strategies of increasing the efficiency [41, 44, 45, 50]. However, every review concluded that there is a great potential for organic materials to make "electronics everywhere".

1.4 Importance of Electrochemistry of *n*-type Organic Materials

A complete molecular picture on π-conjugated oligomers and polymers, their excited-state photodynamics reveal the charge/electron/energy- transfer properties [38-50]. These properties finally determine the ease of electron-transport in organic PV devices as electron deficiency of *n*-type materials especially having a strong impact on the injection of charges at the elctrodes. Based upon both (i) oxidation potentials or ionization potentials (both are related to energy of HOMO) and (ii) reduction potentials or electron affinities (both are related to energy of LUMO), tailoring of electron deficient *n*-type materials can be made to better facilitate injection of electron charges at the electrodes. Since *n*-type materials with relatively low-energy LUMOs can be more readily reduced than more electron rich materials, electron deficiencient *n*-type materials with different substituents are also very important in applications where charge needs to be electrically injected rather than photogenerated [42, 43, 45].

Another important impressive criterion of *n*-type materials is π-stacking [10, 43], in general, leads to higher mobilities. The mechansim behind high mobility is strong electronic coupling between molecules, which is associated with excellent overlap between π-systems on adjacent molecules. In general, the linear extension of π-system tends to raise HOMO and lower LUMO making the molecule both easier to oxidize and easier to reduce [43]. The HOMO and LUMO levels give rise to the band gap energy and hence a molecular band picture that is directly having influence on the corresponding heterojunction PV devices. The electrochemical properties, therefore, needs to be studied in detail for determining the electron deficiency (reduction ability) and electronic performance of *n*-type materials.

Rylene diimides can exhibit relatively high electron affinities, high electron mobilities, and excellent chemical, thermal, and photochemical stabilities [4]. The electron deficiency arises from the substitution of aromatic core with two sets of π-accepting imides groups that are again mutually conjugated. As shown in Figure 1.1, the widely used rylene-imides include naphthalene- and perylene- imide dyes. Therefore, the naphthalene and perylene derivatives have been used not only as building blocks for electronic devices such as organic light emitting diodes, dye lasers, optical switches and photodetectors, but also as electron acceptors in conjunction with electron donors for studying photoinduced energy- and electron-transfer processes leading to PV devices.

Herein, the thesis presents two excellent soluble and color tunable n-type oligomeric diimides in addition to the three other n-type organic materials based on perylene and naphthalene chromophores shown in the following diagrams (Figures 1.2 – 1.7) for the purpose of photovoltaic devices. The compounds synthesized by Devrim Özdal, Mustafa E. Özser were especially taken into the part of research in order to study their electrochemical properties as all of the compounds have possessed versatile substituents.

The synthesized compounds were characterized thoroughly to explore all the characteristics, especially, optical/photophysical, thermal and electrochemical properties. The characteristics were determined by various techniques – spectrophotometric such as IR, UV-vis and emission; chromatographic such as GPC; thermogravimetric such as DSC and TGA; and voltammetric such as CV and SWV.
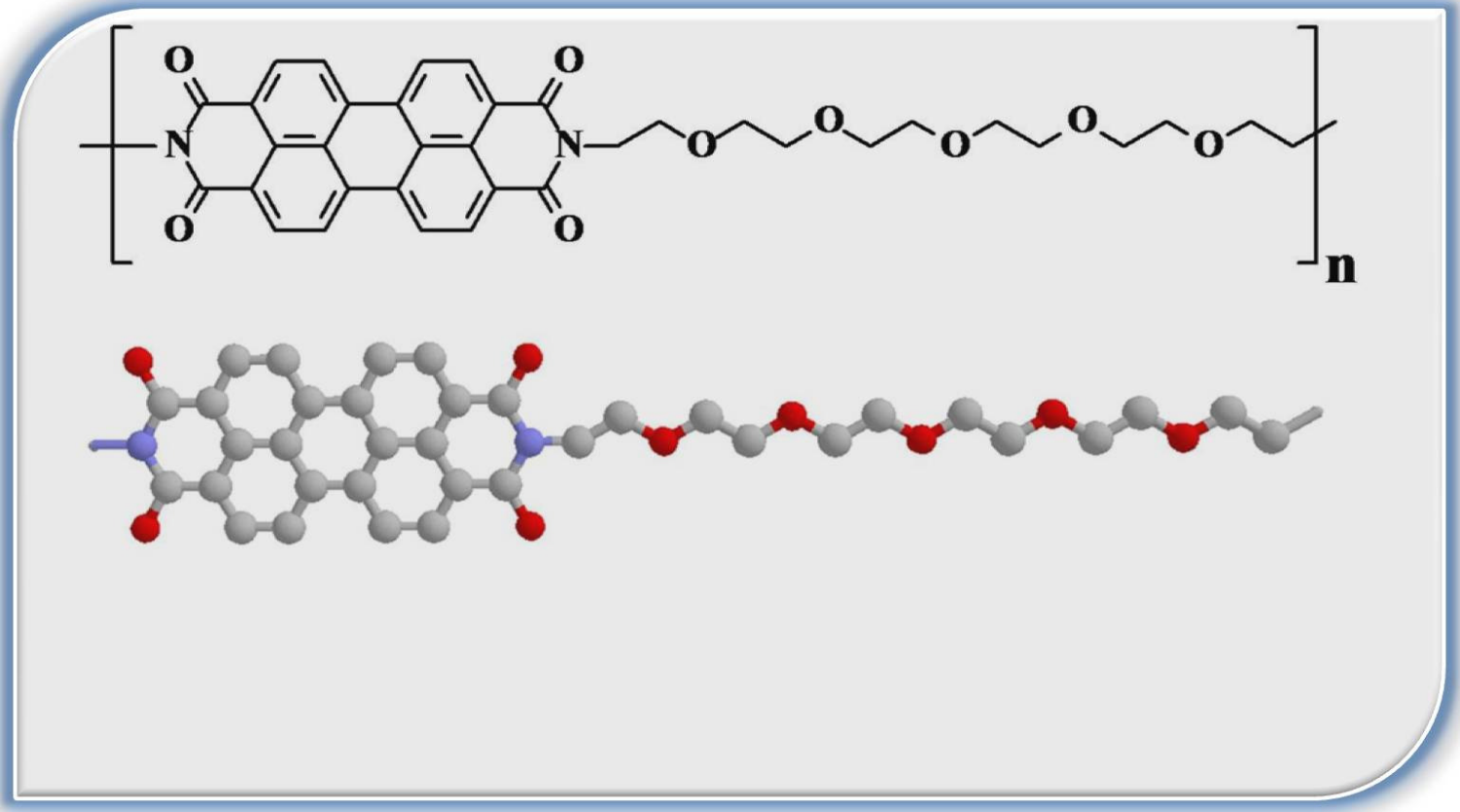
Figure 1.2: Structures of Perylene Oligomeric Diimide, EOPPI (Bodapati and Icil, 2008) [9]
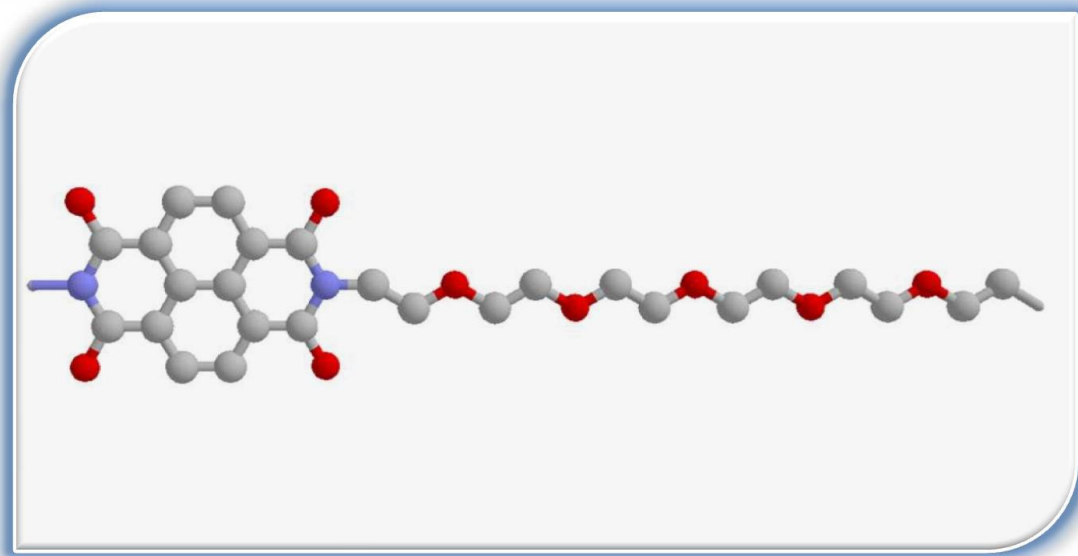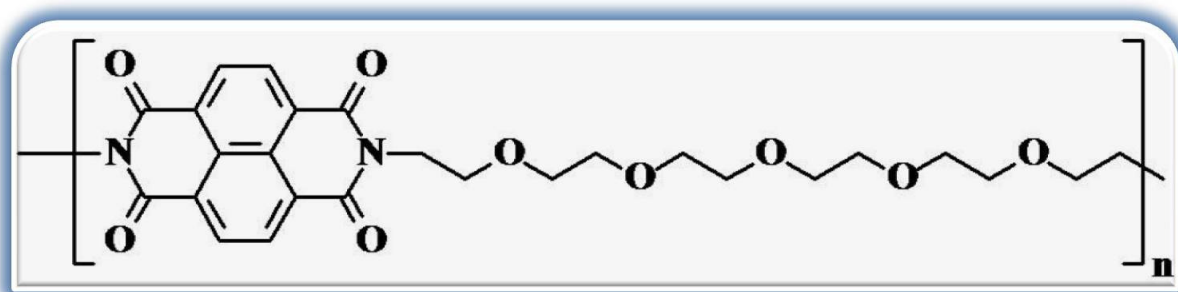
Figure 1.3: Structures of Naphthalene Oligomeric Diimide, EONPI (Bodapati and Icil, 2011, *in print*) [10]
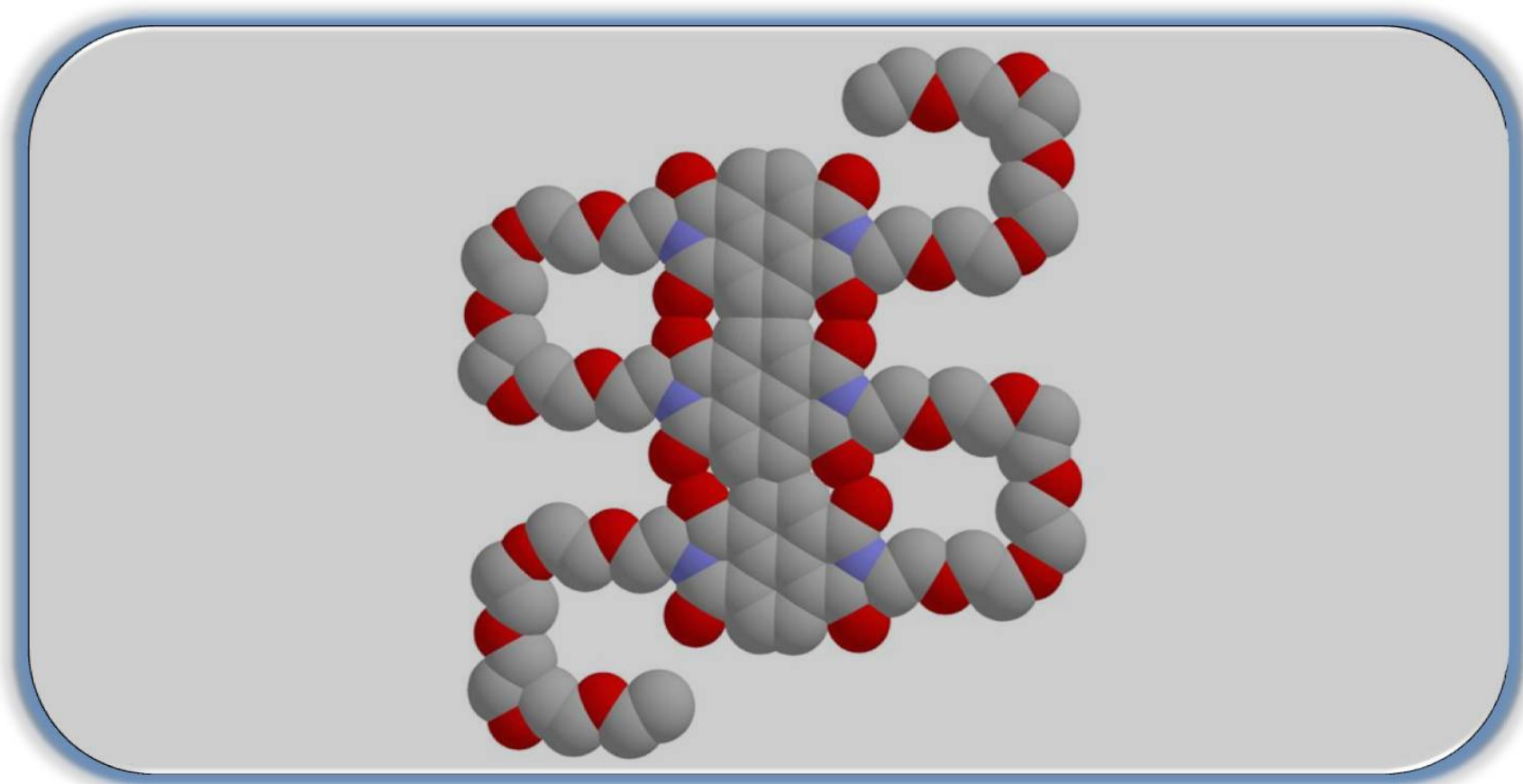
Figure 1.4: Naphthalene Oligomeric Diimide, EONPI and its Probable Spacefill Stacking Diagram (Bodapati and Icil, 2011, *in print*) [10]
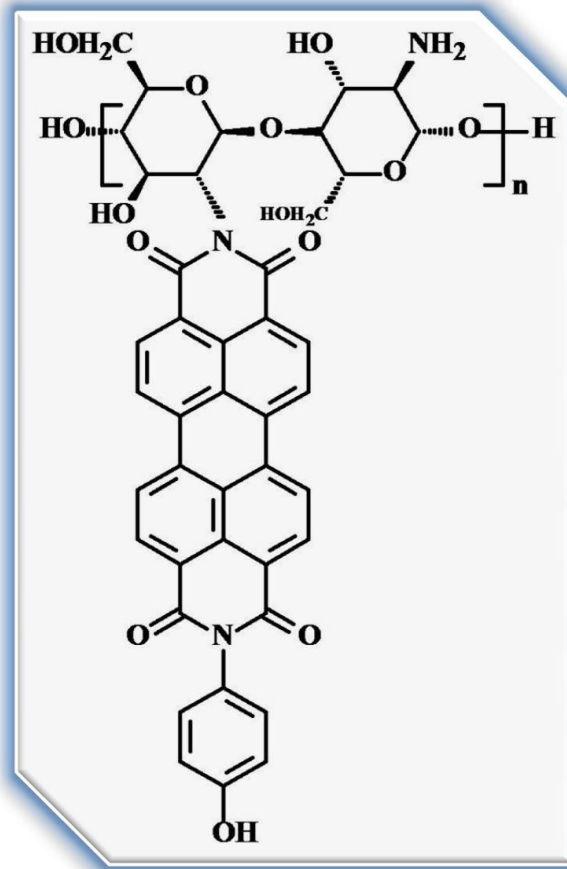
Figure 1.5: Structure of Perylene Dye Substituted Fluorescent Chitosan Polymer

(Ozdal, Asir, Bodapati, and Icil, *in press*) [15]
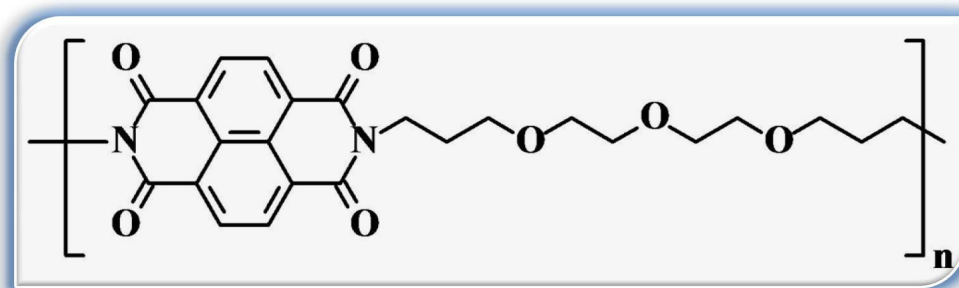
Figure 1.6: Naphthalene Polyimide, TEONPI (Ozser, Bodapati, and Icil *in press*)[59]

Chapter 2

THEORETICAL

2.1 Conventional Solar Cells – The First and Second Generation Photovoltaics

There was a great interest in the research field of solar cells (SCs) for past few decades which resulted in developing a new solar cell manufacturing techniques from the first generation PV cells to the current fourth-generation composite PV technology.

The first generation PV was the basic stage consists of a large-area, single layer p-n junction diode, typically made using a silicon wafer and thus, the first generation PV cells were called as silicon wafer-based solar cells. Although the processing methods are difficult and cost per watt is too high, the conventional silicon SCs are dominant in the commercial production of SCs.
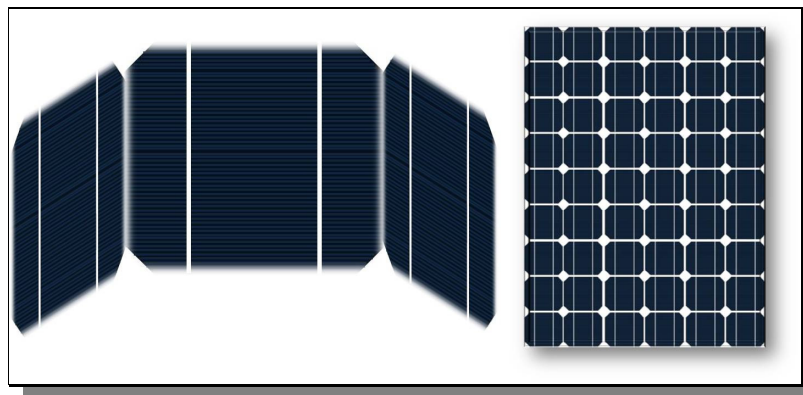
Figure 2.1: A Representative Large-area, First Generation Silicon-wafer PV Cells

13
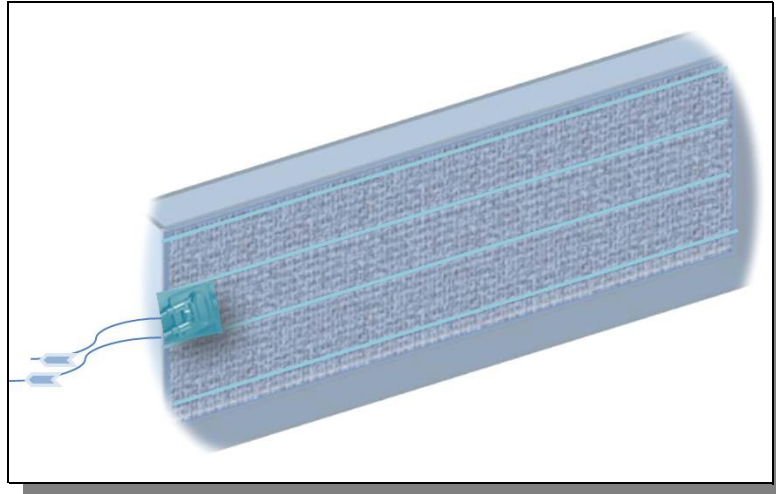
Figure 2.2: A Representative Thin-film, Second Generation Silicon PV Cell

In the second generation PV cells, PV materials based on thin-film deposits of semiconductors were established. These devices were initially designed to be high-efficient and multiple-junction PV cells. For some extent, they have been developed to address energy requirements and production costs of first generation cells. Later, the advantages such as reduced mass of material required for cell design and corresponding reduced costs of thin-film PV materials were noted and various semiconductor materials for thin-film PV cells were developed. Although the efficiencies of these materials were lower comparing to the efficiencies of first generation SCs, the investigation continued because of low manufacturing costs [51-54].

2.2 Photovoltaic Characterization of Conventional Solar Cells

In order to understand organic semiconductor photovoltaics (PVs), simple conventional PVs and their theory need to be explored. The physical phenomenon, photovoltaic effect which is responsible for converting electromagnetic radiation to electrical energy can be better explained with semiconductor theory [51-54].

2.2.1 Photogeneration of Charge Carriers

A conventional PV cell made from silicon consists of *n*-type semiconductor in contact with a *p*-type semiconductor. In general, by the process of doping, silicon is doped with another material, for example, with a more valence electron element, phosphorous; the resulting silicon is called *n*-type. In the similar way, *p*-type silicon would be resulted when doped with boron, an element with one less valence electron than silicon. When a photon hits silicon, the following three processes can occur.

a. If the photon that hits is lower in energy, the photon may pass straight through silicon

b. The photon can reflect off the surface of silicon

c. If the photon energy is higher than the silicon band gap value, the photon can be absorbed by the silicon which either (i) generates heat or (ii) generate electron-hole pairs

When the third process occurs, i.e. when the photon is absorbed by silicon, the energy of photon is given to an electron in the crystal lattice of silicon. This causes excitation of that electron from valence band to the conduction band where it is free to move within the semiconductor. By the similar mechanism, a hole is formed when doped with a *p*-type material. In the other way, the excited electron leaves an empty place in the valence band, forming a hole. Holes, just really are the absence of

electrons, so they carry the opposite (positive) charge. The presence of a missing covalent bond allows the bonded electrons of neighboring atoms to move into the empty holes, leaving another hole behind, and thus a hole can migrate through the lattice. This can be concluded as the photons absorbed in the semiconductor create mobile electron-hole pairs, the charge carriers.

2.2.2   Separation of Charge Carriers

After the process of generation of electron-hole pairs, for producing electricity, the electrons and holes must be separated and move towards the electrodes. In a solar cell, there are two main modes for charge carrier separation. 1-Drift of charge carriers: which driven by an electrostatic field established across the device. 2-Diffusion of charge carriers: from a zone of high carrier concentration to a zone of low carrier concentration. The former mode is the dominant mode of charge carrier separation that occurs in the traditional p-n junction SCs. On the other hand, in non-p-n junction SCs (typically third generation PVs such as dye and polymer thin-film SCs), the previous general electrostatic field, the drift, is absent and the dominant mode of separation is via charge carrier diffusion.

2.2.3   The Traditional p-n Junction

When *p*-type and *n*-type silicon are placed in contact with each other it forms a junction called as a p-n junction. In general, the term junction refers to the boundary interface where the two regions (*p*- and *n*-) of the semiconductor meet. The following set of diagrams explains the phenomenon that occurs at the junction.

(a)

p-n junction

depletion zone   p-n junction

p   *n*

p   *n*

● electrons in *n*-type silicon

○ holes in *p*-type silicon

(b) Depletion zone formation

hole flow

p   *n*

OFF

ON

electron flow

+   −

(c)   FORWARD BIASED

p   *n*

OFF

ON

−   +

(d)   REVERSE BIASED
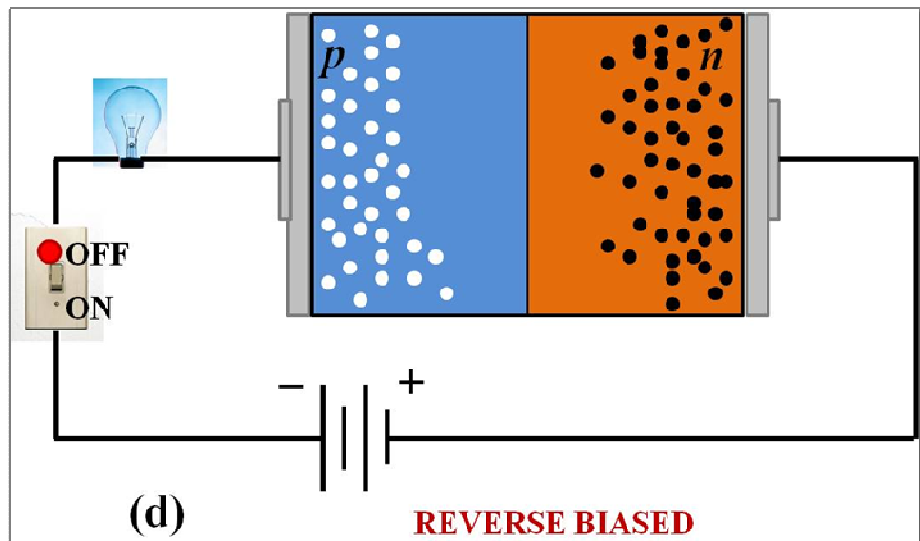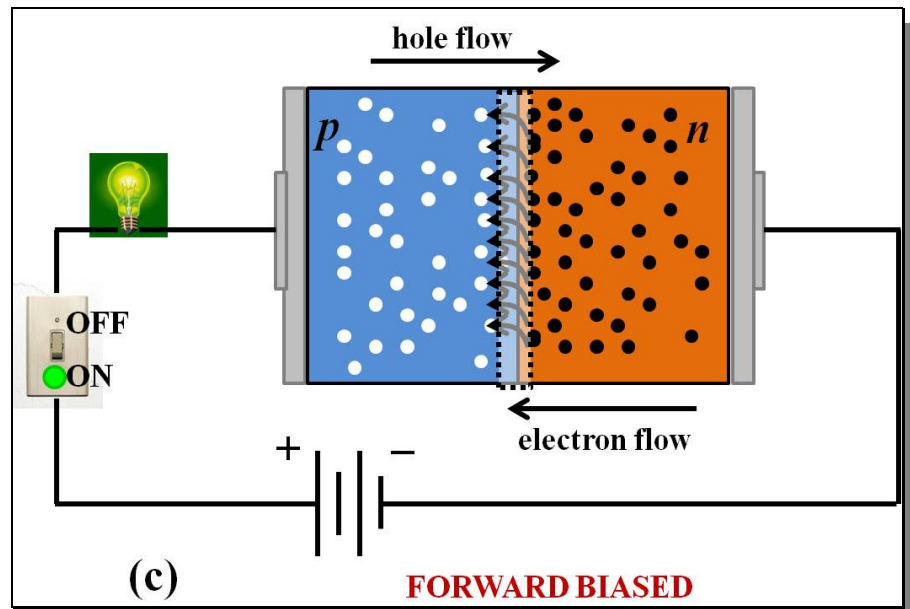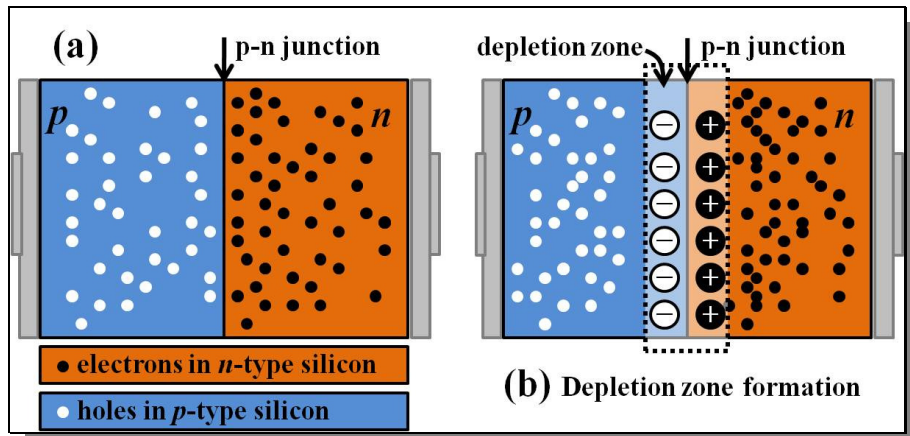
Figure 2.3: The Phenomena Occur at a Traditional p-n Junction of a Solar Cell

17

Part (a) of the Figure 2.3 shows the *n*-type material having free electrons (shown in black dots) and the *p*-type material having holes (shown in white dots). In part (b), a depletion zone was developed. This is because, free electrons on the *n*-side and free holes on *p*-side wander across the junction initially; when a free electron meets a free hole, it can 'drop into it', which results in cancelling of each other and hence a region depleted of any moving charges. Moreover, this leaves a small electrical imbalance inside the crystal lattice. Since the *n*-region is missing some electrons it will obtain a positive charge, the extra electrons that filled the holes in the *p*-region will give it a negative charge. This electrical imbalance never allows generating power. Now, any free charge which wanders into the depletion zone finds itself in a region with no other free charges. This exerts a force on the free charge, driving it back to its 'own side' of the junction away from the depletion zone. This causes the depletion zone swept clean of free charges. At this point, a free charge requires extra energy to overcome the forces from the donor/acceptor atoms to be able to cross the zone. The junction therefore acts like a barrier, blocking any charge flow (current) across the barrier.

From part (c) of the figure, an external power source (a battery) is connected where the negative terminal of the battery is connected to the *n*-type silicon and positive terminal to the *p*-type silicon. Like charges repel each other implying the free electrons pushed towards the p-n junction and to the positive terminal of the external power source; free holes towards the negative terminal (repelled by the positive terminal) of the external power source. If the voltage pushing the electrons and holes has sufficient strength to overcome the depletion zone (approximately 0.7 V for a typical silicon diode), current passes through the diode. When a diode is arranged this way with a power source, it is said to be forward-biased.

When the reverse connections were made (*n*-type silicon to the positive terminal and *p*-type silicon to the negative terminal of external power source), opposite charges attract each other. This results in attraction of positive charged holes (of *p*-type silicon) towards the negative terminal and negatively charged electrons (of *n*-type silicon) to the positive terminal. This causes the charge carriers to be pulled away from the p-n junction and hence an essential larger depletion region creation resulting in no current flow. When a diode is arranged this way with a power supply, it is called reverse-biased.

2.2.4   Factors Affecting the Efficiency of Solar Cells

Although there are several important measures that characterize SCs, the most obvious one is the efficiency. That is, the total amount of electrical power (product of current and voltage) produced for a given amount of solar energy shining (sunshine) on the cell; in terms of percentage, it is expressed as *solar conversion efficiency*.

In simple words, it can be concluded that all the processes responsible for conversion of solar energy into electrical energy affect the efficiency. The following diagram better explains efficiency dependence on particular processes occur in SCs.
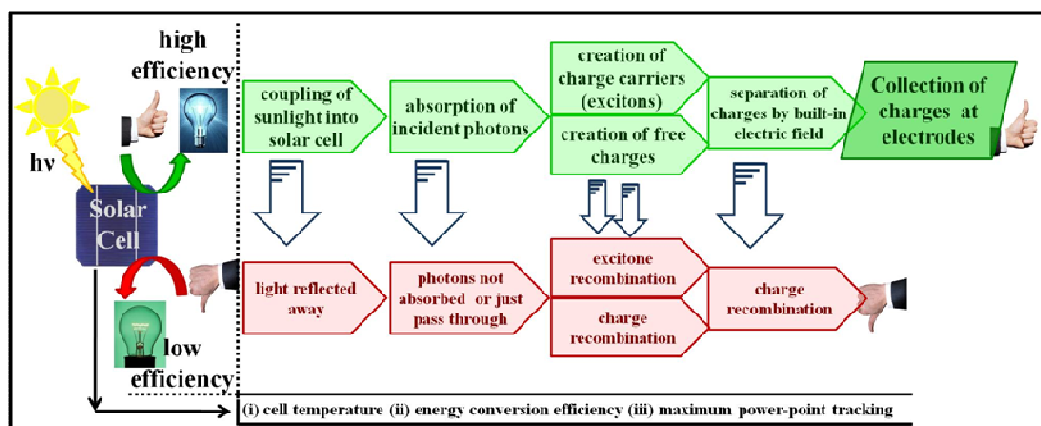
Figure 2.4: Factors that Affect the Efficiency of Solar Cells

19

The illustration shown in Figure 2.4 explores that much of the energy from sunlight reaching a SC is lost before it can be converted into electricity. The starting step explains that all the photons that strike the surface of the cell are not absorbed to generate charge carriers. Furthermore, a PV cell cannot respond to the entire spectrum of sunlight to absorb all the photons. Some photons may not possess enough energy (lower than band gap energy of the semiconductor) to free an electron and some photons (with higher energy than band gap energy) may be wasted as surplus by re-emitting as heat or light. Thus, the inefficient interactions of sunlight with SC material waste so much of original energy available.

Charge carriers in a SC may inadvertently recombine before they are collected at respective electrodes to contribute cell's current. Direct and indirect recombinations are the two possible types where in the former one, light-generated electrons and holes randomly encounter each other and recombine; whereas the later one arises due to the defects in the crystal structure, presence of impurities making the charge carriers recombine easily at the surface or interface of the SC.

Another three critical factors presented in the Figure 2.4 characterize the SC and its efficiency. The first factor, operating temperature of a SC where all most all SCs work best at low temperatures as determined by their material properties. This is because of two main reasons. 1- Much of the light energy striking the cell becomes heat, 2- the band gap of intrinsic semiconductor shrinks. The second factor, energy conversion efficiency (ECE) describes the percentage of power converted and collected, when a SC is connected to an external circuit. The term, ECE is exactly calculated using the ratio of the maximum power point divided by the input light irradiation under the standard test conditions, and the surface area of the SC. In order to increase the ECE, two methods are implemented. One is reducing the reflection of

incident light with an antireflection coating, and the other one is optical confinements of incident light with textured surfaces. As a third affecting factor, tracking of maximum power point (MPP) was ascribed. The MPP operates with DC to DC high efficiency converter that presents an optimal and suitable output power. The MPP was shown in Figure 2.5 and discussed in the next **Section 2.2.5**. Thus, tracking of MPP also somewhat affects the efficiency of a SC.

2.2.5   Maximum Power Point and Fill-factor
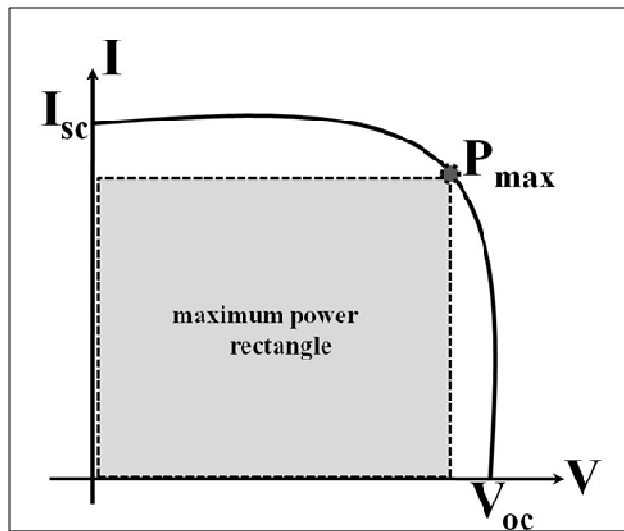
Figure 2.5: Maximum Power Point (MPP) and Fill-factor (ff) from I-V Curve

The representative I-V characteristic graph shown in Figure 2.5 illustrates that the maximum power is generated by the conversion device at a point where the area of the rectangle is largest defined by the fill-factor (ff). The ff was defined as follows.

$$ff = \frac{P_{max}}{V_{oc}} = \frac{V_{max}\, I_{max}}{V_{oc}\, I_{sc}}$$

(Equn. 2.1)

The photo generated current is equal to the current produced by the cell at short circuit (V = 0). The open circuit voltage is obtained when I = 0, and no power is generated under short or open circuit.

When the output voltage of the SC is very low, the output current changes little as the voltage changes, so the SC is similar to the constant current source; whereas, when the voltage is over a critical value and keeps rising, the current will fall sharply and the SC is similar to the constant voltage source. As the output voltage keeps rising, the output power has a maximum power point. The function of catching the MPP is to change the equivalent load taken by the SC, and adjust the working point of the SC in order that the SC can work on the maximum power point when the temperature and radiant intensity are both changing.

2.3 Organic Solar Cells – The Third Generation Photovoltaics

Organic solar cells, one of the third-generation PVs are very different from the previously discussed first and second-generation PVs as they have different bonding system and thus do not rely on a traditional p-n junction to separate photogenerated charge carriers. Third generation contains a wide range of potential solar innovations including photoelectrochemical cells, polymer solar cells, nanocrystalline cells, and dye-sensitized solar cells.
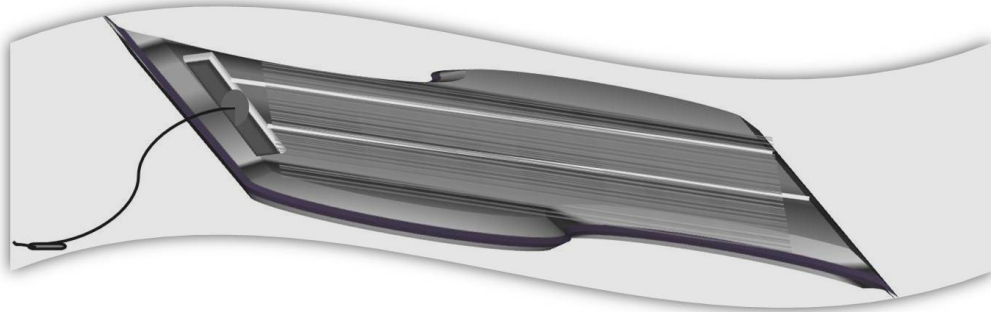
Figure 2.6: A Representative Third Generation Organic-based Solar Cell

The remarkable point concerning third generation SCs is their 'high efficiency/low cost'; which is 'high efficiency/high cost', 'low efficiency/low cost' for first and second generations respectively. The efficiencies of organic SCs reported were quite low comparing to first generation SCs; and that the high efficiencies reported were limited to research-laboratory scale. Still, because of the potential exists, there is a random growth towards the goal of high efficiency and hence the commercialization. The main advantages make them promising alternatives over conventional SCs are their easy processability and tunable optical properties [52-54].

2.3.1 The Principle behind the Design
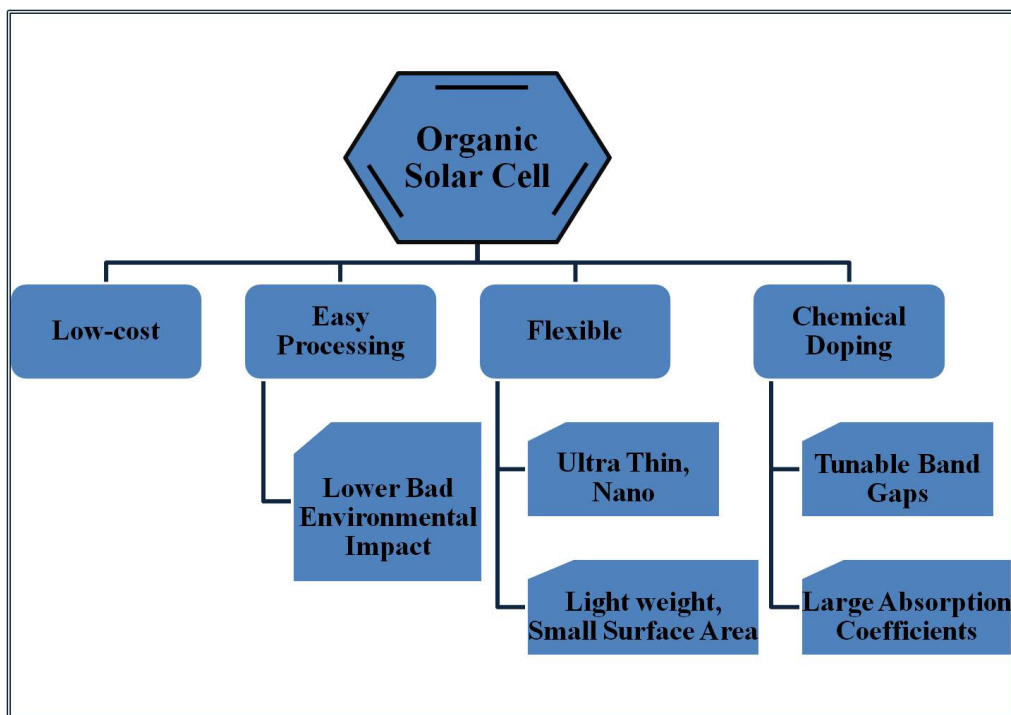
Figure 2.7: Factors Leading to the Design of Organic Solar Cells

An organic solar cell is a photovoltaic cell composed of organic semiconductors or conjugated polymers that are conductive, light absorbing, and charge transportable materials. Several organic semiconductors and conjugated polymers suitable for PVs can be manufactured at lower costs. Moreover, their properties can be tuned according to the necessity by changing their substituents or by doping them with desired materials. Therefore, in conjugated polymers both optical absorption and charge transport are dominated by partly delocalized π and π^* orbitals (the detailed mechanism of charge transport is discussed in next section). This provides tunable band gaps with a variety of absorption capacities. In addition to these interesting properties, they are solution processable, possess film forming abilities, and possess

attracting optical properties. These characteristics inspired the research of PVs to prepare low weight and ultra-thin organic PVs unlike the conventional silicon PVs.

The difference in mechanism of charge transport (from conventional silicon SCs) combining with high absorption capacity per unit area were used as principles in designing organic SCs against conventional silicon SCs which include highly refined silicon (achieved by numerous hard processing steps) assembled in large surface areas. On the other hand, organic SCs rather improvement need to address many questions such as low stability, low efficiency, and uncertainty in molecular picture of organic materials.

2.3.2 The Concept of Exciton(s) – The Mechanism of Charge Transport

Charge transport in organic SCs is dependent on π-bonding orbitals and quantum mechanical wave-function overlap of organic semiconductors composed of conjugated materials. Therefore, the terms, conduction and valence bands discussed in the previous sections of conventional SCs will be shifted to the analogous highest occupied and lowest unoccupied molecular orbitals (HOMO/LUMO). Molecular orbitals (MOs) are created due to molecular interactions of the 'p' orbitals of the carbon atoms in the conjugated backbone. These molecular interactions create bonding-π and antibonding-$\pi*$ molecular orbitals and therefore organic SCs operate in a fundamentally different way. The difference in energy between the two levels produces the band gap that determines the optical properties of the material. Conventional semiconductors are held together by strong covalent bonds that extend three dimensionally, resulting in electronic bands that give rise to its semiconducting properties. Whereas, organic materials have similar intramolecular covalent bonds but are held together by weak intermolecular van der waals interactions. As a consequence, all electronic states are localized on single molecules and do not form

bands. When organic materials are photoexcited, it results in a strong Coulombically bound electron-hole charge pair referred to as "exciton" unlike automatic generation of free charge carriers in conventional SCs. As excitons are strongly bound and do not spontaneously dissociate into charge pairs, generation of charge carrier separation does not necessarily result from absorption of light. Charge transport thus depends on the ability of the charge carriers to pass from one molecular orbital to another. Because of the quantum mechanical tunneling nature of the charge transport, and its subsequent dependence on a probability function, this transport process is commonly referred to as hopping transport. The charge carriers hopping from molecule to molecule are dependent on the energy gap between HOMO and LUMO levels. Carrier mobility is reliant upon the abundance of similar energy levels for the electrons or holes to move to and hence will experience regions of faster and slower hopping [44, 45, 47].

2.3.3 Single Layer Organic Photovoltaics
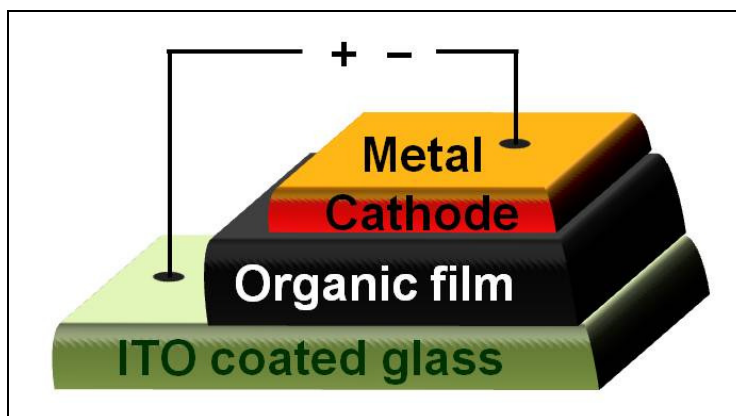
Figure 2.8: A Representative Basic Structure of a Monolayer Organic PV cell

Being the simplest device structure of organic photovoltaic cells, single layer/homojunction organic SCs are typically made by sandwiching the organic

material (polymer) between two metal electrodes (conducting contacts) of different work functions. The work function is the amount of energy necessary to pull an electron from a material. As shown in Figure 2.8, the widely used metallic contacts are indium tin oxide (ITO) with high work function and low work function metals such as Al, Ca, or Mg. the simplest form among various organic photovoltaic cells. The difference in work function between the two metallic conductors provides an electric field in the organic layer. When the organic layer absorbs light, electrons will be excited to LUMO and leave holes in the HOMO forming excitons. The potential created by the different work functions is seldom sufficient to break up the photogenerated exciton pairs, pulling electrons to the positive electrode (low work function electrode) and holes to the negative electrode (high work function electrode). The current and voltage resulting from this process creates power. Since exciton diffusion lengths are short, typically 1 – 20 nm, only those excitons generated in a small region within ≤ 20 nm from the contacts contribute to the photocurrent. In other words, exciton diffusion limits charge carrier generation in such a device. Therefore, charge carrier generation is a function not only of bulk optical absorption but also of available mechanisms for exciton dissociation. Other negative factors are non-radiative recombination at the interfaces and non-geminate recombination at impurities or trapped charges.

In practice, single layer organic PV cells of this type do not work well. They have low quantum efficiencies (~1%) and low power conversion efficiencies (~0.1%). A major problem with them is the electric field resulting from the difference between the two conductive electrodes to separate the photogenerated excitons. Often the electrons recombine with the holes rather than reach the electrode. Using electric field to break up excitons is not the best way, heterojunction based cells which rely

27

on different mechanism (generatin of effective fields) are developed to increase the efficiency [52-54].

2.3.4 Bilayer (Donor/Acceptor) Organic Photovoltaics
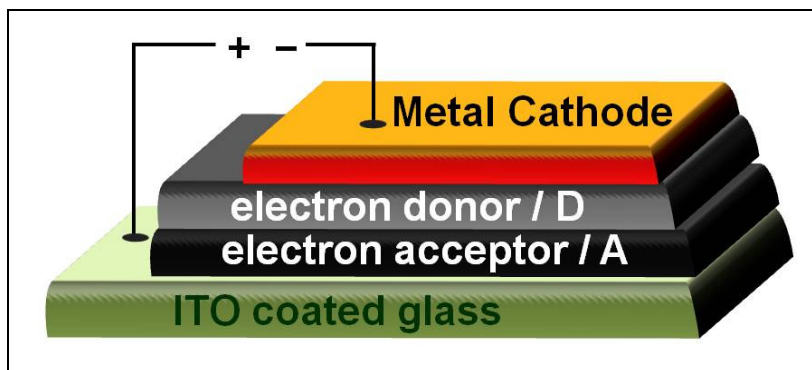
Figure 2.9: A Representative Basic Structure of a Double Layer Organic PV cell

In order to overcome the limitations of Monolayer organic PVs, bilayer organic PVs are introduced with stacking of two different layers in between the two electrically conductive electrodes (Figure 2.9). Most of the developments that have improved performance of organic PV devices are based on donor-acceptor (D/A) heterojunctions. These two different layers of materials have differences in electron affinity and ionization energy; therefore electrostatic forces are generated at the interface between the two layers. If both electron affinity and ionization potential are greater in one material (the electron acceptor) than the other (the electron donor) then the interfacial electric field drives charge separation. For an efficient charge transfer, the LUMO and the HOMO of the donor should lie above those of the acceptor as shown in Figure 2.10. Figure 2.10 explains that the donor, D contacts the higher and the acceptor, A contacts the lower work function metal surfaces to achieve good electron and hole collection respectively. Photogenerated excitons can only be dissociated in a thin layer at the interface/heterojunction and thus the device is

exciton diffusion limited. Therefore, the materials are chosen properly to make the differences (differences in electron affinity and ionization energy) large enough (provided that the differences in potential energy are larger than the exciton binding energy), so these local electric fields are strong, which may break up the photogenerated excitons much more efficiently than the single layer photovoltaic cells do. This kind of bilayer architecture is also called planar donor-acceptor heterojunctions [2, 52-54].
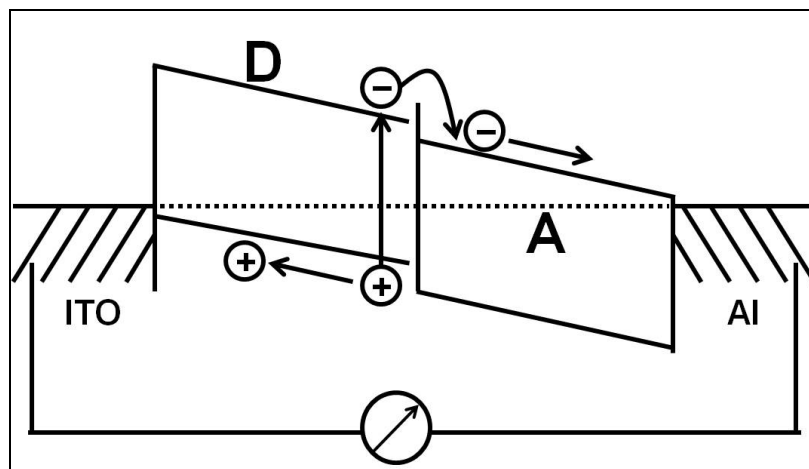
Figure 2.10: Mechanism of Charge Carrier Separation in a Bilayer Organic PV cell (Diagram is drawn neglecting all kinds of possible band bending due to energy level alignments)

While the formation of a classical p-n junction requires doped semiconductors with free charge carriers to form the electric field in the depletion region, the charge transfer in bilayer heterojunction between undoped D/A materials is due to the differences in the ionization potential and electron affinity of the adjacent materials. As shown in Figure 2.10, upon photon absorption in the donor D, the electron is excited from HOMO to LUMO. If the electron acceptor A is in close proximity, the

electron may be transferred to the LUMO of A which is energetically potential when $I_D^* - A_A - U_C < 0$, where I_D^* is the ionization potential of the excited donor (D*), A_A is the electron affinity of acceptor, and U_C is the effective Coulomb interaction, respectively. The release in electron energy may then be used to separate the electron and the hole from their Coulomb potential. This photoinduced charge transfer (CT) only occurs under illumination, since it needs the excitation energy of the electron in the donor to reach the LUMO of the acceptor. There are some experimental indications supported by theoretical considerations of a formation of an interfacial dipole between D/A phases independent of illumination. This can stabilize the charge separated state by a repulsive interaction between the interface and the free charges. Therefore, the success of the D/A concept lies to a great extent in the relative stability of the charge separated state. Thus, the recombination rate between holes in D and electrons in A is several orders of magnitude lower than the forward CT rate.

After the excitons are dissociated at the materials interface, the electrons travel within the *n*-type acceptor and the holes travel within the *p*-type donor material. Hence holes and electrons are effectively separated from each other and although charge recombination is greatly reduced and it depends more on trap densities. As a consequence, the photocurrent dependency on illumination intensity can be linear.

The efficiency of this type of planar heterojunction device is limited, however, by the exciton diffusion length, which is the distance over which excitons travel before undergoing recombination, approximately 5–10 nm in most organic semiconductors. Excitons formed at a location further than 5–10 nm from the heterojunction cannot be harvested. In other words, in order for most excitons to diffuse to the interface of layers and break up into carriers, the layer thickness should also be in the same range with the diffusion length. However, typically a polymer layer needs a thickness of at

least 100 nm to absorb enough light. At such a large thickness, only a small fraction of the excitons can reach the heterojunction interface. The active area of this type of SC is thus limited to a very thin region close to the interface, which is not enough to absorb most of the solar radiation flux. To address this problem, a new type of heterojunction PV cells is designed, which is the dispersed heterojunction photovoltaic cells.

2.3.5 Blend Layer (Dispersed Heterojunction) Organic Photovoltaics

The essence of bulk heterojunction is to blend donor and acceptor components in a bulk volume so that each D/A interface is within a distance less than the exciton diffusion length of each absorbing site. This was the basic principle applied in order to overcome the difficulties observed in the previous bilayer planar D/A heterojunctions. Moreover, the most efficient organic-polymer SCs to date were based on this architecture [2, 52].
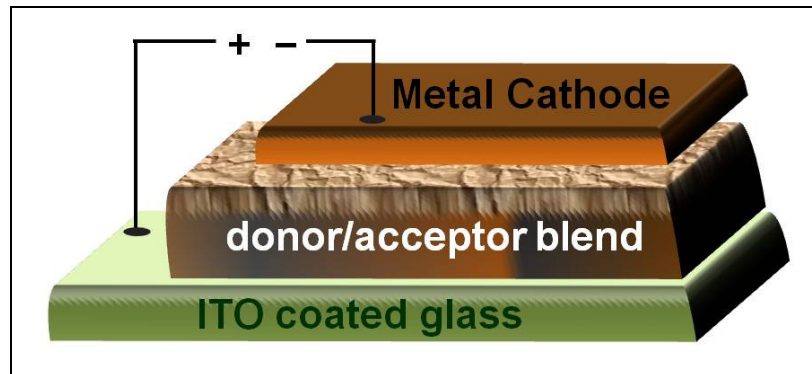
Figure 2.11: A Representative Blend Dispersed Heterojunction Organic PV cell

In this type of PV cell, the electron donor and acceptor are mixed together, forming a nanoscopically phase-separated polymer blend in the active layer (blend is shown in Figure 2.11). This leads to donor and acceptor domains, separated by a

large interfacial area. If the domain size in either material is similar to the exciton diffusion length, then wherever an exciton is photogenerated in that material, it is likely to diffuse to an interface and break up (Figure 2.12). Electrons move to the acceptor domains then were carried through the device and collected by one electrode, and holes were pulled in the opposite direction and collected at the other side. Compared to the bilayer architecture, in a bulk-heterojunction structure, excitons have to diffuse a much shorter distance to the interface and charge generation takes place throughout the bulk-blend, leading to high charge photogeneration efficiency (Figure 2.12).
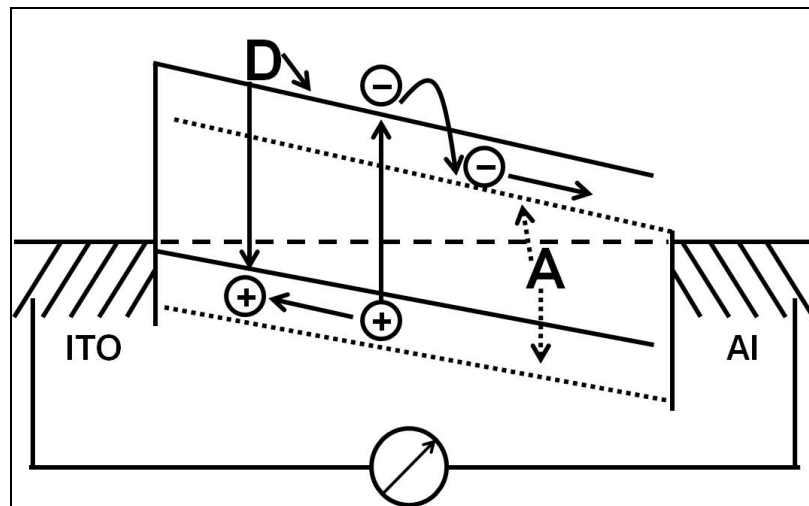
Figure 2.12: Mechanism of Charge Carrier Separation in Heterojunction PV cell (Donor, D is blended with the acceptor, A throughout the whole film. Thus photogenerated excitons can be dissociated into charges at any place) [2, 52]

If continuous paths or network exist in each material (D and A) from the interface to the respective electrodes, then the separated charge carriers may travel to the metal contacts and deliver to the external circuit. These percolated pathways that required for blend architecture is different from bilayer architecture where the D and A phase

32

contact the anode and cathode selectively. Therefore, unlike bilayer architecture, in the blend structure PV cell, the D/A phase have to form a bicontinuous and interpenetrating network. Hence, the bulk heterojunction devices made of blended D/A materials are much more sensitive to the morphology in the blend. This strong dependence on morphology of the blend is the main drawback of dispersed heterojunction architecture concept.

2.3.6 Dye Sensitized Solar Cells

The PV devices of third generation that can mostly challenge the inorganic solid-state junction devices are dye sensitized solar cells (DSSCs) according to Gratzel, the inventor of DSSCs [55]. The basic principle applied in DSSCs is replacing the contact phase to the semiconductor by an electrolyte, liquid, gel or solid, thereby forming a photo-electrochemical cell. Therefore, optical absorption and the charge separation processes occur by the association of a sensitizer as light-absorbing material with a wide band gap semiconductor of nanocrystalline morphology.
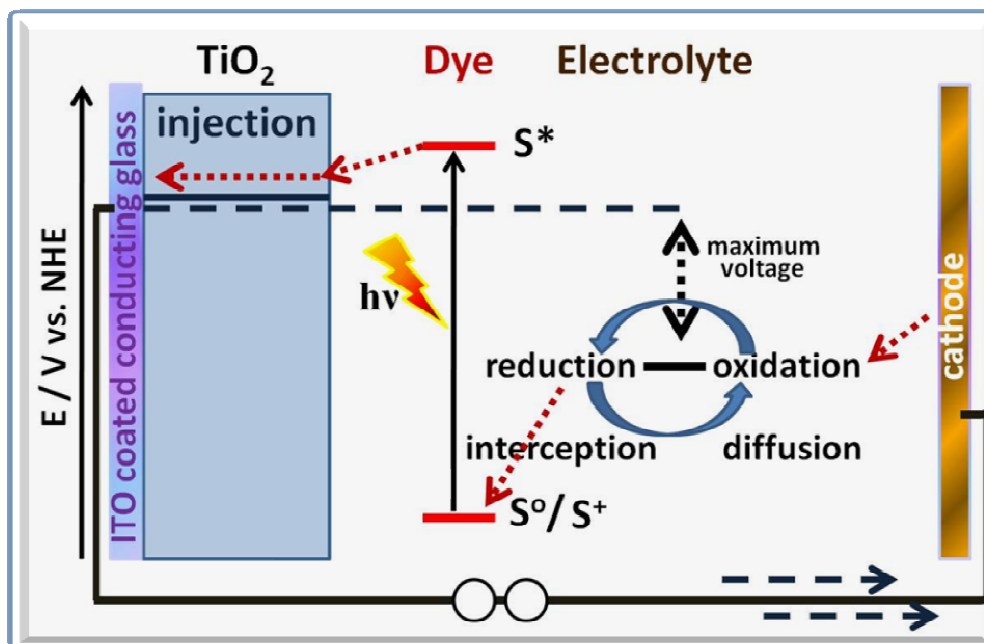
Figure 2.13: General Operation of a Dye Sensitized Solar/Photovoltaic Cell

33

At the heart of a typical DSSC system, a mesoporous oxide (commonly TiO$_2$ is used) layer composed of nanometer sized particles have been sintered together to allow for electronic conduction. This TiO$_2$ layer is deposited on a conductive ITO glass. The dye is placed over the above semiconductor film, in contact with an electrolyte. The excitation of the dye upon irradiation is followed by injection of the resulting electrons into the conduction band of the semiconductor, from where they reach the cell anode (usually a conductive glass) by diffucion (as a result of an electron concentration ingradient). Regeneration of dye electrons occurs through donation from a redox electrolyte in contact with the dye. This typically occurs through an organic solvent containing an iodide/triiodide couple. Triiodide is reduced in turn at the counter electrode, while electron migration from the anode to the counter electrode closes the circuit. The voltage generated is equal to the difference between the Fermi level of the electron in the solid TiO$_2$ and the redox potential of the electrolyte [55, 56].

Currently, an intensive research on fourth-generation composite PV technology is focused worldwide in parallel with continuous development on the SCs based on previous generations. 4th generation SCs are based on polymers with nanoparticles to make a single multispectrum layer. Later, the layers can be stacked to make more efficient and cheaper multispectrum SCs. However, the investigation continues for large scale PV generation of electricity to become economically feasible. Especially, there has been recent development and rapid progress in the fabrication of PVs and optoelectronic molecular materials using organic semiconductors.

2.4 *p*- and *n*- Type Organic Semiconductors

Organic electronics such as organic light emitting diodes (OLEDs), organic thin film transistors, organic field effect transistors, organic capacitors, printable circuits, organic material based sensors, and organic photovoltaic devices were all based on organic semiconductors. These organic semiconductors are mostly composed of organic materials which are highly conjugated molecules or polymers that support the injection and therefore allow the mobility of charge carriers. As it has been discussed in the previous sections, like their inorganic counterparts, organic material based devices operate because of some specific properties and interactions among *p*- and *n*- type conducting and/or semiconducting materials.

2.4.1 *p*-type Organic Semiconductors

A great majority of *p*-type electronic organic materials have been investigated and well-characterized. The well known *p*-type semiconductors are acenes such as pentacene, heterocyclic oligomers such as oligo- and poly- thiophenes. These materials can become conducting when electrons are added or removed from the conjugated π-orbitals via doping. That is, these conjugated molecules involving π-conjugation have high HOMO levels and exhibit electron-donating properties. The most notable property, electrical conductivity, therefore arises from the delocalization of electrons along the polymer backbone and thus developing in an extended π-system with a filled valence band; resulting the name 'synthetic metals'. However, conductivity is not only the exciting property that arises from delocalization but also results in various optical properties. Doping is usually performed at much higher levels in conducting polymers than in semiconductors. For example, *p*-doping is the partial oxidation of the polymer by a chemical oxidant or an

35

electrode and causes depopulation of the bonding *p* orbital (HOMO) with the injection of "holes". *n*-Doping is the partial reduction of the polymer by a chemical reducing agent or electrode with the injection of electrons in the antibonding *p* system (LUMO). When electrons are removed (*p*-doping) or added (*n*-doping) from the conjugated π-system, a charged unit termed as 'bipolaron' is formed. When the bipolaron moves as a unit up and down the polymer chain, it results in the conductivity of the polymer. Reduction of the conducting polymer, *n*-doping, is much less common than *p*-doping. For example, an early study of electrochemical *n*-doping of poly(bithiophene) found that the *n*-doping levels are less than those of *p*-doping, the *n*-doping cycles were less efficient, the number of cycles required to reach maximum doping was higher, and the *n*-doping process appeared to be kinetically limited, possibly due to counterion diffusion in the polymer [53, 54].

2.4.2   *n*-type Organic Semiconductors

In contrast to *p*-type, *n*-type organic materials developed were limited to a small number. This is due to the difference in molecular design of both types. In the molecular design point of view, designing electron-rich conjugated polymers (*p*-type) is easier than electron-poor ones (*n*-type). Moreover, the developed *n*-type materials were having some serious drawbacks such as poor solubility, poor stability (in air), and somewhat difficulty of synthesis. Therefore, there is a need for new stable *n*-type organic materials that can improve the performance and durability of organic devices.

Most of the polymers currently used as *n*-type materials in PVs are hydrocarbon-based polymers with electron-withdrawing substituents such as cyano or nitro groups in addition to the famous fullerene, perylene, and naphthalene derivatives [53, 54].

2.4.3   Characterization of *p*- and *n*-type Materials

The polymers or conjugated compounds which act as *p*- and *n*- type materials need to be well characterized in order to find their potential to use in material devices. The following properties play a key role in identifying the compound's stability and therefore its use in various applications.

2.4.3.1 Optical Properties and Photophysics

The photophysics of molecular systems (both *p*- and *n*- types) are strongly influenced by their environment as those characteristics are not intrinsic to the material itself. The influence of a solvent is one major function that affects the photophysics of the material in addition to the affect of processing and operational conditions.

There are several desirable characteristics of *p*- and *n*- type materials which are organic electronic application specific. All these characteristics can be revealed by the well-characterization of following optical, electrochemical, thermal and photochemical properties of the materials.
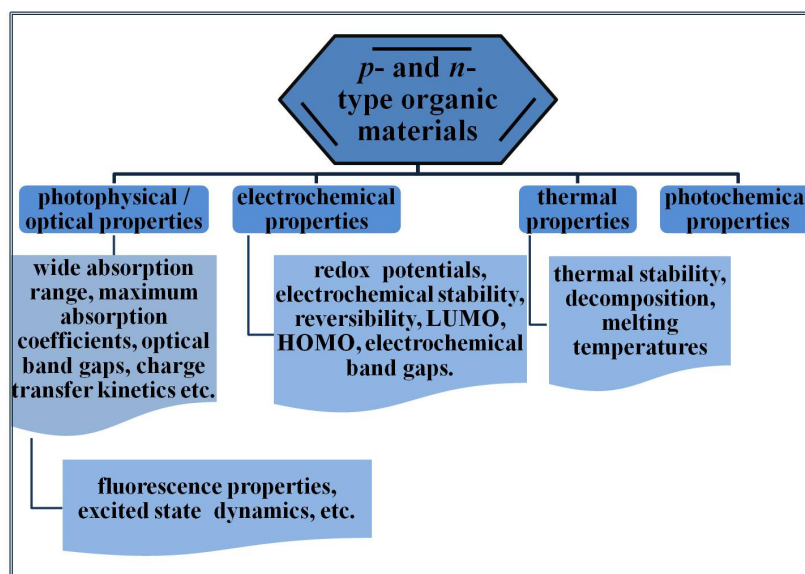
Figure 2.14: Characterization of *p*- and *n*- type Materials

2.4.3.2 Electrochemical Properties

Electrochemical properties of *p-* and *n-* type materials such as Redox potentials, HOMOs, LUMOs and Electrochemical band gaps (E_g) make a complete band structure of the material and thus help identifying the suitable electron donor, corresponding to a D/A system for PV device architecture. One best way to measure the electrochemical parameters (calculations were shown in Chapter 4) is to record the cyclic/squarewave voltammograms of the compound by implying voltammetry techniques. In addition, the cyclic volyammograms reveal the concerned electrochemical stability and reversibility of the material.

2.4.3.3 Thermal Properties

By using various thermogravimetric analysis techniques such as DSC and TGA, thermal properties of these materials can be investigated. The properties such as decomposition temperature, decay of weight at the function of temperature, glass transition temperature, and melting point, etc. help to picture the thermal stability of the material for its use in various molecular devices.

Chapter 3

EXPERIMENTAL

3.1 Materials

All the chemicals were used directly without any further purification. But the solvents were distilled based on particular purpose according to the standard literature procedures (Perrin and Armarego, 1980). Pure spectroscopic grade solvents were used for spectroscopic measurements. 1,4,5,8-naphthalenetetracarboxylic dianhydride, perylene-3,4,9,10-tetracarboxylic dianhydride, 2-[2-(2-{2-[2-(2-Hydroxy-ethoxy)-ethoxy]-ethoxy}-ethoxy)-ethoxy]-ethanol (hexaethylene glycol) were obtained from Aldrich.

3.2 Instruments

^{1}H (400 MHz) and ^{13}C NMR (100 MHz) spectra were recorded on a Bruker/XWIN spectrometer in CDCl$_3$. Tetramethyl silane (TMS) was used as an internal standard.

FT-IR spectra were obtained at 4 cm^{-1} resolution with KBr pellets at 32 co-averaged scans using Mattson Satellite FTIR spectrometer.

UV spectra in solutions were measured on a Varian-Cary 100 spectrometer. UV spectrum in solid state was obtained in thin film using a Perkin-Elmer UV/VIS/NIR Lambda 19 spectrometer, equipped with solid accessories.

Emission spectra were recorded using a Varian-Cary Eclipse Fluorescence spectrophotometer.

Elemental analysis was performed on a Carlo-Erba-1106 C, H, and N analyzer.

Thermal analyses were carried out on a Diamond Differential Scanning Calorimeter (DSC) at a heating rate of $10\ ^{\mathrm{o}}C \cdot min^{-1}$ in nitrogen. Thermo Gravimetric Analysis (TGA) thermograms were obtained on a Tg-Ms: Simultane TG-DTA/DSC apparatus STA 449 Jupiter from Netzsch, equipped with Balzers Quadstar 422 V at a heating rate of $10\ ^{\mathrm{o}}C \cdot min^{-1}$ in nitrogen.

The weight-average molecular weight (M_w) and number-average molecular weight (M_n) were determined by gel permeation chromatography (GPC) with a high performance liquid chromatography (HPLC) system from "Thermo Separation Products" using two columns (PSS-PFG, 7 μm 10^2 and $10^3\ \overset{\mathrm{o}}{A}$), with isocratic pump, autosampler, in combination with a detector Shodex RI71. The samples were to run in hexafluoroisopropanol (HFIP) with 0.05 M potassiumtrifluoracetate (KTFAc) and calibrated with polymethylmethacrylate (12 narrow PMMA) standard at $23\ ^{\mathrm{o}}C$. The oligomer, EONPI was completely soluble in HFIP. The solution was filtered through a 1 μm filter unit and 50 μm was injected for the GPC measurement.

Intrinsic viscosity was measured at $25\ ^{\mathrm{o}}C$ in *m*-cresol, using an Ubbelohde viscometer unless otherwise specified the conditions. The intrinsic viscosity [η] was obtained by measuring specific viscosity η_sp at five different concentrations, plotting $\log(\eta_\mathrm{sp}/c)$ vs c and extrapolating to zero concentration.

Some of the products were isolated by Flash column chromatography performed on *Merck silica gel* 60 (0.063 – 0.20 mm or 0.040 – 0.063 mm). All solvents were distilled prior to the column use.

The redox properties of the compounds were studied by cyclic voltammograms and square wave voltammograms. Cyclic voltammograms in solutions were performed using a three-electrode cell with a polished 2 mm glassy carbon as working electrode and Pt as counter electrode. The concentrations of the solutions were 10^{-3} M in electroactive material and 0.10 M in supporting electrolyte tetrabutylammoniumhexafluorophosphate (TBAPF6). Data was recorded on EG & GPAR 273A COMPUTER-CONTROLLED POTENTIOSTAT. Ferrocene was used as internal reference. For the compounds, TEONPI and HP-CH, the measurements were carried out on "The Gamry Instruments, REFERENCE 600 Potentiostat/Galvanostat/ZRA".

Fluorescence lifetime measurements were performed by time correlated single photon counting technique (FLS920, Edinburgh Instruments).

3.3 Methods of Syntheses

In this section, syntheses methods of electron acceptors were presented. As electron-accepting (*n*-type) materials, four different compounds composed of perylene and naphthalene moieties were established [9, 10, 15, 59]. The well known perylene and naphthalene dyes [9-15, 57-59] were prepared by modeling with different kinds of substituents. In addition to the promising perylene and naphthalene polymers, some oligomers were also prepared which possess great stabilities, high fluorescence quantum yields and color tunabilities [9, 10].

(i) With a specially synthesized diamine, EODA (Scheme 3.1), based on hexaethylene glycol; a concentration dependent color tunable perylene oligomeric diimide (Bodapati and Icil, 2008) was synthesized (Scheme 3.2) [9].

(ii) By using the same diamine, EODA (Scheme 3.1), a light emitting, solvent and concentration dependent color tunable naphthalene oligomeric diimide (Scheme 3.3) was synthesized (Bodapati and Icil, 2011, *in print*) [10].

(iii) A similar commercial diamine with three ethoxy groups was used to produce a naphthalene polyimide by Mustafa E Ozser (Ozser, Bodapati, and Icil *in press*). For comparison and for the purpose of PV cells, electrochemical properties of the compound were explored. (Scheme 3.4) [59].

(iv) A perylene substituted fluorescent chitosan polymer synthesized by Devrim Ozdal (Ozdal, Asir, Bodapati, and Icil, *in press*) (Scheme 3.5) was also included in the list of electron-accepting materials to explore in detail the electrochemical properties of perylene dyes [15].

The diamine, 2-[2-(2-{2-[2-(2-amino-ethoxy)-ethoxy]-ethoxy}-ethoxy)-ethoxy]-ethylamine, EODA was synthesized via three steps (Scheme 3.1) (Zych and Iversion, 2000), (Bodapati and Icil, 2008) [9].
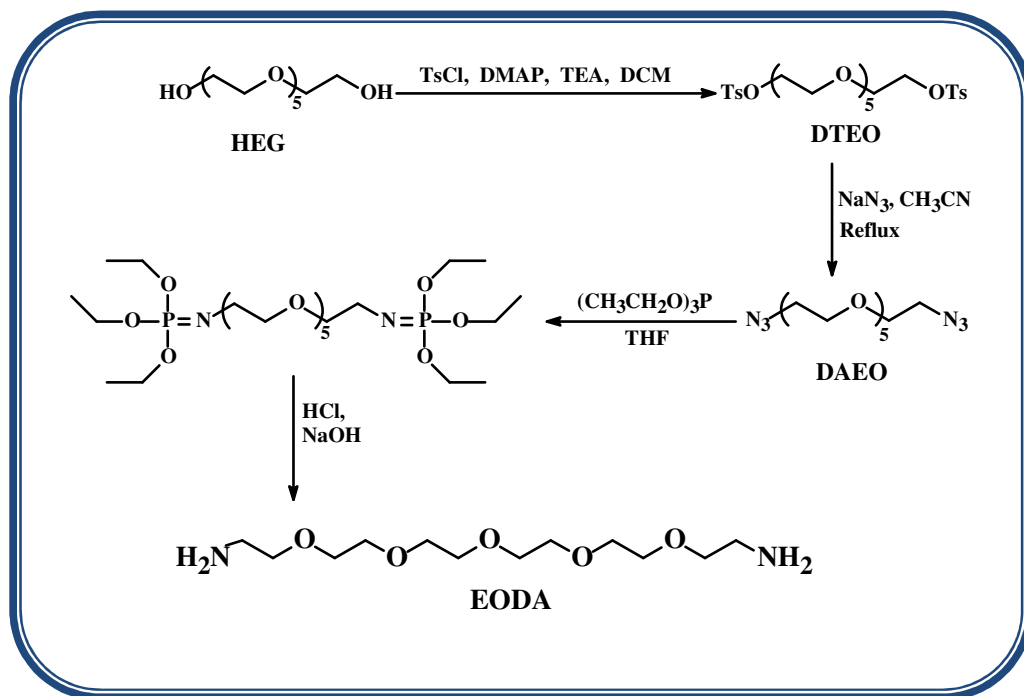
Scheme 3.1: Synthesis of 2-[2-(2-{2-[2-(2-amino-ethoxy)-ethoxy]-ethoxy}-ethoxy)-ethoxy]-ethylamine, EODA (Bodapati and Icil, 2008) [9].

A highly soluble, flexible – rigid – flexible, perylene oligomer dye, termed EOPPI was synthesized by the reaction between the chromophore, perlyene 3,4,9,10-tetracarboxylic dianhydride (PDA) and diamine, EODA (Scheme 3.2).
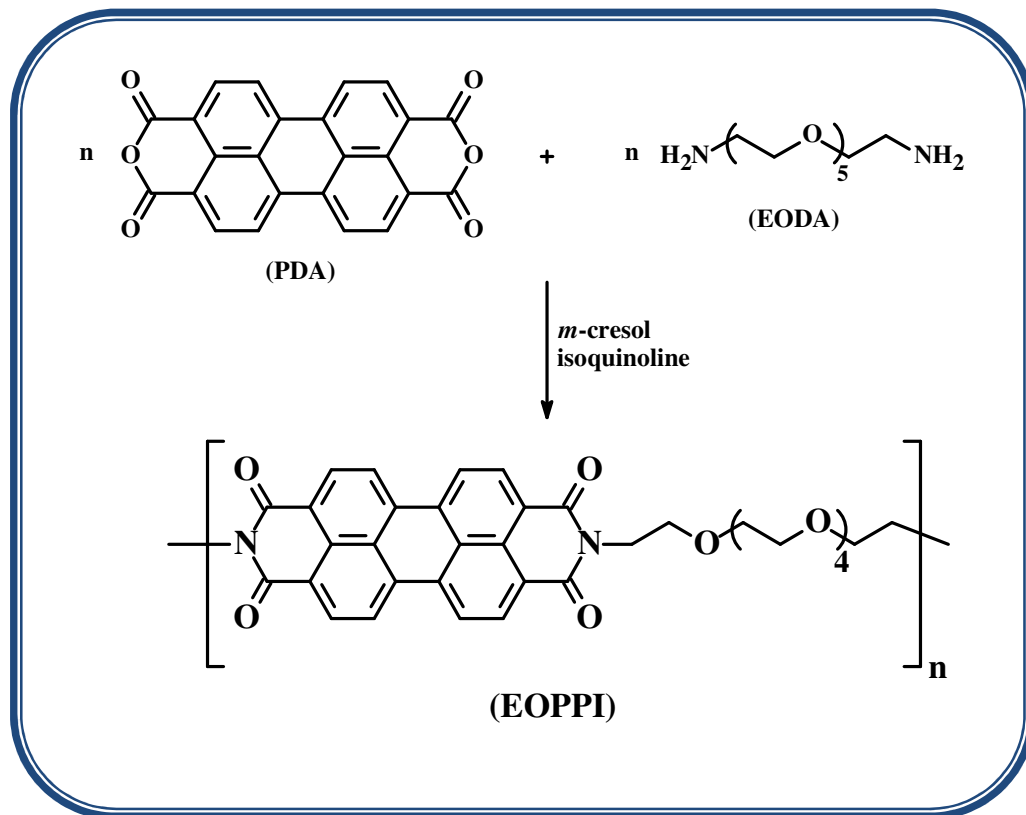
Scheme 3.2: Synthesis of Perylene-3,4,9,10-tetracarboxylic acid-Bis-(*N,N′*-Bis 2-[2-(2-{2-[2-(2-hydroxy-ethoxy)-ethoxy]-ethoxy}-ethoxy)-ethoxy]-ethylpolyimide, EOPPI (Bodapati and Icil, 2008) [9].

Similar to the perylene oligomeric dye, a naphthalene oligomeric dye (EONPI) was synthesized by the reaction between 1,4,5,8-naphthalenetetracarboxylic dianhydride, NDA and diamine, EODA (Scheme 3.3) (Bodapati and Icil, 2011, *in print*) [10].
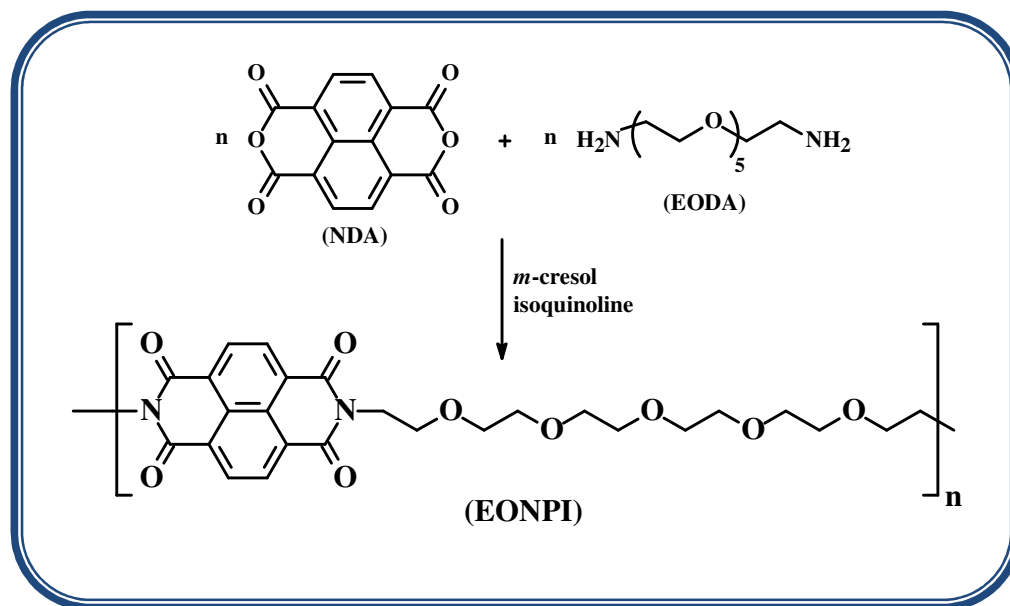
Scheme 3.3: Synthesis of naphthalene-1,4,5,8-tetracarboxylic acid-bis-(*N*,*N*′-bis 2-[2-

(2-{2-[2-(2-hydroxy-ethoxy)-ethoxy]-ethoxy}-ethoxy)-ethoxy]-ethyl polyimide,

EONPI (Bodapati and Icil, 2011, *in print*) [10].

A new polyimide was synthesized by Mustafa E Ozser using naphthalene dianhydride (NDA) as hydrophobic rigid unit and another aliphatic ehoxy amine as flexible spacer. The polymer synthesis scheme was shown below (Scheme 3.4) (Ozser, Bodapati, and Icil, *in press*) [59].
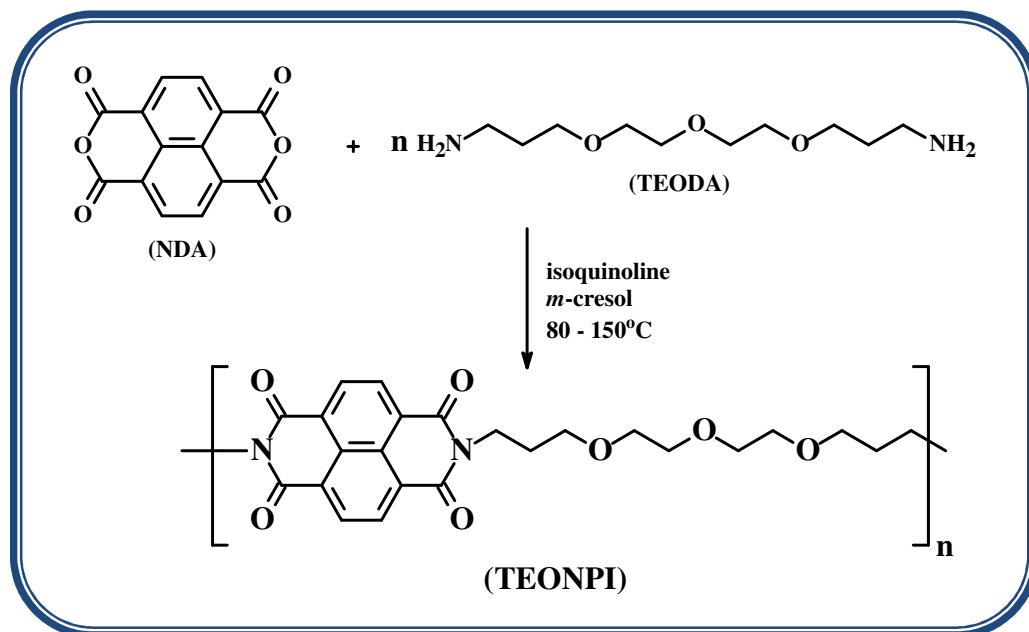
Scheme 3.4: Synthesis of Poly[bis-*N,N′*-(3-(2-(2-(3-aminopropoxy)-ethoxy)-ethoxy)-propyl)-1,4,5,8-naphthalene imide], TEONPI (Ozser, Bodapati, and Icil, *in press*) [59].

A novel perylene polymer was synthesized by Ozdal recently. For the first time, a biopolymer, chitosan (CH) was substituted on a perylene monoimide dye (OH-PMI) (Scheme 3.5) (Ozdal, MS Thesis) (Ozdal, Asir, Bodapati, and Icil, *in press*) [15].
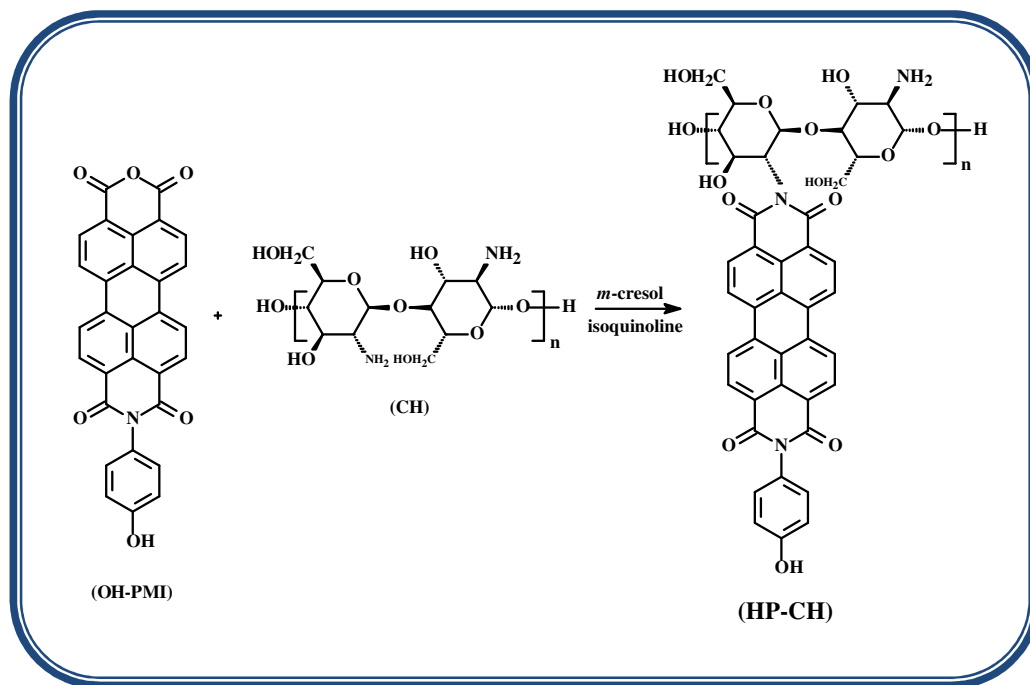
Scheme 3.5: Synthesis of *N*-(4-hydroxyphenyl)-3,4,9,10 perylene tetracarboxylic-3,4-anhydride-9,10-imide conjugated chitosan, HP-CH (Ozdal, Asir, Bodapati, and Icil, *in press*) [15].

3.4 Importance of Synthetic Designs of Electron-accepting (*n*-type) Materials

Perylene and Naphthalene dyes were most attractive with high stabilities and possess outstanding applications in many fields of industry. Several perylene and naphthalene dyes were reported in literature. The most of the dyes reported were either poor or appreciably soluble. In order to make the organic *n*-type materials more commercial, easy processability of the compounds is a necessary criterion in addition to the exciting optical properties.   The present work was focused on the design and synthesis of perylene and naphthalene dyes that are highly soluble and possess good photochemical, electrochemical, and thermal stabilities, so that they are suitable to photonic applications and photovoltaics in combination of electron donating polymers. The main advantage of perylene and naphthalene dyes is their reactivity with amines and therefore the desired properties can be easily tailored with various substituents. It is, therefore, easy to model the dyes according to the architecture of bulk-hetero junction PVs and thereby to improve the power conversion efficiency.

3.5 Synthesis of Perylene-3,4,9,10-tetracarboxylic acid-Bis-(*N*,*N'*-Bis 2-[2-(2-{2-[2-(2-hydroxy-ethoxy)-ethoxy]-ethoxy}-ethoxy)-ethoxy]-ethylpolyimide, EOPPI

(Bodapati and Icil, 2008)
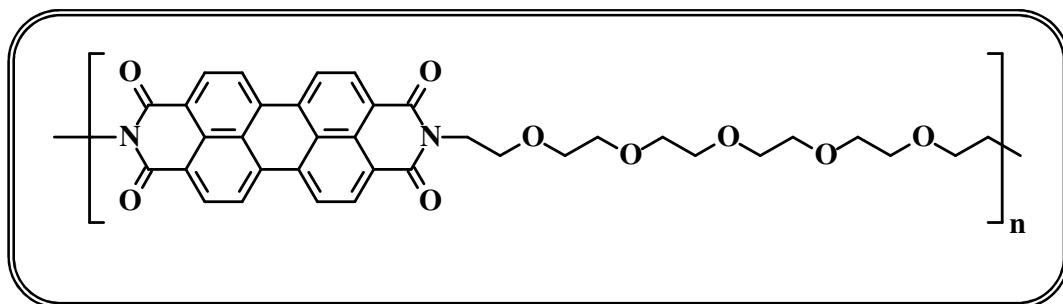
With the specially synthesized diamine (EODA) and perylenetetracarboxylic dianhydride, the flexible-rigid-flexible perylene oligomer was synthesized and characterized in detail.

3.6 Synthesis of Naphthalene-1,4,5,8-tetracarboxylic acid-bis-(*N*,*N*′-bis 2-[2-(2-{2-[2-(2-hydroxy-ethoxy)-ethoxy]-ethoxy}-ethoxy)-ethoxy]-ethyl polyimide, EONPI

(Bodapati and Icil, 2011, *in print*)
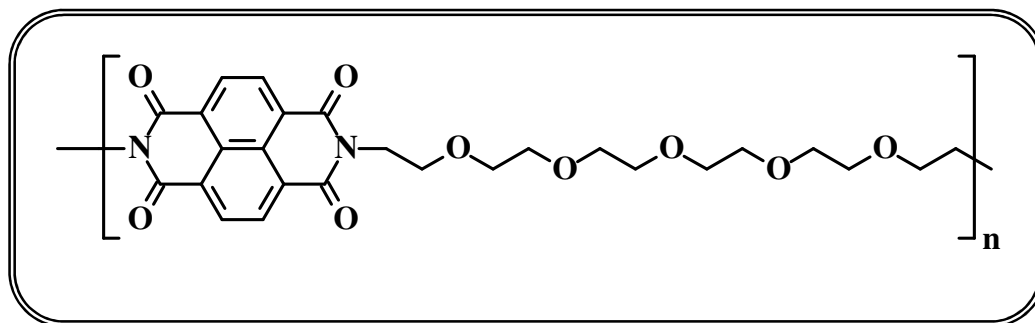
1,4,5,8-naphthalenetetracarboxylic dianhydride (0.513 g, 1.91 mmol), 2-[2-(2-{2-[2-(2-amino-ethoxy)-ethoxy]-etoxy}-ethoxy)-ethoxy]-ethylamine **(EODA)** (0.535 g, 1.91 mmol) were heated in a carefully dried solvent mixture (40 mL *m*-cresol and 10 mL isoquinoline) under nitrogen atmosphere at 100 ^{o}C for 6 h, at 120 ^{o}C for 3 h, at 150 ^{o}C for 5 h and finally at 180 ^{o}C for 8 h. The reaction water was collected in the Dean-Stark trap attached to the system. The solution was allowed to cool and was poured into 300 mL diethyl ether. The precipitate was filtered off and dried at 100 ^{o}C under vacuum overnight. The crude product was purified by crystallization from dichloromethane/diethyl ether to obtain the polymer as a shining black powder.

Yield: 90% (0.882 g); **Color:** Black shining powder; **mp:** >300 ^{o}C.

FT-IR (KBr, cm^{-1}): ν = 3065, 2865, 1704, 1665, 1580, 1335, 1105.

UV-Vis (CHCl$_3$) λ$_{max}$, nm: 343, 361, 380, 397, 414.

Fluorescence (CHCl$_3$) λ$_{max}$, nm: 392, 409, 513. Φ_f = 0.017.

Anal. calcd for (C$_{26}$H$_{28}$N$_2$O$_9$)$_n$, (512.52)$_n$: C, 60.92; H, 5.52; N, 5.47. **Found:** C, 62.91; H, 4.76; N, 5.09.

3.7 Synthesis of Poly[bis-*N*,*N*′-(3-(2-(2-(3-aminopropoxy)-ethoxy)-ethoxy)-propyl)-1,4,5,8-naphthalene imide], TEONPI

(Ozser, Bodapati, and Icil, *in press*)
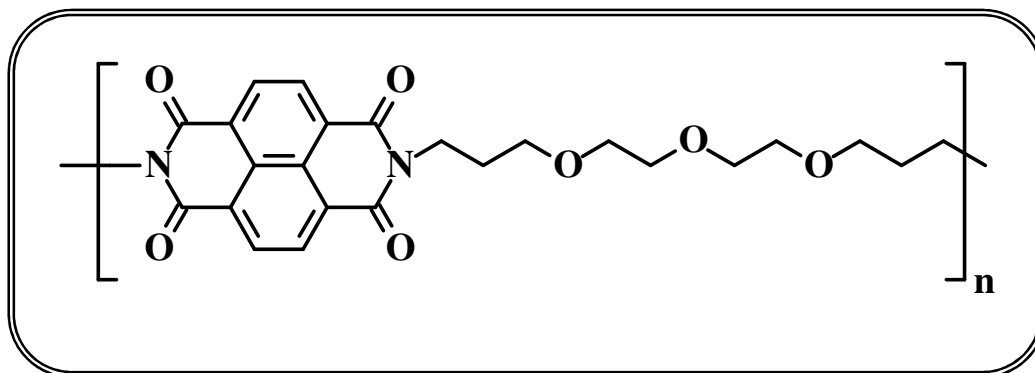
By the classical one step condensation between 1,4,5,8-naphthalenetetracarboxylic dianhydride **(NDA)** and 4,7,10-trioxa-1,3-tridecanediamine **(TEODA)**, the polymer was synthesized by Mustafa E Ozser.

3.8   Synthesis   of   *N*-(4-hydroxyphenyl)-3,4,9,10   perylene tetracarboxylic-3,4-anhydride-9,10-imide conjugated chitosan, HP-CH

(Ozdal, MS Thesis)

(Ozdal, Asir, Bodapati and Icil, *in press*)
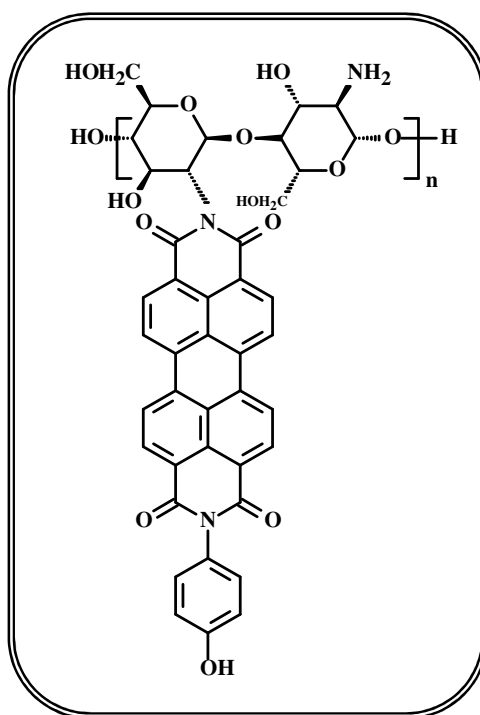
The fluorescent perylene substituted chitosan polymer was synthesized by Devrim Özdal first time in literature by introducing low molecular weight chitosan onto the perylene dye.

3.9 General Synthesis Reaction Mechanism of Electron-accepting (*n*-type) Materials

STEP 3

Proton abstraction

Proton abstraction

+ 2 HO$^{\ominus}$ + 2

STEP 4

2 + 2 $^{\ominus}$OH $\longrightarrow$ 2 + 2 H$_2$O
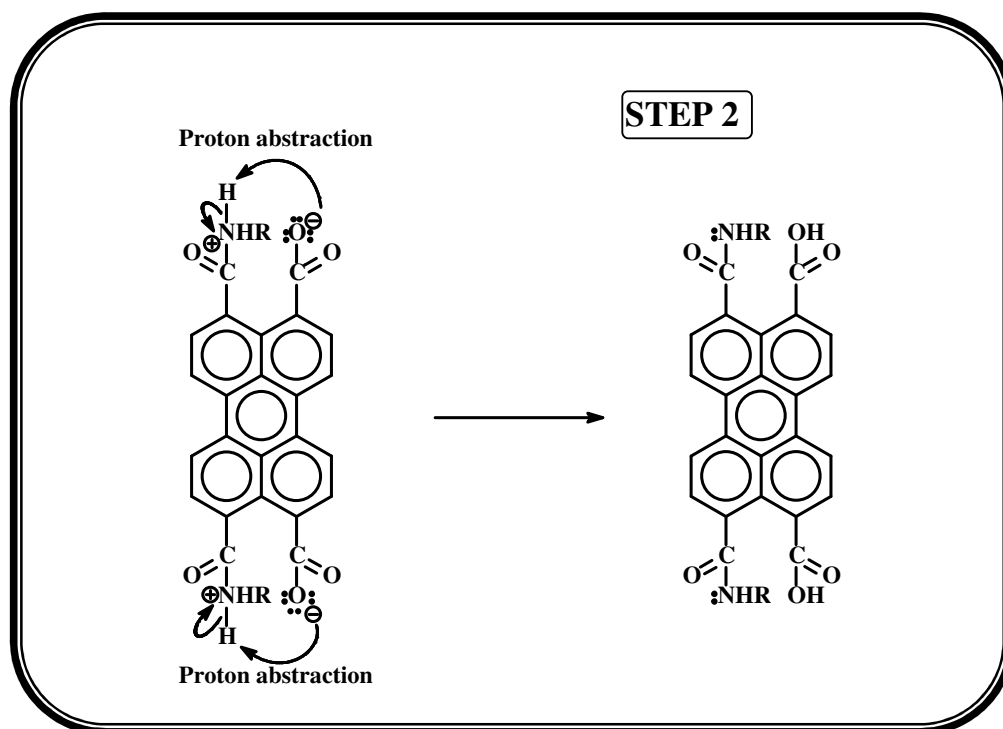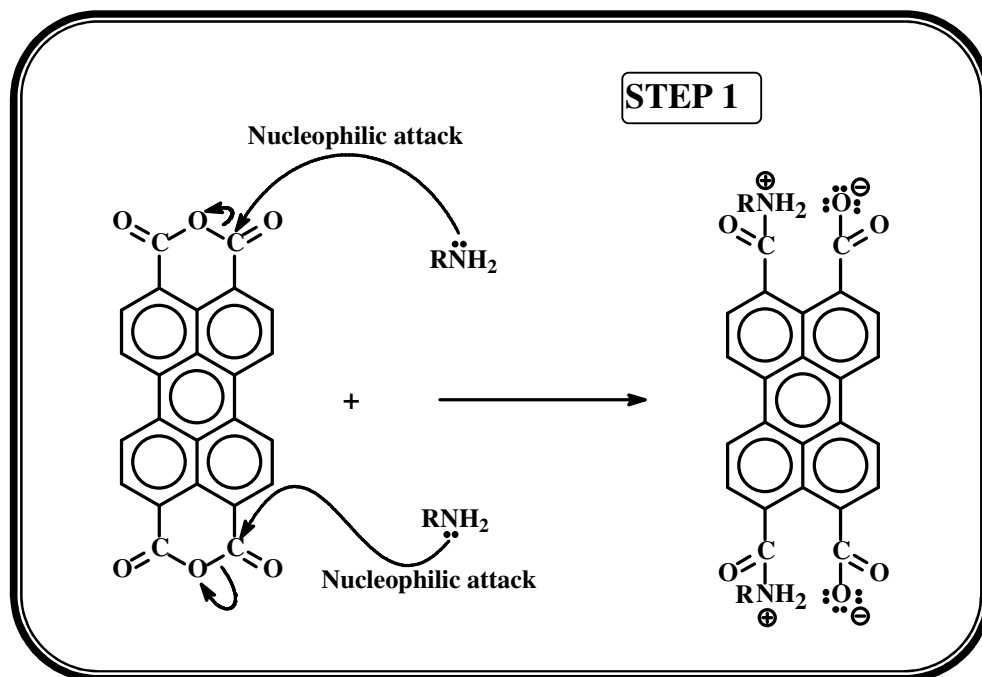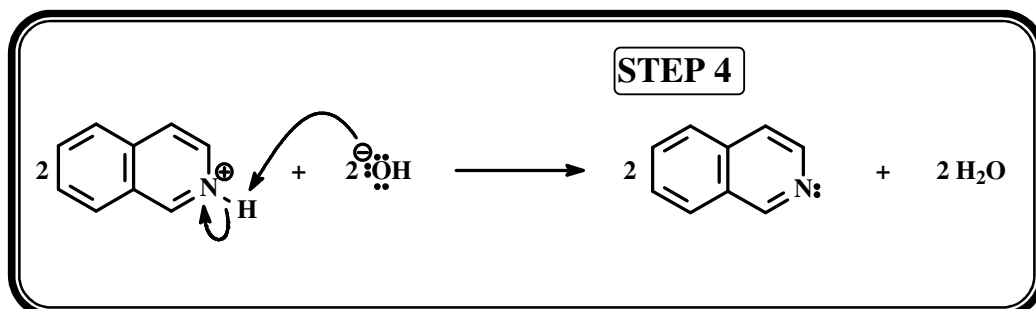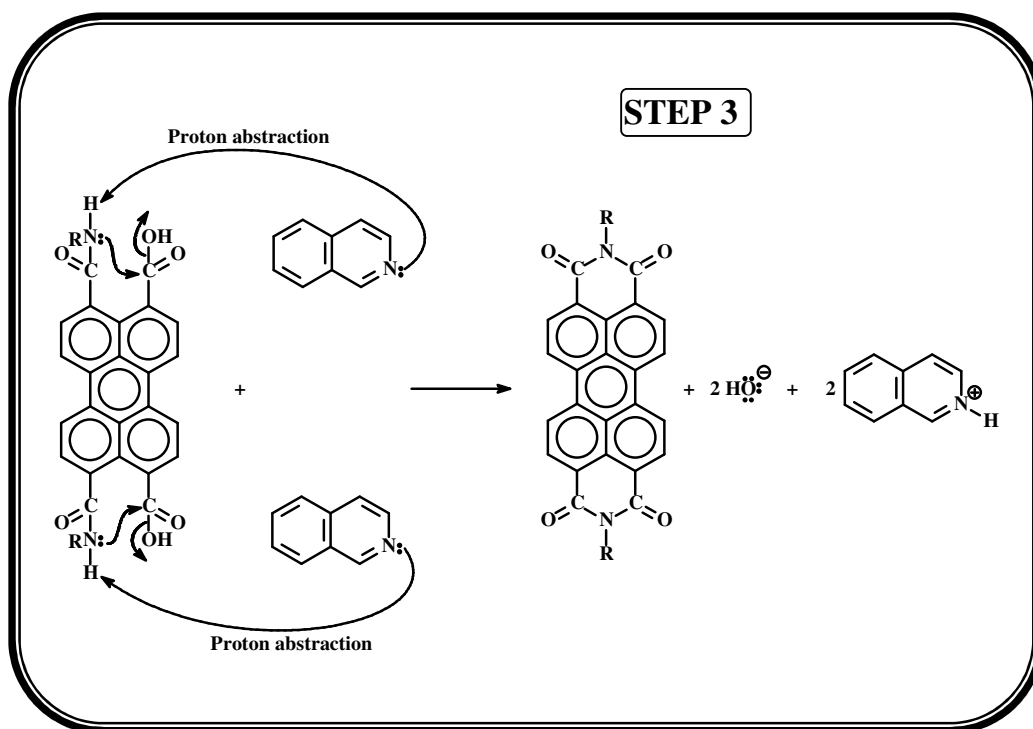
Chapter 4

DATA AND CALCULATIONS

4.1 Determination of Molecular Weights

The weight-average molecular weight (M_w) and number-average molecular weight (M_n) of EOPPI, EONPI, fluorescent chitosan and chitosan compounds were determined by gel permeation chromatography (GPC).

Intrinsic viscosities ($[\eta]$) of the compounds were measured using an Ubbelohde viscometer. To obtain the kinematic viscosity (in cSt), the efflux time (in seconds) was multiplied by the corresponding viscometer constant. The dynamic viscosity (in mPa.s) was obtained by the multiplication of kinematic viscosity and density (in g/mL). The intrinsic viscosity $[\eta]$ was obtained by measuring specific viscosity (η_{sp}) at five different concentrations (c) and applied Huggins equation, plotting $\log(\eta_{sp}/c)$ vs. c and extrapolating to zero concentration.

The viscosity average molecular weights (M_v) of CH and HP-CH were especially determined by Mark-Houwink-Sakurada's equation $[\eta] = KM_v^a$; where 'K' and 'a' are the constants that depend on the solvent-polymer system. Although, there is a considerable deviation in the equation for any solvent-temperature system proposed by Mohammad R. Kasaai [60], we have first determined the MHS constants by using that equation. Later, the approximate M_v of the chitosan polymer was measured.

4.1.1 Measurement of Intrinsic Viscosity [η]

Intrinsic Viscosity of EOPPI:

m-Cresol was used as solvent for EOPPI and a total of five different concentrations were prepared. *m*-Cresol was especially chosen to make sure the efflux time of the solvent will be beyond 150 sec. Each measurement was repeated three times and the average efflux time was considered for calculating the intrinsic viscosity. The following table illustrates the efflux times of *m*-cresol and the average efflux time.

Table 4.1: Data of efflux times of *m*-cresol at 25 $^{\circ}$C

Solvent	Efflux Time (sec)	Avg. Efflux Time (sec)
***m*-cresol**	262.76	262.67
	262.63	
	262.62	

In the similar way, for five different concentrations (*c*) of EOPPI in *m*-cresol, the average efflux times were tabulated below.

Table 4.2: Average efflux times data of EOPPI at 25 $^{\circ}$C

Concentration (g/dL)	Avg. Efflux Time (sec)
0.2	265.69
0.1	259.23
0.05	258.32
0.01	258.44
0.005	255.99

According to the following formulae, all the viscosity parameters were calculated

for each concentration and they were presented in the Table 4.3.

$$\eta_{relative} - \frac{t}{t_0} = \frac{\text{efflux time of solution}}{\text{efflux time of solvent}}$$

$$\eta_{specific} = \eta_{relative} - 1$$

$$\eta_{inherent} = \frac{\ln(\eta_{relative})}{c}$$

$$\eta_{reduced} = \frac{(\eta_{specific})}{c}$$

Table 4.3: Viscosity parameters of EOPPI

Concentration (g/dL)	$\eta_{relative}$	$\eta_{specific}$	$\eta_{reduced}$	$\log\left(\frac{\eta_{specific}}{c}\right)$
0.2	1.0115	0.0115	0.06	−1.2403
0.1	0.9869	−0.0131	−0.13	0.8827
0.05	0.9834	−0.0166	−0.33	0.4789
0.01	0.9839	−0.0161	−1.61	−0.2068
0.005	0.9746	−0.0254	−5.08	−0.7059

According to Huggins equation,

$$\log\left(\frac{\eta_{specific}}{c}\right) = \log[\eta] + k'[\eta]c$$

(Equn. 4.1)

Where, k': The Huggins constant for moderate concentrations

$[\eta]$: Intrinsic viscosity in dLg^{-1}

The linear fit plot of $\log\left(\dfrac{\eta_{\text{specific}}}{c}\right)$ **vs.** *c* (Figure 4.1) gives the intercept "$\log[\eta]$"

which provides the intrinsic viscosity of the solution.
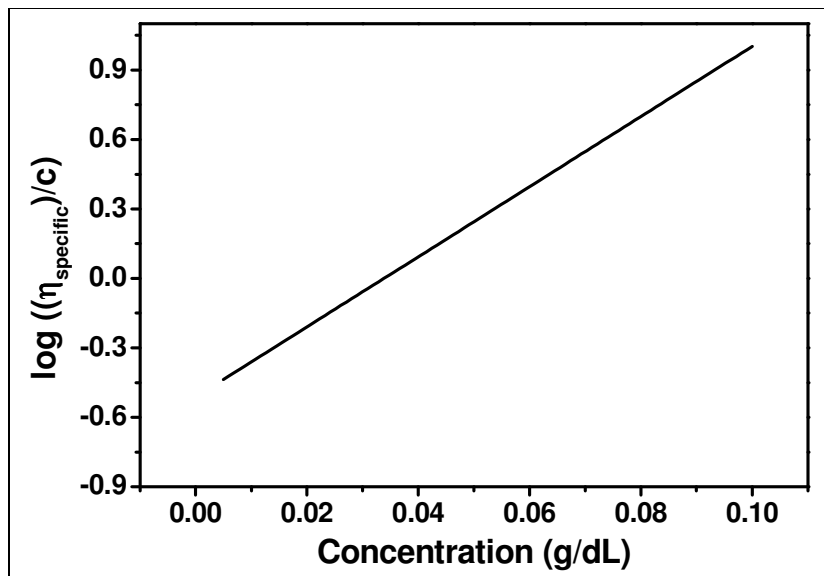
Figure 4.1: Plot of Reduced Viscosity vs. Concentration of EOPPI

The intercept of the plot found from Figure 4.1 is –0.51.

⇨ $\log[\eta] = -0.51$

⇨ $[\eta] = 10^{-0.51} = 0.3 \text{ dLg}^{-1}$

⇨ $[\eta] = 0.3 \text{ dLg}^{-1}$

 In the similar manner, intrinsic viscosities of all reported oligomeric diimides and polyimides (EONPI, CH, HP-CH, and TEONPI) were calculated at 25 $^\circ$C (unless otherwise mentioned) and their data was tabulated below (Table 4.4). Especially for the biopolymer, chitosan (CH) and perylene substituted fluorescent chitosan polymer, viscosity molecular weights were determined on the basis of equations reported in literature.

Table 4.4: Intrinsic viscosities of the synthesized *n*-type materials

Compound	Solvent	$[\eta]$ (dLg^{-1})
EOPPI	*m*-Cresol	0.30
EONPI	*m*-Cresol	0.28
TEONPI	*m*-Cresol	0.40
HP-CH	dimethylacetamide	0.40[a] (9.0)[b]
CH*	0.1 M NaCl/0.1% TFAc	4.00

*CH is the commercial biopolymer, chitosan; [a]measured at 70 $^\circ$C,[b]at 25 $^\circ$C

Based on Mark-Houwink-Sakurada's equation (Equn. 4.2), another equation for any solvent-system was reported for calculation of viscosity molecular weight by Kasaai [61]. Although there was considerable error in the equation reported, a general rough estimate of M_v was calculated for CH and HP-CH.

$$[\eta] = KM_v^a$$

(Equn 4.2)

Exponent $'a'$ of Mark-Houwink equation was first estimated by the following equation.

Exponent $'a'$:

$$a = 0.6202 + \left(\frac{0.699\,\chi}{(0.4806+\chi)}\right) \qquad \textbf{(Equn 4.3)}$$

Where, $\chi = \left(\frac{DA}{(pH\times\mu)}\right)$

DA: Degree of acetylation of chitosan

pH: pH of eluent

μ: Ionic strength of eluent = $0.5 \, \Sigma_i \, m_i z_i^2$

m_i: Molality, **z_i:** Charge number of ionic species 'i'

Viscosity Molecular Weight (M_v) of Chitosan:

The eluent used in the measurement was 0.1 M NaCl/0.1% CF$_3$COOH. Based on the eluent, the molalities of ionic species were calculated.

m_i of 0.1 M NaCl = 0.1 molal

z_i of 0.1 M NaCl = 1

m_i of 0.1% CF$_3$COOH = 0.0135 molal (d=1.5251 g/mL)

z_i of 0.1 % CF$_3$COOH = 1

Ionic strength, μ, of eluent = $0.5 \, \Sigma_i \, m_i z_i^2$

$\Rightarrow$ μ = 0.5 × [(0.1×1^2) + (0.0135×1^2)]

$\Rightarrow$ **μ = 0.0567**

DA = 20% (Aldrich)

pH = 2 of the eluent

$$\chi = \left(\frac{DA}{(pH \times \mu)} \right) = \left(\frac{\frac{20}{100}}{(2 \times 0.0567)} \right) = 1.7637$$

χ = 1.7637

Exponent $'a' = 0.6202 + \left(\frac{0.699 \, \chi}{(0.4806 + \chi)} \right) = 0.6202 + \left(\frac{0.699 \times 1.7637}{(0.4806 + 1.7637)} \right)$

Exponent $'a'$ = 1.1695

From the same reference,

Constant K:

$$\log(K{\times}10^{-5}) = [(-5.7676 \times \text{exponent } 'a') + 5.9232]$$

$\Rightarrow$ $\log(K{\times}10^{-5}) = [(-5.7676 \times 1.1695) + 5.9232]$

$\Rightarrow$ $K{\times}10^{-5} = -0.822$

$\Rightarrow$ $K = 1.51{\times}10^{-6}$ **dL/g**

Using the calculated value of intrinsic viscosity and Mark-Houwink equation, viscosity molecular weight was determined for CH.

$$[\eta] - KM_v^a$$

$\Rightarrow$ $4 = (1.51{\times}10^{-6}) \times M_v^{1.1695}$

$\Rightarrow$ $M_v = 309$ **kDa**

4.2 Calculations of Optical Parameters

4.2.1 Maximum Extinction Co-efficients (ε_{max})

According to the Beer-Lambert's law, from the linear relationship between absorbance and concentration of absorbing species, the maximum extinction co-efficients of the compounds were calculated from the following equation [63].

$$\varepsilon_{max} = \frac{A}{cl}$$

(Equn. 4.5)

Where, ε_{max}: Maximum extinction co-efficient in $L \cdot mol^{-1} \cdot cm^{-1}$ at λ_{max}

A: Absorbance

c: Concentration in mol L^{-1}

l: Path length in cm

ε_{max} **Calculation of EONPI:**
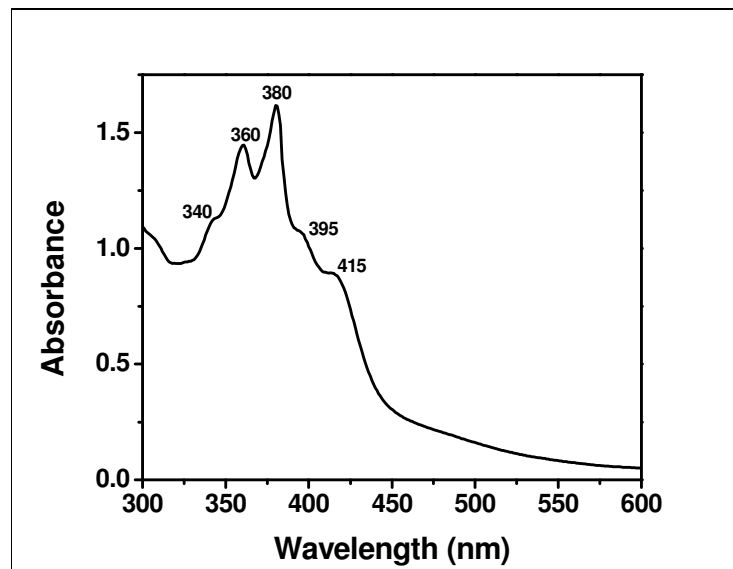
Figure 4.2: Absorption Spectrum of EONPI in Chloroform at 1×10^{-5} M

64

The absorption spectrum of EONPI (Figure 4.2) reveals that the absorption was found as 1.618 for the concentration of 1×10^{-5} M at the wavelength, (λ_{max}) 380 nm.

$$\Rightarrow \quad \varepsilon_{max} = \frac{1.618}{1\times10^{-5} \text{ M} \times 1 \text{ cm}} = 161800 \text{ L} \cdot \text{mol}^{-1} \cdot \text{cm}^{-1}$$

$$\Rightarrow \quad \varepsilon_{max} \text{ of EONPI } = 161800 \text{ L} \cdot \text{mol}^{-1} \cdot \text{cm}^{-1}$$

In the similar way, the molar absorptivity of the compounds was calculated and the resulting values were tabulated in the following table (Table 4.5).

Table 4.5: Molar absorptivity data of EOPPI and EONPI

Compound	Concentration	Absorbance	λ_{max}	ε_{max}
EOPPI	1×10^{-5} M	1.500	527 nm	150000 L · mol^{-1} · cm^{-1}
EONPI	1×10^{-5} M	1.618	380 nm	161800 L · mol^{-1} · cm^{-1}

4.2.2 ε_{max} Calculation of EONPI from the Plot of Absorbance vs. Concentration

Based on the Beer Lambert's Law, the ε_{max} was calculated from the plot of absorbance and concentration. A minimum of five different concentrations of the compound's solutions were prepared and their maximum absorbances respecting to the maximum absorption wavelength were recorded for each concentration. Later, the slope calculated from the plot of absorbance vs. concentration yielded the maximum molar absorption co-efficient.

Table 4.6: Concentration and the their corresponding absorbances data of EONPI

Concentration	λ_{max}	Absorbance
1×10^{-6} M	380 nm	0.186
2×10^{-6} M	380 nm	0.343
5×10^{-6} M	380 nm	0.820
1×10^{-5} M	380 nm	1.618
2×10^{-5} M	380 nm	3.174
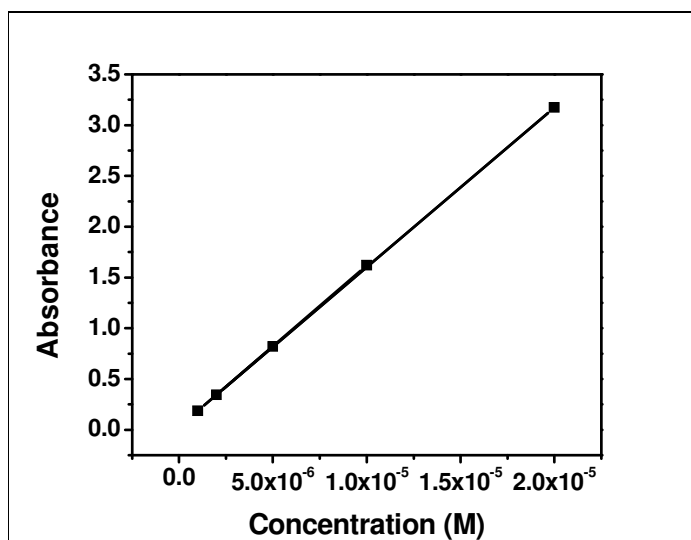
Figure 4.3: Plot of Absorption vs. Concentration of EONPI

The slope of the plot, ε_{max}, is 157400 L · mol^{-1} · cm^{-1}.

Table 4.7: Molar absorptivity data of EONPI in different solvents

Solvent	λ_{max} (nm)	ε_{max}* (L · mol^{-1} · cm^{-1})
Chloroform	380 nm	157400 (161800)
NMP	380 nm	125900 (130200)
MeOH	357 nm	155400 (187000)
DMF	380 nm	110900 (112870)
DMSO	381 nm	108400 (110100)

* The values are calculated from the plots of absorbance vs. concentration and the values in the parentheses are calculated from the formula ($\varepsilon_{max} = A/c$l) for the concentration, 1×10^{-5} M.

4.2.3 Fluorescence Quantum Yields (Φ_f)

When a chromophore/fluorophore absorbs a photon of light with enough energy, an energetically excited state is formed. The end result of this process is returning to the ground state by deactivation. There are many deactivation processes such as fluorescence, internal conversion, vibrational relaxation and intersystem crossing, etc. Among these, fluorescence is the important radiative process where the deactivation of energy occurs by the emission of a photon and other listed processes are related to non-radiative loss of energy as heat to the surroundings. Intersystem crossing is the transition from singlet to the triplet manifold and subsequent final non-radiative deactivation. These processes were better indicated in Jablonski diagram (Figure 4.4).
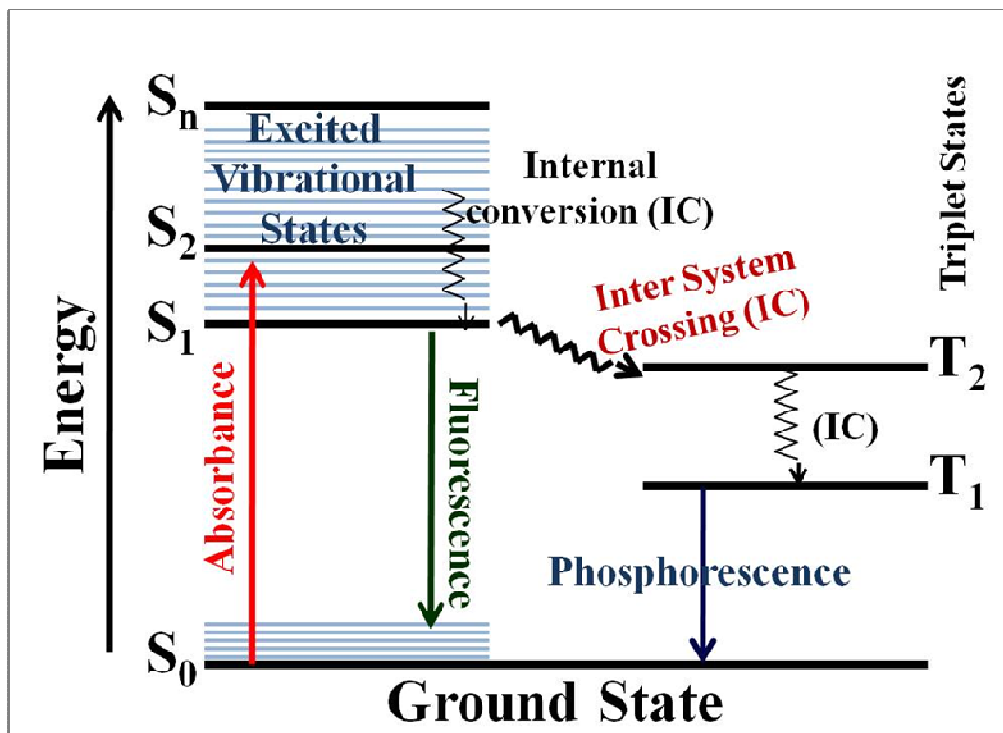
Figure 4.4: A General Jablonski Diagram

The fluorescence quantum yield (Φ_f) is the ratio of photons absorbed to the photons emitted through fluorescence. The most reliable method for recording Φ_f is the comparative method of Williams et al., [62] which involves the use of well characterized standard samples with known Φ_f values. Essentially, solutions of the standard and test samples with identical absorbance at the same excitation wavelength can be assumed to be absorbing the same number of photons. Hence, a simple ratio of the integrated fluorescence intensities of the two solutions (recorded under identical conditions) will yield the ratio of the quantum yield values. Since Φ_f for the standard sample is known, it is trivial to calculate the Φ_f for the test sample.

$$\Phi_u = \frac{A_{std}}{A_u} \times \frac{S_u}{S_{std}} \times \left(\frac{n_u}{n_{std}}\right)^2 \times \Phi_{std}$$

(Equn. 4.6)

Where, Φ_u: Fluorescence quantum yield of unknown

A_{std}:   Absorbance of the reference at the excitation wavelength

A_u: Absorbance of the unknown at the excitation wavelength

S_{std}:   The integrated emission area across the band of reference

S_u: The integrated emission area across the band of unknown

n_{std}:   Refractive index of reference solvent

n_u: Refractive index of unknown solvent

Φ_{std}:   Fluorescence quantum yield of reference. [57, 63]

N,N'-bis(dodecyl)-3,4,9,10-perylenebis(dicarboximide) reported by Icil in 1997 was used as reference for the fluorescence quantum yield measurements of perylene dyes [57]. The reference compound was having Φ_f = 1 in CHCl$_3$ solution. The perylene dyes reported were excited at the wavelength, λ_{exc} = 485 nm similar to the reference.

For the naphthalene dyes reported, anthracene in ethanol (with Φ_f = 0.27) was used as reference and the compounds were excited at λ_{exc} = 360 nm [10, 14].

Fluorescence Quantum Yield of Dimer-EOPPI:

Dimer-EOPPI was dissolved in methanol and the reference compound was dissolved in chloroform. Their absorbances were measured followed by their fluorescence spectra and the corresponding integrated emission area. The data was listed below.

A_{std} = 0.1015, A_u = 0.1, S_{std} = 12318.15, S_u = 8949.93, n_{std} = 1.4429 at 20 ^{o}C, n_u = 1.3284 at 20 ^{o}C, Φ_{std} = 1.0

From equation 4.2,

$$\Phi_{EOPPI} - \frac{0.1015}{0.1} \times \frac{8949.93}{12318.15} \times \left(\frac{1.3284}{1.4429}\right)^2 \times 1$$

$\Rightarrow$ Φ_f **of Dimer-EOPPI = 0.63**

The fluorescence quantum yields of dimer-EOPPI were measured by the method described above in different solvents and they were tabulated below (Table 4.8).

Table 4.8: Fluorescence quantum yields of EOPPI and EONPI in different solvents

Solvent	EOPPI Φ_f	EONPI Φ_f
$CHCl_3$	0.47	0.017
TCE	0.31	–
NMP	0.38	–
CH_3OH*	0.63*	0.023
DMF	0.55	0.012
DMSO	0.12	–
H_2O	–	0.032

*The measured value is belonging to the Dimer-EOPPI

Although, the Φ_f of naphthalene dyes are lower in general, for comparison, the measurements were carried out for EONPI and the results were given in the table (Table 4.8) in addition to Φ_f of EOPPI.

4.2.4 Half-width of the Selected Absorption ($\Delta\bar{\nu}_{1/2}$)

The half-width of the selected maximum absorption generally considered as full width at half maximum and is defined as full or half-width of the curve at half of the maximum intensity [9, 10].

$$\Delta\bar{\nu}_{1/2} = \bar{\nu}_I - \bar{\nu}_{II}$$

(Equn. 4.7)

Where, $\bar{\nu}_I$, $\bar{\nu}_{II}$: The frequencies from the absorption spectrum in cm^{-1}

$\Delta\bar{\nu}_{1/2}$: Half-width of the selected maximum absorption in cm^{-1}
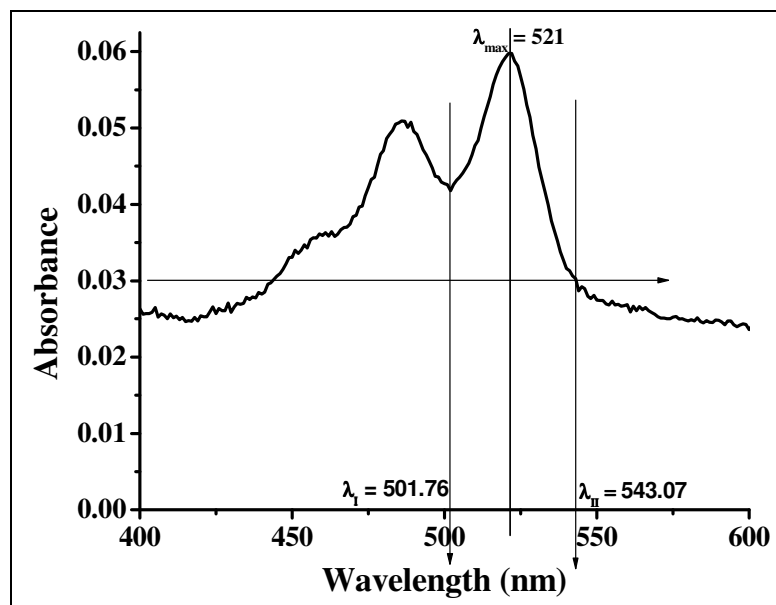
Figure 4.5: Absorption Spectrum of Dimer-EOPPI in CH_3OH

From the Figure 4.5,

λ_I = **501.76 nm**

$$\Rightarrow \lambda_I = 501.76 \text{ nm} \times \frac{10^{-9} \text{ m}}{1 \text{ nm}} \times \frac{1 \text{ cm}}{10^{-2} \text{ m}} = 5.0176 \times 10^{-5} \text{ cm}$$

$$\Rightarrow \bar{v}_I = \frac{1}{5.0176 \times 10^{-5} \text{ cm}} = 19929.85 \text{ cm}^{-1}$$

λ_{II} = **543.07 nm**

$$\Rightarrow \lambda_{II} = 543.07 \text{ nm} \times \frac{10^{-9} \text{ m}}{1 \text{ nm}} \times \frac{1 \text{ cm}}{10^{-2} \text{ m}} = 5.4307 \times 10^{-5} \text{ cm}$$

$$\Rightarrow \bar{v}_{II} = \frac{1}{5.4307 \times 10^{-5} \text{ cm}} = 18413.83 \text{ cm}^{-1}$$

$$\Delta \bar{v}_{1/2} = \bar{v}_I - \bar{v}_{II} = 19929.85 \text{ cm}^{-1} - 18413.83 \text{ cm}^{-1} = 1516.02 \text{ cm}^{-1}$$

$\Rightarrow \Delta\bar{v}_{1/2} = 1516.02$ cm^{-1}

The half-widths of the compounds are necessary for calculating the theoretical radiative lifetimes of the compounds. By using the above method, the half-widths were calculated and presented below in Table 4.9.

Table 4.9: Half-width of the selected absorptions of compounds EOPPI and EONPI

	EOPPI			EONPI		
Solvent	λ_I (nm)	λ_{II} (nm)	$\Delta\bar{v}_{1/2}$ (cm^{-1})	λ_I (nm)	λ_{II} (nm)	$\Delta\bar{v}_{1/2}$ (cm^{-1})
CHCl$_3$	511	527	1156.21	367	390	1545.34
CH$_3$OH*	502*	543*	1516.02*	368	388	1382.06
DMF	509	543	1221.51	370	401	2145.03

*The measured values are belonging to the Dimer-EOPPI

4.2.5 Theoretical Radiative Lifetimes (τ_0)

The theoretical radiative lifetime refers to the theoretical lifetime of an excited molecule in the absence of radiationless transitions.

$$\tau_0 = \frac{3.5 \times 10^8}{\bar{v}_{max}^2 \times \varepsilon_{max} \times \Delta\bar{v}_{1/2}}$$

(Equn. 4.8) [64]

Where, τ_0: Theoretical radiative lifetime in ns

$\bar{v}_{max}$: Mean frequency of the maximum absorption band in cm^{-1}

ε_{max}: The maximum extinction coefficient in L · mol^{-1} · cm^{-1} at the maximum absorption wavelength, λ_{max}

$\Delta\bar{v}_{1/2}$: Half-width of the selected absorption in units of cm^{-1}

Theoretical Radiative Lifetime of Dimer-EOPPI:

From the Equation 4.8 and its calculation method, ε_{max} of Dimer-EOPPI in CH$_3$OH was calculated as 120000 L $\cdot$ mol^{-1} $\cdot$ cm^{-1}.

From the Figure 4.3, λ_{max} = **521 nm**

$$\lambda_{max} = 521 \text{ nm} \times \frac{10^{-9} \text{ m}}{1 \text{ nm}} \times \frac{1 \text{ cm}}{10^{-2} \text{ m}} = 5.21 \times 10^{-5} \text{ cm}$$

$$\Rightarrow \bar{v}_{max} = \frac{1}{5.21 \times 10^{-5} \text{ cm}} = 19193.86 \text{ cm}^{-1}$$

$$\Rightarrow \bar{v}_{max}^2 = (19193.86 \text{ cm}^{-1})^2 = 3.684 \times 10^8 \text{ cm}^{-2}$$

Now, the theoretical radiative lifetime can be calculated from the Equation 4.8

$$\tau_0 = \frac{3.5 \times 10^8}{\bar{v}_{max}^2 \times \varepsilon_{max} \times \Delta\bar{v}_{1/2}} = \frac{3.5 \times 10^8}{(19193.86)^2 \times 120000 \times 1516.02}$$

$$\Rightarrow \tau_0 = 5.22 \times 10^{-9} \text{ ns}$$

$$\Rightarrow \tau_0 = 5.22 \text{ ns}$$

According to this method of calculation, theoretical radiative lifetimes were calculated for the compounds in different solvents and the data was presented below.

Table 4.10: Theoretical radiative lifetimes of EOPPI in different solvents

		EOPPI			
Solvent	λ_{max} **(nm)**	ε_{max} **(L · mol^{-1} · cm^{-1})**	$\bar{\nu}^2_{max}$ **(cm^{-2})**	$\Delta\bar{\nu}_{1/2}$ **(cm^{-1})**	τ_0 **(ns)**
CHCl$_3$	527	150000	3.59×10^8	1156.21	5.46
CH$_3$OH*	521*	120000*	3.68×10^8	1516.02	5.22
DMF	526	130000	3.62×10^8	1221.51	6.09

*The measured values are belonging to the Dimer-EOPPI

Table 4.11: Theoretical radiative lifetimes of EONPI in different solvents

		EONPI			
Solvent	λ_{max} **(nm)**	ε_{max} **(L · mol^{-1} · cm^{-1})**	$\bar{\nu}^2_{max}$ **(cm^{-2})**	$\Delta\bar{\nu}_{1/2}$ **(cm^{-1})**	τ_0 **(ns)**
CHCl$_3$	380	157400	6.925×10^8	1545.34	2.08
CH$_3$OH	378	155400	6.999×10^8	1382.06	2.33
DMF	380	110900	6.925×10^8	2145.03	2.12

4.2.6 Theoretical Fluorescence Lifetimes (τ_f)

The theoretical fluorescence lifetime refers to the theoretical average time of the molecule stays in the excited state before fluorescence (emitting a photon).

$$\tau_f = \tau_0 \times \Phi_f$$

(Equn. 4.9) [64]

Where, τ_f: Fluorescence lifetime in ns

   τ_0:   Theoretical radiative lifetime in ns

   Φ_f: Fluorescence quantum yield

Theoretical Fluorescence Lifetime of Dimer-EOPPI:

$\tau_f = \tau_0 \times \Phi_f$

From the data calculated above by using Equations 4.6 and 4.8,

   ⇨ τ_f = 5.22 ns × 0.63

   ⇨ **τ_f = 3.29 ns**

The theoretical fluorescence lifetimes of the other compounds synthesized and reported were also calculated using the above Equation 4.9. The results were tabulated in the following tables.

Table 4.12: Theoretical fluorescence lifetimes data of EOPPI and EONPI

Solvent	EOPPI			EONPI		
	Φ_f	τ_0 (ns)	τ_f (ns)	Φ_f	τ_0 (ns)	τ_f (ns)
CHCl$_3$	0.47	5.46	2.57	0.017	2.08	0.036
CH$_3$OH*	0.63*	5.22*	3.29*	0.023	2.33	0.054
DMF	0.55	6.09	3.35	0.012	2.12	0.025

*The measured values are belonging to the Dimer-EOPPI

4.2.7 Fluorescence Rate Constants (k_f)

The theoretical fluorescence rate constant for the compounds are calculated by the following equation.

$$k_f = \frac{1}{\tau_0}$$

(Equn. 4.10) [9, 10, 64]

Where, k_f: Fluorescence rate constant in s^{-1}

τ_0:   Theoretical radiative lifetime in s

Fluorescence Rate Constant of Dimer-EOPPI:

$\Rightarrow k_f = \dfrac{1}{5.22 \times 10^{-9} \, s} = 1.92 \times 10^8 \, s^{-1}$

$\Rightarrow k_f = 1.92 \times 10^8 \, s^{-1}$

The theoretical fluorescence rate constants were calculated in the similar manner for EOPPI and EONPI in different solvents and the values were given in the following table.

Table 4.13: Fluorescence rate constants data of EOPPI and EONPI

Solvent	EOPPI		EONPI	
	τ_0 (ns)	$k_f(s^{-1})$	τ_0 (ns)	$k_f(s^{-1})$
$CHCl_3$	5.46	1.83×10^8	2.08	4.81×10^8
CH_3OH^*	5.22*	1.92×10^8*	2.33	4.29×10^8
DMF	6.09	1.64×10^8	2.12	4.72×10^8

*The measured values are belonging to the Dimer-EOPPI

4.2.8 Rate Constants of Radiationless Deactivation (k_d)

The rate constants of radiationless deactivations of the compounds were calculated by the following equation.

$$k_d = \left(\frac{k_f}{\Phi_f}\right) - k_f$$

Where, k_d: Rate constant of radiationless deactivation in s^{-1}

   k_f: Fluorescence rate constant in s^{-1}

   Φ_f: Fluorescence quantum yield

Rate Constant of Radiationless Deactivation of Dimer-EOPPI:

$$\Rightarrow k_d = \left(\frac{1.92 \times 10^8 \, s^{-1}}{0.63}\right) - 1.92 \times 10^0 \, s^{-1} = 1.13 \times 10^8 \, s^{-1}$$

$$k_d = 1.13 \times 10^8 \, s^{-1}$$

The following table gives the calculated rate constants of radiationless deactivation for EOPPI and EONPI.

Table 4.14: Rate constants of radiationless deactivation data of EOPPI and EONPI

Solvent	EOPPI			EONPI		
	Φ_f	$k_f\,(s^{-1})$	$k_d\,(s^{-1})$	Φ_f	$k_f\,(s^{-1})$	$k_d\,(s^{-1})$
CHCl$_3$	0.47	1.83×10^8	2.06×10^8	0.017	4.81×10^8	2.78×10^{10}
CH$_3$OH*	0.63	1.92×10^8*	1.13×10^8*	0.023	4.29×10^8	1.82×10^{10}
DMF	0.55	1.64×10^8	1.34×10^8	0.012	4.72×10^8	3.89×10^{10}

*The measured values are belonging to the Dimer-EOPPI

4.2.9 Oscillator Strengths (f)

The dimensionless quantity, oscillator strength, expresses the strength of an electronic transition and is calculated by the following equation.

$$f = 4.32 \times 10^{-9} \, \Delta \bar{v}_{1/2} \, \varepsilon_{max}$$

(Equn. 4.12) [10]

Where, f: Oscillator strength

$\Delta \bar{v}_{1/2}$: Half-width of the selected absorption in units of cm^{-1}

ε_{max}:   The maximum extinction coefficient in $L \cdot mol^{-1} \cdot cm^{-1}$ at the maximum absorption wavelength, λ_{max}

Oscillator Strength of Dimer-EOPPI:

$\Rightarrow$ $f = 4.32 \times 10^{-9} \, \Delta \bar{v}_{1/2} \, \varepsilon_{max}$

$\Rightarrow$ $f = 4.32 \times 10^{-9} \times 1516.02 \times 120000 = 0.79$

$\Rightarrow$ $f = 0.79$

The following table gives the calculated rate constants of radiationless deactivation for EOPPI and EONPI.

Table 4.15: Oscillator strengths data of EOPPI and EONPI

Solvent	EOPPI			EONPI		
	$\Delta \bar{v}_{1/2}$ (cm^{-1})	ε_{max} [a]	f	$\Delta \bar{v}_{1/2}$ (cm^{-1})	ε_{max} [a]	f
CHCl$_3$	1156.21	150000	0.77	1545.34	157400	1.05
CH$_3$OH*	1516.02*	120000*	0.79*	1382.06	155400	0.93
DMF	1221.51	130000	0.69	2145.03	110900	1.03

* The measured values are belonging to the Dimer-EOPPI
[a] ε_{max} data is given in ($L \cdot mol^{-1} \cdot cm^{-1}$)

78

4.2.10 Singlet Energies (E_s)

Singlet energy is the minimum amount of energy required for a chromophore/fluorophore to get excited from ground state to an excited state.

$$E_S = \frac{2.86 \times 10^5}{\lambda_{max}}$$

Where, E_s: Singlet energy in kcal mol^{-1}

λ_{max}:   The maximum absorption wavelength in $\overset{o}{A}$

Singlet Energy of Dimer-EOPPI:

$\Rightarrow$ $E_S = \frac{2.86 \times 10^5}{\lambda_{max}} = \frac{2.86 \times 10^5}{5210} = 54.9$ kcal mol^{-1}

$\Rightarrow$ $E_s = $ **54.9 kcal mol^{-1}**

The singlet energies were calculated in the similar manner for EOPPI and EONPI and the data was given in the following table.

Table 4.16: Singlet energies data of EOPPI and EONPI

Solvent	EOPPI		EONPI	
	λ_{max} ($\overset{o}{A}$)	E_s (kcal mol^{-1})	λ_{max} ($\overset{o}{A}$)	E_s (kcal mol^{-1})
CHCl$_3$	5270	54.3	3800	75.3
CH$_3$OH*	5210*	54.9*	3780	75.7
DMF	5260	54.4	3800	75.3

* The measured values are belonging to the Dimer-EOPPI

4.3 Calculations of Electrochemical Parameters

According to the theory discussed in Chapter 2 under electrochemistry section 2.5, all the required electrochemical parameters were calculated. The interpretation of the data and the results were discussed in Chapter 5 in detail.

4.3.1 Redox Potentials/Half Wave Potentials ($E_{1/2}$)

The redox potential can be obtained from a cyclic voltammogram by calculating the average value of the anodic and cathodic peak potentials. The subscript ½ indicates that the potential is obtained approximately at the half-height of the cathodic and anodic peaks and therefore is sometimes called as the half-wave potential. At these points the concentrations of the reduced and oxidized species are equal. Here, the concentration refers to the concentration of a given species on the electrode but not in the bulk solution.

$$E_{1/2} = \frac{E_{pc} + E_{pa}}{2}$$

(Equn. 4.14) [65, 66]

Where, $E_{1/2}$:   Half-wave potential in V

      E_{pc}:   Cathodic peak potential in V

      E_{pa}:   Anodic peak potential in V

Redox Potentials of EOPPI:

The cyclic voltammograms of EOPPI presented in Figure 4.57 indicate two reversible redox processes. In the two processes, the cathodic and anodic waves are symmetric with respect to each other and thus each redox process is reversible.

From the cyclic voltammogram, first, the redox potentials were calculated relative to the reference electrode.

$$E_{red1,1/2} \text{ vs. Ag/AgNO}_3 = \frac{E_{pc} + E_{pa}}{2} = \frac{(-0.741) + (-0.800)}{2} = 0.771 \text{ V}$$

$$E_{red2,1/2} \text{ vs. Ag/AgNO}_3 = \frac{E_{pc} + E_{pa}}{2} = \frac{(-0.959) + (-1.025)}{2} = -0.992 \text{ V}$$

Where, $E_{red1,2}$ represents the first and second redox processes.

From the anodic and cathodic peak potentials, the peak potential separations for the two redox processes can be estimated by the following equation which indicates the number of electrons transferred. According to the equation, a fast one-electron process gives a peak potential separation about 59 mV.

$$\Delta E_p = E_{pa} - E_{pc} = \frac{0.059}{n} \text{ V}$$

(Equn. 4.15) [65, 66]

Peak Potentials Separations of EOPPI:

$$\Delta E_p = E_{pa} - E_{pc}$$

⇨ $\Delta E_{p, 1} = (-0.741) - (-0.800) = 0.059$ V

⇨ $\Delta E_{p, 1} = $ **59 mV**

⇨ $\Delta E_{p, 2} = (-0.959) - (-1.025) = 0.066$ V

⇨ $\Delta E_{p, 2} = $ **66 mV**

The oxidation potential of internal reference, ferrocene was estimated as 0.175 V.

Therefore, $E_{ox} = $ **0.175 V**

Now, the redox potentials can be expressed relative to the internal reference, ferrocene (Fc).

$$E_{red,1/2} \text{vs. Fc} = (E_{red,1/2} \text{vs. Ag/AgNO}_3) - (F_{ux} \text{vs. Ag/AgNO}_3)$$

$\Rightarrow$ $E_{red1,1/2}$vs. Fc = $(-0.771) - (+0.175) = -0.946$ V

$\Rightarrow$ $E_{red1,1/2}$vs. Fc = -0.946 V

$\Rightarrow$ $E_{red2,1/2}$vs. Fc = $(-0.992) - (+0.175) = -1.167$ V

$\Rightarrow$ $E_{red1,1/2}$vs. Fc = -1.167 V

In the similar manner, the redox potentials of all the compounds were calculated and the values were tabulated in Table 4.18.

4.3.2 Energies of LUMO Levels

According to the empirical relationship proposed by Bredas and co-workers [67, 68] on the basis of a detailed comparison between valence effective Hamiltonian calculations and experimental electrochemical measurements, a correlation was expressed to calculate the absolute energies of Lowest Unoccupied Molecular Orbital (LUMO) level with respect to the vacuum level.

$$E_{LUMO} = -(4.8 + E_{1/2})$$

(Equn. 4.16) **[67, 68]**

Where, E_{LUMO}:   Energy of LUMO level in eV

$E_{1/2}$:   Redox potential of analyte ($E_{red1,1/2}$vs. Fc)

Table 4.17: Electrochemical data of *n*-type materials at a scan rate of 100 mVs^{-1}

Compound	E_{pc} / V	E_{pa} / V	ΔE_p / mV	$E_{1/2}$ vs. (Ag/AgCl) / V	E_{Fc} vs. (Ag/AgCl) / V	$E_{1/2}$ vs. Fc / V
EOPPI in CH$_2$Cl$_2$*	−0.741	−0.800	59	−0.771	0.175	−0.946
	−0.959	−1.025	66	−0.992	0.175	−1.167
EONPI in CH$_2$Cl$_2$	−0.682	−0.824	142	−0.753	0.350	−1.103
	−1.044	−1.170	126	−1.107	0.350	−1.457
EONPI in (50:50) CH$_3$OH + CH$_3$CN	−0.505	−0.569	64	−0.537	0.380	−0.917
HP-CH in DMAc[a]	−0.319	−0.415	96	−0.367	0.586	−0.953
	−0.556	−0.660	104	−0.608	0.586	−1.194
TEONPI in CHCl$_3$	−0.448	−0.636	188	−0.542	0.513	−1.055
	−0.845	−0.748	97	−0.797	0.513	−1.310
	−0.924	−1.017	93	−0.971	0.513	−1.484
Poly PTDI in CHCl$_3$	−0.448	−0.636	188	−0.542	0.513	−1.055
	−0.448	−0.636	188	−0.542	0.513	−1.055

*For EOPPI, the reference electrode was (Ag/AgNO$_3$)

[a]DMAc: Dimethylacetamide

E_{LUMO} **of EOPPI:**

$$E_{LUMO} = -\left(4.8 + E_{1/2}\right)$$

$$\Rightarrow E_{LUMO} = -\left(4.8 + (-0.946\ V)\right) = -3.854\ V$$

$$\Rightarrow E_{LUMO} = -3.854\ V$$

The LUMO values were calculated according to the procedure explained above for different compounds and listed them in the following table (Table 4.19).

4.3.3 Optical Band Gap Energies (E_g)

The optical band gap energy is calculated from the absorption spectrum of the compound by extrapolating the maximum absorption band to zero-absorbance and by using the following equation (Equn 4.17).

$$E_g = \frac{1240\ eV\ nm}{\lambda}$$

(Equn. 4.17) [9, 10, 63-66]

Where, E_g: Band gap energy in eV

λ: Cut-off wavelength of the absorption band in nm

Band Gap Energy of EOPPI:

The maximum absorption band (0→0 absorption band) and the corresponding extrapolation to zero absorbance are shown below (Figure 4.6) and the resultant wavelength measured was 552 nm.

84
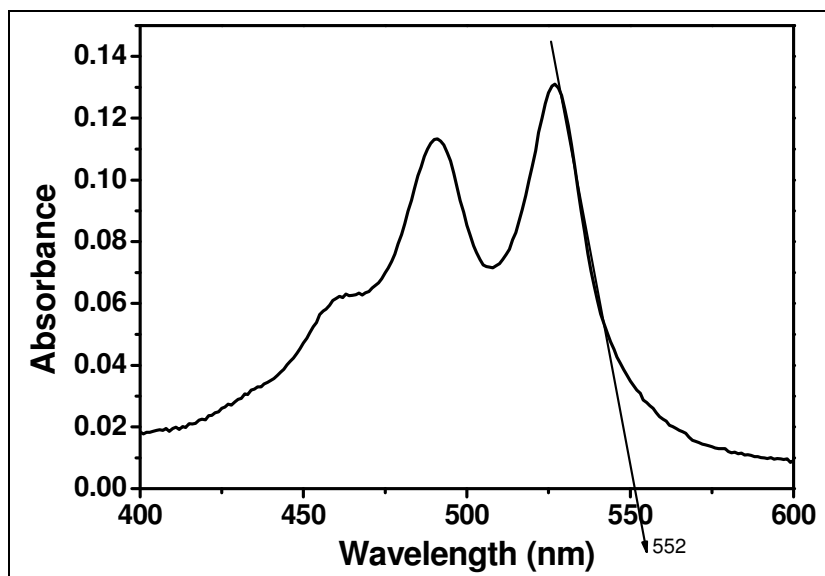
Figure 4.6: Absorption Spectrum of EOPPI

$$E_g = \frac{1240 \ eV \ nm}{\lambda}$$

$\Rightarrow E_g = \frac{1240 \ eV \ nm}{\lambda} = \frac{1240 \ eV \ nm}{552} = 2.246 \ eV$

$\Rightarrow E_g = 2.246 \ eV$

4.3.4 Energies of HOMO Levels

The Highest Occupied Molecular Orbital energy values were calculated from the LUMO and E_g Values followed by the equation given below.

$$E_{HOMO} = E_{LUMO} - E_g$$

(Equn. 4.18) [9, 10, 63-66]

Where, E_{HOMO}:   Energy of HOMO level in eV

E_{LUMO}:   Energy of LUMO level in eV

85

E_g: Optical Band gap energy in eV

E_{HOMO} of EOPPI:

$$E_{HOMO} = E_{LUMO} - E_g$$

⇨ $E_{HOMO} = -3.854\ V - 2.246\ V = -6.1\ V$

⇨ $E_{HOMO} = -6.1\ V$

The HOMO values were calculated according to the procedure explained above for all n-type compounds reported and listed them in the following table.

Table 4.18: LUMO, Optical Band Gap (E_g) and HOMO data of n-type materials at a scan rate of 100 mVs^{-1}

Compound	E_{LUMO} / eV	E_g / eV	E_{HOMO} / eV
EOPPI in CH_2Cl_2*	−3.85	2.24	−6.09
EONPI in CH_2Cl_2	−3.69	2.71	−6.40
EONPI in (50:50) $CH_3OH + CH_3CN$	−3.88	3.12	−7.00
HP-CH in DMAc[a]	−3.85	2.28	−6.13
TEONPI in $CHCl_3$	−3.75	3.15	−6.90

*For EOPPI, the reference electrode was (Ag/AgNO$_3$)
[a]DMAc: Dimethylacetamide

4.3.5 Diffusion Constants (D)

The Randles-Sevcik equation given below was used to calculate the diffusion co-efficients of EOPPI. The equation describes the effect of scan rate on the peak current. For the well-known ferrocene/ferrocenium couple, i_p depends not only on the concentration anddiffusional properties of the electroactive species but also on scan rate. Provided, the plot i_p vs. $v^{1/2}$ gives the evidence for a chemically reversible redox process.

$$i_p = (2.69 \times 10^5)\, n^{3/2}\, v^{1/2}\, D^{1/2}\, A\, c$$

<div align="right">(Equn. 4.19) [65, 66]</div>

Where, i_p: is i_{pc}, the cathodic peak current from the cyclic voltammogram of EOPPI

$v^{1/2}$: Scan rate used to record the cyclic voltammogram of EOPPI

n: Number of electrons

D: Diffusion constant in $cm^2 s^{-1}$

A: Area of working electrode in cm^2

c: Concentration of the electroactive species (mol cm^{-3})

Equation 4.19 can be rearranged to calculate the Diffusion constant, D.

$$D = \frac{\left(\frac{i_{pc}}{v^{1/2}}\right)^2}{\left[\left(2.69\times10^5 A s mol^{-1} V^{-1/2}\right)^2 \times (n^{3/2})^2 \times (Ac)^2\right]}$$

$\left(\dfrac{I_{pc}}{v^{1/2}}\right)$: Slope of the plot i_{pc} vs. $v^{1/2}$ in units of $[(\mu A)\times(mV)^{-1/2}\times(s)^{1/2}]$

$A = \pi r^2$ (with diameter 2 mm, r = 1 mm = 0.1 cm)

$c = 1\times10^{-3}$ M $= 1\times10^{-6}$ mol cm^{-3}

Equation	y = a + b*x	
Adj. R-Square	0.98502	
	Value	Standard Error
D Intercept	-0.09401	0.08536
D Slope	0.0779	0.00429
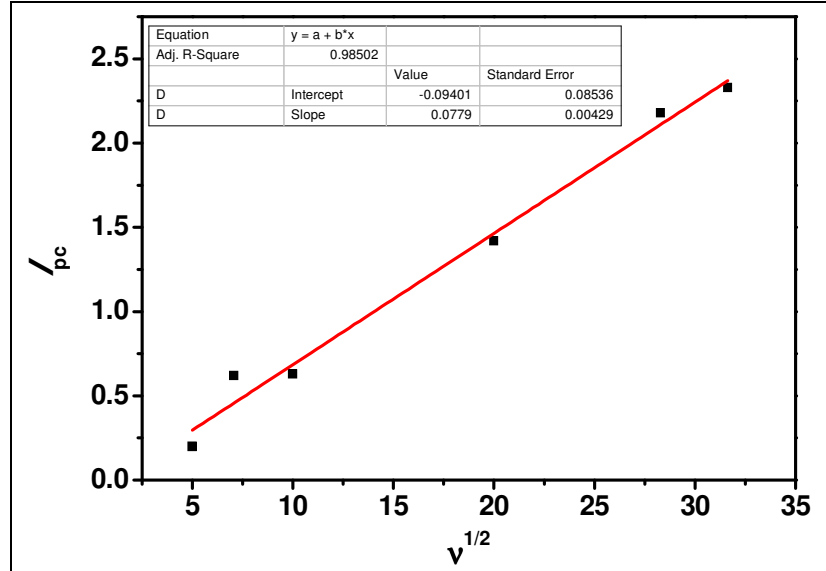
Figure 4.7: Plot of i_{pc} vs. Scan rate of EOPPI

The slope of the plot of i_{pc} vs. $v^{1/2} = 0.0779$ $(\mu A)\times(mV)^{-1/2}\times(s)^{1/2}$

$$D = \dfrac{\left(\frac{I_{pc}}{v^{1/2}}\right)^2}{\left[(2.69\times10^5 A s mol^{-1}V^{-1/2})^2\times(n^{3/2})^2\times(Ac)^2\right]}$$

$\Rightarrow$ D=

$$\dfrac{\left(0.0779\left[(\mu A)\times(mV)^{-\frac{1}{2}}\times(s)^{\frac{1}{2}}\right]\right)^2}{\left[\left(2.69\times10^5 A\,s\,mol^{-1}\,V^{-\frac{1}{2}}\right)^2\times\left((4)^{\frac{3}{2}}\right)^2\times\left((3.14\times(0.1\ cm))^2\times(1\times10^{-6}\ mol\,cm^{-3})\right)^2\right]}$$

$\Rightarrow$ $\mathbf{D_{EOPPI} = 1.33 \times 10^{-9}\ cm^2 s^{-1}}$

In the similar way, the diffusion constant of EONPI was calculated from the data of i_{pc} and scan rate (Figures 4.63 and 4.64, Table 4.17) and reported below.

$$\mathbf{D_{EONPI} = 3.52 \times 10^{-10}\ cm^2 s^{-1}}$$

Table 4.19: Diffusion constants data of *n*-type materials

Compound	$\mathbf{D\ (cm^2 s^{-1})}$
EOPPI in CH_2Cl_2	1.33×10^{-9}
EONPI in CH_2Cl_2	3.52×10^{-10}
EONPI in $CH_3CN + CH_3OH$ (50:50)	3.02×10^{-9}
HP-CH in DMAc*	1.68×10^{-10}

*DMAc: Dimethylacetamide

4.4 Förster/Fluorescence Resonance Energy Transfer (FRET)

FRET is a mechanism that describes energy transfer between two chromophores. The energy is passed *nonradiatively* between molecules. The 'donor' molecule, D, which is a fluorophore, absorbs a photon and transfers this energy *nonradiatively* to the acceptor molecule, A.

According to Förster, the critical molecular separation, in other words, the critical transfer distance (R_0) below which transfer occurs during the excitation lifetime is shown to be calculable from the absorption and fluorescence spectra and the excitation lifetime of the molecule.

4.4.1 Critical Transfer Distances (R_0)

$$R_0^6 = \frac{8.785 \times 10^{-5} \kappa^2 \Phi_D J}{n^4}$$

$$J = \int_0^\infty F_D(\lambda) \, \varepsilon_A(\lambda) \, \lambda^4 \, d\lambda$$

(Equn. 4.20) [69, 70]

Where, κ^2: Orientation factor ($\kappa^2 = 0.67$ for normally distributed molecules)

Φ_D: Fluorescence quantum yield of donor

J : Overlap integral between the fluorescence spectrum of donor and the molar absorption spectrum of acceptor

n : Refractive index of solvent

$F_D(\lambda)$: Peak-normalized fluorescence spectrum of the donor

$\varepsilon_A(\lambda)$: Extinction co-efficient of acceptor in $\text{mol}^{-1}\text{Lcm}^{-1}$ at the wavelength

λ : Maximum wavelength of acceptor in nm

R_0: Critical transfer distance in $\overset{o}{A}$

4.4.2 Critical Transfer Distance (R_0) Between EOPPI and Cobalt(II) Chloride

In order to study the energy transfer of EOPPI, $CoCl_2$ was selected as electron acceptor and both the compounds were dissolved in methanol and measured the required absorption of acceptor and fluorescence of donor. The overlap of the absorption spectrum of acceptor and fluorescence spectrum of donor (Figure 4.32) reveals the probable energy transfer of EOPPI to the acceptor.

From the fluorescence spectrum of the donor, EOPPI (Figure 4.8), the normalized area $F_D(\lambda) = 52.14$
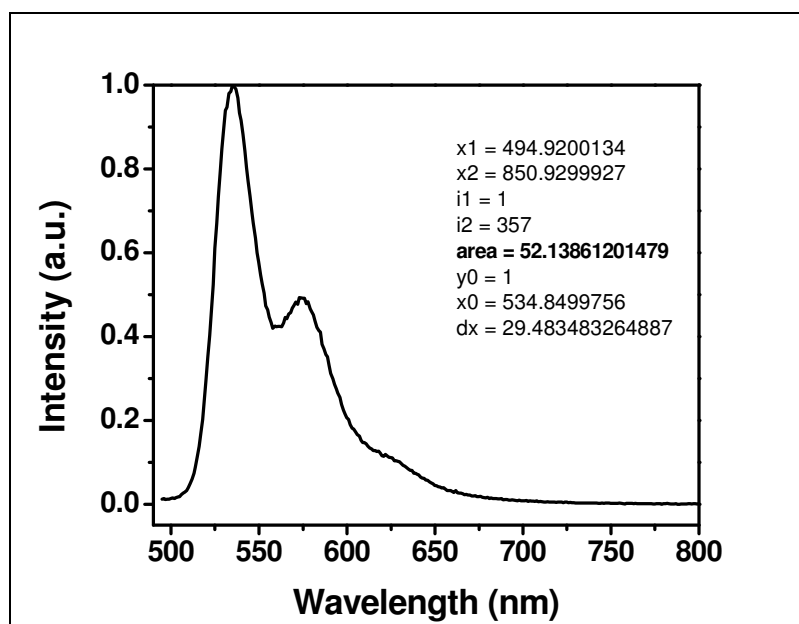
Figure 4.8: Normalized Fluorescence Spectrum of the Donor, EOPPI ($c = 1\times10^{-5}$ M)

in the Absence of Acceptor, Cobalt(II) Chloride

From the UV spectrum of cobalt(II) chloride (Figure 4.9), molar absorptivity $\varepsilon_A(\lambda)$ at $\lambda = 530$ nm is 11.8.
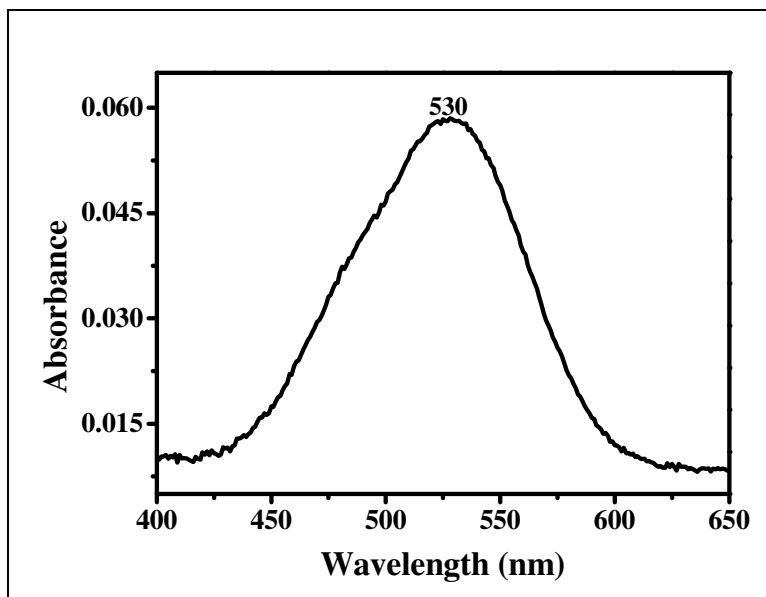
Figure 4.9: Absorption Spectrum of Cobalt(II) Chloride at c = 5×10^{-3} M

⇨ $J = \int_0^\infty F_D(\lambda) \, \varepsilon_A(\lambda) \, \lambda^4 \, d\lambda$

⇨ $J = 52.14 \times 11.8 \times (530)^4$

⇨ $J = 4.8546 \times 10^{13}$

⇨ $R_0^6 = \dfrac{8.785 \times 10^{-5} \, \kappa^2 \, \Phi_D \, J}{n^4}$

⇨ $R_0^6 = 8.785 \times 10^{-5} \times 0.67 \times 0.63 \times 4.8546 \times 10^{13} / (1.3284)^4$

⇨ $R_0^6 = 5.78 \times 10^8$

⇨ $R_0 = 28.9 \ \overset{o}{A}$

4.4.3 Rate Constants for Bimolecular Fluorescence Quenching (k_q)

The rate constant for bimolecular fluorescence quenching was calculated by Stern-Volmer plot and from the following equation.

$$\frac{I_0}{I} = 1 + k_q \tau_0 [Q]$$

(Equn. 4.21) [71]

Where, $\dfrac{I_0}{I}$: Relative fluorescence intensity

I_0: Emission intensity of donor in the absence of acceptor

I: Emission intensities of donor in presence of acceptor at different

Concentrations

k_q: Rate Constant for Bimolecular Fluorescence Quenching

τ_0: Theoretical radiative lifetime of donor on the absence of quencher

From the Figure 4.34 the emission intensities of EOPPI were estimated in the absence (I_0) and presence (I) of quencher (at different concentrations) and plotted the intensities of donor vs. concentration of quencher.

The plot was shown in Figure 4.35 and the linear regression data of the linear fit plot was shown in the diagram.

Slope of the plot from linear regression data = $k_q \tau_0$ = 55.48

$$\Rightarrow k_q = (55.48/5.22 \times 10^{-9}) = 1.06 \times 10^{10} \text{ M}^{-1} \text{ s}^{-1}$$

$$k_q = 1.06 \times 10^{10} \text{ M}^{-1} \text{ s}^{-1}$$

93
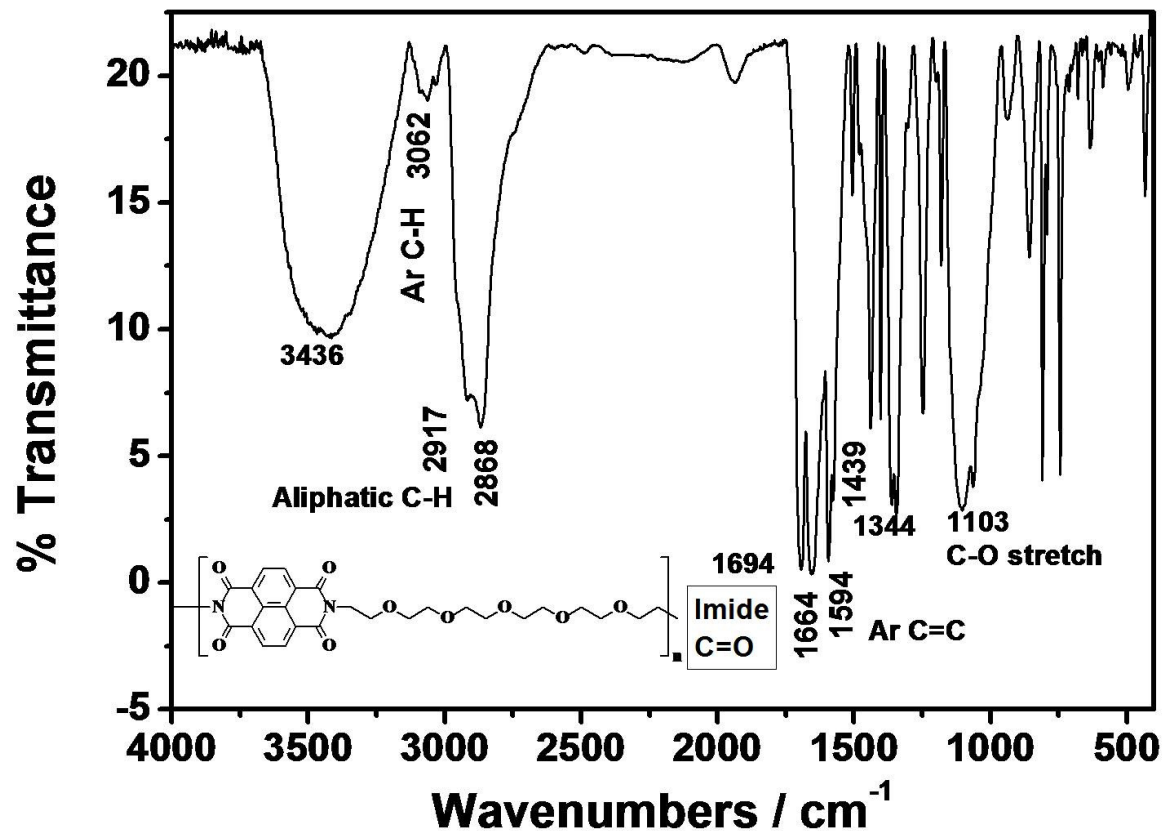
Figure 4.10: FT-IR Spectrum of EOPPI
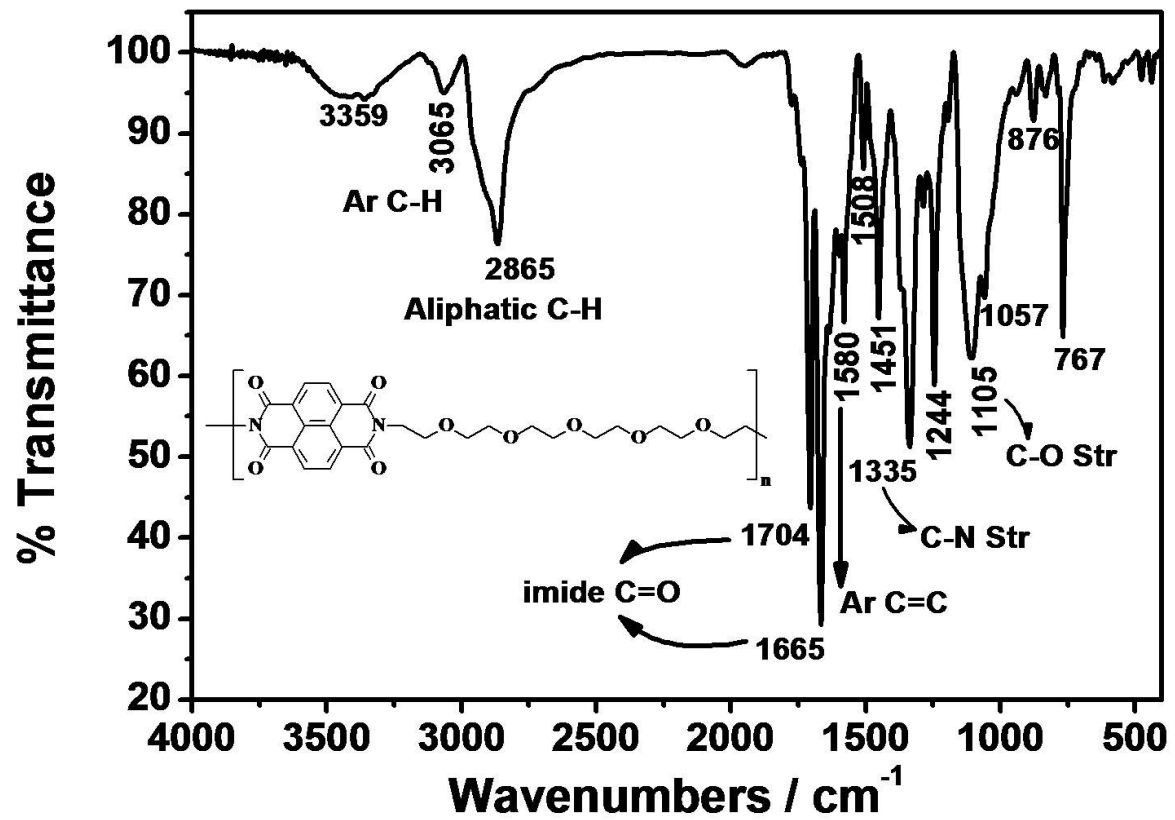
Figure 4.11: FT-IR Spectrum of EONPI
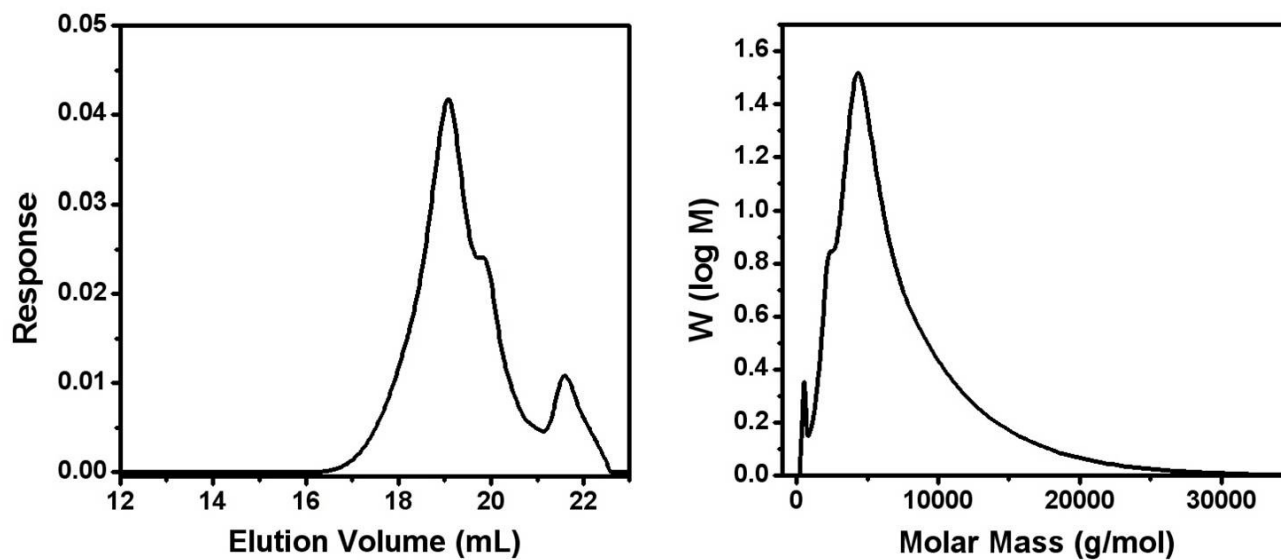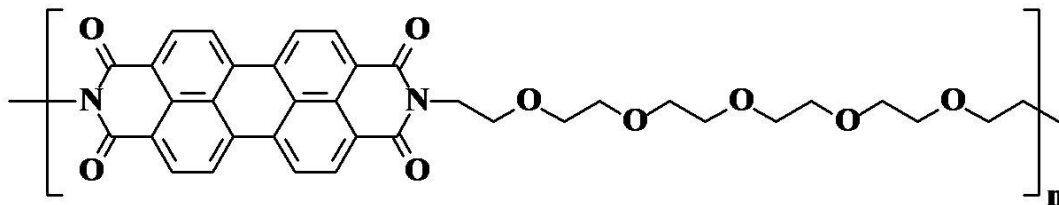
Figure 4.12: GPC Chromatograms of EOPPI
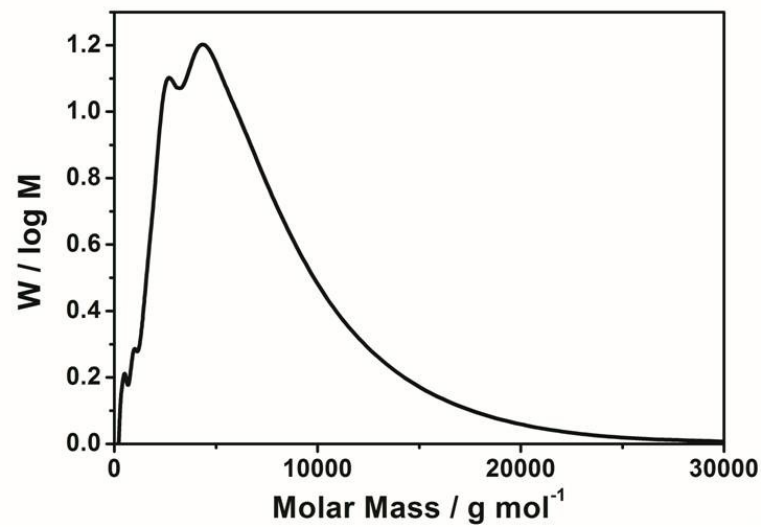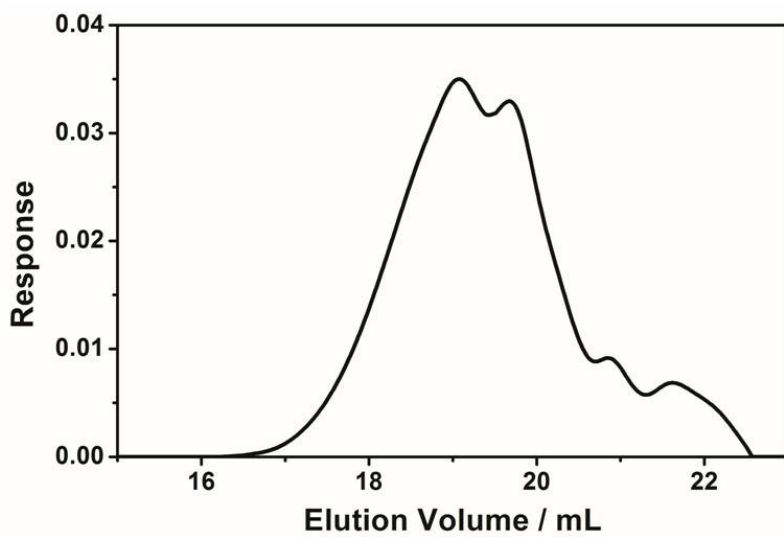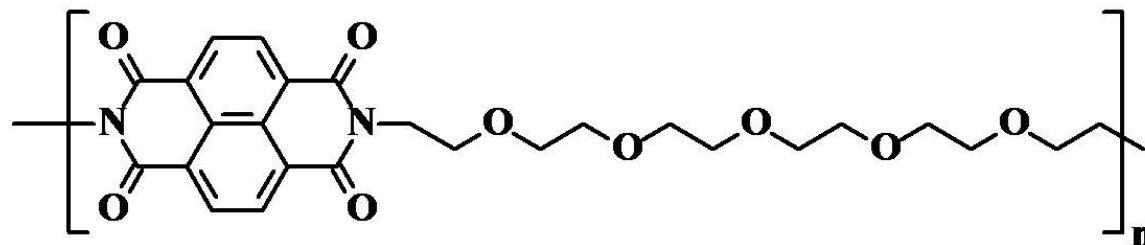
Figure 4.13: GPC Chromatograms of EONPI

97
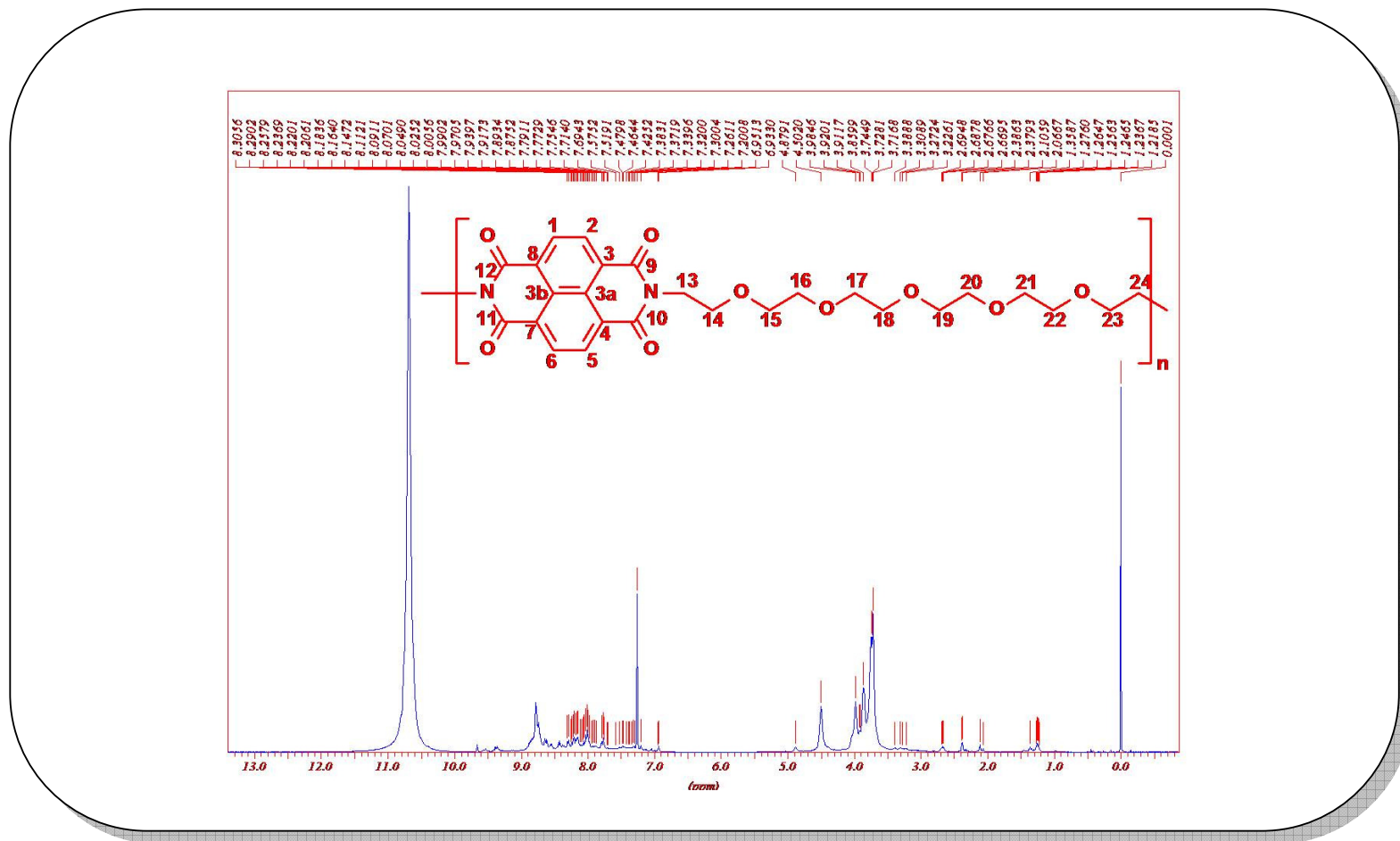
Figure 4.14: ^{1}H NMR spectrum of EONPI in the mixture of CDCl$_3$ + CF$_3$COOH (1:1)
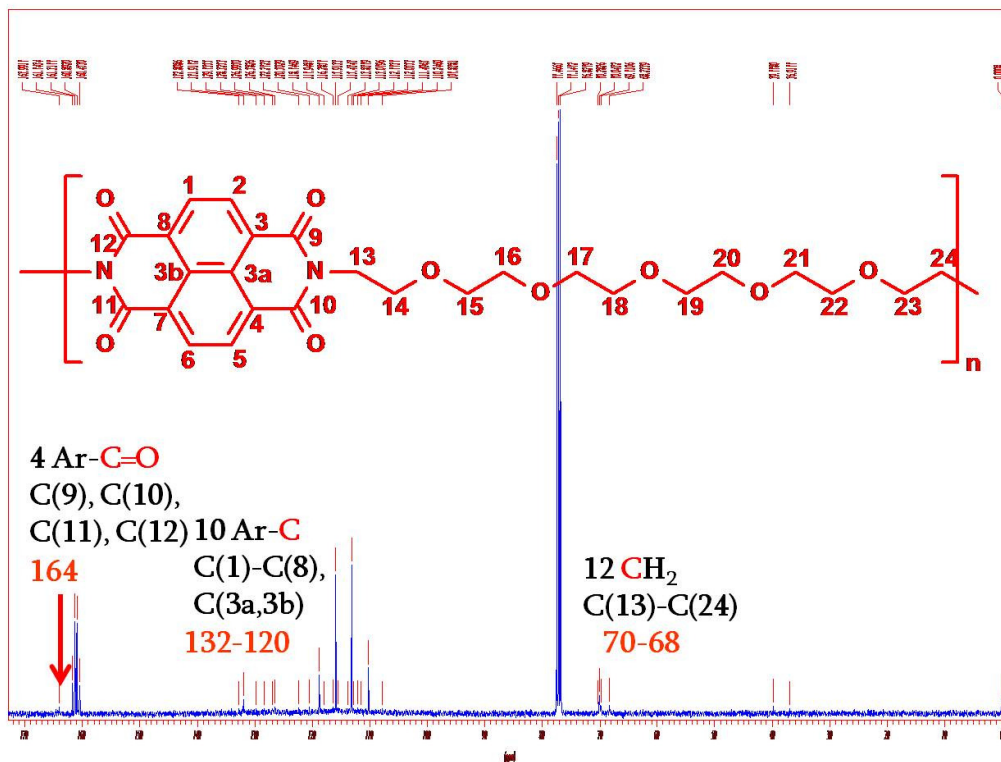
Figure 4.15: ^{13}C NMR spectrum of EONPI in the mixture of $CDCl_3$ + CF_3COOH (1:1)
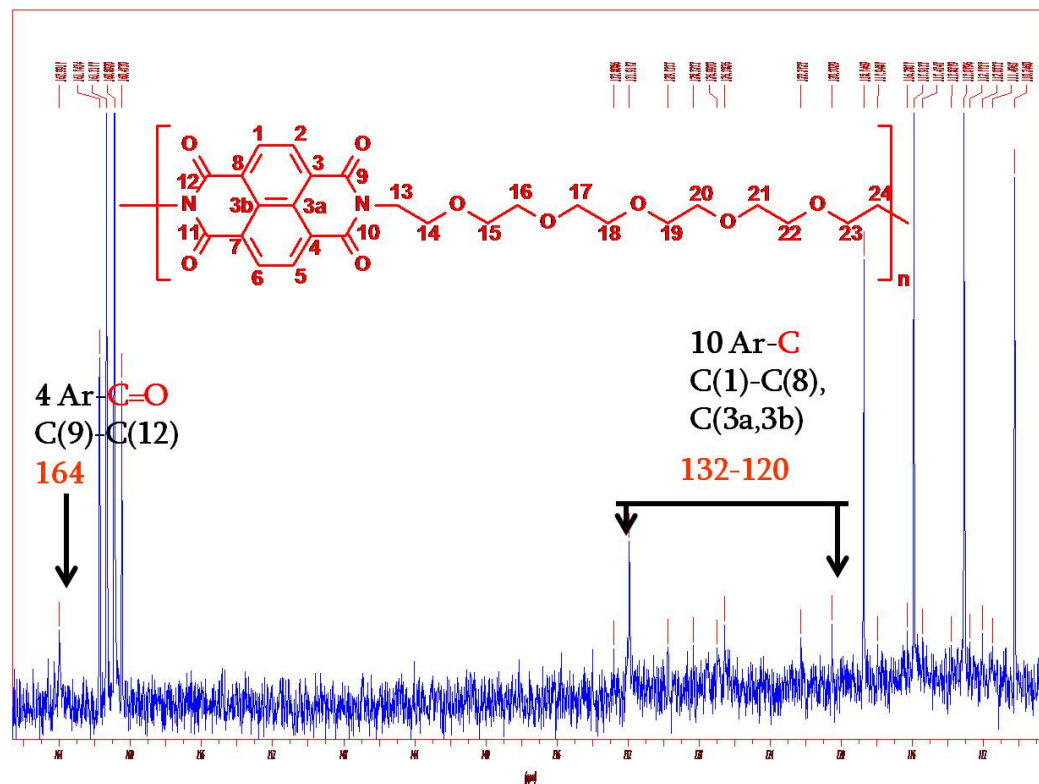
Figure 4.16: ^{13}C NMR spectrum of EONPI in the mixture of CDCl$_3$ + CF$_3$COOH (1:1)
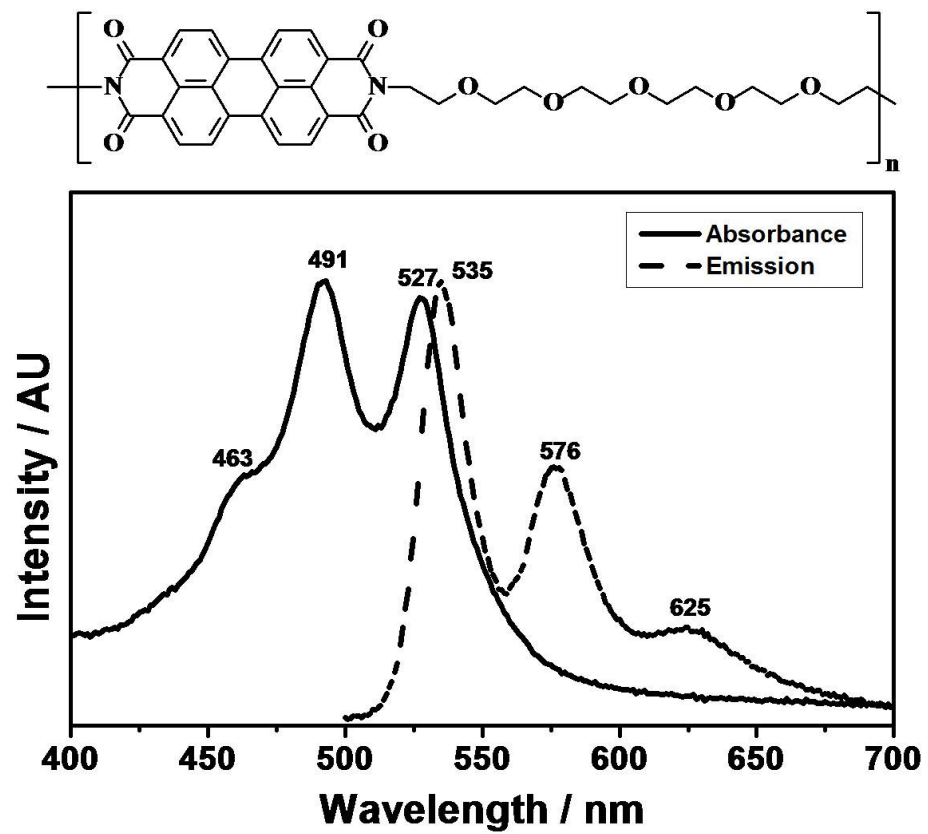
Figure 4.17: UV-vis Absorption and Emission Spectra of EOPPI in CHCl$_3$ at 1×10^{-5} M
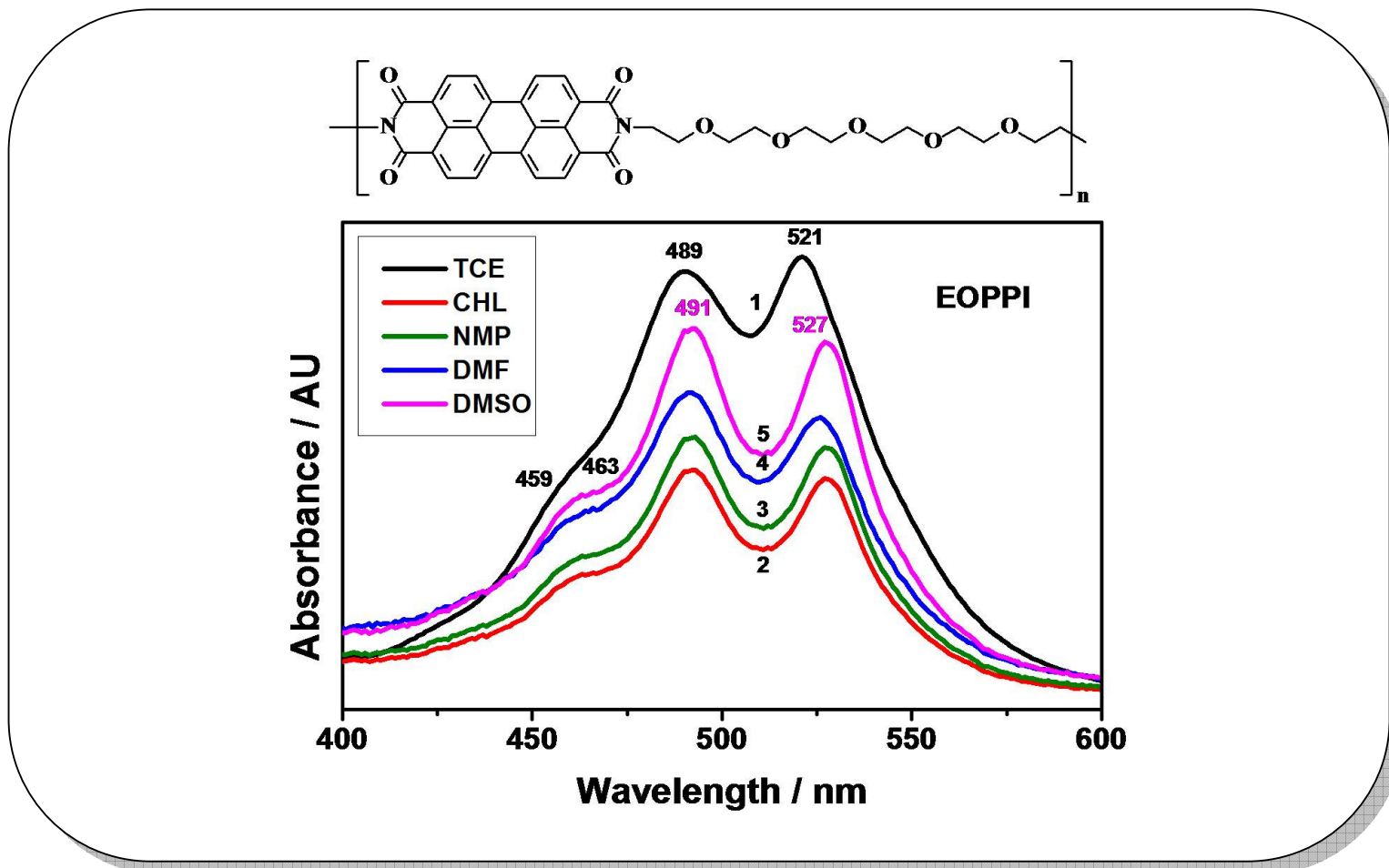
Figure 4.18: Comparison of UV-vis Absorption Spectra of EOPPI in Various Solvets
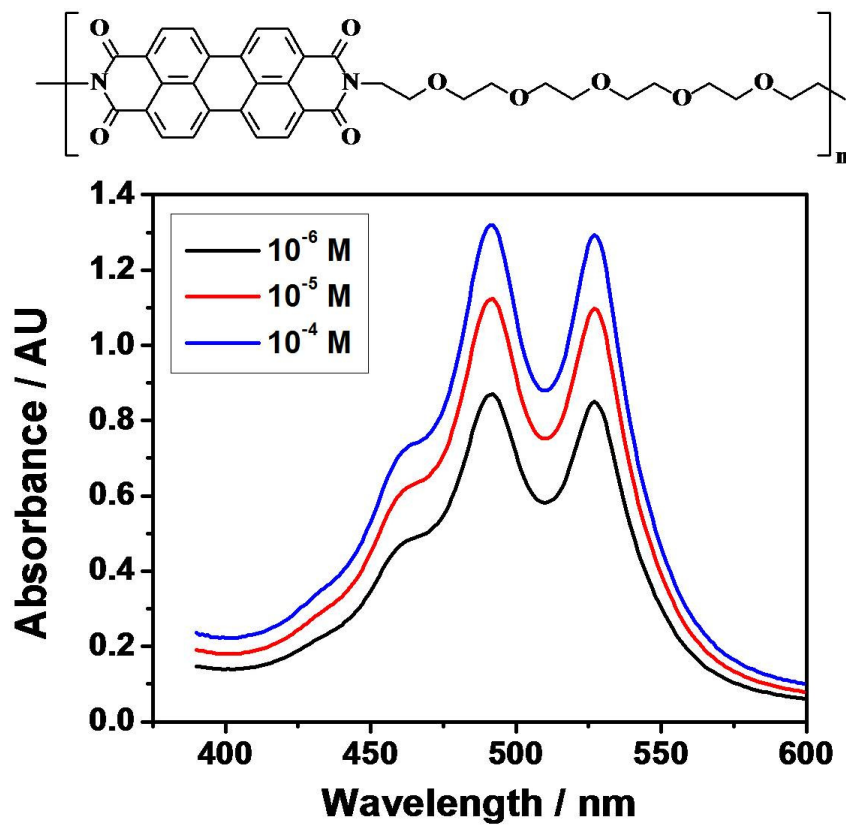
Figure 4.19: Dependence of Concentration on UV-vis Absorption Spectra of EOPPI in CHCl$_3$

Figure 4.20: Solid-state Absorption Spectrum of EOPPI
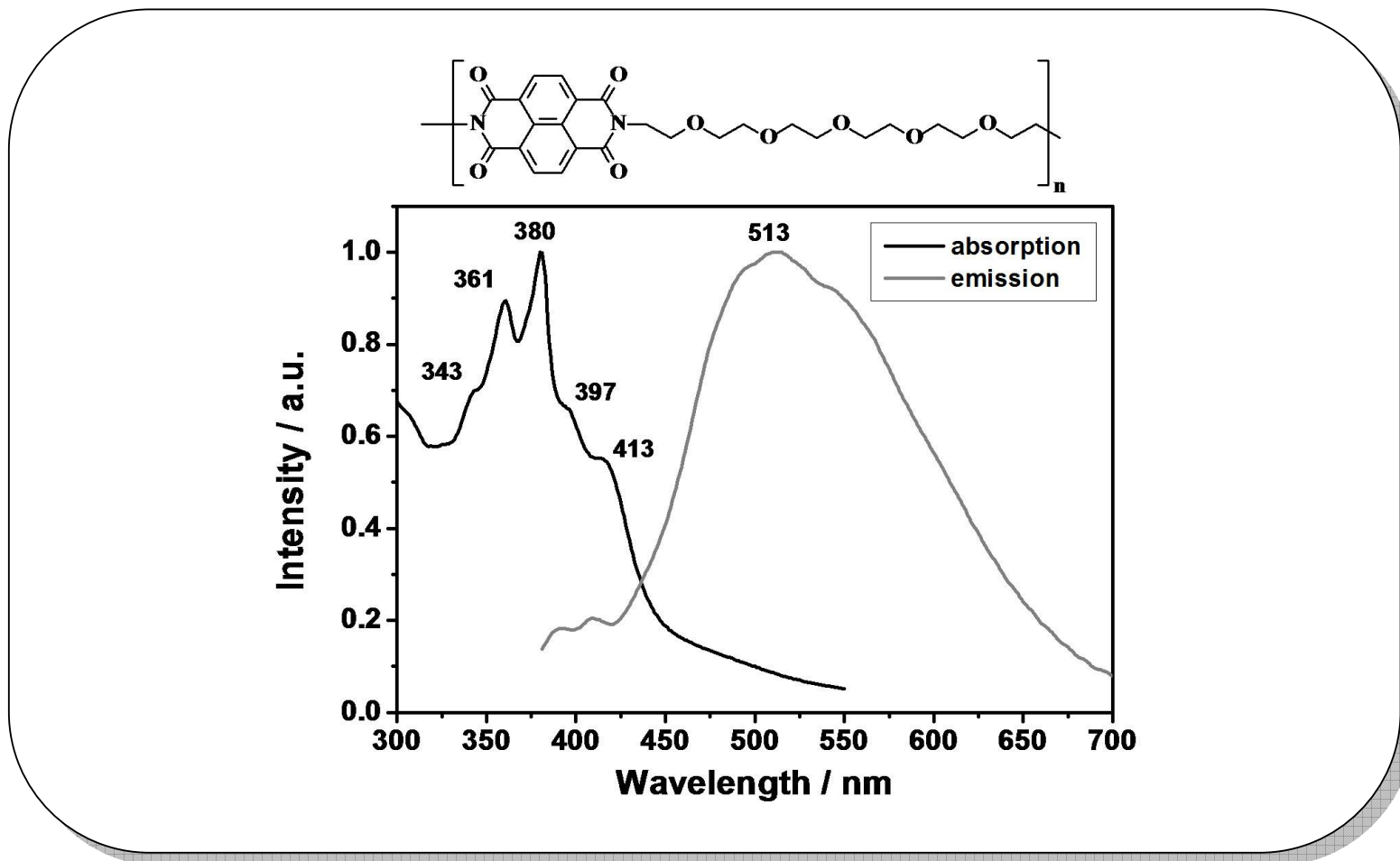
Figure 4.21: UV-vis Absorption and Emission Spectra of EONPI in CHCl$_3$ at 1×10^{-5} M

105

Figure 4.22: Comparison of UV-vis Absorption Spectra of EONPI in Variuos Solvets
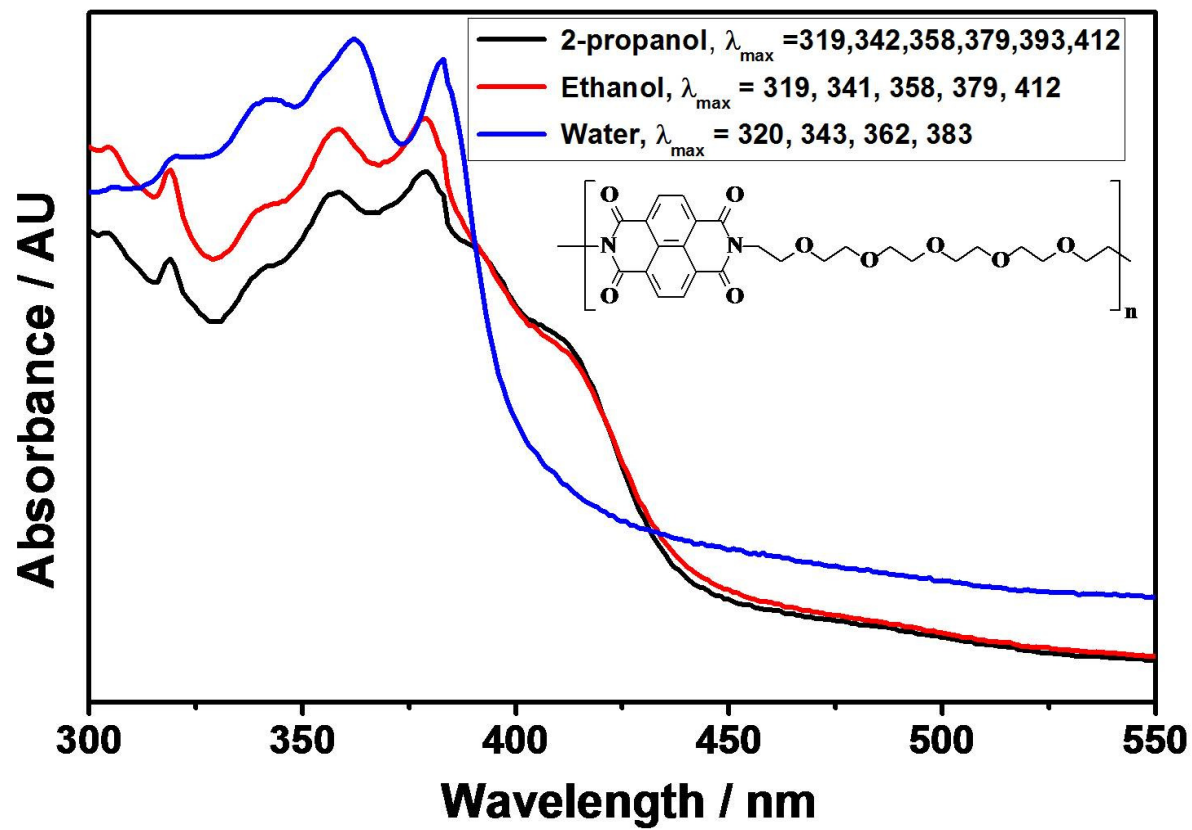
Figure 4.23: Comparison of UV-vis Absorption Spectra of EONPI in Protic Solvets
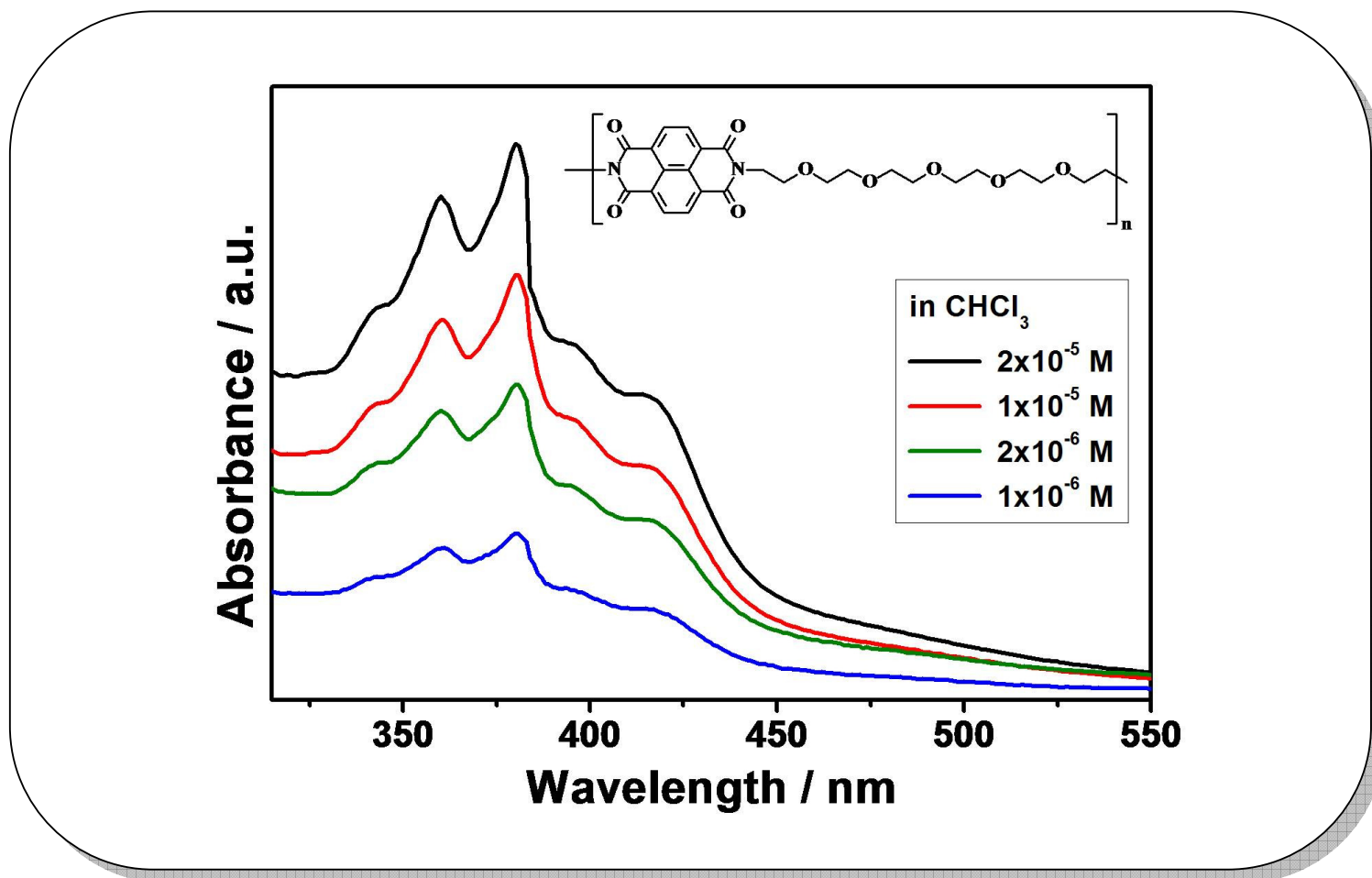
Figure 4.24: Dependence of Concentration on UV-vis Absorption Spectra of EONPI in CHCl$_3$
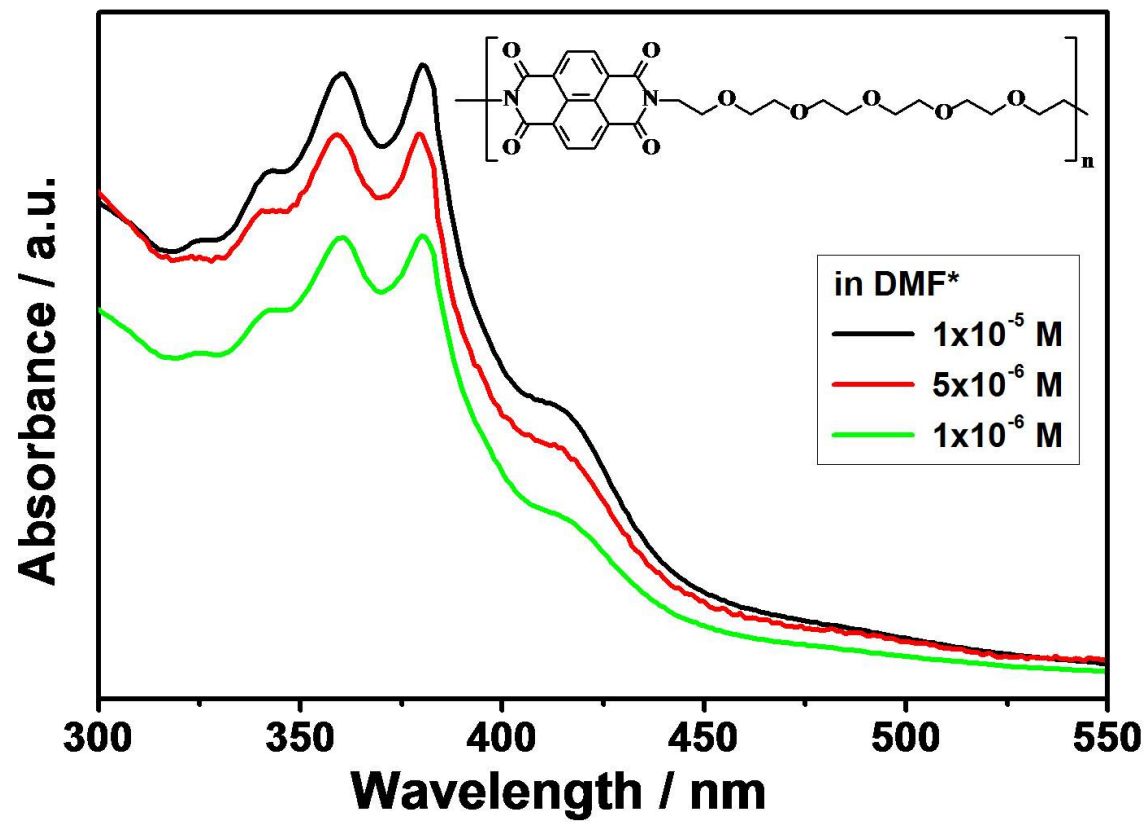
Figure 4.25: Dependence of Concentration on UV-vis Absorption Spectra of EONPI in DMF
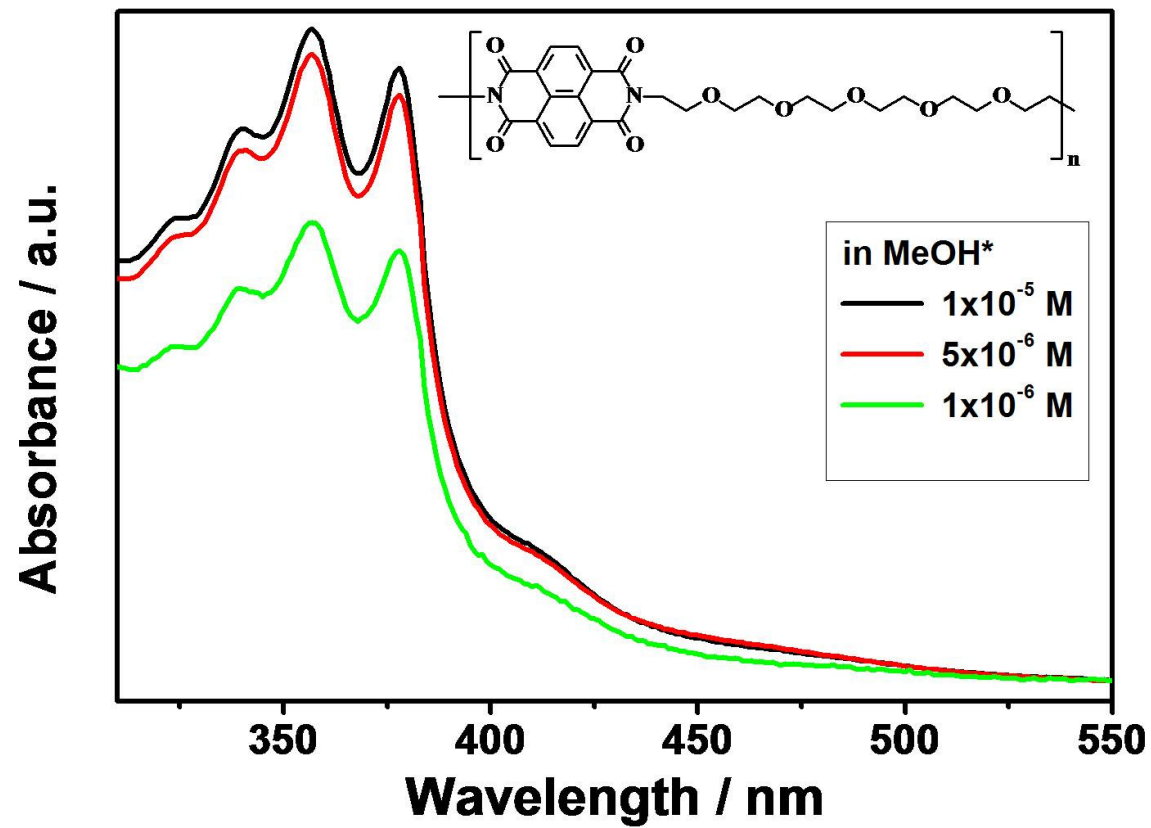
Figure 4.26: Dependence of Concentration on UV-vis Absorption Spectra of EONPI in CH$_3$OH
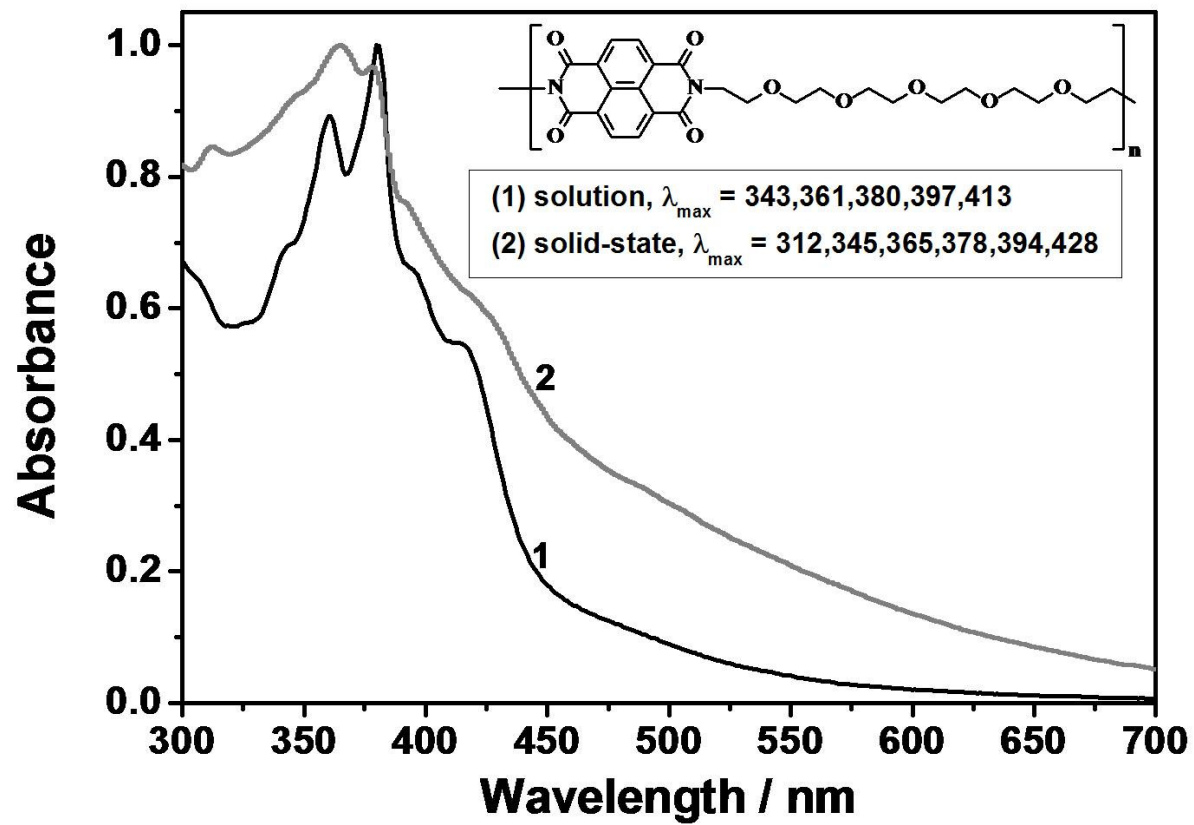
Figure 4.27: Comparison of UV-vis Absorption Spectra of EONPI in Solution and Solid-state
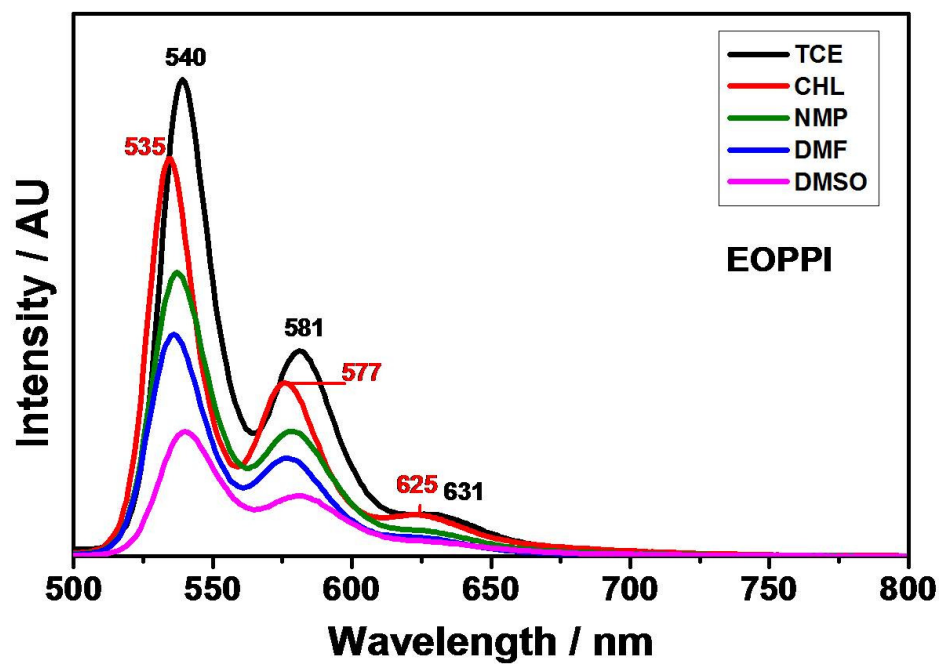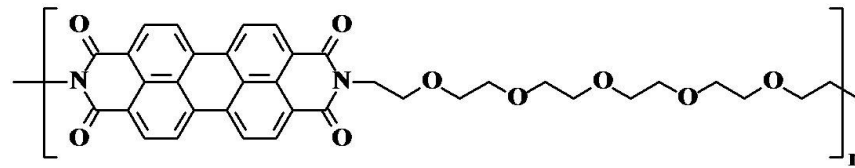
Figure 4.28: Emission Spectra of EOPPI (at λ_{exc} = 485 nm) in Various Solvents
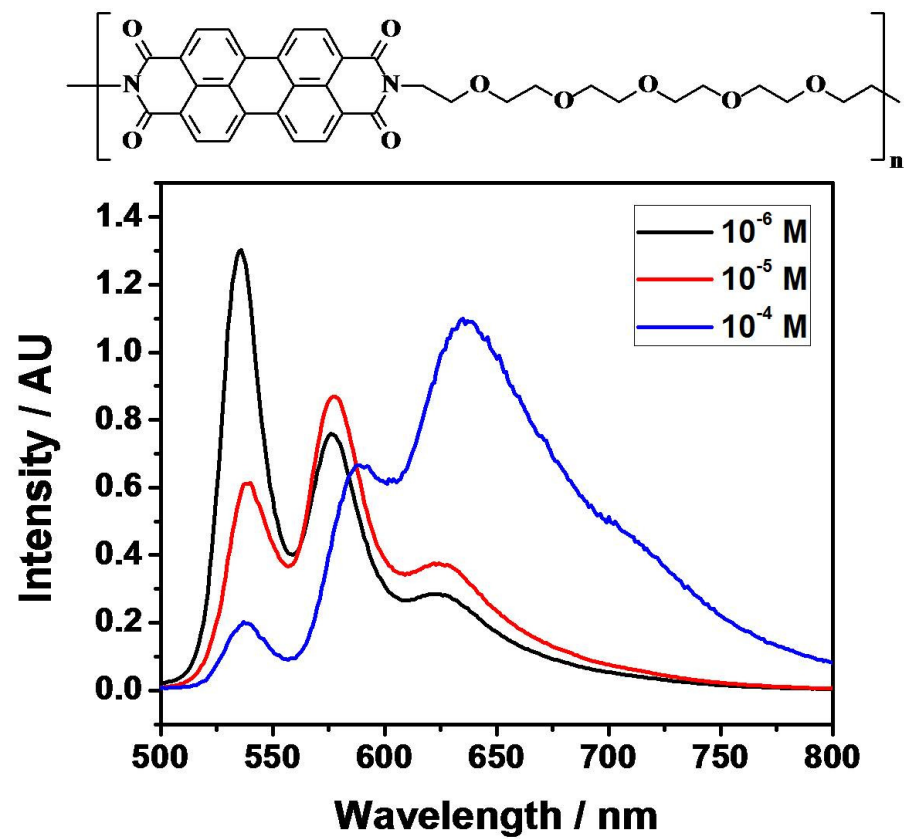
Figure 4.29: Dependence of Concentration on Emission Spectra of EOPPI in CHCl$_3$
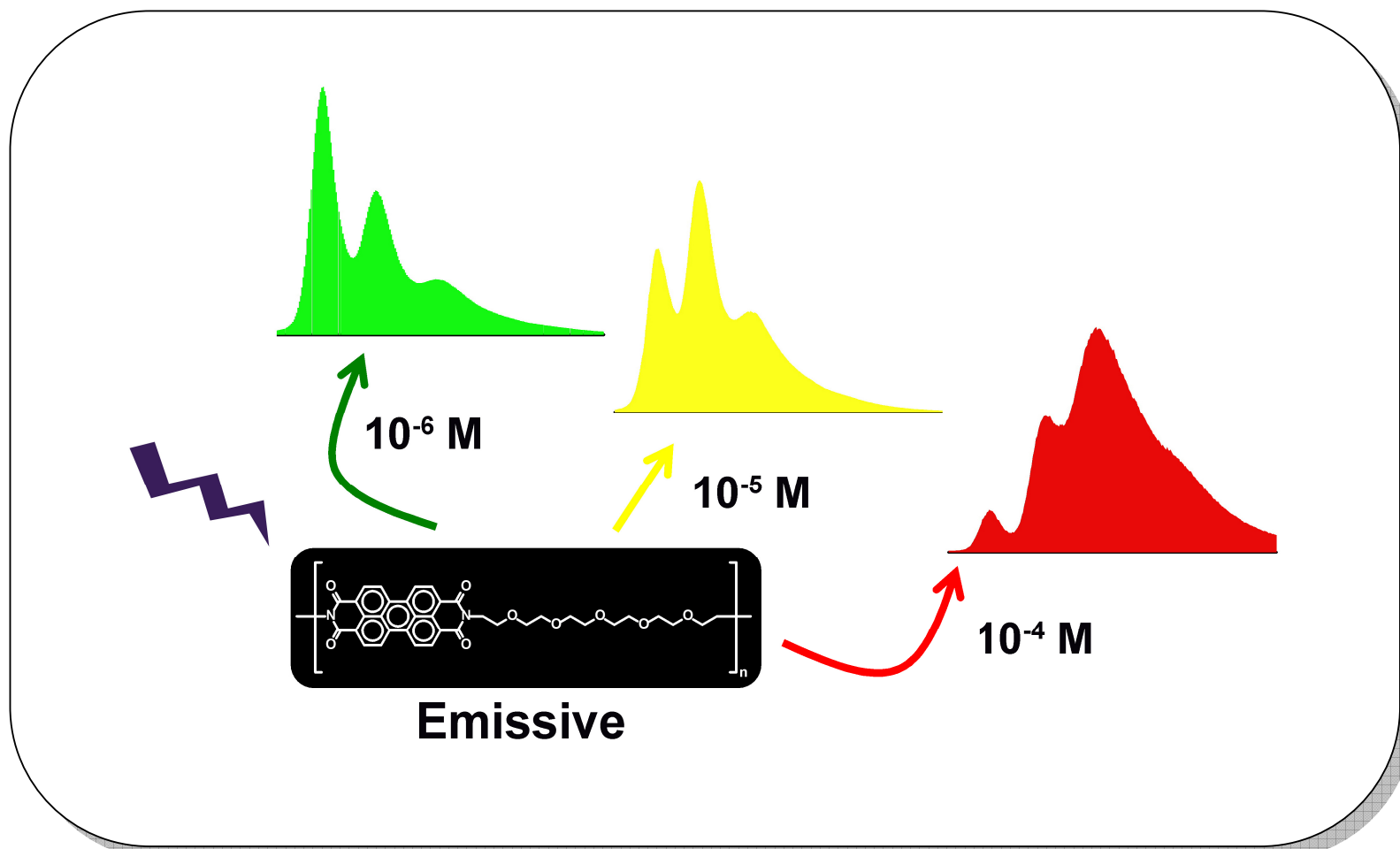
Figure 4.30: Dependence of Concentration on Emission Spectra and Respective Color Tunability of EOPPI in CHCl$_3$
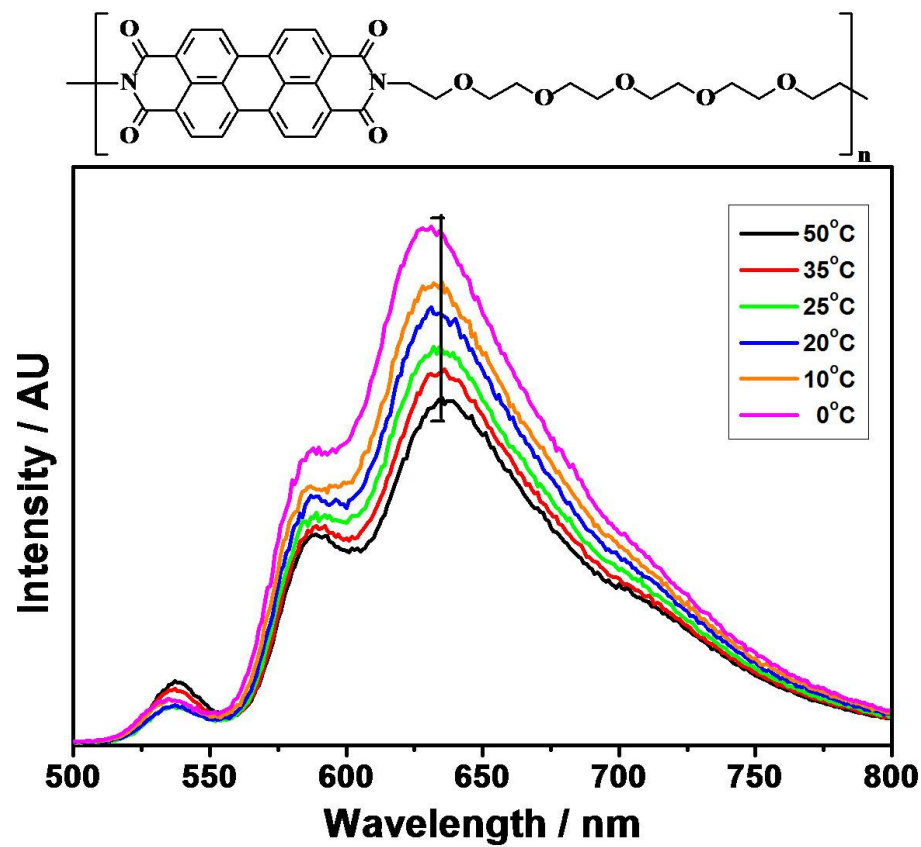
Figure 4.31: Effect of Temperature on Emission Spectra of EOPPI in CHCl$_3$ 1×10^{-5} M
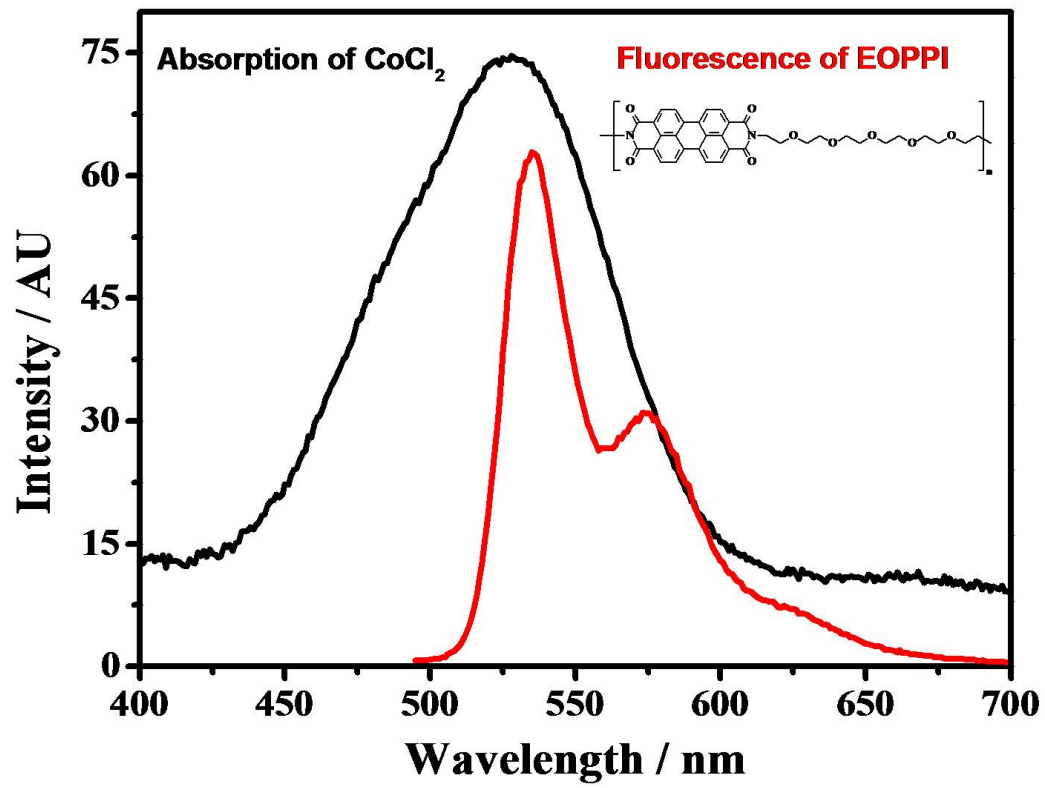
Figure 4.32: Overlap of Absorption Spectrum of Acceptor, CoCl$_2$ and Emission Spectrum of Donor, EOPPI
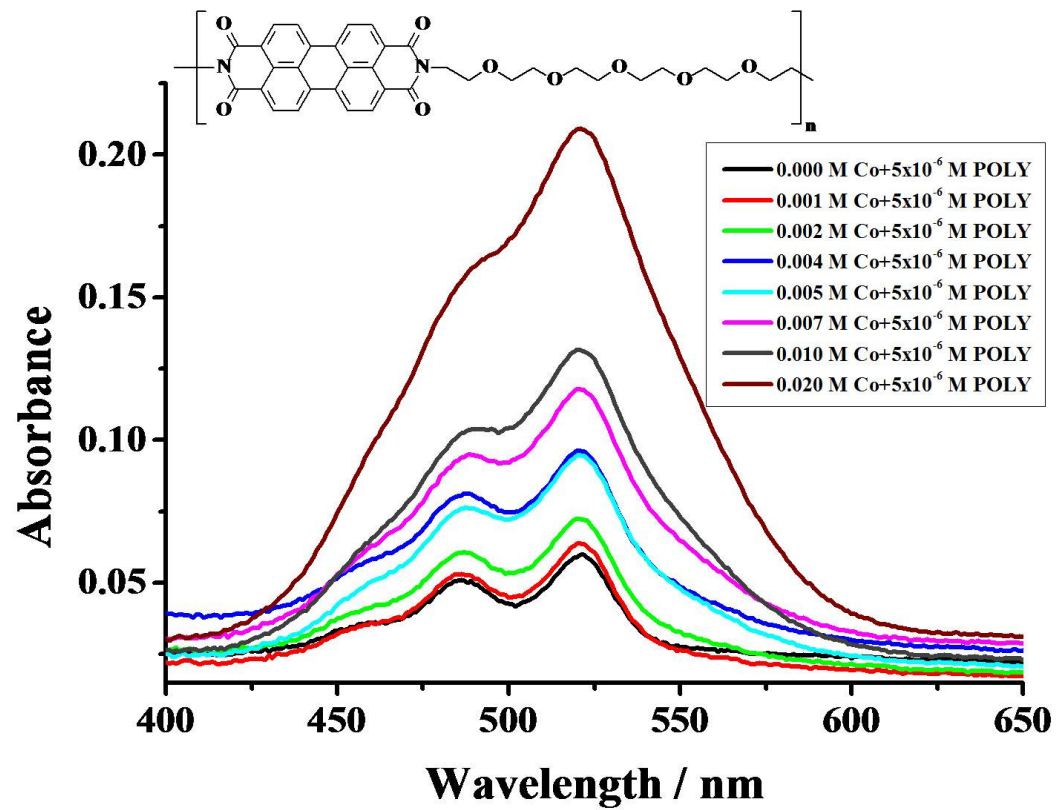
Figure 4.33: Effect of CoCl$_2$ Concentration on UV-vis Spectra of EOPPI
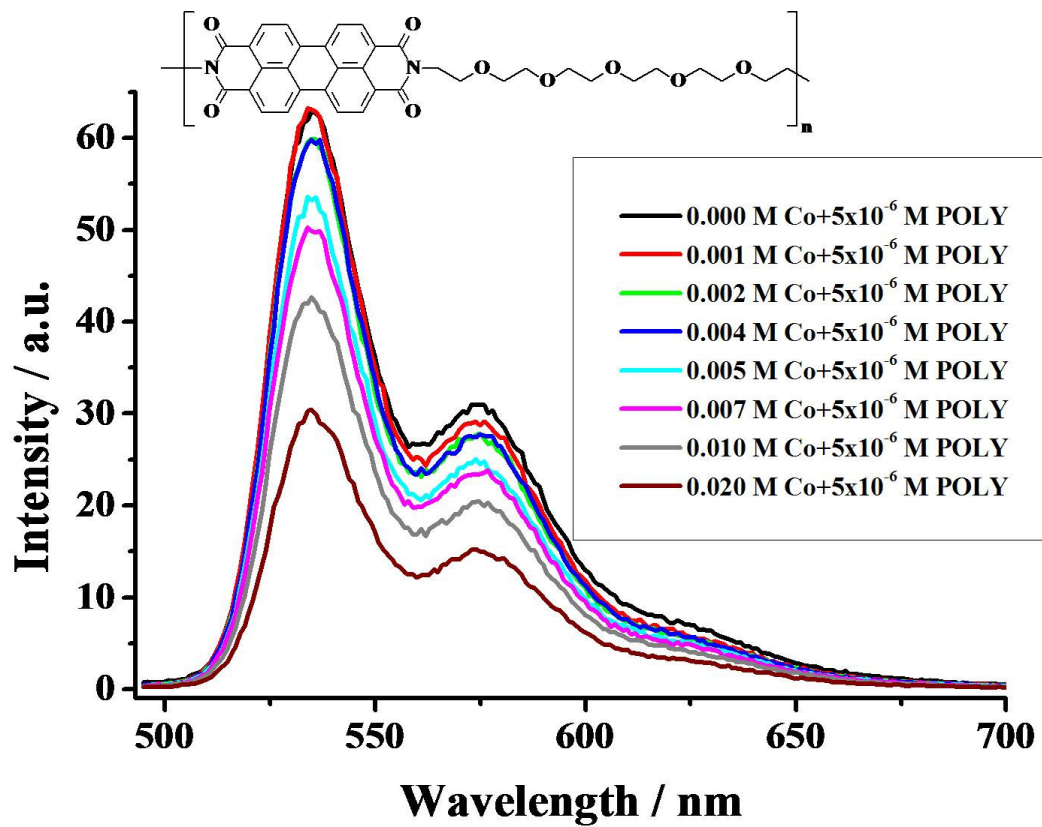
Figure 4.34: Effect of CoCl$_2$ Concentration on Emission Spectra of EOPPI

Figure 4.35: Stern-Volmer Plot of Fluorescence Quenching of EOPPI Using Co^{2+} ions in Methanol
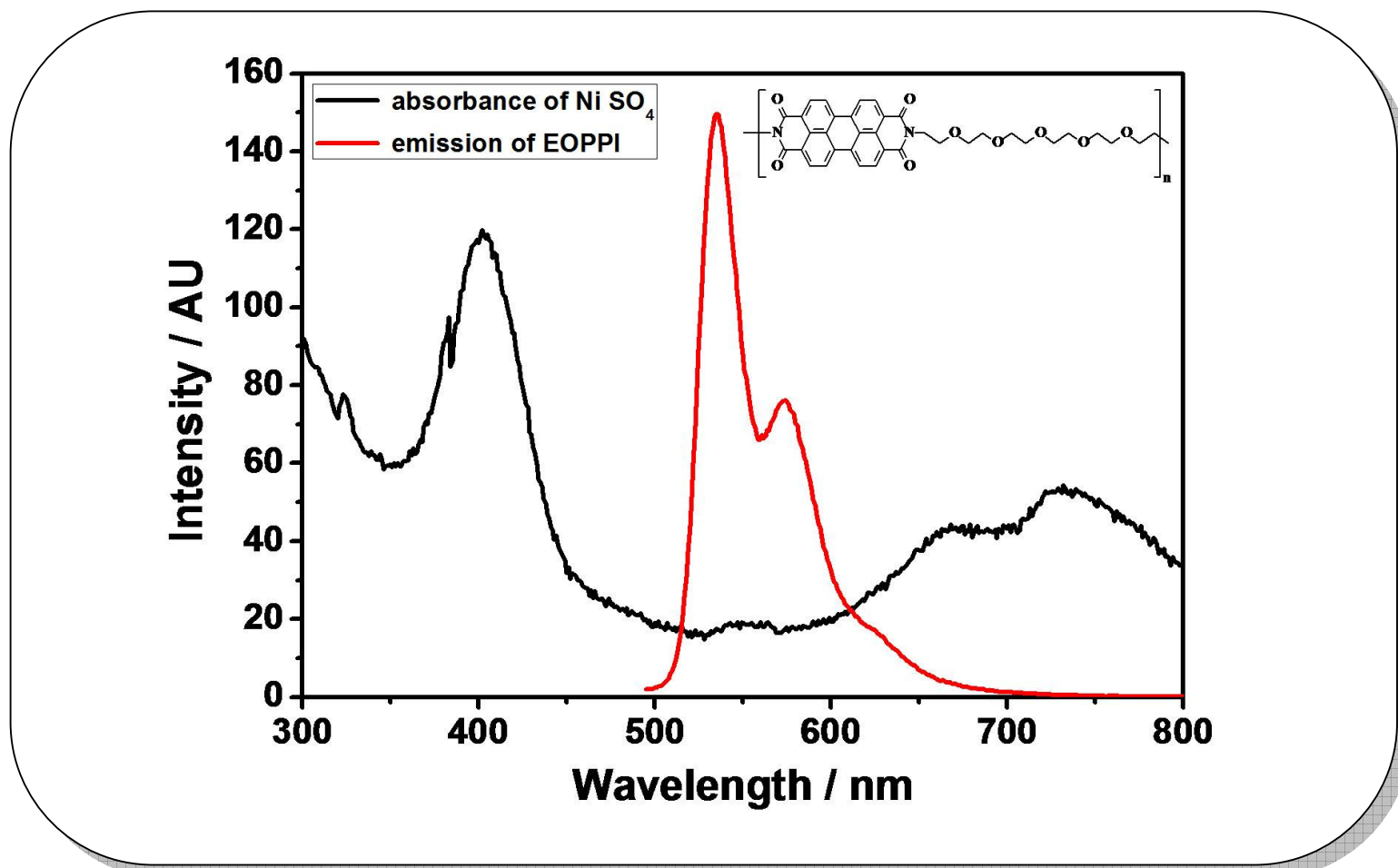
Figure 4.36: Overlap of Absorption Spectrum of Acceptor, $NiSO_4$ and Emission Spectrum of Donor, EOPPI

120
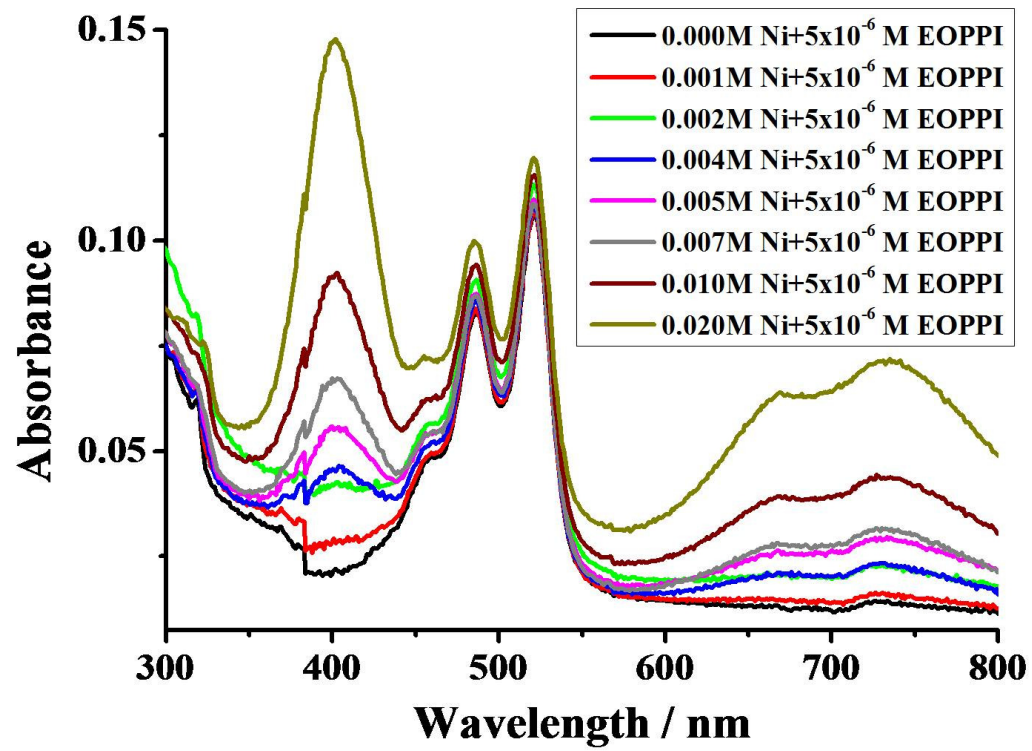
Figure 4.37: Effect of NiSO$_4$ Concentration on UV-vis Spectra of EOPPI
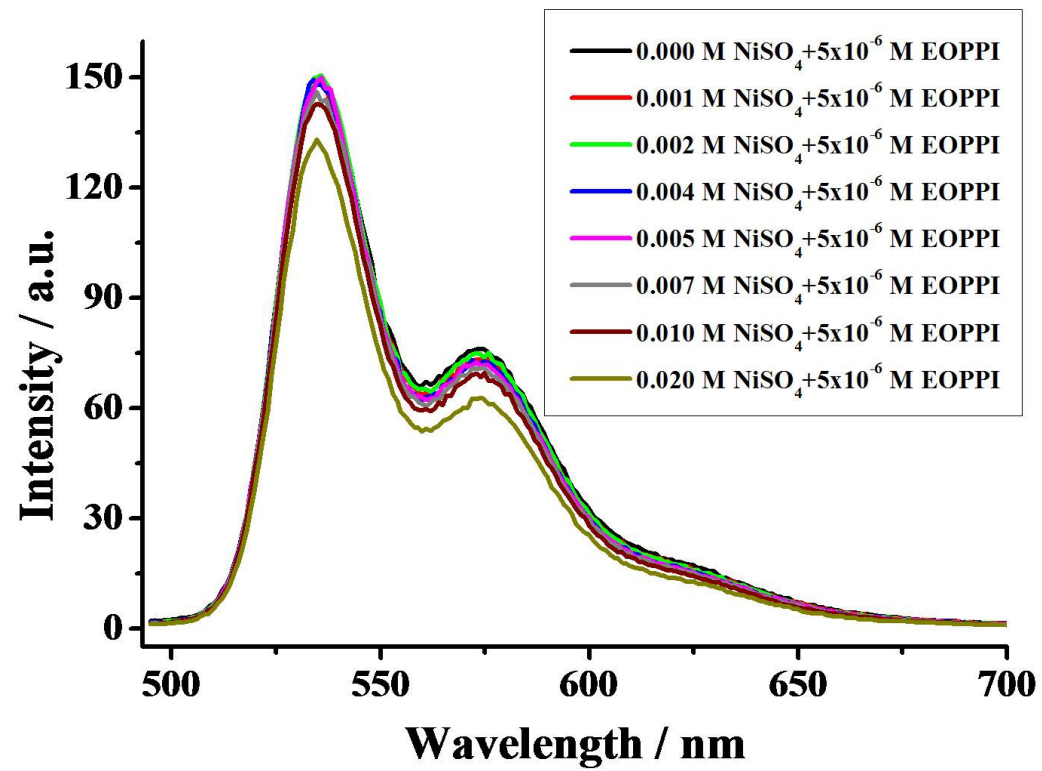
Figure 4.38: Effect of NiSO$_4$ Concentration on Emission Spectra of EOPPI

Figure 4.39: Stern-Volmer Plot of Fluorescence Quenching of EOPPI Using Ni^{2+} ions in Methanol
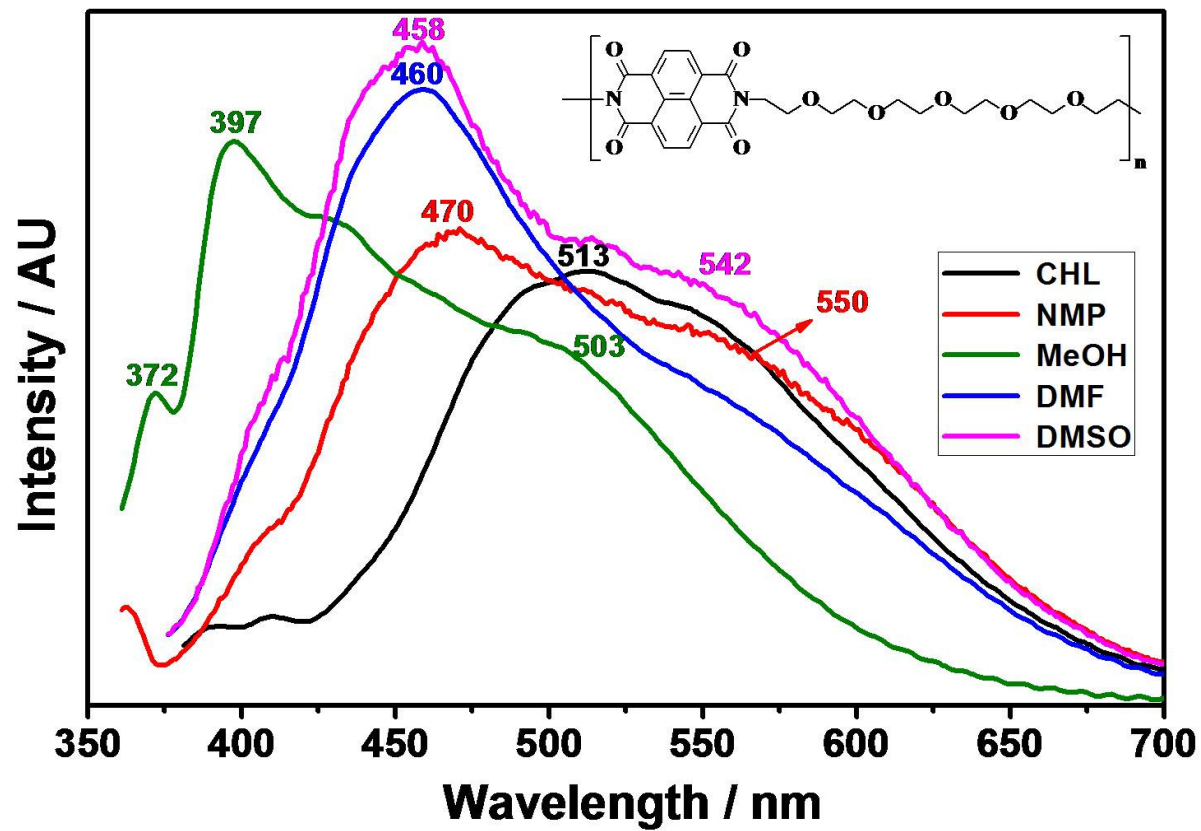
Figure 4.40: Emission Spectra of EONPI (at λ_{exc} = 360 nm) in Various Solvents
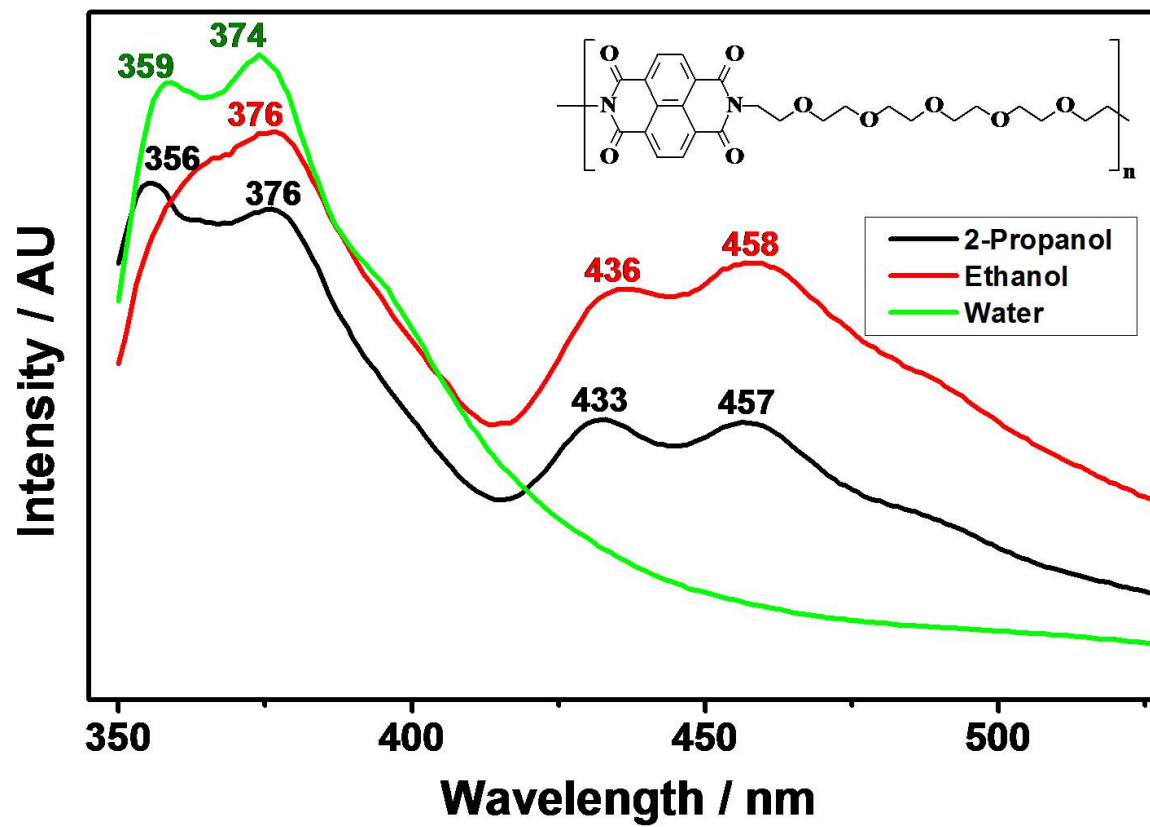
Figure 4.41: Comparison of Emission Spectra of EONPI in Protic Solvets

125
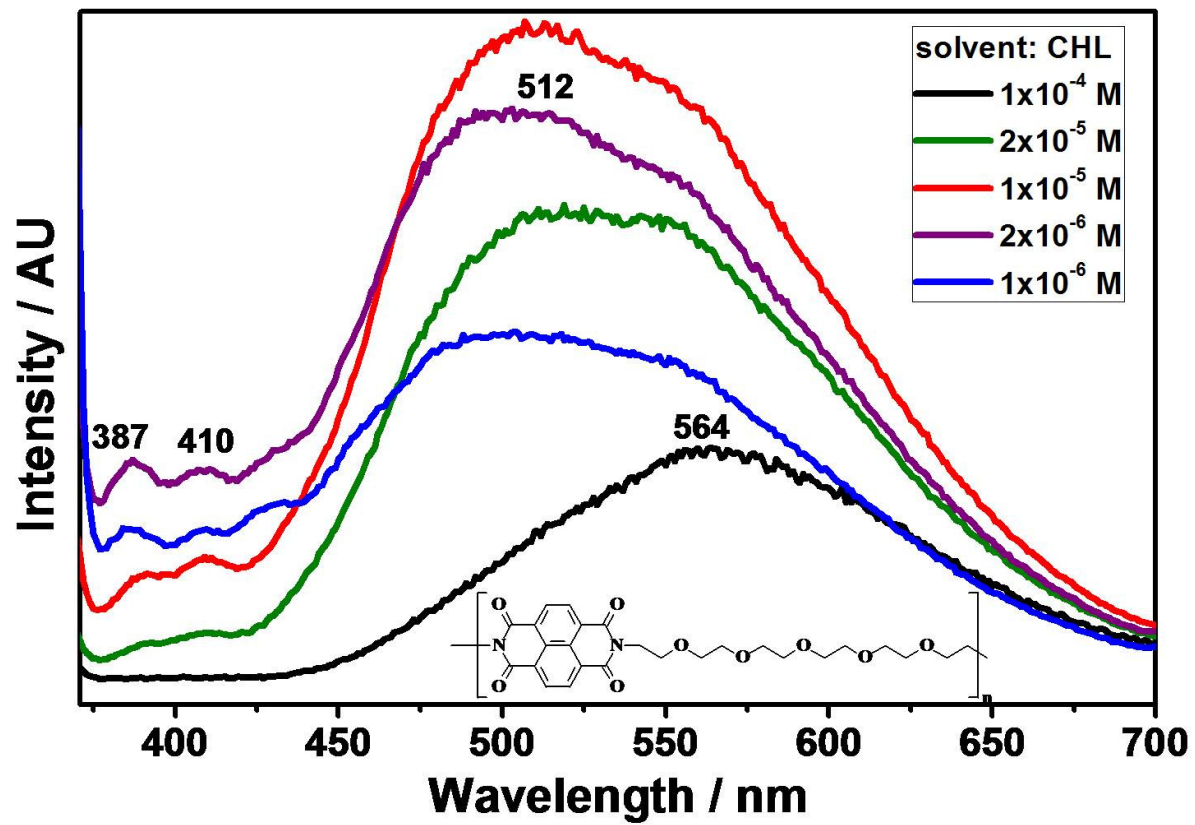
Figure 4.42: Effect of Concentration on Emission Spectra of EONPI in CHCl$_3$

Figure 4.43: Effect of Concentration on Emission Spectra of EONPI in NMP
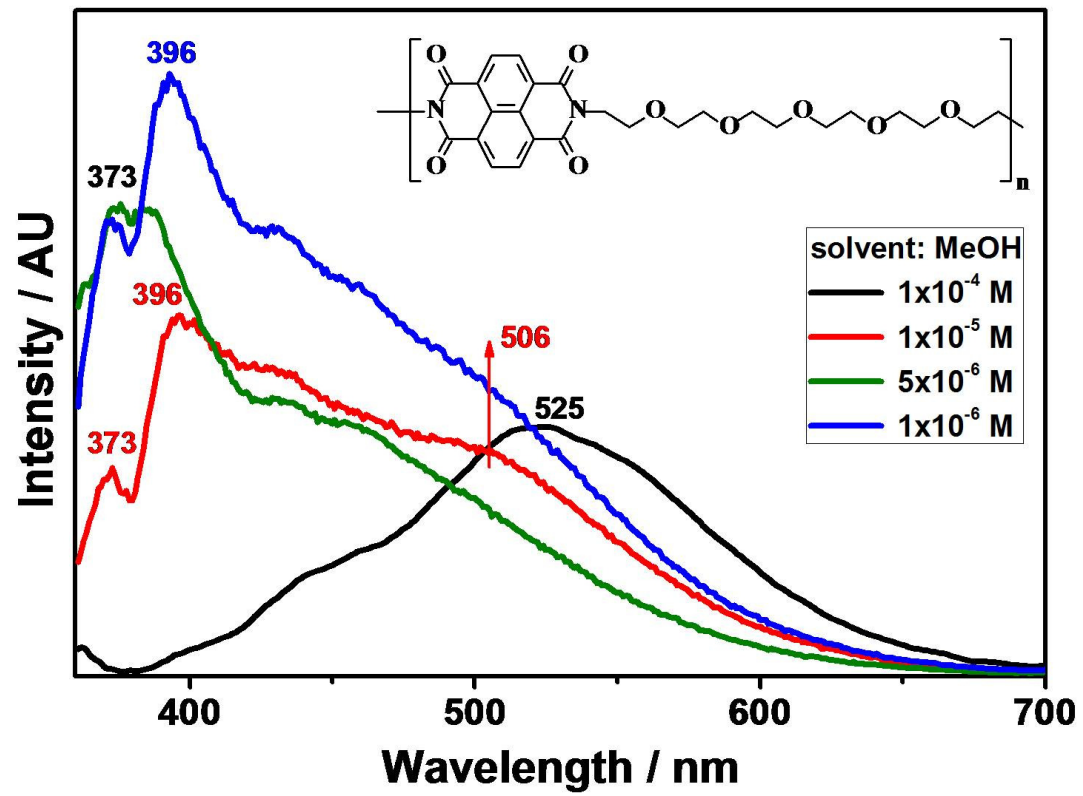
Figure 4.44: Effect of Concentration on Emission Spectra of EONPI in CH$_3$OH
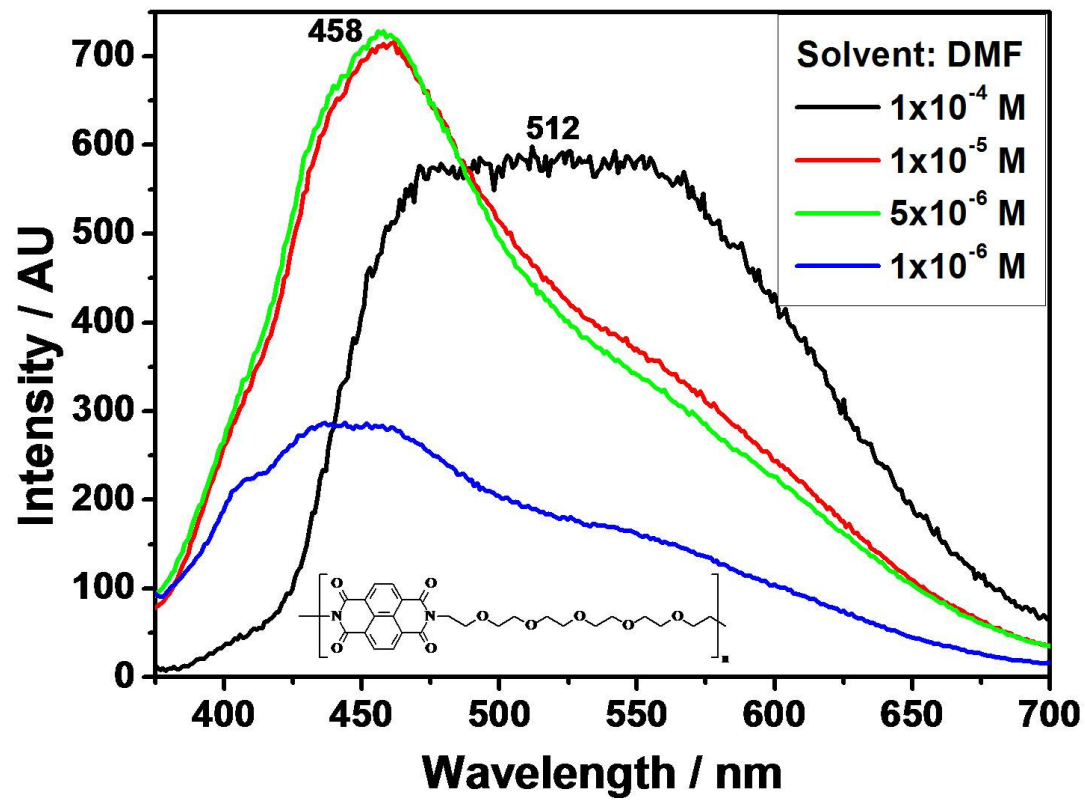
Figure 4.45: Effect of Concentration on Emission Spectra of EONPI in DMF
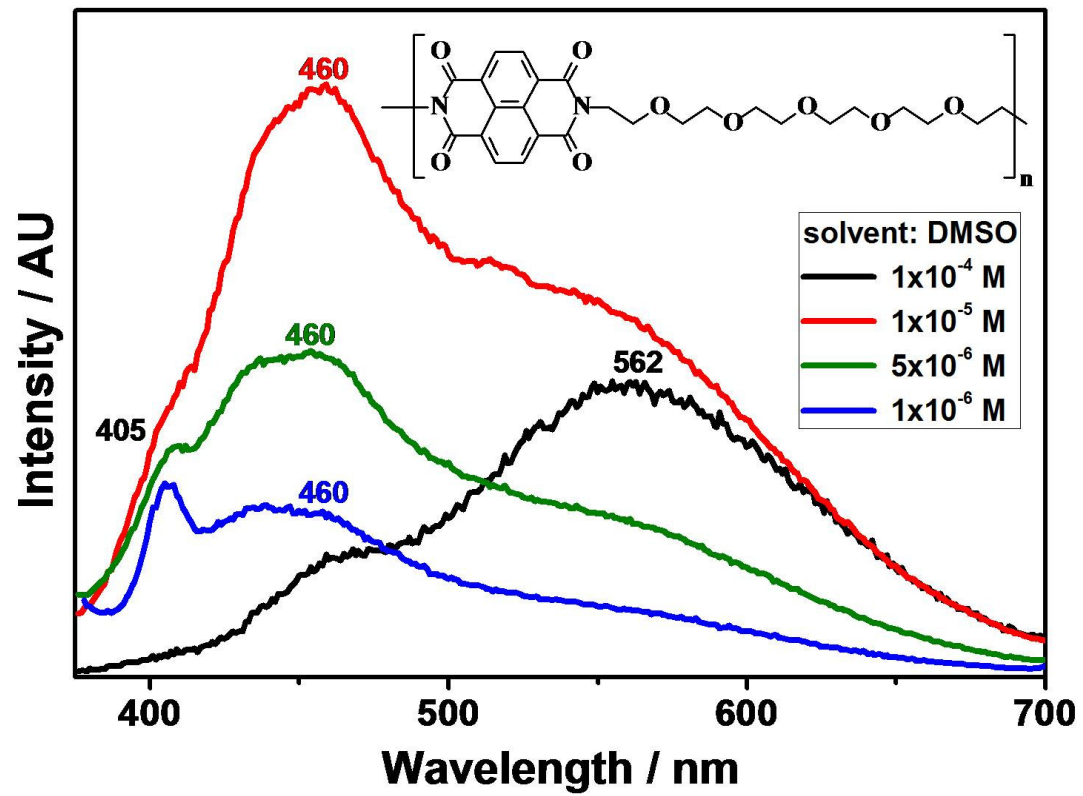
Figure 4.46: Effect of Concentration on Emission Spectra of EONPI in DMSO
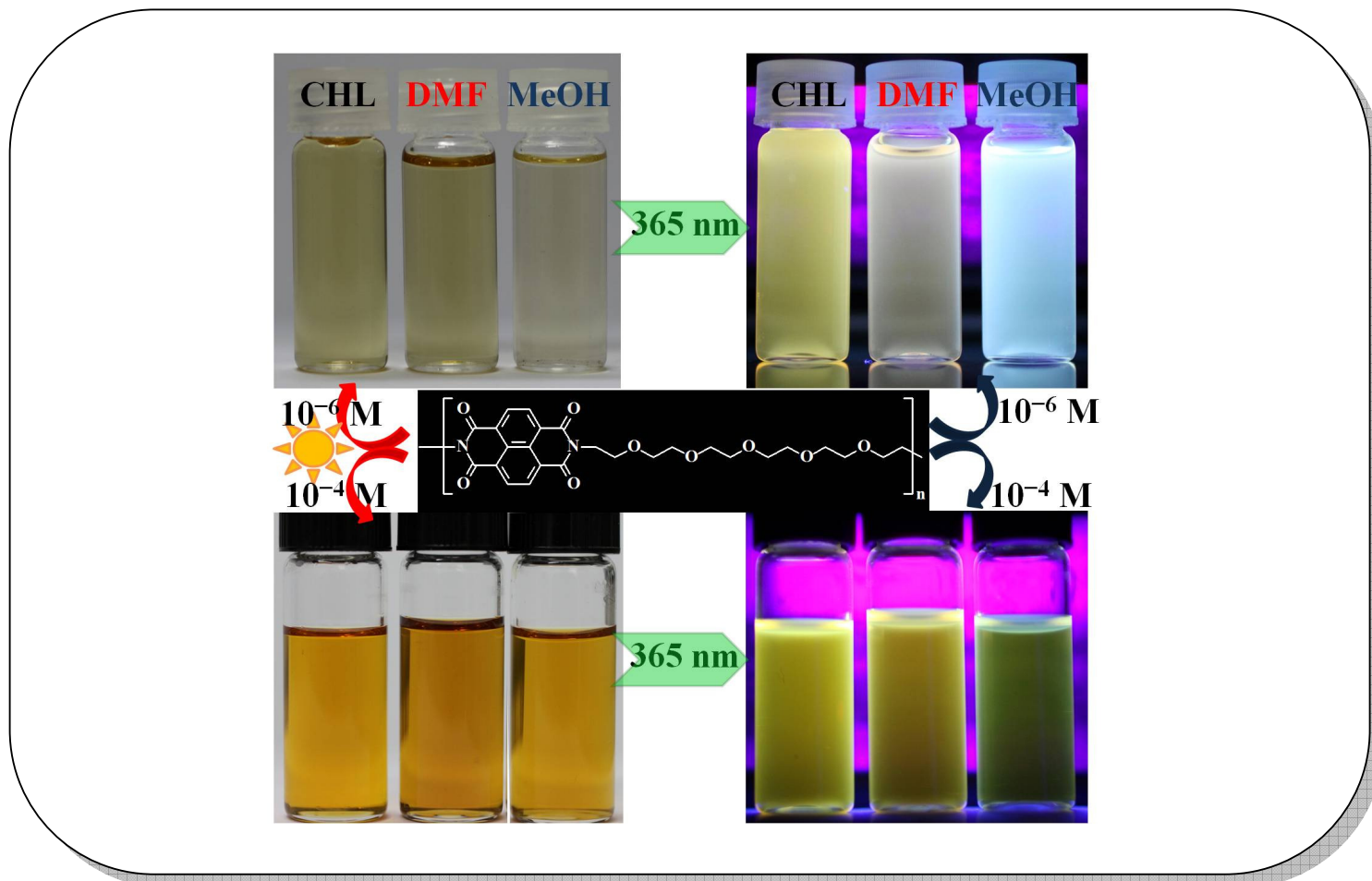
Figure 4.47: Dependence of Solvent Polarity and Proticity on Emission Spectra and Respective Color Tunability of EONPI
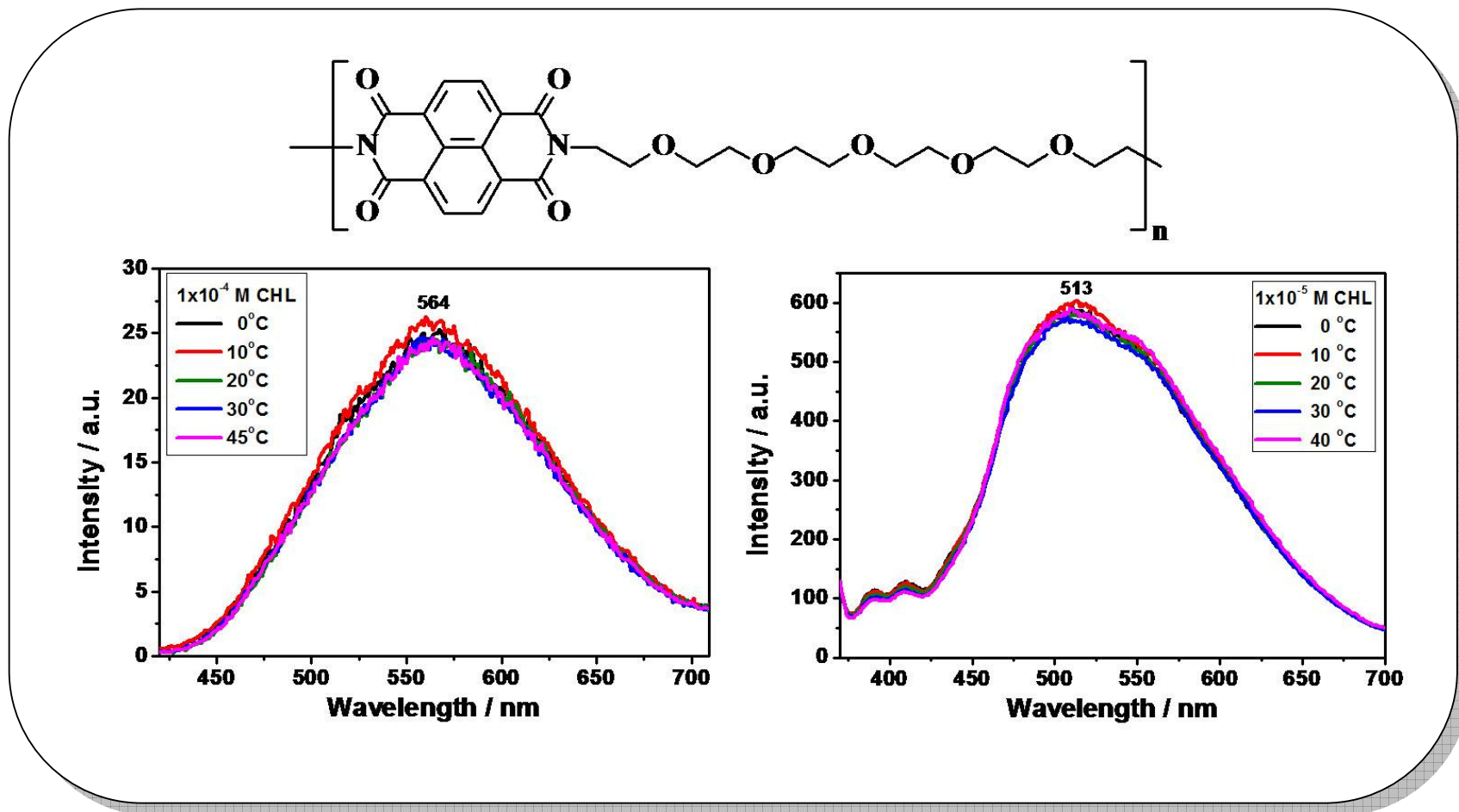
Figure 4.48: Effect of Temperature on Emission Spectra of EONPI in CHCl$_3$ at Different Concentrations
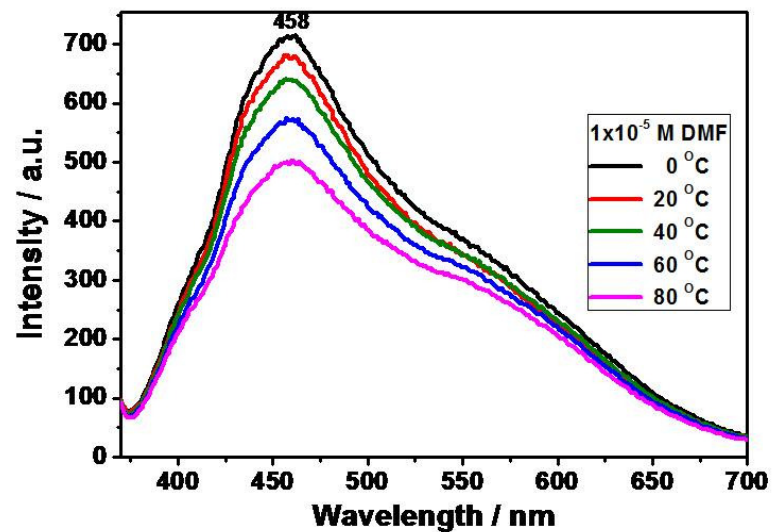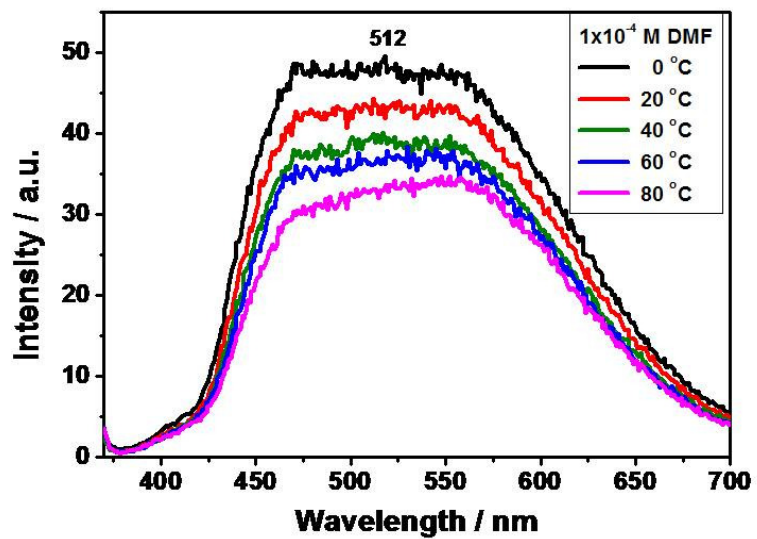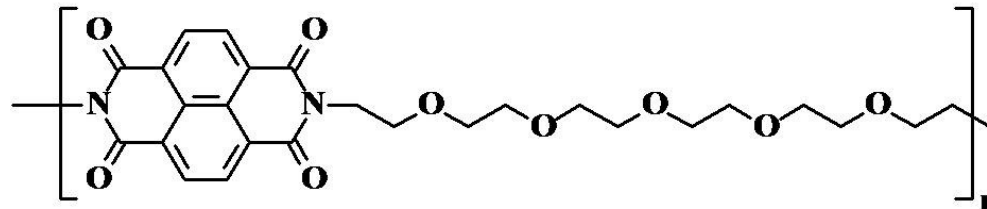
Figure 4.49: Effect of Temperature on Emission Spectra of EONPI in DMF at Different Concentrations
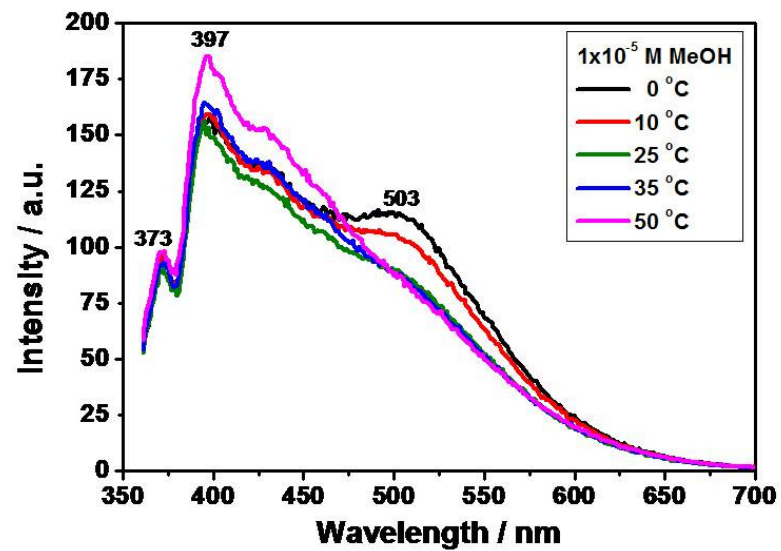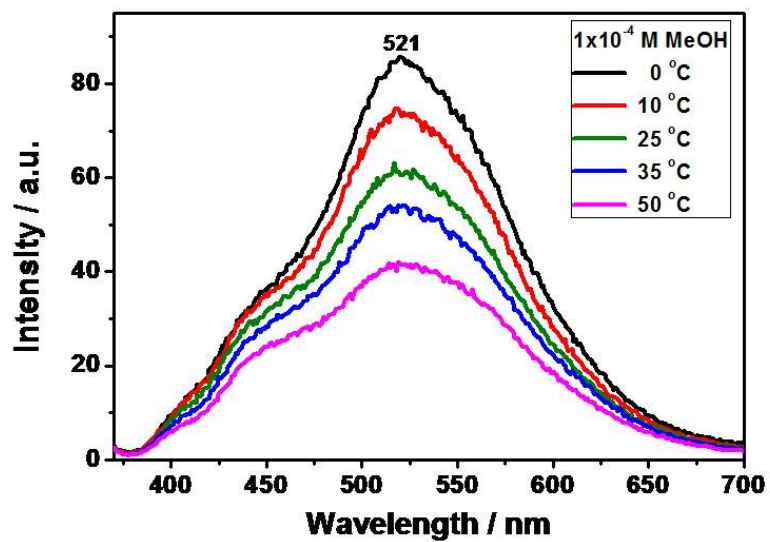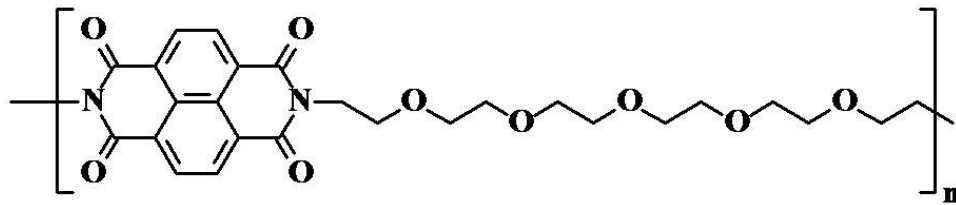
Figure 4.50: Effect of Temperature on Emission Spectra of EONPI in CH$_3$OH at Different Concentrations

Figure 4.51: Excitation Dependent Emission Spectra of EONPI in CH$_3$OH

Figure 4.52: Excitation Dependent Emission Spectra of EONPI in DMF
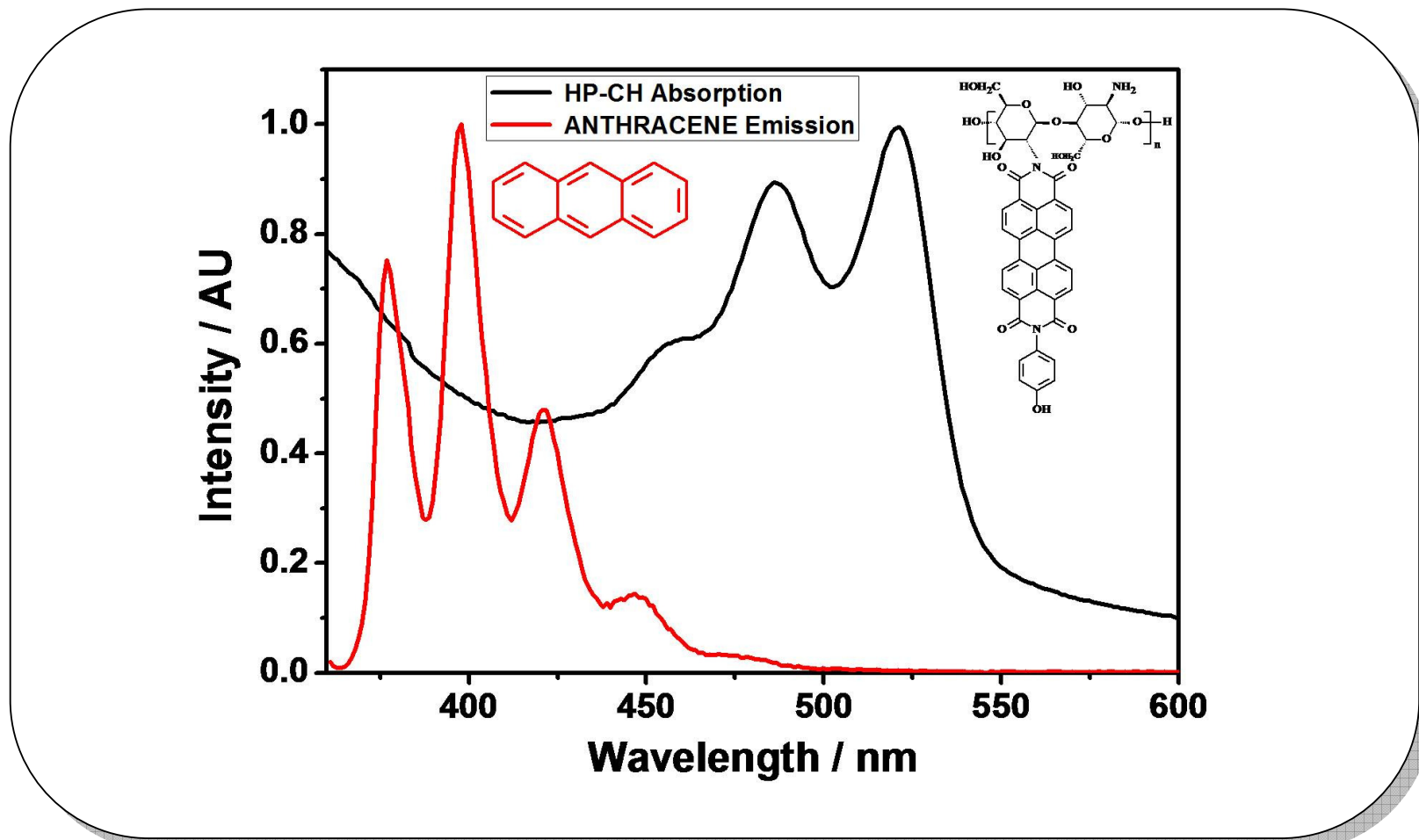
Figure 4.53: Overlap of Absorption Spectrum of Acceptor, HP-CH and Emission Spectrum of Donor, Anthracene
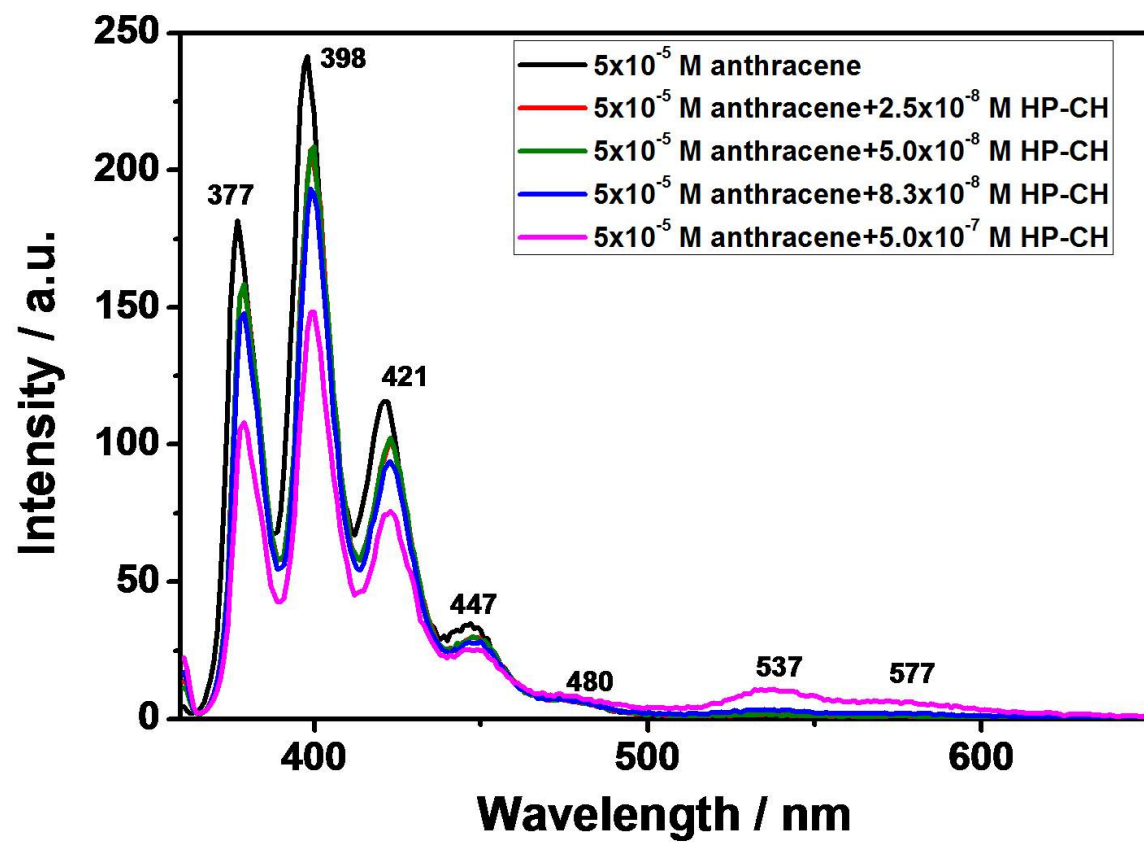
Figure 4.54: Effect of HP-CH Concentration on Emission Spectra of Anthracene
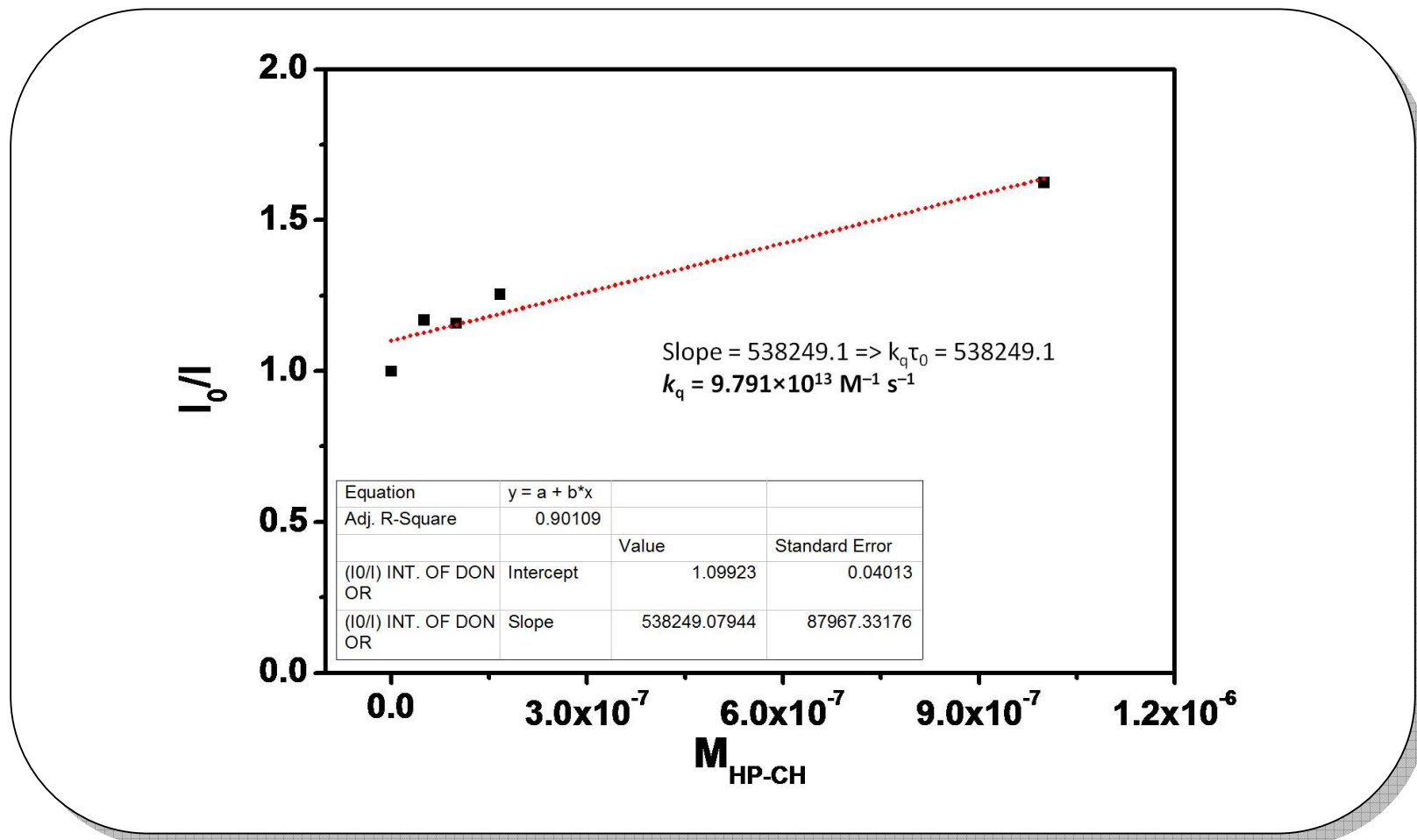
Figure 4.55: Stern-Volmer Plot of Fluorescence Quenching of Anthracene Using HP-CH in Methanol
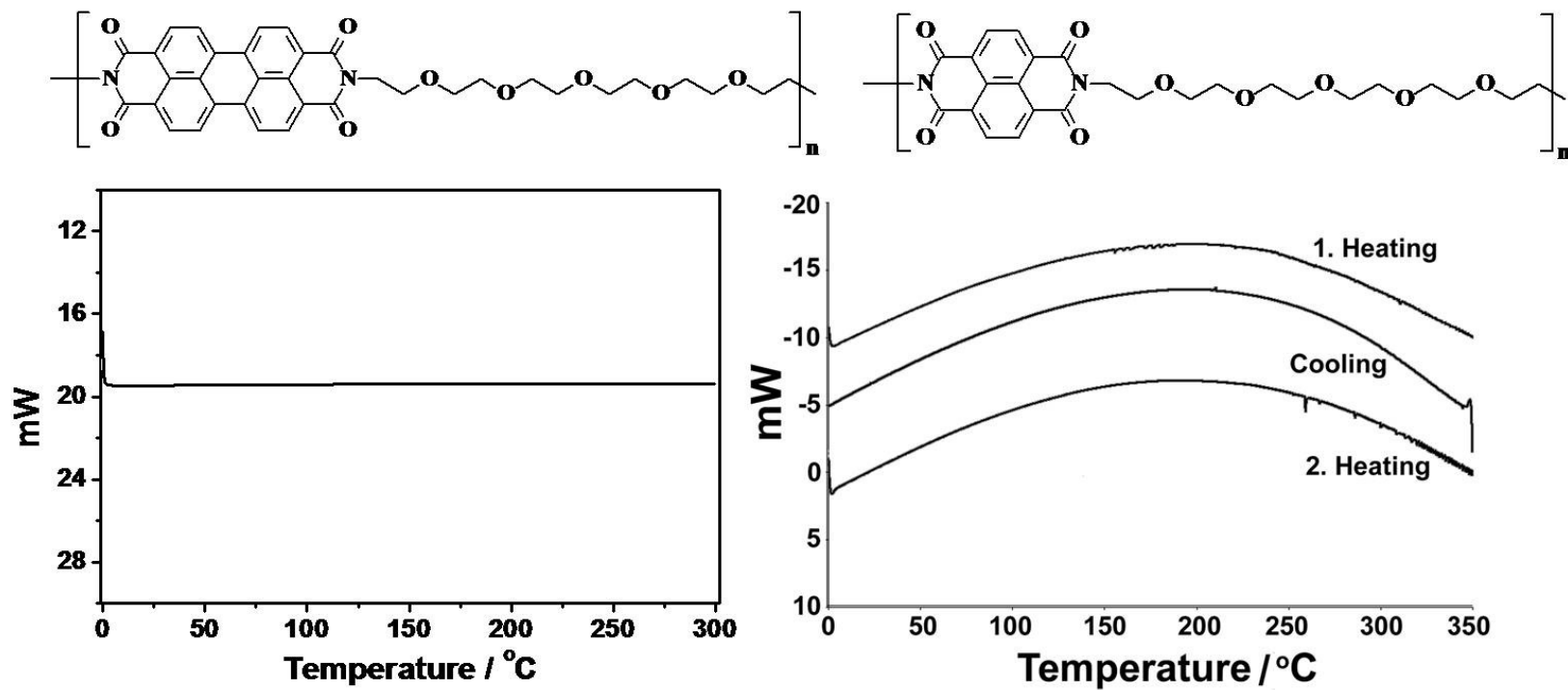
Figure 4.56: DSC Thermograms of EOPPI and EONPI at a Heating Rate of 10 K/min under Nitrogen Atmosphere
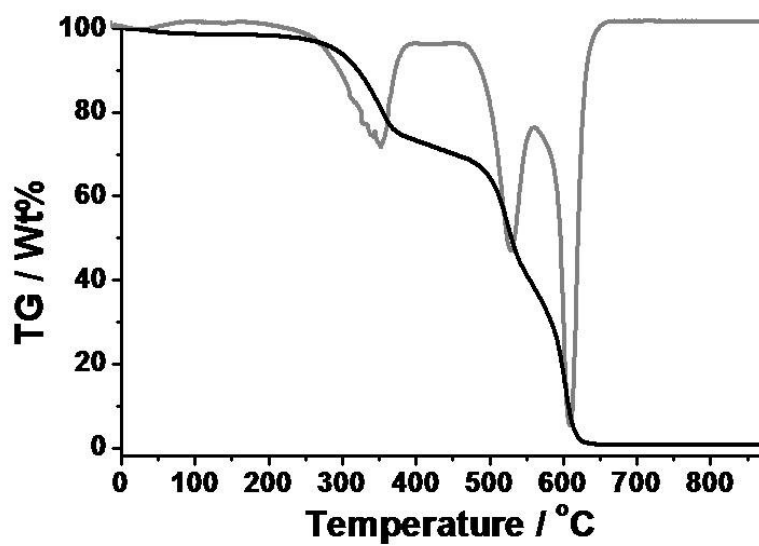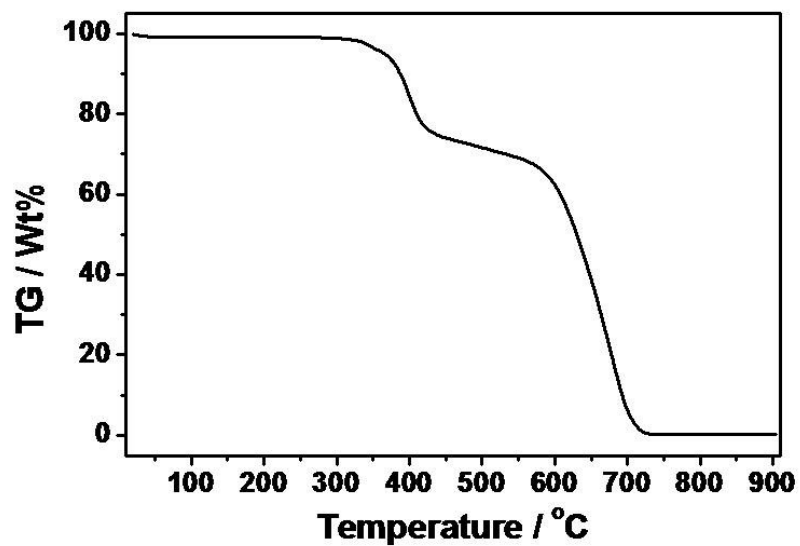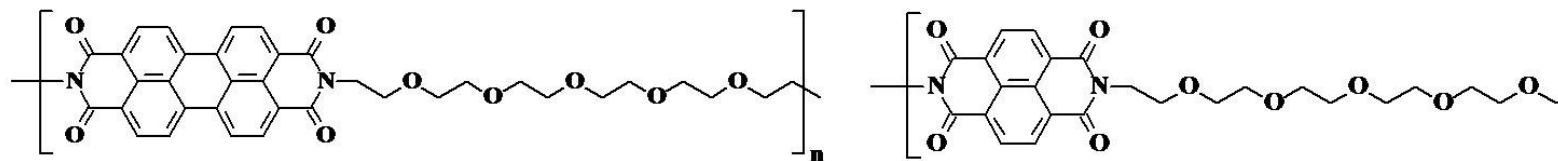
Figure 4.57: TGA Curves of EOPPI and EONPI at a Heating Rate of 10 K/min under Oxygen Atmosphere

141
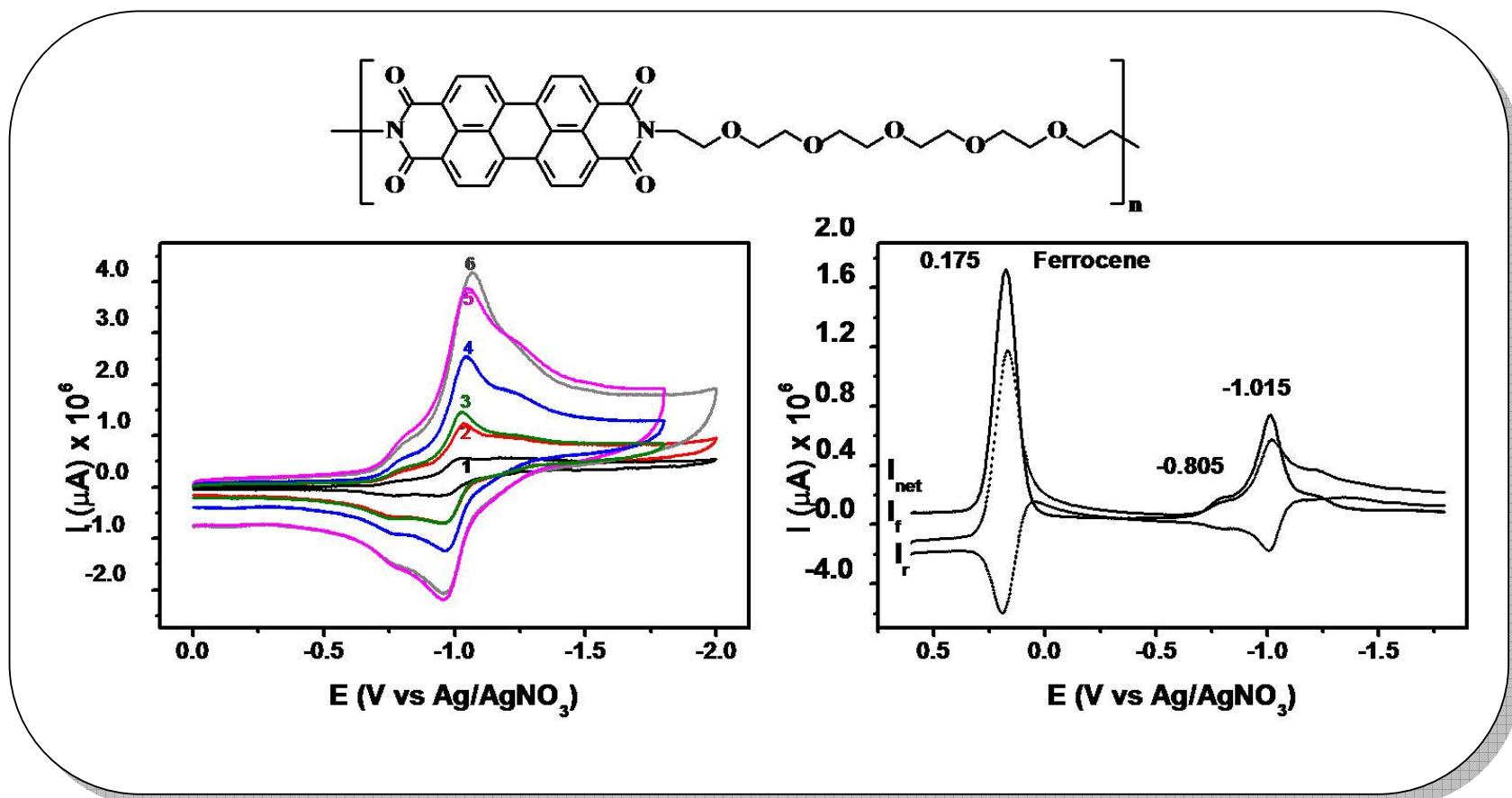
Figure 4.58: Cyclic Voltammograms at Different Scan Rates (1: 25 mVs^{-1}, 2: 50 mVs^{-1}, 3: 100 mVs^{-1}, 4: 400 mVs^{-1}, 5: 800 mVs^{-1} and 1000 mVs^{-1}) and Squarewave Voltammograms of EOPPI in CH$_2$Cl$_2$ /supporting electrolyte TBAPF$_6$)

Figure 4.59: Effect of Variation of Scan Rates on the Peak Currents of EOPPI, Plot of I_{pc} vs. Suare Root of Scan Rate in CH_2Cl_2
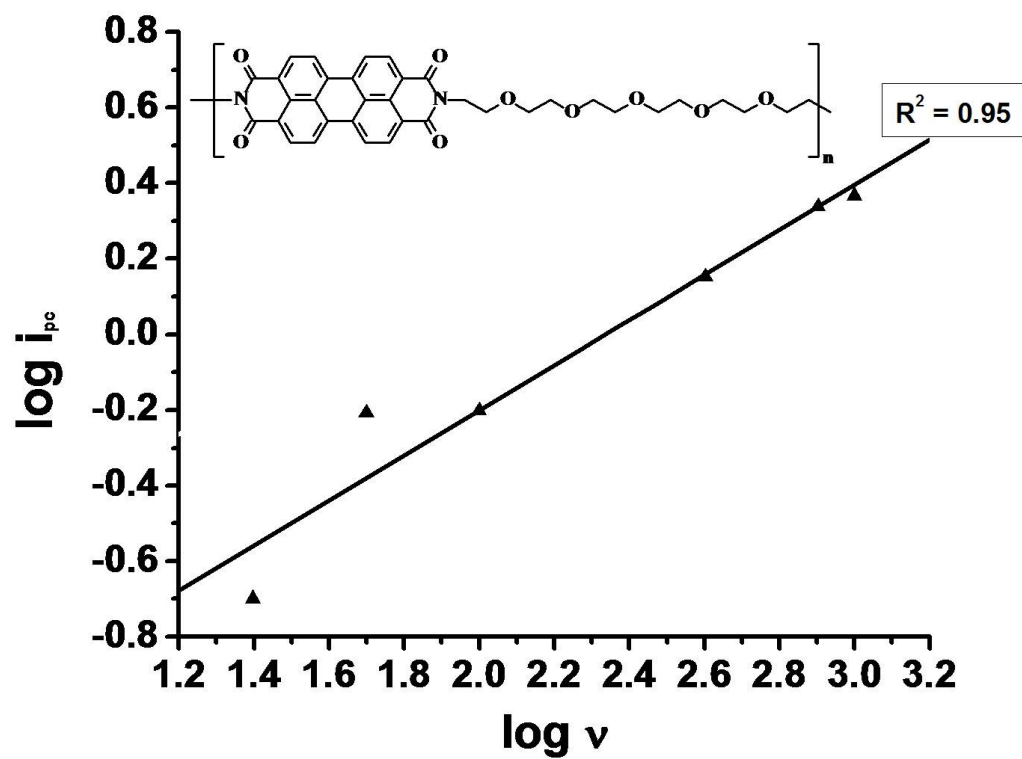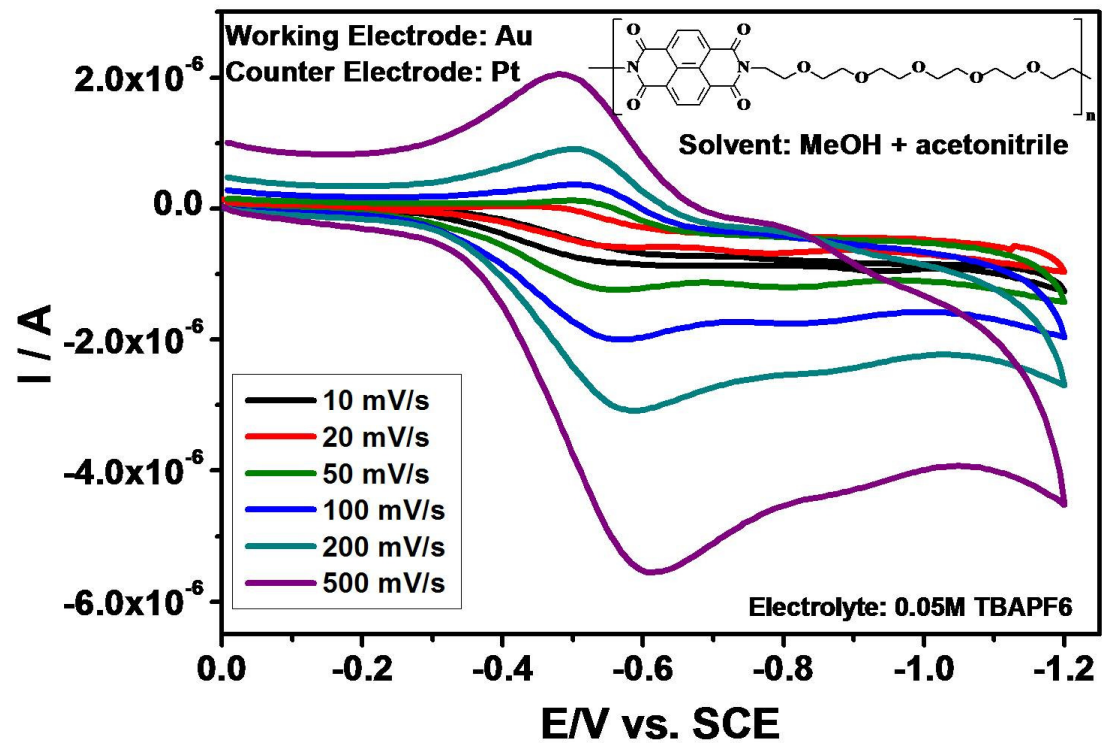
Figure 4.60: Effect of Variation of Scan Rates on the Peak Currents of EOPPI, Plot of (log I_{pc}) vs. log Scan Rate in CH_2Cl_2

Figure 4.61: Cyclic Voltammograms of EONPI at Different Scan Rates in CH_2Cl_2

Figure 4.62: Cyclic Voltammograms of EONPI at Different Scan Rates in $CH_3OH + CH_3CN$ (50:50)
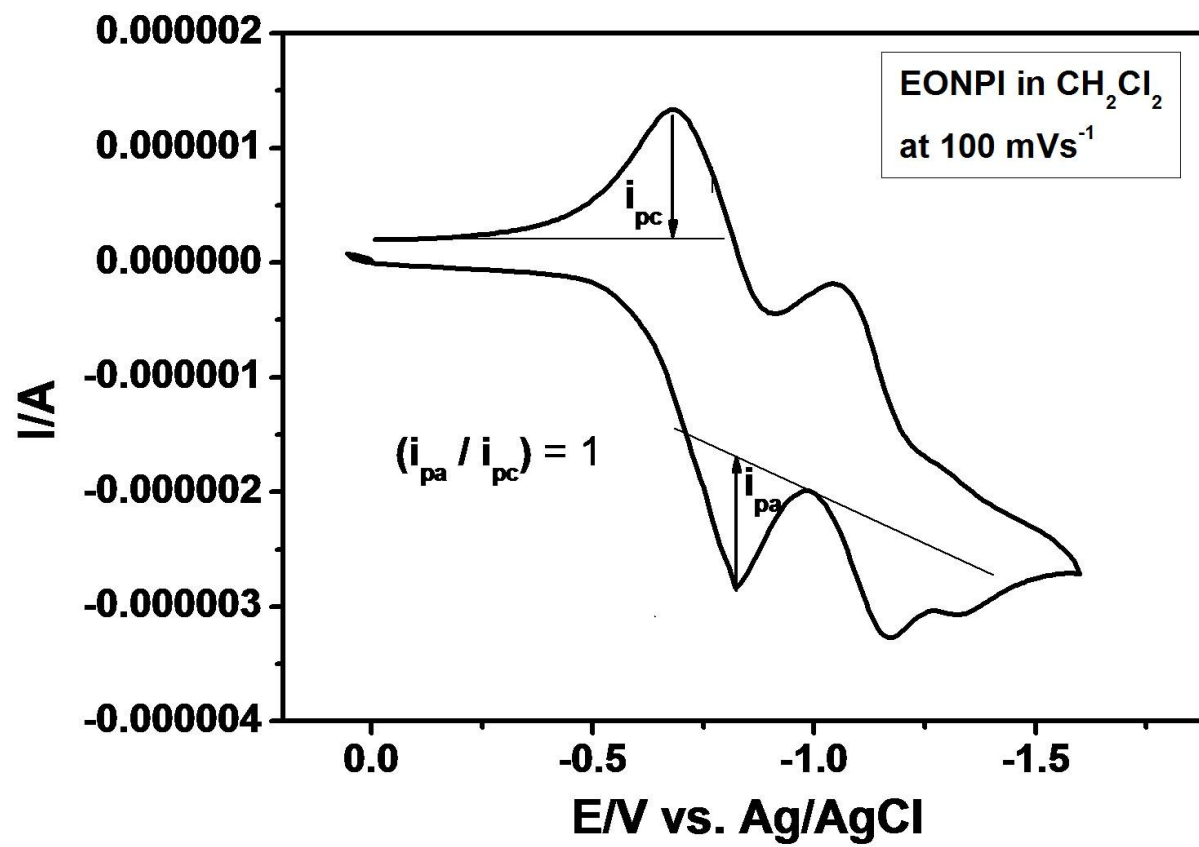
Figure 4.63: Calculation of Peak Currents (i_{pc} and i_{pa}) of EONPI

The following are the data shown within the figure:

Equation	y = a + b*x		
Adj. R-Square	0.93036		
		Value	Standard Error
D	Intercept	0.10589	0.18208
D	Slope	0.08009	0.0125

$R^2 = 0.95$

$$D = \frac{\left(\frac{i_{pc}}{v^{1/2}}\right)^2}{\left[\left(2.69\times10^5\,A\,s\,mol^{-1}\,V^{-1/2}\right)^2\times(n^{3/2})^2\times(Ac)^2\right]}$$

$n = 4$

$A = \pi r^2 = 0.0314\ cm^2$

$c = 2 \times 10^{-3}\ mol/L$

$D = 3.52 \times 10^{-10}\ cm^2/sec$
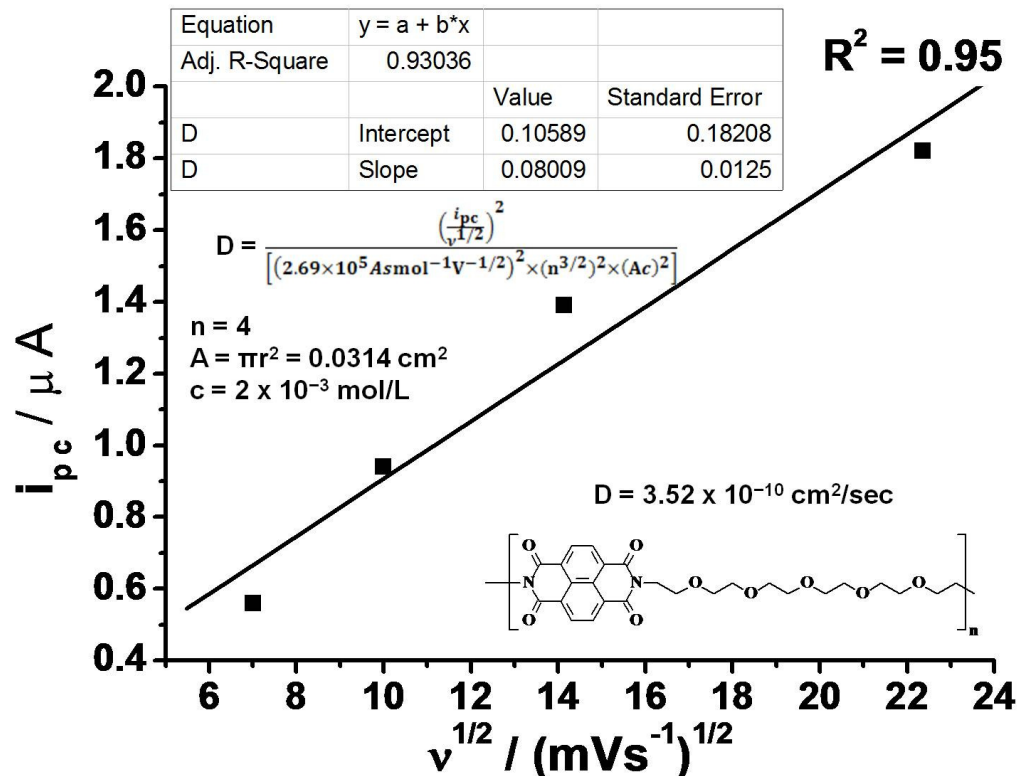
Figure 4.64: Effect of Variation of Scan Rates on the Peak Currents of EONPI, Plot of I_{pc} vs. Suare Root of Scan Rate in CH_2Cl_2 and Calculation of Diffusion Constant (D)

148
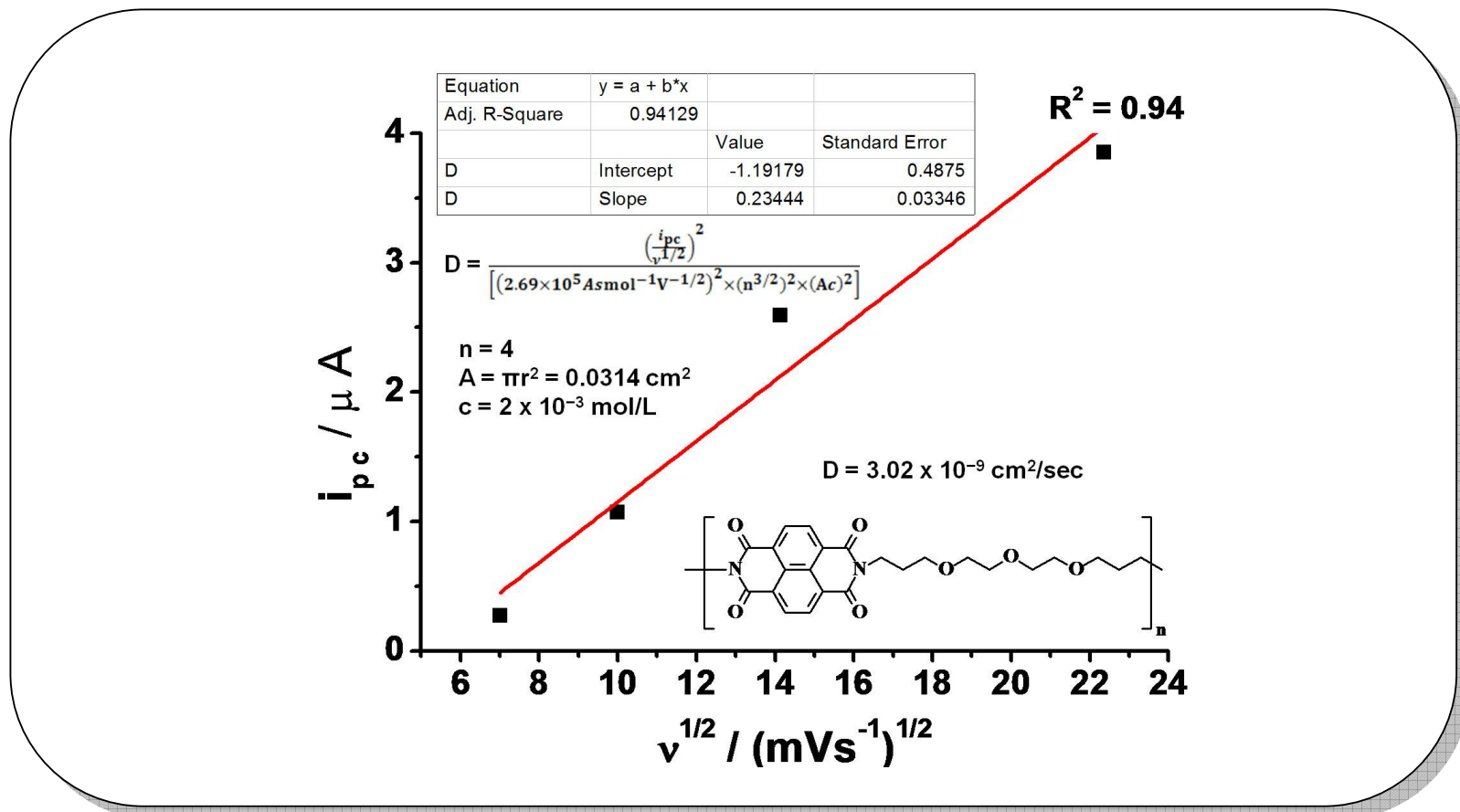
Figure 4.65: Effect of Scan Rates on the Peak Currents of EONPI, Plot of I_{pc} vs. Square Root of Scan Rate in $CH_3OH + CH_3CN$ (50:50) and

Calculation of Diffusion Constant (D)
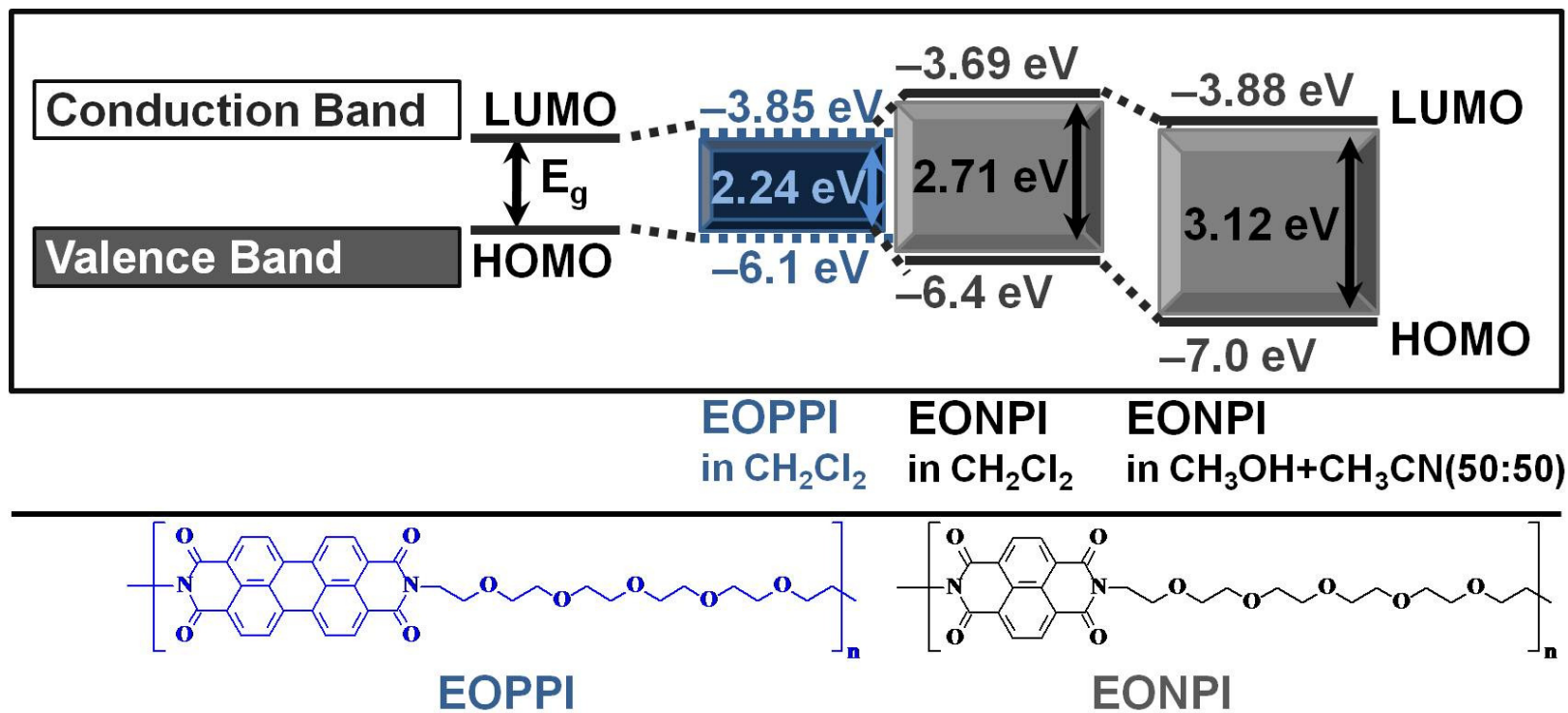
Figure 4.66: Band Gap Energy Diagrams of EOPPI and EONPI
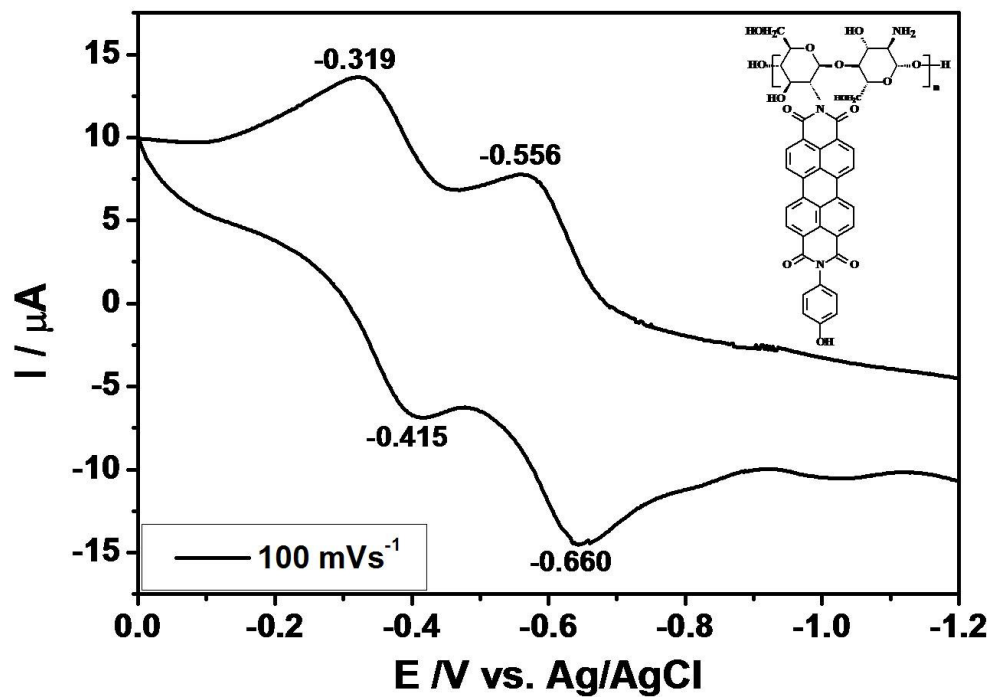
Figure 4.67: Cyclic Voltammogram of HP-CH at 100 mVs^{-1} in Dimethylacetamide (DMAc) and Calculations of Peak Potentials
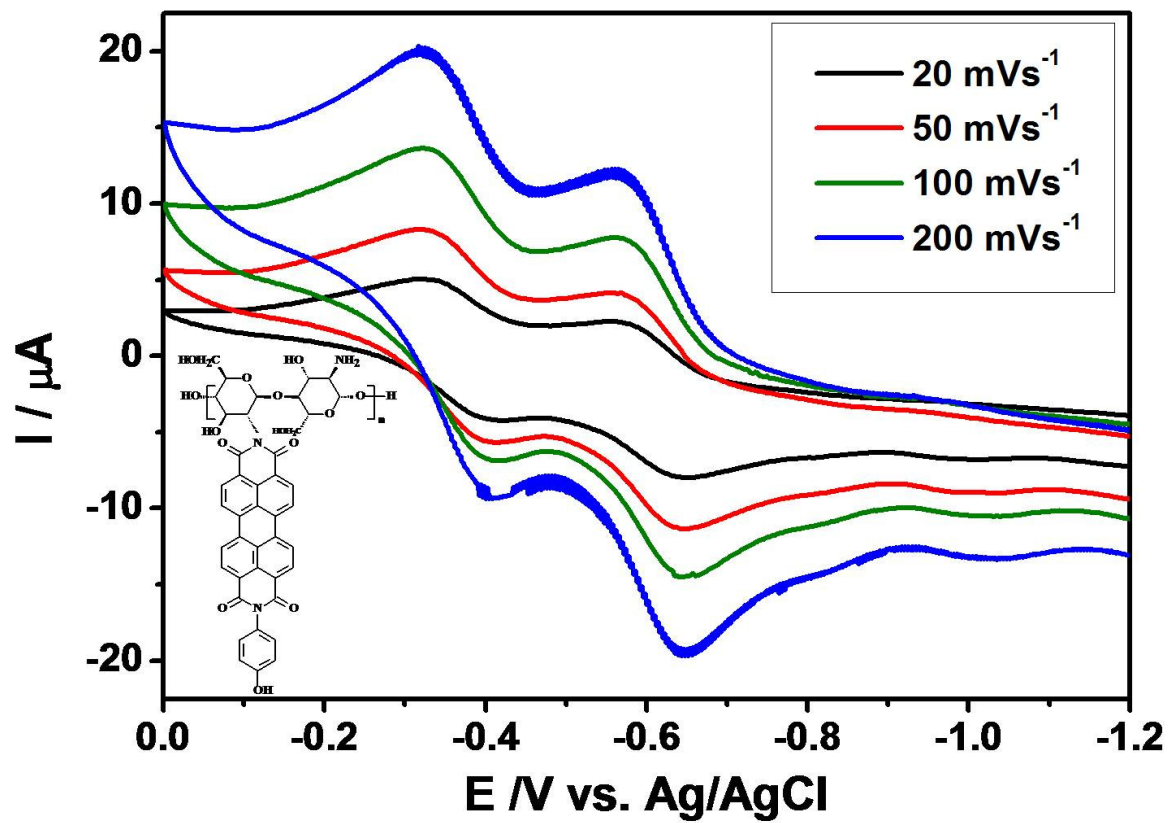
Figure 4.68: Cyclic Voltammograms of HP-CH at Different Scan Rates in DMAc
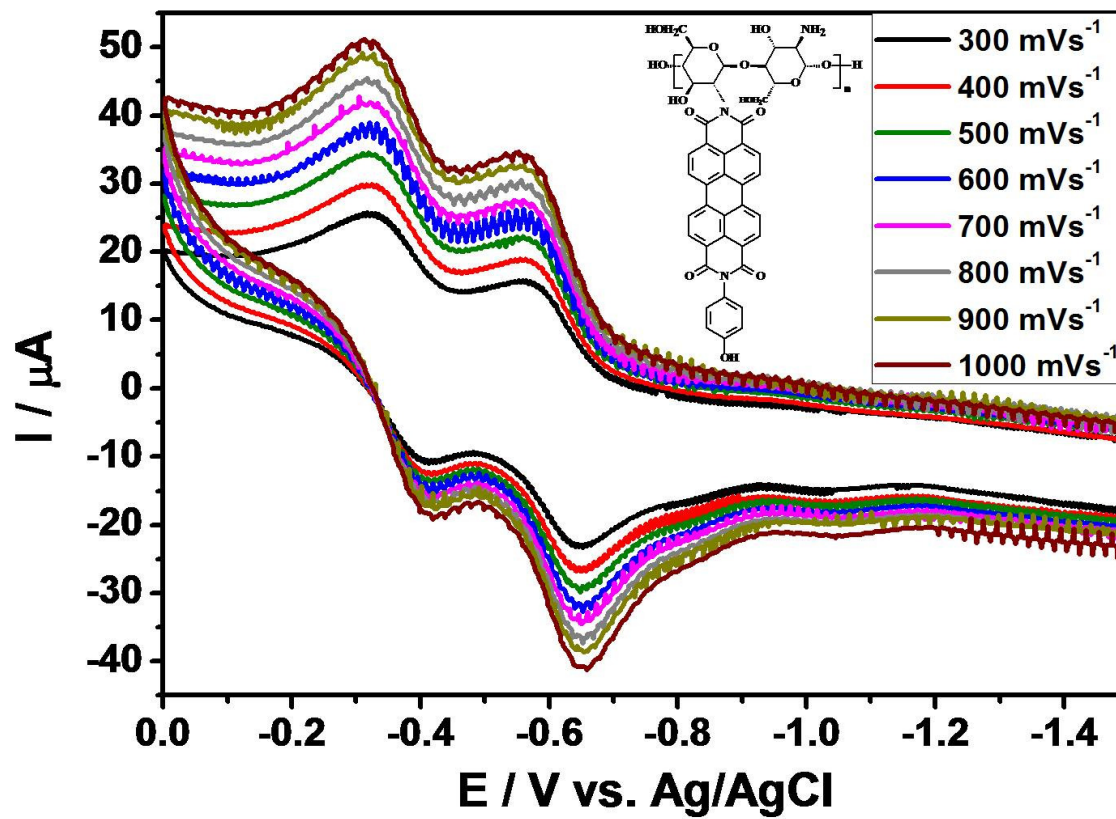
Figure 4.69: Cyclic Voltammograms of HP-CH at Different Scan Rates in DMAc
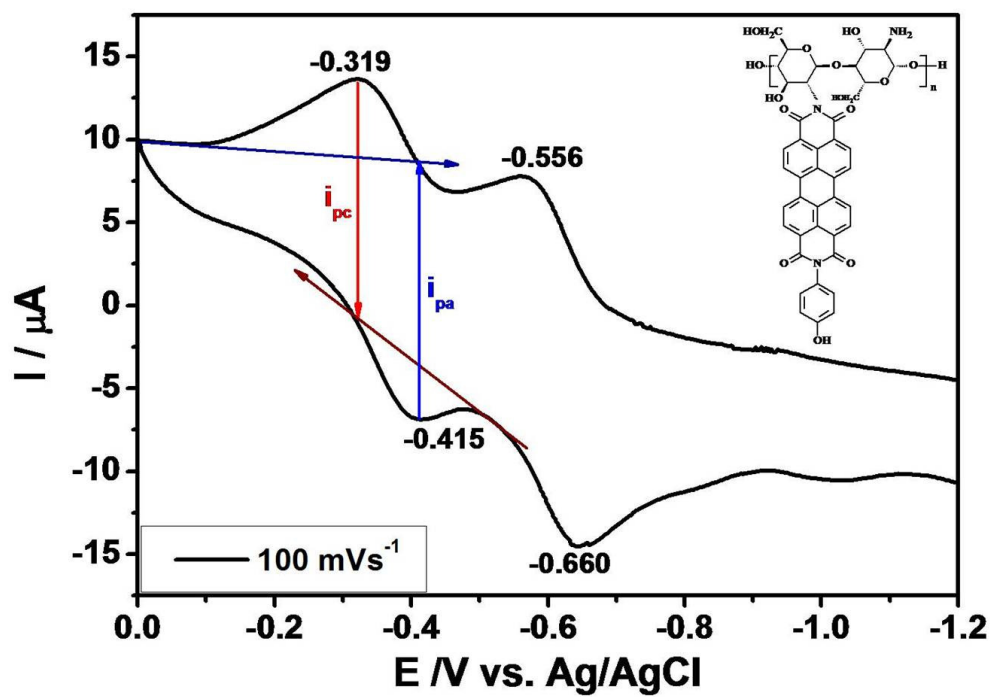
Figure 4.70: Calculation of Peak Currents (i_{pc} and i_{pa}) of HP-CH
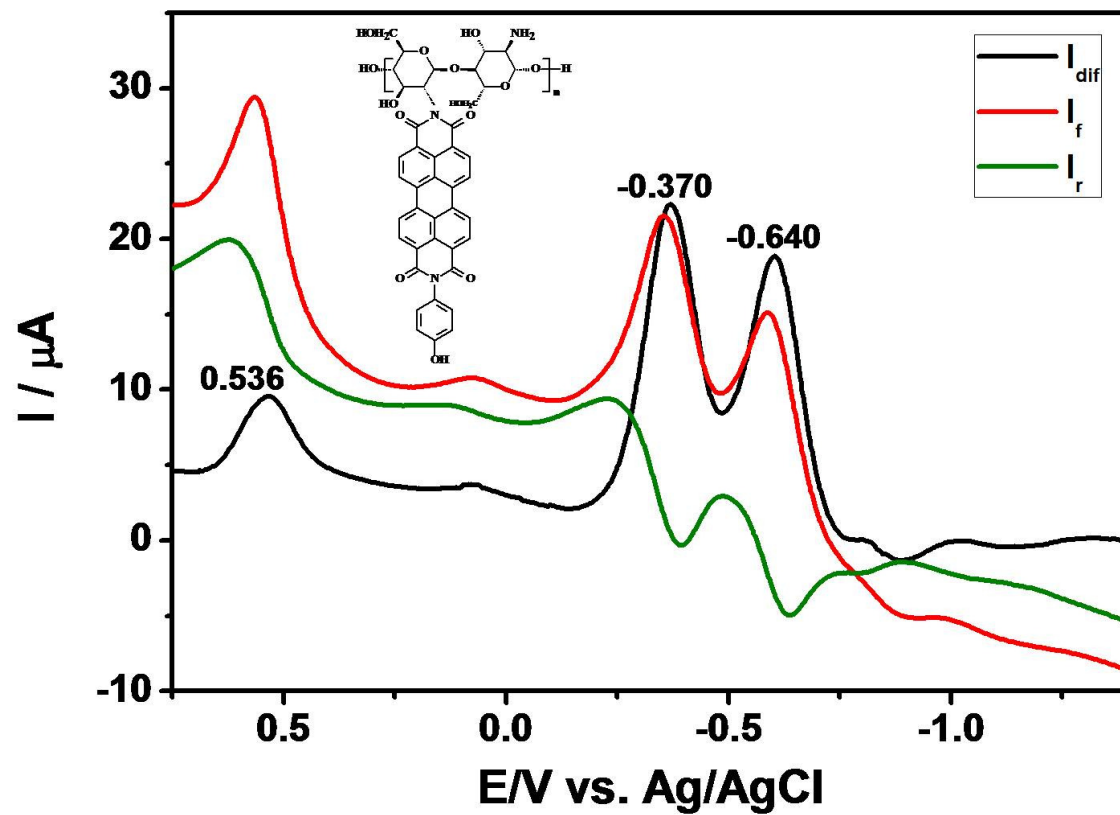
Figure 4.71: Squarewave Voltammograms of HP-CH in DMAc at a Frequency of 50 Hz
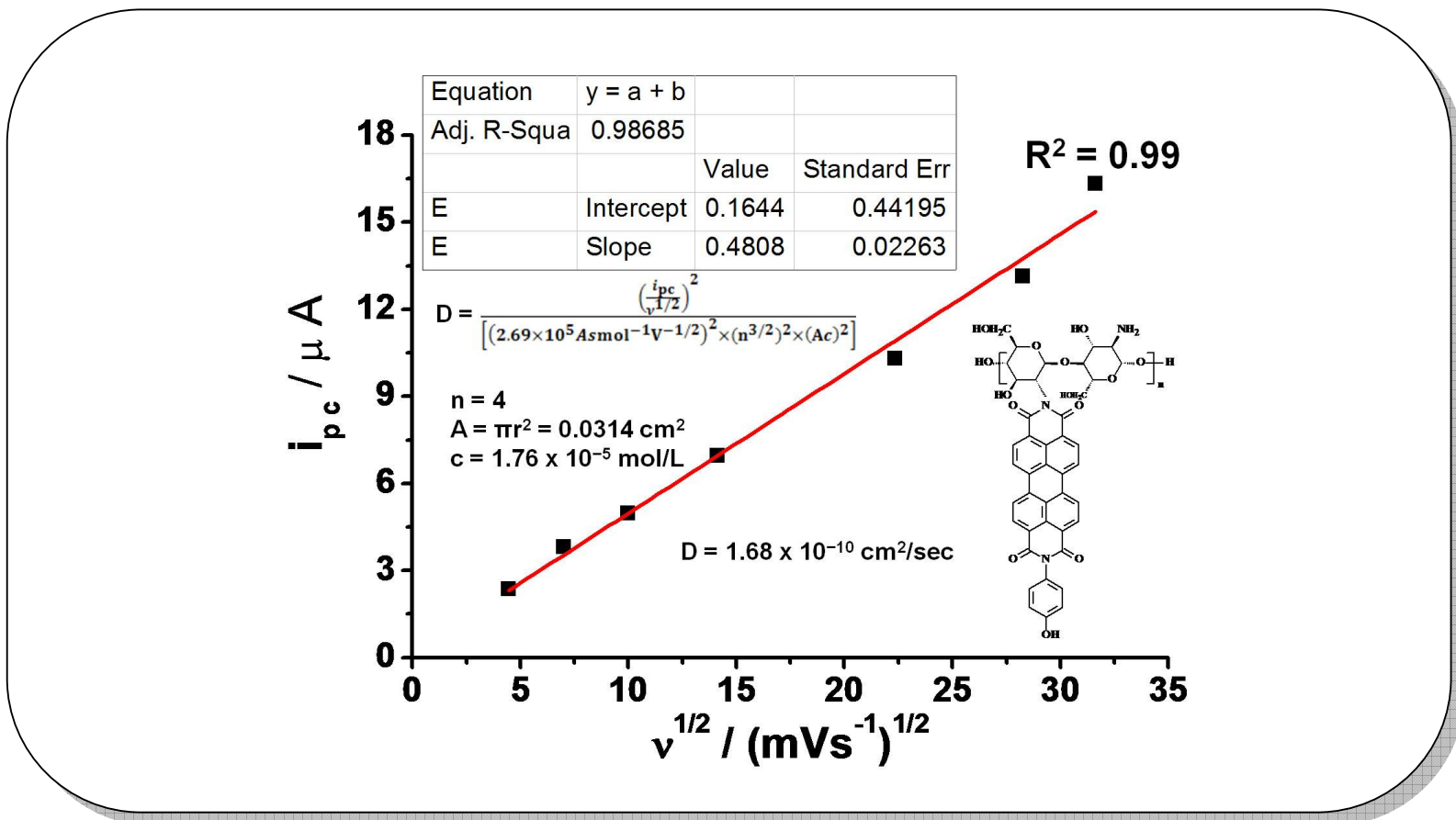
Figure 4.72: Effect of Scan Rates on the Peak Currents of HP-CH, Plot of I_{pc} vs. Square Root of Scan Rate in DMAc and Calculation of

Diffusion Constant (D)
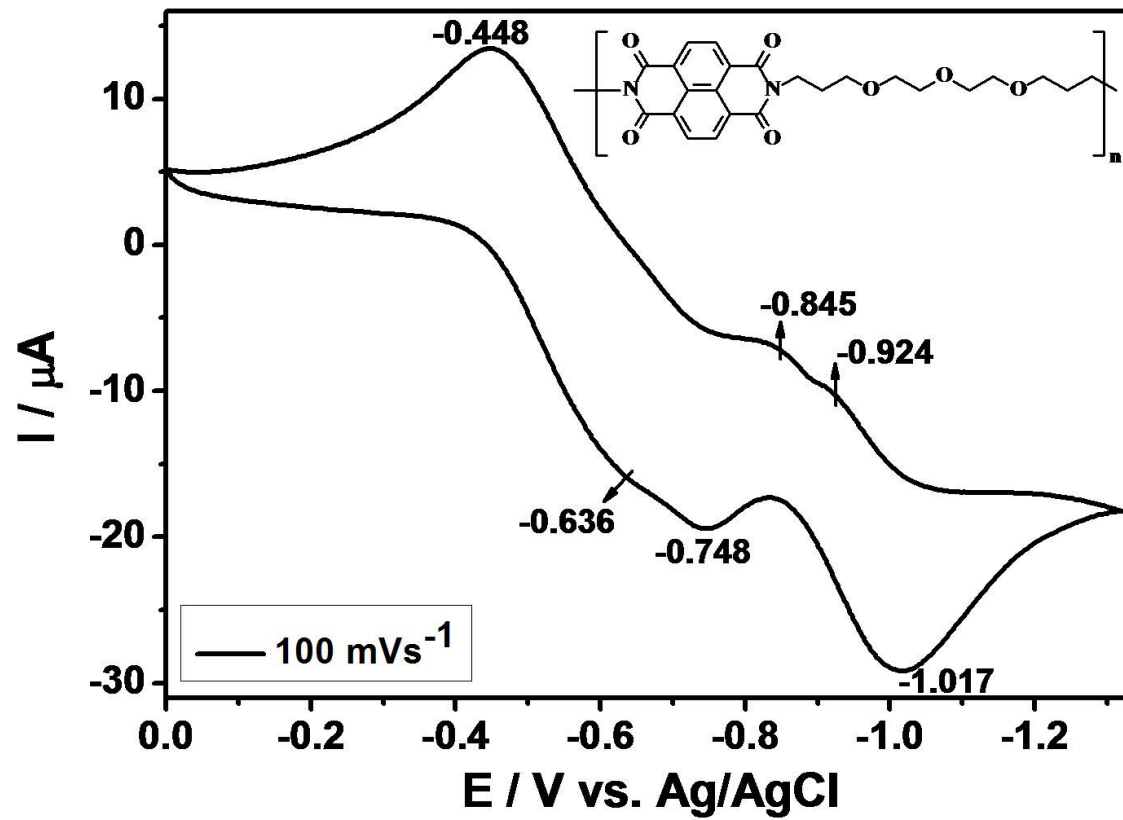
Figure 4.73: Cyclic Voltammogram of TEONPI at 100 mVs^{-1} in Chloroform

157
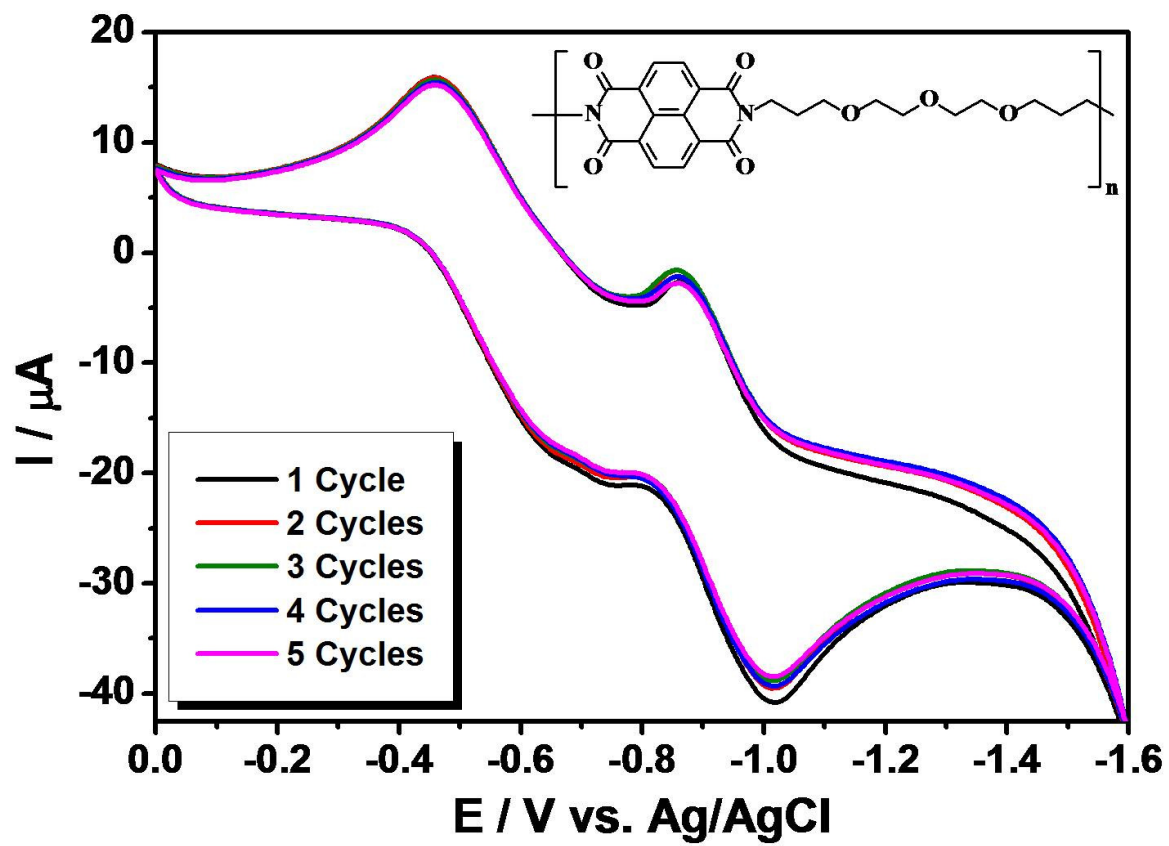
Figure 4.74: Repeated Cycles of Cyclic Voltammograms of TEONPI at 100 mVs^{-1} in Chloroform
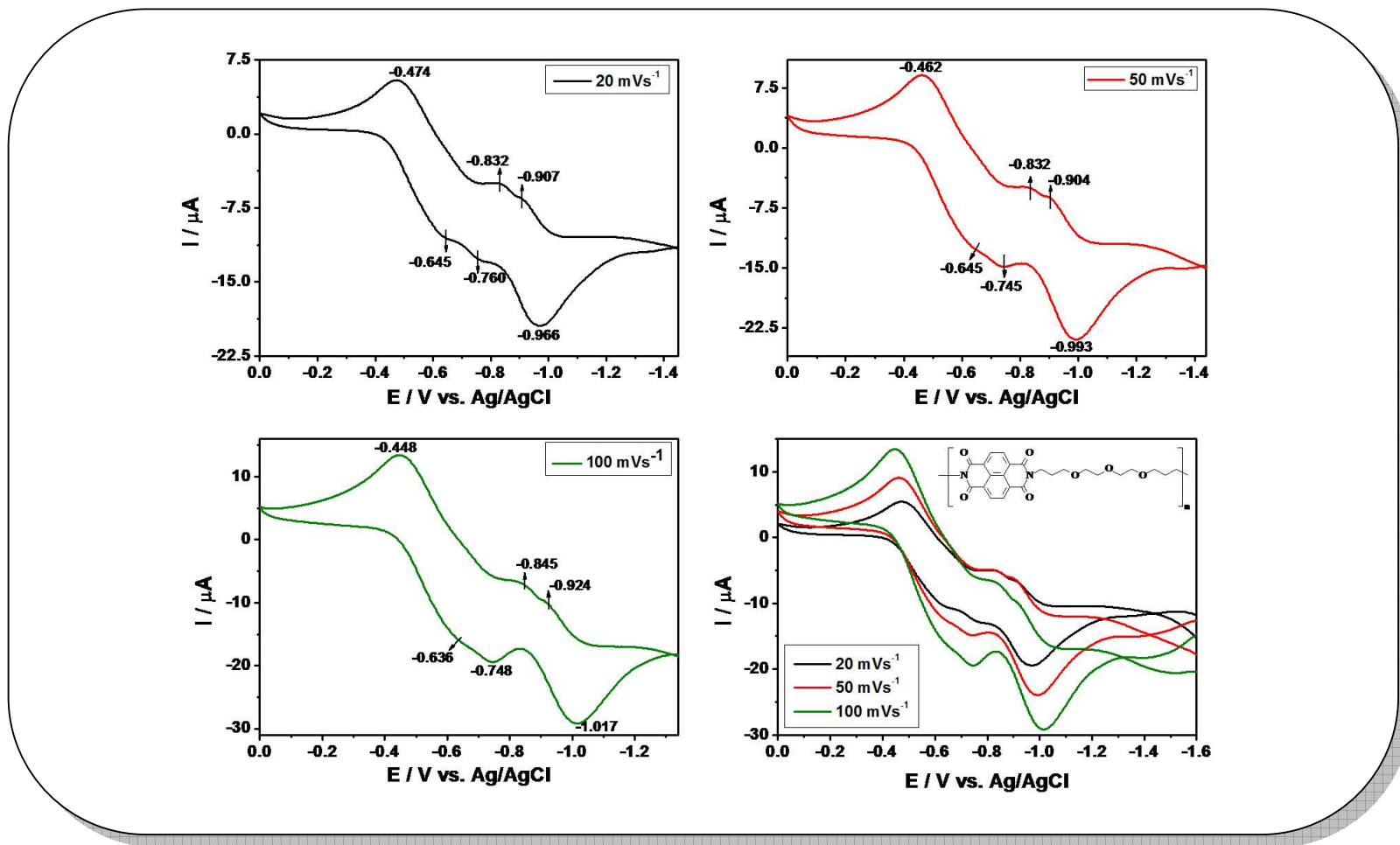
Figure 4.75: Cyclic Voltammograms of TEONPI at Different Scan Rates in Chloroform
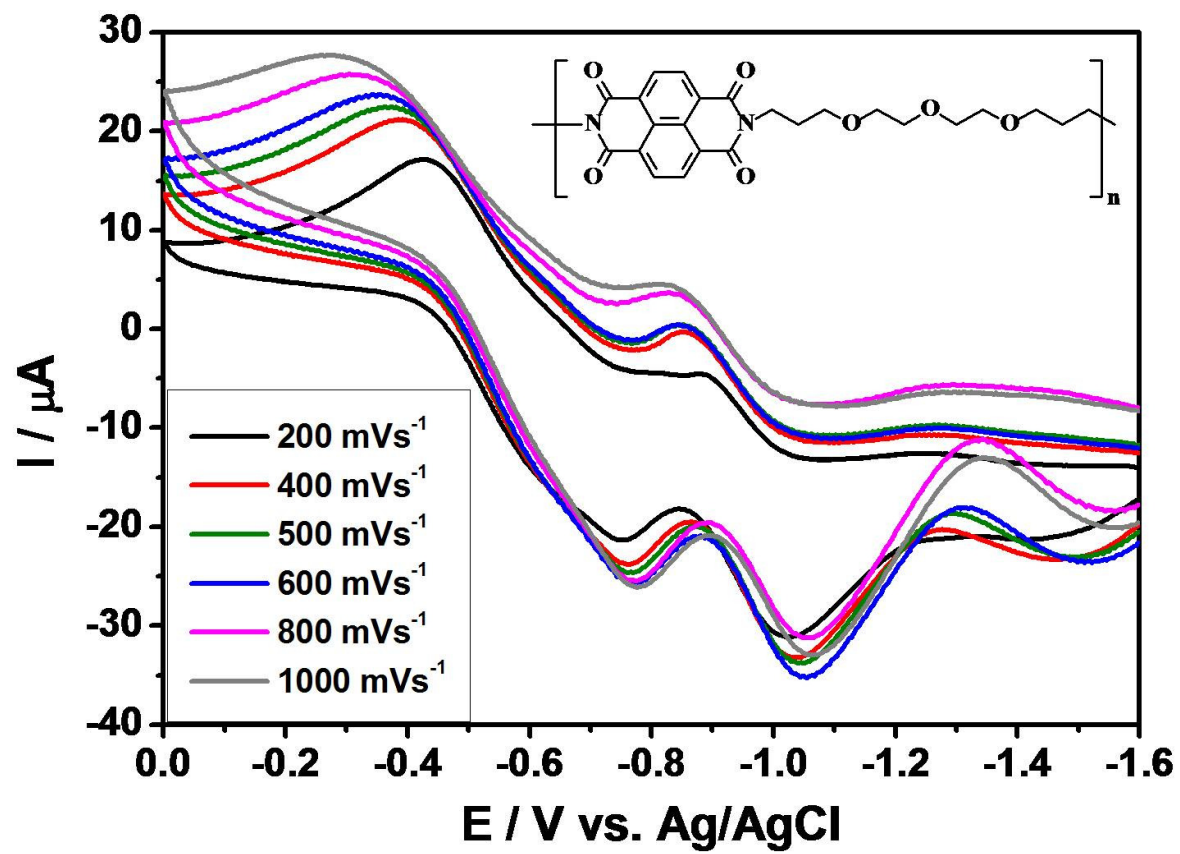
Figure 4.76: Cyclic Voltammograms of TEONPI at Different Scan Rates in Chloroform
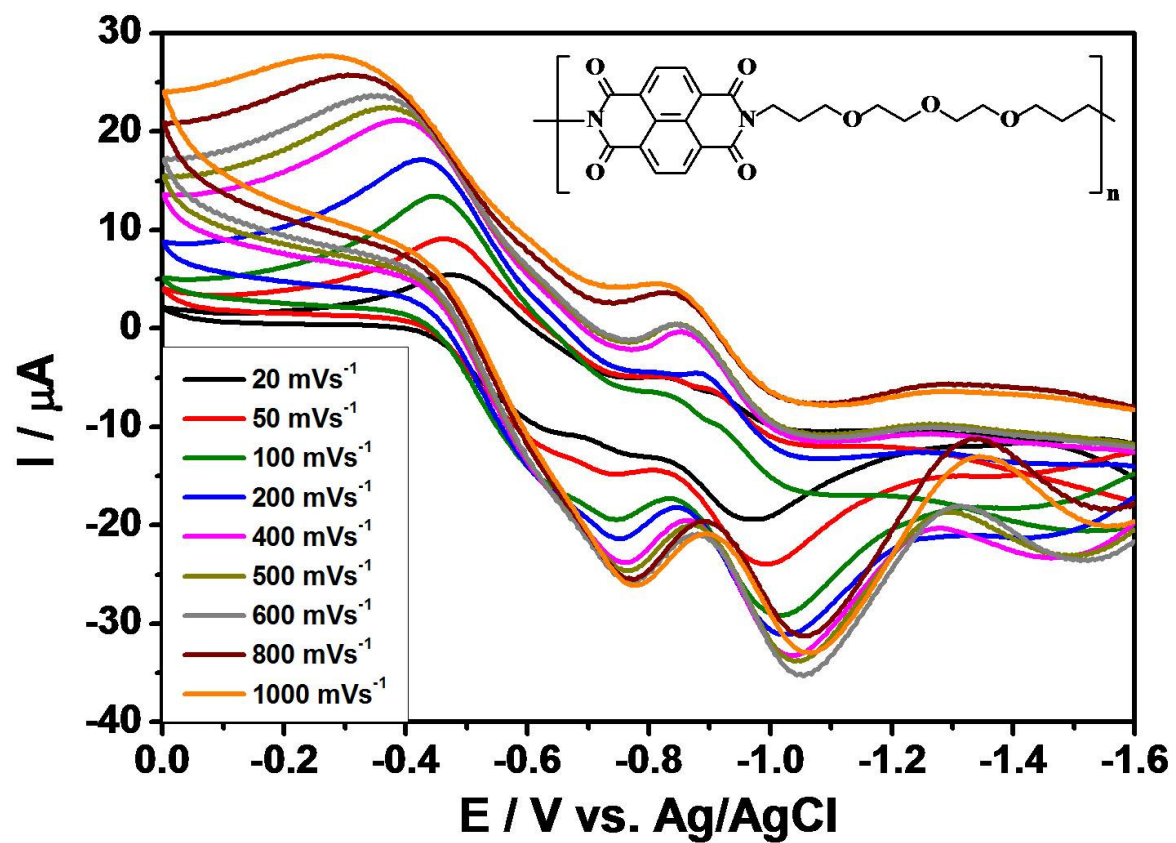
Figure 4.77: Cyclic Voltammograms of TEONPI at Different Scan Rates in Chloroform
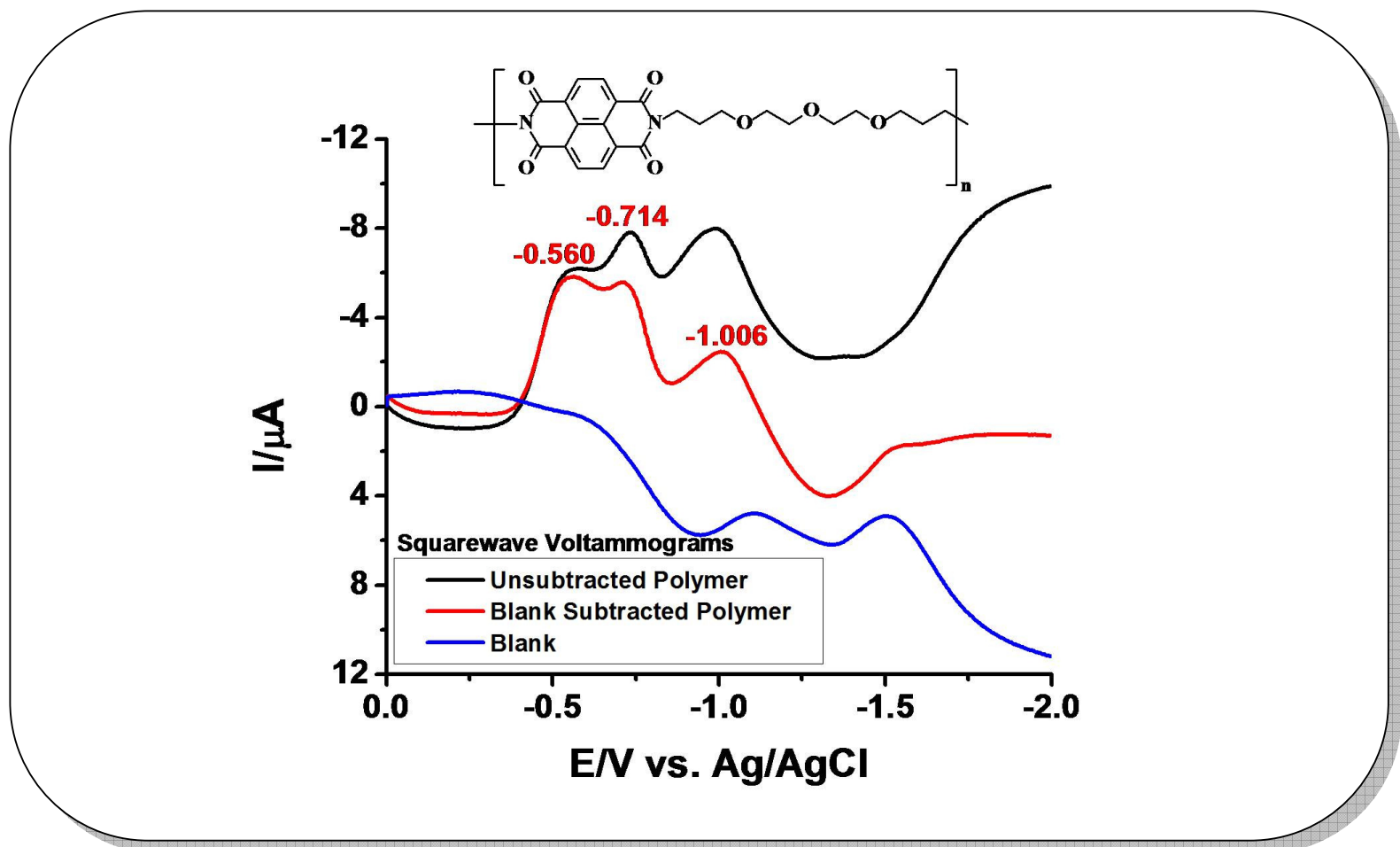
Figure 4.78: Comparison of Squarewave Voltammograms of TEONPI and Blank Solution in Chloroform at a Frequency of 25 Hz
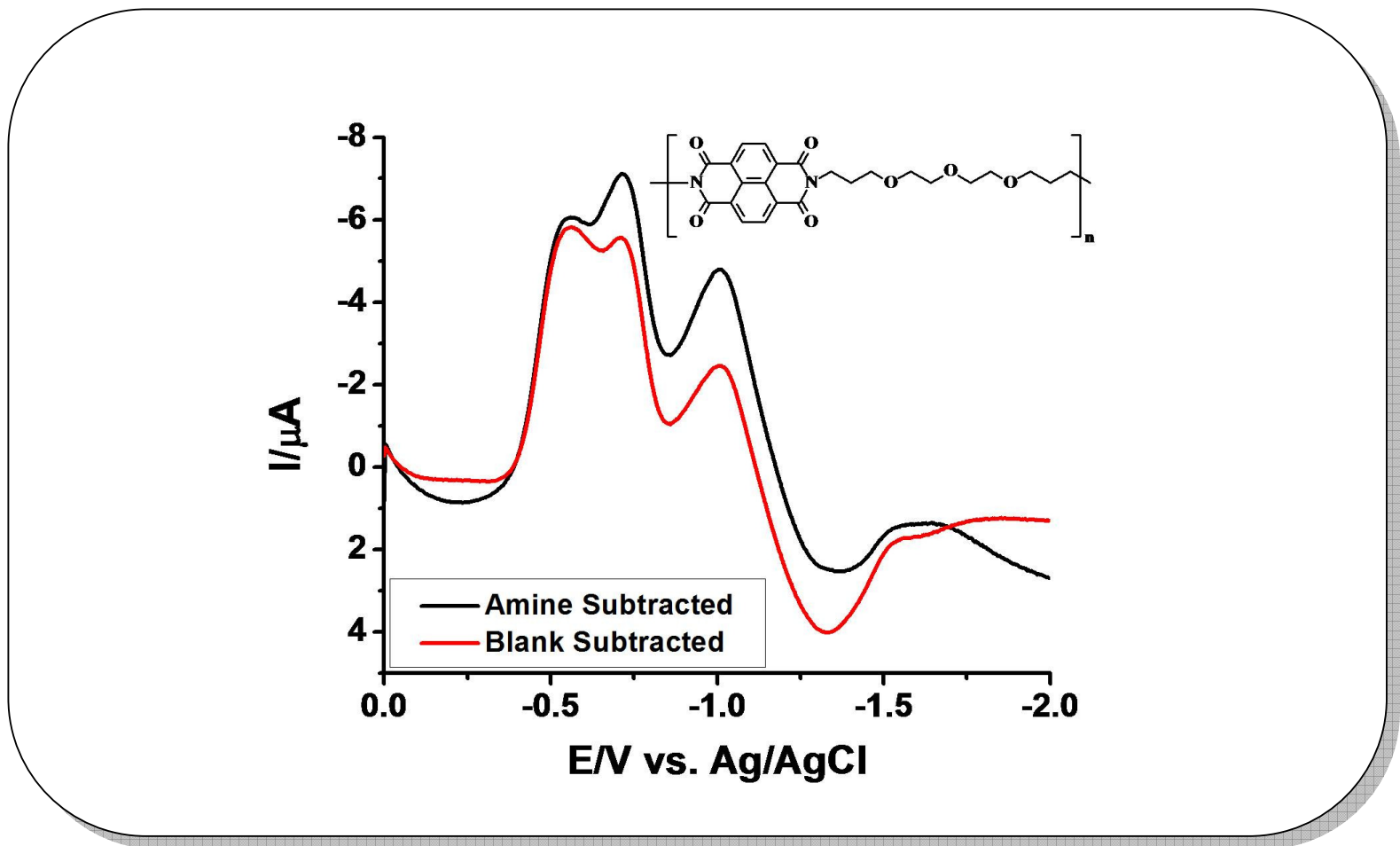
Figure 4.79: Comparison of Subtracted Squarewave Voltammograms of TEONPI in Chloroform at a Frequency of 25 Hz
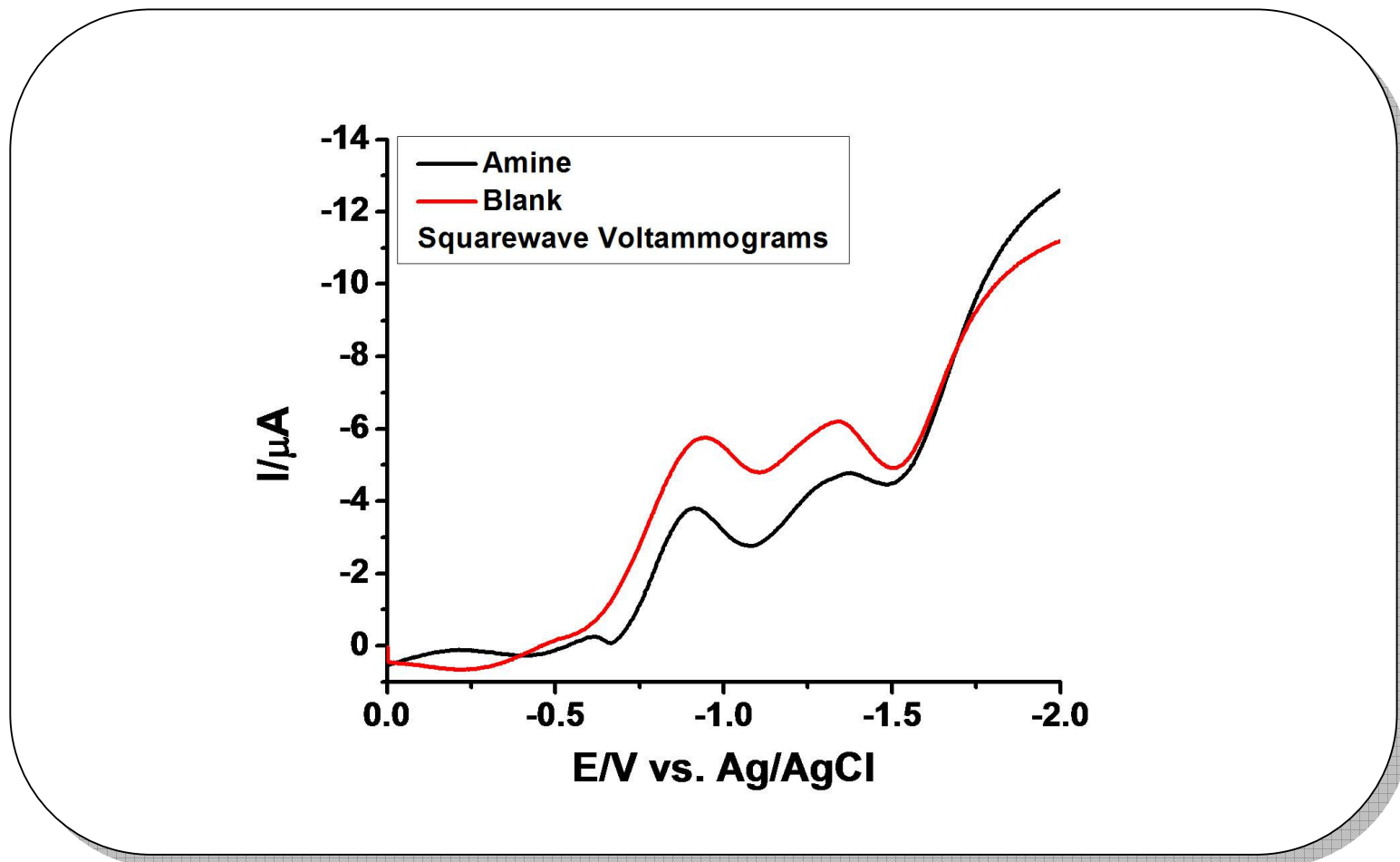
Figure 4.80: Comparison of Squarewave Voltammograms of Amine of TEONPI and Blank Solution in Chloroform at a Frequency of 25 Hz

Chapter 5

RESULTS AND DISCUSSION

5.1 Syntheses of Electron-accepting (*n*-type) Materials

All the electron-accepting (*n*-type) materials listed were synthesized by a condensation polymerization reaction mechanism. The mixture of dried high boiling solvents *m*-cresol and isoquinoline was used as a solvent medium in the syntheses of electron acceptor compounds. Flexible – rigid – flexible designed perylene and naphthalene oligomeric diimide dyes were reported in Schemes 3.2 and 3.3 respectively. The planar perylene and naphthalene tetracarboxylic dianhydride units were selected as hydrophobic chromophore and hexa(ethylene glycol) as the flexible hydrophilic spacer. In order to introduce the flexible moiety in the syntheses of oligomeric dyes, long aliphatic diamine, EODA was synthesized by a three-step reaction mechanism (Scheme 3.1). In the first step, double protection of –OH groups by tosyl chloride was carried out followed by azidation using sodium azide. The final third step was a hydrolysis mechanism to yield the designed diamine. Incorporation of this flexible hydrophilic spacer, EODA tremendously increased the solubility of oligomeric dyes. If perylene oligomeric dye has shown impressive solubility in most of the commercially available organic solvents, naphthalene oligomeric dye on the other hand has shown solubility in both organic and aqueous media.

Scheme 3.4 explores the synthesis of another naphthalene polyimide dye carried out by Ozser with a commercial diamine similar to EODA.

In Scheme 3.5, synthesis of a novel perylene dye substituted fluorescent chitosan polymer was presented (synthesized by Ozdal). It is the first perylene polymer in literature where a chitosan polymer was substituted. First, a perylene monoimide was prepared and was put in reaction with chitosan polymer. By traditional condensation polymerization reaction, the polymer was synthesized in appreciable yield.

5.2 Solubility of Acceptor Compounds

Incorporation of the flexible hexa(ethylene glycol) moieties in the backbone yielded remarkable solubility of oligomeric diimide dyes. As shown in Table 5.1, EOPPI has shown bright solubility in organic medium. However, its dimer has shown appreciable solubility in methanol.

Table 5.1: Solubility of EOPPI

Solubility/Color	
Solvent	**EOPPI**
CHCl$_3$	(+ +) F brown
TCE	(+ +) brown
THF	(– +) F orange
CH$_2$Cl$_2$	(+ +) F orange
Pyridine	(+ +) F orange
Acetone	(– +) F yellow
NMP	(+ +) brown
DMF	(+ +) F pink
CH$_3$CN	(– +) F yellow
DMSO	(+ +) Cherry red
m-Cresol	(+ +) deep pink
CH$_3$COOH	(+ +) orange
CF$_3$COOH	(+ +) deep pink
CH$_3$OH*	(– –)
H$_2$SO$_4$	(+ +) deep violet

(+ +): Soluble at RT, (– +): Soluble on heating at 60 ^{o}C, (– –): insoluble. F: fluorescent. *Dimer of EOPPI has shown appreciable solubility in methanol.

The qualitative solubility and color data of EONPI was tabulated in Table 5.2. Regardless of the type and polarity of the solvent, EONPI has shown excellent solubility in most of the common commercial protic, aprotic and acidic solvents. However, the solubility in aqueous medium was not as impressive as organic medium. Despite the poor solubility of most of polyimides, this new oligomer has

167

shown tremendous solubility. The better solubility noticed by EONPI corresponding to the perylene oligomer (EOPPI) is due to the increased rigidity of hydrophobic perylene chromophore comparing to the naphthalene unit.

Table 5.2: Qualitative solubility data of EONPI

Solubility/Color			
Aprotic Solvents		Protic Solvents	
Solvent	EONPI	Solvent	EONPI
$CHCl_3$	(+ +) F brownish orange	CH_3COOH	(+ +) F brownish orange
TCE	(+ +) F brownish orange	CF_3COOH	(+ +) brownish orange
THF	(− +) F gold	2-Propanol	(+) light yellow
CH_2Cl_2	(+) F brownish orange	Ethanol	(− +) light yellow
m-Cresol	(+ +) F brownish orange	Methanol	(− +) light yellow
Pyridine	(+) F gold	Water	(− +) light yellow
Acetone	(− +) F light yellow	H_2SO_4	(+ +) brownish orange
NMP	(+ +) F brownish orange		
DMF	(+ +) F brownish orange		
CH_3CN	(+) F gold		
DMSO	(+ +) F brownish orange		

[a] Qualitative solubility was determined at a concentration of 100 mg of oligomer in 1 mL of solvent. (+ +): soluble at room temperature; (+): partial soluble at room temperature; (− +): partial soluble on heating; F: fluorescent.

5.3 FT-IR Spectra Analyses

The FT-IR spectra recorded for all the compounds synthesized were completely represented the various functional groups present in their structure. The detailed description of the stretching and bending absorptions of functional groups were explained below.

From Figure 4.10, aromatic C–H stretch at 3062 cm^{-1}, aliphatic C–H stretch at 2917 cm^{-1} and 2868 cm^{-1}, imide C=O stretch at 1694 cm^{-1} and 1664 cm^{-1}, conjugated C=C stretch at 1594 cm^{-1}, aliphatic C-H bending at 1439 cm^{-1}, C–N stretch at 1344 cm^{-1}, CH$_2$–O stretch at 1103 cm^{-1}, C–H bend at 809 cm^{-1} and 744 cm^{-1} prove the structure of EOPPI.

From Figure 4.11, aromatic C-H at 3065 cm^{-1}, broad and intense aliphatic C-H stretch at 2865 cm^{-1}, imide (C=O) stretching at 1704 cm^{-1}, 1665 cm^{-1}, conjugated C=C stretch at 1580 cm^{-1}, C-N stretch at 1335 cm^{-1}, wide CH$_2$-O stretch at 1105 cm^{-1} confirms the structure of EONPI.

5.4 Analyses of GPC Chromatograms and Intrinsic Viscosity

GPC chromatograms of EOPPI showed in Figure 4.12 were obtained from a GPC measurement recorded in HFIP solution. The weight-average molecular weight (M_w) of EOPPI was found as 4460 g/mol with a poly dispersity index (PDI) of 2.33. Such a moderate PDI was probably due to the side reactions upon extension. The oligomer has about seven monomer units. In comparison, viscosity measurement was performed to measure intrinsic viscosity in m-cresol at 20 ^{o}C. The intrinsic viscosity calculated, 0.3 dL/g, was in good support of molecular weight obtained from GPC data.

GPC measurement of EONPI was also recorded in HFIP solution (Figure 4.13). The number average (M_n) and weight average (M_w) molecular weights were 2030 g/mol and 4430 g/mol respectively with a broad distribution (PDI–2.20) as expected from a polycondensation reaction. According to M_w, the oligomeric diimide possessed eight monomer units. The chromatograms show that they are having monomodal molar mass distributions and moderate PDIs, which are the typical characteristics of a classical step-growth polymerization. Intrinsic viscosity was measured as 0.28 dL/g in m-cresol at 25 ^{o}C. The measured intrinsic viscosity of the oligomer was in good agreement with the GPC data.

M_w of the reported dye substituted chitosan was 467,000 with a broad distribution (PDI $\cong$ 8.35) (in dimethylacetamide at 70 ^{o}C), whereas about 460,000 was estimated for Chitosan (CH) with PDI $\cong$ 10.62 (in 0.1 M NaCl/0.1% TFAc at 25 ^{o}C) by Ozdal. For comparison, intrinsic viscosities were measured in the similar manner of EOPPI and EONPI.

The found intrinsic viscosity of CH polymer was 4 dL/g, which is in perfect agreement with the various reported viscosities of different CH and derivative polymers. Although, there is a considerable deviation in the equation proposed by Mohammad R. Kasaai [60, 61], an approximate M_v was measured (Aldrich given the range of M_v of commercial CH polymer as 50,000 – 190,000 Daltons) for the chitosan polymer. By using the equations (Equns. 4.3-4.4) reported for any solvent-temperature system, we have measured the MHS constants ($K = 0.151 \times 10^{-5}$, $a = 1.17$) and M_v as 309 kDa in 0.1 M NaCl/0.1% TFAc solvent system. The found 309 kDa is not perfectly matching with the given range by Aldrich. But, as mentioned earlier, there was a deviation itself in the proposed equation and the value that found was in better approximation.

Similarly, the intrinsic viscosity ($[\eta] = 0.4$ dL/g) of HP-CH in dimethyl acetamide was mesured at 70 $^\circ$C; whereas 9.0 dL/g was noted at 25 $^\circ$C which shows the great effect of temperature on intrinsic viscosity. It is noteworthy that the intrinsic viscosity of HP-CH was higher than CH which is an expected result when compared the perylene dye substituted chitosan and chitosan alone.

5.5 Analyses of NMR Spectra

Perylene-3,4,9,10-tetracarboxylic acid-Bis-(*N,N′*-Bis 2-[2-(2-{2-[2-(2-hydroxy-ethoxy)-ethoxy]-ethoxy}-ethoxy)-ethoxy]-ethylpolyimide, EOPPI

1H NMR (CDCl₃ + CF₃COOD (1:1), ppm): dH 8.56 (br s, 4Ar–H, H–C(1), H–C(6), H–C(7), H–C(12)), 8.31 (br s, 4Ar–H, H–C(2), H–C(5), H–C(8), H–C(11)), 4.50–3.74 (m, 12CH₂, H2–C(17)–H2–C(28)) [9].

13C NMR (CDCl₃ + CF₃COOD (1:1), ppm): dC 164.24, 134.59, 132.25, 124.82, 121.94, 77.41, 77.30, 77.09, 76.78, 70.43, 69.79, 68.44, 68.18, 66.54, 39.64, 28.55 [9].

Naphthalene-1,4,5,8-tetracarboxylic acid-bis-(*N*,*N*′-bis 2-[2-(2-{2-[2-(2-hydroxy-ethoxy)-ethoxy]-ethoxy}-ethoxy)-ethoxy]-ethyl polyimide, EONPI
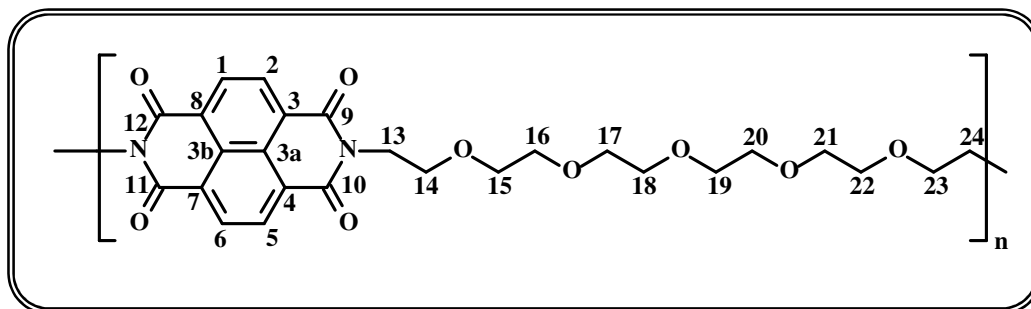
^{1}H NMR (400 MHz, CDCl$_3$ + CF$_3$COOD (1:1), ppm): 8.78 (br s, 4Ar-H), 4.50-3.72 (m, 12CH$_2$, H$_2$-C(13) - H$_2$-C(24)) (Figure 4.14) [10].

^{13}C NMR (100 MHz, CDCl$_3$ + CF$_3$COOD (1:1), ppm): 164.59 and 163.97 (4 C=O), 131.90, 129.71, 128.31, 126.54 (10 ArC), 70.03, 69.72, 68.51, 68.21, 66.58, 39.76 (12 C) (Figures 4.15, 4.16) [10].

5.6 Analyses of UV-vis Absorption Spectra

5.6.1 UV-vis Absorption Spectra of EOPPI

The absorption and emission spectra of EOPPI in chloroform solution (10^{-5} M) were shown in Figure 4.17. The respective absorbance maxima are 463, 491 and 527 nm respectively, which are the typical three absorption bands of classic perylene dyes. In contrast to the typical perylene dyes, an intensity reversal ($0 \rightarrow 1$ absorption band intensity is higher than $0 \rightarrow 0$ absorption band) was noticed for EOPPI. Figure 4.18 shows the overlap of UV–vis absorption of EOPPI in various solvents. The spectral shapes are similar in all solvents except some blue shifted absorption peaks (459, 489 and 521 nm) in 1,1,2,2-tetrachloroethane (TCE). The concentration dependent absorption spectra were figured out in Figure 4.19. With the increase in concentration, the absorbance of EOPPI was increased correspondingly. It is evident from Figures 4.17 and 4.20 that the absorption spectrum of solid-state was quite different from the absorption spectrum of solution. In terms of the spectral shapes (absorption up to 650 nm) and peak positions (Figure 4.20) absorption bands were red shifted by about 20 nm. This is most likely due to strong intermolecular π-π interactions in the solid state.

5.6.2 UV-vis Absorption Spectra of EONPI

Figure 4.21 shows the absorption and emission spectra of EONPI in chloroform solution with absorbance peak maxima at 343, 361, 380 and shoulder bands at 397, 413 nm, respectively. The first three absorption peaks represent the characteristic naphthalene diimide absorptions. The two shoulder bands are related to the intermolecular charge transfer interactions. Figure 4.22 reveals that the first shoulder

observed in chloroform solution at 397 nm (Figure 4.21) was disappeared in the other polar solvents, whereas the second shoulder at 413 nm is gradually decreased and disappeared in polar protic solvent methanol. Moreover, a small red shift occurred in dipolar aprotic solvents from 413 nm to 416 nm when compared to absorption of EONPI in chloroform (Figures 4.21 and 4.22). The disappearance of the shoulder band of 416 nm in methanol was interesting and encouraged to study the effect of protic character on the charge transfer behavior and intermolecular interactions in protic solvents in detail. The absorbance properties of EONPI in protic solvents such as 2-propanol, ethanol and water are shown in Figure 4.23. Interestingly, the absorption intensities of charge transfer peaks of shoulder bands at longer wavelengths were decreased as polarity of solvents increased and disappeared completely in water. Similar to the aprotic solvents shown in Figure 4.22, 4 nm red shift was noticed for $0{\rightarrow}0$ and $0{\rightarrow}1$ absorption bands in water comparing to the absorption of EONPI in 2-propanol. Another important vibronic band at high energy was noticed in polar protic spectra (Figure 4.23) and in dipolar aprotic solvents NMP, DMF, and DMSO (Figure 4.22) which is attributed to the probable protonation interactions of proton-donor solvent with oxygen and/or nitrogen acceptors and disruption of planarity. More interestingly, absorption intensity of $0{\rightarrow}1$ peak was intensified corresponding to $0{\rightarrow}0$ peak in high dipolar aprotic solvent, DMSO and high polar protic solvents methanol and water. This shows the weak aggregation tendency in high polar solvents (Table 5.3).

175

Table 5.3: Ratio of absorption intensities of EONPI in different solvents

	Aprotic Solvents		
Solvent	$A^{0\rightarrow1}$	$A^{0\rightarrow0}$	$A^{0\rightarrow0}/A^{0\rightarrow1}$
CHCl$_3$	1.449	1.623	1.12
NMP	1.261	1.301	1.03
DMF	1.114	1.130	1.01
DMSO	1.134	1.104	0.97
	Protic Solvents		
2-propanol	0.277	0.288	1.04
Ethanol	0.363	0.369	1.02
Methanol	1.978	1.844	0.93
Water	0.461	0.444	0.96

The molar extinction coefficients for the $0\rightarrow0$ absorption bands of EONPI were measured in all the above nonpolar, dipolar aprotic and protic solvents (Tables 4.5, 4.7 and 5.4). Surprisingly, the values measured were quite high comparing with those found in literature. In chloroform solution, it was estimated as 157400 L mol^{-1} cm^{-1} at 380 nm. In order to confirm the high molar absorptivity, it was obtained by the absorption measurements which were carried out in seven solutions of different concentrations and from the slope of plots of the absorption versus concentration (correlating coefficients ≥ 0.99) (Table 4.6 and 4.7 shows the absorbances and molar absorptivities data). The unexpected high molar absorptivity could be attributed to intermolecular charge transfer and π-π^* electron transitions of the conjugated molecule. Additionally, the extinction coefficients gradually decreased with increasing polarity of solvent, attributed to respective solute-solvent interactions being much stronger in polar solvents. In contrast, the high molar extinction coefficient in methanol could be due to respective charge transfer interactions. It is

Table 5.4: Absorption wavelengths λ_{abs} (nm), maximum absorption wavelengths $\lambda_{abs,max}$ (nm), emission wavelengths λ_{em} (nm), maximum emission wavelengths $\lambda_{em,max}$ (nm), absorption wavelengths of 0→0 transition $\lambda_{abs,\,0-0}$ (nm), molar absorptivities of 0→0 transition ε (L · mol^{-1} · cm^{-1}), excimer emission wavelengths $\lambda_{excimer}$ (nm), stokes shifts $\Delta\bar{v}$ (cm^{-1} (eV)) and fluorescence quantum yields Φ_f data of EONPI

Solvent	λ_{abs}	$\lambda_{abs,max}$	λ_{em}	$\lambda_{em,max}$	$\lambda_{abs,\,0-0}$	ε	$\lambda_{excimer}$	$\Delta\bar{v}$	Φ_f
Aprotic Solvents									
CHCl$_3$	343, 361, 380, 397, 413	380	392, 409, 513	513	380	157400	513	75188 (9.3)	0.017
NMP	346, 362, 382, 416	382	470, 550	470	382	125900	470	113636 (14.1)	
DMF	325, 343, 360, 380, 416	380	460, 555	460	380	110900	460	125000 (15.5)	0.012
DMSO	326, 344, 362, 382, 416	362	458, 542	458	382	108400	458	131579 (16.3)	
Protic Solvents									
2-Propanol	319, 342, 358, 379, 393, 412	379	356, 376, 433, 457	356	379		376	–3333333 (–413.3)	
Ethanol	319, 341, 358, 379, 412	379	376, 436, 458	376	379		376	–3333333 (–413.3)	
Methanol	326, 340, 357, 378	357	372, 397, 435, 503	397	378	155400	397	526316 (65.3)	0.022
Water	320, 343, 362, 383	362	359, 374	374	383		374	–1111111 (–137.8)	0.032
solidstate									
	312, 345, 365, 378, 394, 428	365							

clear from Table 5.4 and Figures 4.22 and 4.23 that the extinction coefficients are strongly dependent on solvent polarity and proticity. Figures 4.24 – 4.26 explore the absorption behavior at different concentrations of nonpolar, dipolar aprotic and protic solvents. At higher concentration, $2x10^{-5}$ M, in chloroform, the shoulder bands at 397 nm and 413 nm were stronger comparing to the lower concentrations (Figure 4.24). Figure 4.25 shows the absorption spectra in DMF at three different concentrations and as the concentration decreased gradually, the absorption intensities of $0{\to}0$ and $0{\to}1$ bands became equal. Additionally, the charge transfer peak at 416 nm reduced in intensity as the concentration is lowered. The absorption spectra in methanol (Figure 4.26) reveal that irrespective of concentration the absorption intensity reversal was noticed ($0{\to}1$ absorption band intensity is higher than $0{\to}0$ absorption band) (Table 5.3).

On the other hand, the absorption spectrum of oligomeric diimide, EONPI in solid-state (Figure 4.27, Table 5.4) was different from the solution absorption spectrum indicating the difference in intermolecular interactions in both states, revealing the broader spectral shape in solid-state. Additionally, the most intensive absorption in solid state was found at 365 nm ($0{\to}1$ absorption band) unlike the maximum absorption band at 380 nm (of $0{\to}0$ absorption band) in chloroform solution. Moreover, EONPI gives rise to three charge-transfer band maxima around 312, 394 and 428 nm (Figure 4.27, Table 5.4).

178

5.7 Analyses of Fluorescence Spectra

5.7.1 Emission Spectra of EOPPI

All the emission spectra of EOPPI were taken at 485 nm excitation wavelength and are shown in Figures 4.28 – 4.31. The emission bands and Stoke shift value in CHL for EOPPI are 535, 577, 625 and 8 nm, respectively (Figures 4.17 and 4.28). Red-shifted emission in TCE comparing to the other solvents (541, 582 and 631 nm) can be noticed from the emission spectra of EOPPI in various solvents (Figure 4.28). The relative fluorescence quantum yields were determined in various solvents using N,N'-didodecyl-3,4,9,10- perylenebis (dicarboximide) in chloroform (Φ_f = 1.0) as standard (Equn. 4.6). The fluorescence quantum yields of compounds are measured and given in Table 4.8. Interestingly, the dimer-EOPPI has shown high fluorescence quantum yield in methanol. Meanwhile, the low fluorescence quantum yields in various solvents are attributed to the re-absorption of emitted photons and the selfquenching due to the intra and intermolecular interactions.

As shown in Figure 4.29 at three different concentrations in chloroform, the peak maxima and the shapes were completely changed with changing concentration. Even at lowest concentration, 1×10^{-6} M, the resultant reciprocal transitions that are exhibited by mirror symmetry of the fluorescence spectrum for all the absorption bands were not noticed (Figures 4.17, 4.19 and 4.29). At 1×10^{-6} M, the maximum emission intensity was noticed at 535 nm among the emission peak maxima at 535, 576 and 623 nm, respectively. When the concentration was increased by 10 fold, the maximum emission intensity was shifted to 576 nm comparing to the previous 1×10^{-6} M concentration. Moreover, with a small red shift (535 nm at 1×10^{-6} M to 540 nm at 1×10^{-5} M) the emission peak maximum at 540 nm is reduced in intensity

comparing to 576 nm. The reason behind this unusual decrease in intensity of $0 \rightarrow 0$ emission band is the overlap between the absorption and emission spectra of compounds which could lead to re-absorption of the emitted photons by ground state and to the probable intra and intermolecular interactions. After another 10 fold increase in concentration (making the total concentration of 1×10^{-4} M), intensity of $0 \rightarrow 0$ emission band was diminished completely and a drastic change in peak shapes and maxima was noticed. Emission band intensity at 587 nm $(0 \rightarrow 1)$ reduced while the emission at 629 nm $(0 \rightarrow 2)$ increases significantly. The net emission was observed at 629 nm (Figure 4.29). These unusual changes in emission and resulting net emission shifts at different concentrations correspond to color tunability (Figure 4.30). The color tunability was pictured in Figure 4.30 where the oligomeric perylene diimide emits green, yellow and red colored light at 1×10^{-6} M, 1×10^{-5} M and 1×10^{-4} M, respectively. Wang et al. have reported similar tunability and attributed this result to the existence of folded polymers [72], which leads to the emission of different colors as the folded chromophoric oligomers become larger.

Figure 4.31 shows the effect of temperature on fluorescence properties of EOPPI. Upon heating, the emission maxima are slightly blue shifted and decreased in emission intensity. This optical change could be related to the conformational transition of the conjugated backbone and to aggregation of oligomer. This property is in agreement with the literature data [73, 74].

5.7.2 Energy Transfer Studies of EOPPI

The perylene dyes would give photosensitized energy-electron transfer processes from singlet state [70]. Interestingly, EOPPI acts as an energy donor when combined with a quencher such as $CoCl_2$ and $NiSO_4$ by the mechanism of Förster resonance energy Transfer (FRET). The short range Dexter exchange mechanism could be effective as well. Figures 4.32 – 4.39 explain the singlet energy transfer mechanism of oligomeric diimide, EOPPI when combined with quenchers $CoCl_2$ and $NiSO_4$. An efficient overlap between the absorbance spectrum of quencher and emission spectrum of donor is considered as a primary requirement which indicates the probable transfer of energy by FRET mechanism. Figures 4.32 and 4.36 reveal that the overlap between $CoCl_2$ and EOPPI is more efficient comparing to the couple $NiSO_4$ and EOPPI. Although the overlap is not as efficient as $CoCl_2$ and EOPPI couple, $NiSO_4$ appreciably quenched the fluorescence of donor, EOPPI and the quenching rate was measured by the fluorescence spectra and by using Stern-Volmer plot.

Figures 4.33 and 4.37 indicate the effect of quencher concentration on corresponding absorbance of donor, EOPPI. For both couples, a gradual increase in absorbance of donor was noticed with increase in concentration of quencher. On the other hand, it is evident that the reverse trend was occurred for emission spectra of donor (Figures 4.34 and 4.38). With a gradual increase in concentrations of quenchers, the fluorescence of donor was reduced effectively. This indicates the probable energy transfer from EOPPI to the quencher by FRET mechanism.

The Stern-Volmer plots drawn (Figures 4.35 and 4.39) for the couples $CoCl_2$ and EOPPI and $NiSO_4$ and EOPPI indicate the quenching and respective rate constants for bimolecular fluorescence quenching. The rate constant for bimolecular

fluorescence quenching was estimated from the corresponding emission intensity ratios of donor and respective theoretical fluorescence lifetimes that are measured from the absorption spectra of donor. The quenching rate constant was high for $CoCl_2$ and EOPPI couple (1.06×10^{10} M^{-1} s^{-1}) comparing to the $NiSO_4$ and EOPPI couple (1.24×10^9 M^{-1} s^{-1}), as expected from the better overlap between quencher and donor of $CoCl_2$ and EOPPI couple. The critical transfer distance (R_0) measured for $CoCl_2$ and EOPPI couple was $28.9 \overset{o}{A}$. These results show that the energy transfer occurs from EOPPI to the quenchers by long-range FRET mechanism.

5.7.3 Emission Spectra of EONPI

All the emission spectra of EONPI were taken at 360 nm excitation wavelength and are shown in Figures 4.21, and 4.40 – 4.52. As seen in Figure 4.21, the emission spectrum is not a mirror image of corresponding absorption spectrum like EOPPI oligomeric diimide with the same diamine. All the emission spectra of EONPI measured were striking with exciting device application possible properties. In all kinds of solvents reported, EONPI exhibited excimer like emission (Figures 4.40 and 4.41, Table 5.4). The emission maxima were observed at 513 nm in chloroform, 470 nm in NMP, 460 nm in DMF and 458 nm in DMSO, respectively (Figure 4.40). Especially in chloroform, the excimer emission was red shifted comparing to other solvents which is attributed to π-stacked interactions and all the excimers appeared in all solvents is an important indication of strong intermolecular interactions between planar oligomer chains in solution. A large Stokes shifts were observed in all aprotic solvents and increased gradually with the increase in solvent polarity (Table 5.4). These large solvent dependent Stokes shifts indicate three major phenomena, (i) the excitation occurred to excited singlet S_2 state; (ii) the lowest energy electronic

transition has profound charge transfer character; and (iii) the intermolecular interactions in the ground and excited states are different from each other.

Figure 4.41 explore the emission properties of EONPI in protic solvents. In the similar manner of their absorption spectra, the emission properties were different from the aprotic solvents. Contrary to aprotic solvent emission spectra, the excimer emission bands were blue shifted. These higher energy excimer emission bands shapes were dramatically changed and the most blue shift was occurred in most polar protic solvent, water. The highest energy excimer band resulted in water is attributed to the disruption of the intermolecular interactions, π-stacking and planarity of the oligomeric diimide. Because of the drastic blue shifts in excimer-band maxima in protic solvents, anti Stokes shifts were resulted (Table 5.4). However, the large Stokes shift observed in methanol comparing to the other solvents is attributed to the probable intermolecular interactions and charge transfer character. It is evident from all the emission spectra that there exist specific interactions between naphthalene oligomeric diimide and aprotic, protic solvents which have a great influence on the photophysical properties of EONPI.

The fluorescence quantum yields were measured in different solvents by using the reference anthracene as a standard. In general, the fluorescence quantum yields of naphthalene dyes were lower because of the effect of inter system crossing. Interestingly, the quantum yields were rised (similar to their corresponding high extinction coefficients) comparing to the literature values of naphthalene dyes but still they are lower in percentage. The increased quantum yield in chloroform comparing to the ones in literature could be attributed to the increase in rigidity which reduces the loss of energy via radiationless thermal vibrations. On the other hand, there is an increase in fluorescence quantum yield in protic solvents with

increase in proticity. This is due to the probable hydrogen-bonding talent of solvent molecules which have the ability to modify n,π^* – π,π^* energy gap, shifting the n,π^* state to the blue and π,π^* state to the red. If the solvent is more polar and protic with better hydrogen bond formation ability, it results in decrease of inter system crossing rate and thus will give high luminescence.

Figures 4.42 – 4.47 explain the effect of concentration on fluorescence and resulting excimer-emission properties of EONPI. In Figure 4.42, the concentration dependent emission spectra in chloroform were presented which reveal that at highest concentration 1×10^{-4} M, a red shifted excimer band was occurred. The same trend was noticed in other solvents. This red shifted emission at high concentration can be explained by the stacking and hydrogen bonding interactions. On the contrary, when the concentration was gradually decreased in dipolar aprotic and protic solvents, the excimer emission maxima were blue shifted (Figures 4.43 – 4.46). This indicates that the ground electronic state is more polar than the excited state S_2, and therefore better stabilized by polar salvation with lowering of energy. Hence, the transition occurs at a shorter wavelength at lower concentrations.

5.7.4 Color Tunability of EONPI

Figure 4.47 shows the concentration and solvent dependent color tunability of EONPI in three types (nonpolar, dipolar aprotic and protic) of solvents. From the above discussed concentration dependent emission spectra in different solvents (Figures 4.42 – 4.46), it is clear that EONPI emits light at various wavelength maxima (in chloroform: 564, 513 at 10^{-4} M, 10^{-4} M; in DMF: 512, 444 at 10^{-4} M, 10^{-4} M; in methanol: 525, 397 at 10^{-4} M, 10^{-6} M, respectively) representing different colors of visible region from electromagnetic spectrum. In protic solvents, the light emitted by the oligomer shifts from the low energy, long wavelength to the high

energy, short wavelength end of the spectrum. This is attributed to the complex formation with oligomer via the non-bonding electron pair of the electrophilic carbonyl oxygen atom. As a conclusion, under day light, EONPI exhibits golden yellow color in the three reported solvents, chloroform, DMF and methanol at 10^{-6} M; and at 365 nm, light yellow, light blue and strong blue colors were noticed respectively. When the concentration was increased to 10^{-4} M, fluorescence intensity was increased. Under day light, EONPI exhibits fluorescent brown color in the three solvents (chloroform, DMF and methanol) at 10^{-4} M; and at 365 nm, intensive fluorescent yellow in both chloroform and DMF, green light in methanol were noticed respectively. The color tunability and light emitting excimer emission propertiesof the naphthalene oligomeric diimide are very remarkable for future device applications in photonic technology.

5.7.5 Effect of Temperature and Excitation Dependency on Fluorescence Spectra of EONPI

Figures 4.48 – 4.50 reveal the effect of temperature on emission spectra of EONPI in three different solvents at 10^{-4} M, 10^{-5} M concentrations. In all the three solvents, chloroform, DMF and methanol, the excimer bands are red shifted and gradually decreased in intensity at higher concentration. This can be attributed to probable π-stacking interactions. In chloroform, at both concentrations the emission peak shapes and peak positions have shown no effect with temperature change (Figure 4.48). This indicates the stabilization of energy levels by strong hydrogen bonding interactions. On the other hand, an increase in emission range was noticed in DMF and methanol relative to chloroform. Unlike the emission spectra of chloroform, at both concentrations in DMF, a decrease in intensity was observed with increase in temperature (Figure 4.49). This could be attributed to the disruption of the

185

intermolecular interactions and π-stacking. Interestingly, a different behavior was noticed in methanol from the other two solvents (Figure 4.50). At higher concentration, 10^{-4} M, the excimer emission intensity at 512 nm was gradually decreased with increasing temperature; whereas, at lower concentration, 10^{-5} M, emission spectra showed a gradual increase of excimer emission intensity at 397 nm and gradual decrease in intensity at 512 nm as temperature is increased. This behavior indicates that the two bands observed in methanol represent two different emitters and their existence ration with the influence of temperature.

Figures 4.51 and 4.52 show the excitation dependency on fluorescence behavior of EONPI. As it is evident from the figures that the peak shapes were unchanged when excited at different excitation wavelengths in both the solvents chloroform and DMF.

The solid-state emissions of EOPPI and EONPI could not be taken in all attempts due to the weak emission intensity. This was attributed to the self-quenching as a result of efficient energy transfer at solid-state.

5.7.6 Energy Transfer Studies of HP-CH

Similar to the energy transfer studies of EOPPI, energy transfer behavior of HP-CH was studied with anthracene (Figures 4.53 – 4.55). Here, anthracene was used as energy donor molecule and perylene substituted chitosan polymer (HP-CH) was considered as acceptor. Figure 4.53 shows the overlap of absorption and emission spectra of HP-CH and anthracene respectively in methanol. The emission spectra figured out in Figure 4.54 show the decrease of donor fluorescence with increase in concentration of acceptor HP-CH concentration. The measured value of rate constant for biomolecular fluorescence quenching is high (9.79×10^{13} M^{-1} s^{-1}) indicating the efficient transfer of energy from anthracene to perylene dye (Figure 4.55).

5.8 Thermal Stability

Thermal behaviors of the oligomeric diimides were studied by DSC and TGA (Figures 4.56 and 4.57) techniques. Figure 4.56 shows the DSC thermograms recorded for oligomers at three sequential runs (heating, cooling and reheating) (only 2nd heating was shown for EOPPI in the figure). Both EOPPI and EONPI do not exhibit glass transition temperature in the DSC runs (1st and 2nd heating) up to 300 ^{o}C for EOPPI (only the 2nd heat was shown in the figure) and up to 350 ^{o}C for EONPI. At any stage in three different runs, oligomers exhibited no variation in curve shapes and no melting up to 300 ^{o}C for EOPPI and up to 350 ^{o}C for EONPI. The DSC curves of EONPI revealed that the decomposition starts at around 325 ^{o}C.

Thermogravimetric analysis of the oligomeric diimides (Figure 4.57) reveals that EOPPI began to lose mass at 375 ^{o}C, whereas EONPI began to lose at 325 ^{o}C and thus proving the exceptional high thermal stability of the compounds in their kind. The weight loss starting temperatures for some similar polymers (with long aliphatic ethoxy chains at back bone) were reported around 250 ^{o}C and for some of them no literature data was presented up to the best of our knowledge. In addition, for EONPI, only a 27% weight loss was observed between 325 – 455 ^{o}C. After heating to 570 ^{o}C, 57% weight loss was observed followed by a total weight loss of 97.5% up to 650 ^{o}C. At the end of analysis of 900 ^{o}C, 2.5% char yield was noticed. Despite the long aliphatic chains present in the backbone, oligomeric diimides thermal stability was not sacrificed and showed unusual stability in its class of compounds. This could be attributed to the probable intermolecular forces, flexibility and symmetry of the structure (Figure 4.57).

5.9 Electrochemistry of *n*-type Materials

5.9.1 Electrochemistry of EOPPI

Electrochemical properties of the oligomers were investigated through the redox data obtained from cyclic voltammetry (CV) and squarewave voltammetric (SWV) measurements. The CVs of EOPPI were shown in Figures 4.58 – 4.60 that are taken in pure dichloromethane and the redox potentials, electrochemical parameters were summarized in Tables 5.5 and 5.6.

Table 5.5: Electrochemical data of EOPPI

	E_{pc} (V)	E_{pa} (V)	ΔE_p (mV)	$E_{1/2}$ Vs. Ag/AgNO$_3$ (V)	E_{Fc} Vs. Ag/AgNO$_3$ (V)	$E_{1/2}$ Vs. Fc (V)
EOPPI	−0.741	−0.800	59	−0.771	0.175	−0.946
(CH$_2$Cl$_2$)	−0.959	−1.025	66	−0.992	0.175	−1.167

Table 5.6: Cyclic voltammetry data of EOPPI

Scan Rate (mVs^{-1})	EOPPI E_{pa} (V)	E_{pc} (V)	ΔE_p (mV)	i_{pa} (µA)	i_{pc}	i_{pa}/i_{pc}
25	−0.810	−0.741	69	0.20	0.20	1.00
	−1.039	−0.937	102			
50	−0.810	−0.745	65	0.64	0.62	1.03
	−1.035	−0.958	77			
100	−0.800	−0.741	59	0.68	0.63	1.08
	−1.025	−0.959	66			
400	−0.805	−0.747	58	1.43	1.42	1.01
	−1.047	−0.963	84			
800	−0.808	−0.746	62	2.18	2.18	1.00
	−1.050	−0.957	93			
1000	−0.755	−0.812	57	2.33	2.33	1.00
	−1.068	−0.959	109			

EOPPI undergone two fast reversible, one-electron reductions at -0.946 V and -1.167 V (vs. ferrocene/ferrocenium couple) with a $\Delta E_p = 59$ mV and $\Delta E_p = 66$ mV, respectively, in CH_2Cl_2 (Figure 4.58 and Table 5.5). The calculated ΔE_p in the range 60–70 mV for EOPPI shows that reversibility of electron transfers were fairly well maintained in the system.

Table 5.6 reveals that EOPPI possessed completely reversible reduction steps for the entire scanning rate in the region of 25–1000 mVs^{-1}. The calculated cathodic and anodic peak currents ratio (i_{pa}/i_{pc}) were equal to unity and the ΔE_p was about 60–70 mV at each scan rate. Especially, at 100 mVs^{-1}, ΔE_p was exactly 59 mV indicating the high reversibility. Thus, each reduction process indicates reversible, diffusion-controlled one-electron transfer according to the standard reversibility criteria.

The plots drawn for EOPPI in Figures 4.59 and 4.60 shows that the cathodic peak currents against square root of scan rate and log of scan rate were linear with near-unity adjacent R-square values. This fulfills the conditions for diffusion-controlled processes. As shown in Figures 4.59, 4.60 and Table 4.19, the diffusion constant was calculated as 1.33×10^{-9} cm^2/s.

The LUMO energy of the compound was calculated from cyclic and square-wave voltammograms (Figure 4.58, Equn. 4.16) as -3.85 eV. The optical band gap, E_g was calculated from the corresponding absorption spectrum of EOPPI as shown in Figure 4.6 and from Equn. 4.17. E_g was approximately measured as 2.24 eV for EOPPI. From these values, by using the formula (Equn. 4.18) the HOMO energy of the oligomer EOPPI was estimated as -6.09 eV. All values were also tabulated in Table 4.18 with the same amine made naphthalene oligomeric diimide for comparison. The corresponding band energy diagram was shown in Figure 4.66. It can be concluded from the data that EOPPI is electrochemically stable and reversible.

5.9.2 Electrochemistry of EONPI

Figures 4.61 – 4.66 show the cyclic and squarewave voltammetry data measured in different solvents at various scan rates. Tables 5.7 and 5.8 summarize the redox data.

Table 5.7: Electrochemical data of EONPI

EONPI	E_{pc} / V	E_{pa} / V	ΔE_p / mV	$E_{1/2}$ vs. (Ag/AgCl) / V	E_{Fc} vs. (Ag/AgCl) / V	$E_{1/2}$ vs. Fc / V
CH$_2$Cl$_2$	−0.682	−0.824	142	−0.753	0.35	−1.103
	−1.044	−1.170	126	−1.107	0.35	−1.457
CH$_3$OH+CH$_3$CN (50:50)	−0.505	−0.569	64	−0.537	0.38	−0.917

Table 5.8: Cyclic voltammetry data of EONPI in CH$_2$Cl$_2$

Scan Rate (mVs^{-1})	E_{pa} / V	E_{pc} / V	ΔE_p / mV	i_{pa} / µA	i_{pc} / µA	i_{pa}/i_{pc}
50	−0.836	−0.679	157	0.51	0.55	0.9
	−1.173	−1.044	129			
100	−0.824	−0.682	142	1.12	1.11	1.0
	−1.170	−1.044	126			
200	−0.830	−0.679	151	1.43	1.39	1.0
	−1.173	−1.044	129			
500	−0.827	−0.679	148	1.82	1.82	1.0
	−1.177	−1.044	133			

In solvent CH$_2$Cl$_2$, oligomer undergoes two reversible one-electron reductions, the first of which is the reduction of the neutral compound to radical anion (EONPI$^{\cdot-}$)

and the second reduction corresponds to the formation of the dianion (EONPI^{2-}). As shown in Figure 4.61 and Table 5.7, the reduction potentials were –1.103 V and –1.457 V respectively according to ferrocene/ferrocenium couple with peak separations ΔE_p of 142 and 126 mV respectively. The large peak potential separations indicate the poor reproducibility of current due to possible charge transfer kinetics. As apparent from Figure 4.61 and Table 5.8, at different scan rates in CH_2Cl_2, oligomer shows electrochemical reversibility and stability. Thus, each reduction process indicates reversible, diffusion-controlled one-electron transfer according to the standard reversibility criteria.

Table 5.9: Cyclic voltammetry data of EONPI in CH_3OH+CH_3CN (50:50)

EONPI in CH_3OH+CH_3CN (50:50)						
Scan Rate (mVs^{-1})	E_{pa} / V	E_{pc} / mV	ΔE_p / mV	i_{pa} / μA	i_{pc}	i_{pa}/i_{pc}
50	–0.562	–0.500	62	0.25	0.27	0.9
100	–0.569	–0.505	64	1.05	1.07	1.0
200	–0.586	–0.503	83	2.51	2.59	1.0
500	–0.615	–0.500	115	4.18	3.85	1.1

In contrast, oligomer in polar medium (methanol + acetonitrile) does not show such electrochemical reversibility and stability (Figure 4.62). Even the second reduction was unsuccessful. This can be attributed to the rigidity, symmetry of oligomer and disruption in local packing of oligomer by the probable intermolecular hydrogen bonding interactions in high protic solvents. The peak potential for the only one reversible electron reduction according to ferrocene/ferrocenium couple was –0.917 V, which is slightly positive comparing to the reduction in dichloromethane.

191

From Table 5.9, the calculated peak current ratios (Figure 4.63) were equal to unity and the peak separation (ΔE_p) was about 62-115 mV, which is better than electron reductions in dichloromethane. Various electrochemical parameters estimated for EONPI in CH_2Cl_2 and CH_3OH+CH_3CN (50:50) were summarized in Table 4.18. Absolute energy of LUMO levels of EONPI was estimated with respect to the vacuum level by standardizing the redox data to the ferrocene/ferricenium couple which has a calculated absolute energy of -4.8 eV. The estimated band gap energy (E_g), LUMOs, HOMOs in CH_2Cl_2 and CH_3OH+CH_3CN (50:50) were 2.71 eV/-3.12 eV; -3.69 eV/-3.88 eV; -6.04 eV/-7.00 eV, respectively. It is noteworthy that the band gap energy value increased in protic solvent mixture of high polarity than nonpolar solvent dichloromethane (Figure 4.66). Therefore, solvent dependent band gap tunability was evident from the data which imply the chance of using the compound as an electron acceptor in coupled with the respective range electron donors in search of light harvesting systems and for opto-electronic applications.

The plot of peak current (i_{pc}) vs. square root of scan rate ($v^{1/2}$) was linear implying the diffusion controlled processes in both solvents (Figures 4.64 and 4.65). By using Randles-Sevcik equation (Equn. 4.19), the diffusion coefficient (D) was calculated with the cyclic voltammetry data (Tables 5.8 and 5.9). The diffusion coefficient (D) of EONPI in solution was estimated from the slope of the plot i_{pc} vs. $v^{1/2}$. Accordingly, the diffusion coefficients in CH_2Cl_2 and CH_3OH+CH_3CN (50:50) were determined as 3.52×10^{-10} cm^{2}s^{-1} and 3.02×10^{-9} cm^{2}s^{-1} respectively. High precision in ΔE_p ranges provided with the unity value of peak current ratio (i_{pa}/i_{pc}) for the entire scanning rate proves the complete reversibility of reduction processes in oligomeric diimide.

5.9.3 Electrochemistry of HP-CH

Electrochemical properties of the novel perylene substituted fluorescent chitosan polymer were investigated through the redox data obtained from cyclic voltammetry (CV) and squarewave voltammetric (SWV) measurements (Figures 4.67 – 4.72). Chitosan itself is a polyelectrolyte and when combined with perylene dye, an interesting electrochemistry was recorded and the data were described in detail. The CV of HP-CH was shown in Figure 4.67 taken in dipolar aprotic solvent dimethylacetamide and the redox potentials, electrochemical parameters were summarized in Tables 5.10 and 5.11.

Table 5.10: Electrochemical data of HP-CH

	E_{pc} (V)	E_{pa} (V)	ΔE_p (mV)	$E_{1/2}$ Vs. Ag/AgCl (V)	E_{Fc} Vs. Ag/AgCl (V)	$E_{1/2}$ Vs. Fc (V)
HP-CH	−0.319	−0.415	96	−0.367	0.586	−0.953
DMAc	−0.556	−0.660	104	−0.608	0.586	−1.194

HP-CH has shown two reversible one electron reductions at −0.953 V and −1.194 V peak potentials corresponding to ferrocene/ferrocenium couple. The peak potentials are similar to the perylene dyes reported in literature. The peak separations are appreciable (96 mV and 104 mV) as expected from a high dipolar aprotic solvent medium. The peak separations indicate moderate reproducibility of current.

Electrochemical stability of the polymer was examined by measuring repeated cycles of redox processes thoroughly. All the voltammetric measurements were repeated several times and the values of reduction potentials were found to be

reproducible. The compound has shown reversible reduction steps at the entire scanning rate tabulated below (Figures 4.68, 4.69 and Table 5.11).

Table 5.11: Cyclic voltammetry data of HP-CH

Scan Rate	HP-CH in DMAc					
	E_{pc}	E_{pa}	ΔE_p	i_{pa}	i_{pc}	i_{pa}/i_{pc}
(mVs^{-1})	/ V		/ mV	/ μA		
20	−0.319	−0.417	98	2.349	2.354	1.0
	−0.564	−0.648	84			
50	−0.319	−0.412	93	3.962	3.812	1.0
	−0.569	−0.648	79			
100	−0.319	−0.415	96	5.081	4.980	1.0
	−0.556	−0.660	104			
200	−0.322	−0.412	90	7.340	6.956	1.0
	−0.564	−0.648	84			
500	−0.318	−0.413	95	10.539	10.305	1.0
	−0.562	−0.647	85			
800	−0.315	−0.413	98	13.455	13.122	1.0
	−0.562	−0.654	92			
1000	−0.314	−0.419	105	16.286	16.312	1.0
	−0.555	−0.650	95			

For the entire scan rate from 25 – 1000 mV/s, Table 5.11 and Figures 4.68 – 4.70 explore that the calculated peak current ratios (Figure 4.70) were equal to unity and the peak separation (ΔE_p) range was about 84-105 mV. High precision was noticed in ΔE_p values provided with the unity value of peak current ratio (i_{pa} /i_{pc}) for the entire scanning rate which proves the complete reversibility of reduction processes in HP-CH. Squarewave voltammograms (Figure 4.71) show the peaks are reversible as $I_{forward}$ and $I_{reversible}$ are mirror images to each other and the $I_{difference}$ confirms the two reduction processes.

Calculated LUMO, HOMO and E_g values were summarized in Table 4.18 for comparison with other *n*-type materials. Absolute energy of LUMO levels of EONPI was estimated with respect to the vacuum level by standardizing the redox data to the ferrocene/ferricenium couple. The estimated band gap energy (E_g), LUMO, HOMO in DMAc were 2.28 eV, −3.85 eVand −6.13 eV, respectively.

The plot of peak current (i_{pc}) vs. square root of scan rate ($v^{1/2}$) was linear implying the diffusion controlled processes in dipolar aprotic solvent, DMAc (Figure 4.72). By using Randles-Sevcik equation (Equn. 4.19), the diffusion coefficient (D) was calculated with the cyclic voltammetry data (Tables 5.10 and 5.11). The diffusion coefficient (D) of HP-CH in DMAc solution was estimated from the slope of the plot i_{pc} vs. $v^{1/2}$. Accordingly, the diffusion coefficient was determined as 1.68×10^{-10} cm^2s^{-1}. The unity value of peak current ratio (i_{pa}/i_{pc}) for the entire scanning rate proves the electrochemical reversibility and stability of the polymer.

5.9.4 Electrochemistry of TEONPI

Electrochemical properties of the polymer with another flexible diamine were investigated with the redox data obtained from cyclic voltammetry (CV) and squarewave voltammetric (SWV) measurements (Figures 4.73 – 4.80). The CV of TEONPI (at 100 mVs^{-1}) was shown in Figure 4.73 which reveals that a total of three reductions are possible. The CV is different from the usual CVs of similar dyes such as EOPPI and EONPI.

Table 5.12: Electrochemical data of TEONPI at 100 mV s^{-1}

	E_{pc} (V)	E_{pa} (V)	ΔE_p (mV)	$E_{1/2}$ Vs. Ag/AgCl (V)	E_{Fc} Vs. Ag/AgCl (V)	$E_{1/2}$ Vs. Fc (V)
TEONPI	−0.448	−0.636	188	−0.542	0.552	−1.094
in CHCl$_3$	−0.845	−0.748	97	−0.796	0.552	−1.348
	−0.924	−1.017	93	−0.971	0.552	−1.523

Although it looks like three reductions are possible, two of them are very weak and are not reproducible. However, Figure 4.74 shows that at a particular scan rate (100 mV s^{-1}) the peak potentials did not vary with the repeated cycles. The poor reproducibility of the current and respective peak potentials are shown in Figure 4.75. The figure shows that at lowest scan rate (20 mV s^{-1}), the three reduction peak potentials were well appeared. When the scan rate was doubled, the peak potentials especially in the anodic region become negligible. After another double scan rate (100 mV s^{-1}), the anodic peak potential at −0.636 V was almost disappeared and just appeared as a small shoulder. These three scan rates and corresponding peak potentials were overlapped in one figure and the poor reproducibility of cathodic and anodic peaks were clearly observed.

The cyclic voltammograms carried out at higher scan rates (Figures 4.76 – 4.77) clearly indicate that the cathodic peak potentials observed at −0.845 V and −0.924 V and anodic peak potentials observed at −0.636 V and −0.748 V were combined as a single peak potential (for example at 500 mV s^{-1}) and appeared in the cathodic region at −0.852 V and in the anodic region at −0.762 V, respectively. The following table shows the respective peak potentials taken at higher scan rate.

Table 5.13: Electrochemical data of TEONPI at 500 mV s^{-1}

	E_{pc} (V)	E_{pa} (V)	ΔE_p (mV)	$E_{1/2}$ Vs. Ag/AgCl (V)	E_{Fc} Vs. Ag/AgCl (V)	$E_{1/2}$ Vs. Fc (V)
TEONPI	−0.367	−0.762	395	−0.565	0.552	−1.117
in CHCl$_3$	−0.852	−1.042	190	−0.947	0.552	−1.499

Although two reduction potentials were noticed at higher scan rates (Figures 4.76, 4.77), they are not reproducible similar to the peak potentials at lower scan rates (Figure 4.75) as evident from the calculated peak potential separation shown in Table 5.13. Squarewave voltammograms are much sensitive comparing to the cyclic voltammograms and the SWVs were measured (Figures 4.78 – 4.80) for the polymer in order to elucidate the number of peak potentials.

The uncertainity in peak potentials due to the blank solution (consists of supporting electrolyte, TBAPF$_6$ and internal reference, ferrocene) was erased with the SWVs shown in Figure 4.78. The blank solution solution's SWV is quite different from the polymer's SWV. Provided, the blank subtracted SWV of polymer resembles the SWV of unsubtracted polymer indicating the three reduction potentials noticed were belonging to the polymer.

The question of amine presence (which is used for the synthesis of polymer) and its effect on the polymer's reduction was studied and the SWVs are presented in Figures 4.79 and 4.80. Figure 4.80 reveals that both amine and blank solution were having almost same peaks. Therefore, the reduction peak potentials of polymer were unchanged when subtracted the SWVs of polymer from amine and blank solutions (Figure 4.79). It concludes that there are three reduction potentials exist but very week in intensity and thus are not reproducible when scanned at different scan rates.

Chapter 6

CONCLUSION

The project is focused on to synthesis of different *n*-type materials towards device and photonic applications. Based on hydrophobic perylene and naphthalene chromophores and flexible ethylene glycol moieties, a rigid-flexible-rigid system was designed using a specially synthesized diamine. A perylene oligomer dye and a naphthalene oligomer dye were synthesized successfully with high yields and the structures were proved by NMR and elemental analysis. The weight average molecular weights were determined by GPC and in parallel, intrinsic viscosity measurements were carried out. In order to explore their potential applications, a detail characterization of optical, photophysical, thermal and electrochemical properties was performed.

The design of rigid – flexible – rigid system provided remarkable solubility for both perylene and naphthalene oligomers in various common organic solvents. In addition to the organic medium, appreciable solubility in aqueous medium was noticed for EONPI. Excellent solubility means excellent processability of the material concerning device architectures.

Both oligomers possessed very high molar absorptivities that are not reported in literature for similar oligomers with long aliphatic chains. In addition, increased broad absorptions were noticed in solid state comparing to solution absorptions.

When organic photovoltaic devices are considered, the primary aspect insisted is the high absorption ability of organic material to capture as much as photons from solar energy. Hence, the exceptionally high molar absorptivity of the oligomers is an attractive property towards photovoltaic materials.

The conclusion on fluorescence properties of perylene oligomer dye is that it exhibits concentration dependent color tunability by emitting green, yellow and red colors. On the other hand, EONPI has shown both solvent and concentration dependent color tunability by emitting fluorescent yellow, blue and green colors. In addition to the color tunability, EONPI delivered excimer emissions in all common organic and aqueous solvents with a surprising increase in fluorescence quantum yields which were not noticed in literature for similar naphthalene dyes. A large Stokes shifts in aprotic solvents and anti-Stokes shift in protic solvents were also observed. Organic Light Emitting Diodes (OLEDs) and other opto-electronic devices need organic materials with such a light emitting and color tunable capabilities. In that point of view, both oligomers are excellent candidates for opto-electronic and photonic device applications. In addition, the sensitivity of fluorescence to solvent character could be applicable in fluorescent labeling experiments.

Besides to the exciting optical and photophysical properties, both the compounds possessed high thermal stability ($>300\ ^o$C) regardless of long aliphatic chains exist in the oligomer back bone. Every device constructed of organic materials must be resistant to heat and temperature and thus both the oligomeric compounds fulfill the requirement of high thermal stability.

Both the oligomeric dyes exhibited two reversible one-electron reductions in nonopolar solvent and EONPI especially undergone single reversible reduction in

dipolar aprotic and polar protic solvent mixture. Therefore, solvent dependent band gap tunability of EONPI was evident. Both the oligomers showed diffusion controlled electrochemical processes, electrochemical stability and reversibility. The diffusion constants calculated were appreciable for both the oligomers. The energies of LUMO and HOMO levels were measured from the reduction peak potentials.

Any organic polymer based photovoltaic device explains the necessity of efficient absorption of solar energy by lower band gap organic material, related charge carrier formation, charge carrier mobility and charge diffusion to respective electrodes; which are the key driving forces in determining the power generation efficiency of the device. Both the oligomers fit the requirements of such devices with low, tunable band gap energies and appreciable diffusion constants.

It can be finally concluded that the oligomers act as efficient *n*-type organic materials and possess excellent potential applications. The interesting high absorptions, high quantum yields, light-emmiting optical and photophysical processes make them exciting choices for various device architectures.

REFERENCES

[1] Shockley, W., & Queisser, H. J. Detailed Balance Limit of Efficiency of PN Junction Solar Cells. *Journal of Applied Physics.* 32 (1961): 510.

[2] Wöhrle, D., & Meissner, D. Organic Solar Cells. Advance Materials. 3 (1991):129

[3] Kim, J. Y., Lee, K., Coates, N. E., Moses, D., Nguyen, T. –Q., Dante, M., & Heeger, A. J. Efficient tandem polymer solar cells fabricated by all-solution processing. *Science.* 317 (2007): 222.

[4] Weil, T., Vosch, T., Hofkens, J., Peneva, K., & Müllen, K. The Rylene Colorant Family–Tailored Nanoemitters for Photonics Research and Applications. *Angewandnte.Chem. Int. Ed.* 49 (2010): 9068-9093.

[5] Wöhrle, D., Kreienhoop, L., Schnurpfeil, G., Elbe, J., Tennigkeit, B., Hiller, S., & Schlettwein, D. Investigations of n/p-Junction Photovoltaic Cells of Perylenetetracarboxylic Acid Diimides and Phthalocyanines. *J. Mater. Chem.* 5 (1995): 1819-1829.

[6] Quante, H., Geerts, Y., & Müllen, K. Synthesis of Soluble Perylenebisamidine derivatives. Novel Long-Wavelength Absorbing and Fluorescent Dyes. *Chemistry of Materials.* 9 (1997): 495-500.

[7] Shibano, Y., Umeyama, T., Matano, Y., & Imahori, H. Electron-Donating Perylene Tetracarboxylic Acids for Dye-Sensitized Solar Cells. *Organic Letters.* 9 (2007): 1971-1974.

[8] Wang, W., Han, J. J., Wang, L. –Q., Li, L. –S., Shaw, W. J. & Li, A. D. Q. Dynamic π-π Stacked Molecular Assemblies Emit from Green to Red Colors. *Nano Letters.* 3 (2003): 455-458.

[9] Bodapati, J. B., & Icil, H. Highly Soluble Perylene Diimide and Oligomeric Diimide Dyes Combining Perylene and Hexa(ethylene glycol) Units: Synthesis, Characterization, Optical and Electrochemical Properties. *Dyes and Pigments.* 79 (2008): 224-235.

[10] Bodapati, J. B., & Icil, H. A New Tunable Light-Emitting and π-Stacked Naphthalene Oligomer: Synthesis, Photophysics and Electrochemical Properties. *Photochemical and Photobiological Sciences.* (2011, *in print*).

[11] Pasaogullari, N., Icil, H., & Demuth, M. Symmetrical and Unsymmetrical Perylene Diimides: Their Synthesis, Photophysical and Electrochemical Properties. *Dyes and Pigments.* 69 (2006): 118-127.

[12] Yuney, K., & Icil, H. Symmetrical and Unsymmetrical Perylene Diimides: Their Synthesis, Photochemical, and Electrochemical Properties of Naphthalene-1,4,5,8-tetracarboxylic acid-bis-(N,N′-bis-(2,2,4(2,4,4)-trimethylhexylpolyimide)) and Poly(N,N′-bis-(2,2,4(2,4,4)-trimethyl-6-

aminohexyl)3,4,9,10-perylenetetracarboxdiimide. *European Polymer Journal.* 43 (2007): 2308-2320.

[13] Amiralaei, S., Uzun, D., & Icil, H. Chiral Substituent Containing Perylene Monoanhydride Monoimide and its Highly Soluble Symmetrical Diimide: Synthesis, Photophysics and Electrochemistry from Dilute Solution to Solid State. *Photochemical and Photobiological Sciences.* 7 (2008): 936-947.

[14] Asir, S., Demir, A. S., & Icil, H. The Synthesis of Novel, Unsymmetrically Substituted, Chiral Naphthalene and Perylene Diimides: Photophysical, Electrochemical, Chiroptical and Intramolecular Charge Transfer Properties. *Dyes and Pigments.* 84 (2009): 1-14.

[15] Ozdal, D., Asir, S., Bodapati, J. B., & Icil, H. (2011, *in press*).

[16] Yamashita, Y. Organic Semiconductors for Organic Field-Effect Transistors. *Science and Technology of Advanced Materials.* 10 (2009): 024313.

[17] Ahrens, M. J., Fuller, M. J., Wasielewski, M. R. Cyanated Perylene-3-4-dicarboximides and Perylene-3,4:9,10-bis(dicarboximide): facile Chromophoric Oxidants for Organic Photonics and Electronics. *Chemistry of Materials.* 15 (2003): 2684-2686.

[18] Würthner, F. Perylene Bisimide Dyes as Versatile Biulding Blocks for Functional Supramolecular Architectures. *Chemical Communications.* (2004): 1564-1579.

[19] Qu, J., Zhang, J., Grimsdale, A. C., Mllen, K., Jaiser, F., Yang, X., & Neher, D. Dendronized Perylene Diimide Emitters: Synthesis, Luminescence, and Electron and Energy Transfer Studies. *Macromolecules.* 37 (2004): 8297-8306.

[20] Lee, S., Mller, A. M., Al-Kaysi, R., & Bardeen, C. J. Using Perylene-Doped Polymer Nanotubes as Fluorescence Sensors. *Nano Letters.* 6 (2006): 1420-1424.

[21] Bevers, S., Schuttle, S., & McLaughlin, L. W. Naphthalene- and Perylene-Based Linkers for the Stabilization of Hairpin Triplexes. *J. Am. Chem. Soc.* 122 (2000): 5905-5915.

[22] Ofir, Y., Zelichenok, A., & Yitzchaik, S. 1,4;5.8-Naphthalene-tetracarboxylic Diimide Derivatives as Model Compounds for Molecular Layer Epitaxy. *J. Mater. Chem.* 16 (2006): 2142-2149.

[23] Jones, B. A., Facchetti, A., Wasielewski, M. R., & Marks, T. J. Tuning Orbital Energetics in Arylene Diimide Semiconductors. Materials Design for Ambient Stability of *n*-type Charge Transport. *J. Am. Chem. Soc.* 129 (2007): 15259-15278.

[24] Fukaminato, T., Tanaka, M., Doi, T., Tamaoki, N., Katayama, T., Mallick, A., Ishibashi, Y., Miyasaka, H., & Irie, M. Fluorescence Photoswitching of a Diarylethene-Perylenebisimide Dyad Based on Intramolecular Electron Transfer. *Photochemical and Photobiological Sciences.* 9 (2010): 181-187.

[25] Thelakkat, M., Schmitz, C., & Schmidt, H. –W. Fully Vapor-Depossited Thin-Layer Titanium Dioxide Solar Cells. *Adv. Mater.* 14 (2002): 577.

[26] Pandey, A. K., Unni, K. N. N., & Nunzi, J. –M. Pentacene/Perylene Co-Deposited Solar Cells. *Thin Solid Films.* 511-512 (2006): 529-532.

[27] Breeze, A. J., Salomon, A., Ginley, D. S., Gregg, B. A., Tillmann, H., & Hörhold, H. –H. Polymer–Perylene Diimide Heterojunction Solar Cells. *Applied Physics Letters.* 81 (2002): 3085-3087.

[28] Nakamura, J. -I., Yokoe, C., Murata, K., & Takahashi, K. Efficient Organic Solar Cells by Penetration of Conjugated Polymers into Perylene Pigments. *J. App. Phys.* 96 (2004): 6878-6883.

[29] Foster, S., Finlayson, C. E., Keivaanidis, P. E., Huang, Y. –S., Hwang, I., Friend, R. H., Otten, M. B. J., Lu, L. –P., Schwartz, E., Nolte, R. J. M., & Rowan, A. E. Improved Performance of Perylene-Based Photovoltaic Cells Using Polyisocyanopeptide Arrays. *Macromolecules.* 42 (2009): 2023-2030.

[30] Tomizaki, K. -Y., Loewe, R. S., Kirmaier, C., Schwartz, J. K., Retsek, J. L., Bocian, D. F., Holten, D., & Lindsey, J. S. Synthesis and Photophysical Properties of Light-Harvesting Arrays Comprised of a Porphyrin Bearing Multiple Perylene-Monoimide Accessory Pigments. *J. Org. Chem.* 67 (2002): 6519-6534.

[31] Ishi-i, T., Murakami, K. -I., Imai, Y., & Mataka, S. Light-Harvesting and Energy Transfer System Based on Self-Assembling Perylene Diimide-Appended Hexaazatriphenylene. *Org. Lett.* 7 (2005): 3175-3178.

[32] Sautter, A., Kaleta, B. K., Schmid, D. G, Dobrawa, R., Zimine, M., Jung, G., Stokkum, I. H. M. V., Cola, L. D., Williams, R. M., & Würthner, F. Ultrafast Energy-Electron Transfer Cascade in a Multichromophoric Light-Harvesting Molecular Square. *J. Am. Chem.Soc.* 127 (2005): 6719-6729.

[33] Edvinsson, T., Li, C., Pschirer, N., Schneboom, J., Eickemeyer, F., Sens, R., Boschloo, G., Herrmann, A., Mllen, K., & Hagfeldt, A. Intramolecular Charge-Transfer Tuning of Perylenes: Spectroscopic Features and Performance in Dye-Sensitized Solar Cells. *The Journal of Physical Chemistry C.* 111 (2007): 15137-15140.

[34] Bauer, P., Wietasch, H., Lindner, S. M., & Thelakkat, M. Synthesis and Characterization of Donor-Bridge-Acceptor Molecule Containing Tetraphenylbenzidine and Perylene Bisimide. *Chemistry of Materials.* 19 (2007): 88-94.

[35] Beckers, E. H. A., Meskers, S. C. J., Schenning, A. P. H. J., Chen, Z., Würthner, F., Marsal, P., Beljonne, D., Cornil, J., & Janssesn, R. A. J. Influence of Intermolecular Orientation on the Photoinduced Charge Transfer Kinetics in Self-Assembled Aggregates of Donor-Acceptor Arrays. *J. Am. Chem. Soc.* 128 (2006): 649-657.

[36] Balakrishnan, K., Datar, A., Naddo, T., Huang, J., Oitker, R., Yen, M., Zhao, J., & Zang, L. Effect of Side-Chain Substituents on Self-Assembly of Perylene Diimide Molecules: Morphology Control. *J. Am. Chem. Soc.* 128 (2006): 7390-7398.

[37] Ghosh, S., & Ramakrishnan, S. Structural Fine-Tuning of (-Donor-Spacer-Acceptor-Spacer-)$_n$ Type Foldamers. Effect of Spacer Segment Length, Temperature, and Metal-Ion Complexation on the Folding Process *Macromolecules.* 38 (2005): 676-686.

[38] Hoppe, H., & Sariciftci, N. S. Organic Solar Cells: An Overview. *J. Mater. Res.* 19 (2004): 1924-1945.

[39] Brunetti, F. G., Kumar, R., & Wudl, F. Organic Electronics from Perylene to Organic Photovoltaics: Painting a Brief History with a Broad Brush. *J. Mater. Chem.* 20 (2010): 2934-2948.

[40] Günes, S., Neugebauer, H., & Sariciftci, N. S. Conjugated Polymer-Based Organic Solar Cells. *Chem. Rev.* 107 (2007): 1324-1338.

[41] Benanti, T. L, & Venkataraman, D. Organic Solar Cells: An Overview Focusing on Active Layer Morphology. *Photosynthesis Research.* 87 (2006): 73-81.

[42] Pron, A., & Rannou, P. Processible Conjugated Polymers: from Organic Semiconductors to Organic Metals and Super Conductors. *Prog. Polym. Sci.* 27 (2002): 135-190.

[43] Anthony, J. E., Facchetti, A., Heeney, M., Marder, S. R., & Zhan, X. *n*-Type Organic Semiconductors in Organic Electronics. *Adv. Mater.* 22 (2010): 3876-3892.

[44] Bredas, J. –L., Beljonne, D., Coropceanu, V., & Cornil, J. Charge-Transfer and Energy-Transfer Processes in π-Conjugated Oligomers and Polymers: A Molecular Picture. *Chem. Rev.* 104 (2004): 4971-5003.

[45] Deibel, C., Strobel, T., & Dyakonov, V. Role of the Charge Transfer State in Organic Donor-Acceptor Solar Cells. *Adv. Mater.* 22 (2010): 4097-4111.

[46] Kirmaier, C., Hindin, E., Schwartz, J. K., Sazanovich, I. V., Diers, J. R., Muthukumaran, K., Taniguchi, M., Bocian, D. F., Lindsey, J. S., & Holten, D. Synthesis and Excited-State Photodynamics of Perylene-Bis(Imide)-Oxochlorin Dyads. A Charge-Separation Motif. *The Journal of Physical Chemistry B.* 107 (2003): 3443-3454.

[47] Fink, R. F., Seibt, J., Engel, V., Renz, M., Kaupp, M., Lochbrunner, S., Zhao, H. -M., Pfister, J., Würthner, F., & Engels, B. Exciton Trapping in π-Conjugated Materials: A Quantum-Chemistry-Based Protocol Applied to Perylene Bisimide Dye Aggregates. *J. Am. Chem. Soc.* 130 (2008): 12858-12859.

[48] Hennebicq, E., Pourtois, G., Scholes, G. D., Herz, L. M., Russell, D. M., Silva, C., Setayesh, S., Grimsdale, A. C., Müllen, K., Bredas, J. –L., & Beljonne, D. Exciton Migration in Rigid-Rod Conjugated Polymers: An Improved Förster Model. *J. Am. Chem. Soc.* 127 (2005): 4744-4762.

[49] Albinsson, B., & Martensson, J. Excitation Energy Transfer in Donor-Bridge-Acceptor Systems. *Phys. Chem. Chem. Phys.* 12 (2010): 7338-7351.

[50] Würthner, F., & Meerholz, K. Systems Chemistry Approach in Organic Photovoltaics. *Chem. Eur. J.* 16 (2010): 9366-9373.

[51] Balzani, V., Credi, A., & Venturi, M. (2003) Molecular Devices and Machines – A Journey into the Nano World, Wiley-VCH Verlag GmbH & Co. KGaH, Weinheim.

[52] Sun, S. -S., & Sariciftci, N. S. (2005) Organic Photovoltaics Mechanisms, Materials, and Devices, CRC Press, Taylor & Francis.

[53] Brabec, C. J. (2003) Organic Photovoltaics: Concepts and Realization, Springer.

[54] Müller, T. J. J. & Bunz, U. H. F. (2007) Functional Organic Materials: Syntheses, Strategies and Applications, Wiley-VCH.

[55] Gratzel, M. Dye Sensitized Solar Cells. Dye-Sensitized Solar Cells. *J. Photochemistry and Photobiology C: Photochemistry Reviews.* 4 (2003): 145-153.

[56] Lenzmann, F. O., & Kroon, J. M. Recent Advances in Dye-Sensitized Solar Cells. *Advances in Opto Electronics.* (2007): ID 65073.

[57] Icil, H., & Icli, S. Synthesis and Properties of a New Photostable Polymer: Perylene-3,4,9,10-tetracarboxylic Acid-Bis-(N,N′-dodecylpolyimide). *J. Poly. Sci. A: Polym. Chem.* 35 (1997): 2137-2142.

[58] Uzun, D., Ozser, M. E., Yuney, K., Icil, H., & Demuth, M. Synthesis and Properties of N,N′-bis(4-cyanophenyl)-3,4,9,10-perylenebisdicarboximide) and N,N′-bis(4-cyanophenyl)-1,4,5,8-naphthalenediimide). *Journal of Photochemistry and Photobiology A: Chemistry.* 156 (2003): 45-54.

[59] Ozser, M. E., Bodapati, J. B., & Icil, H. (2011, *in press*).

[60] Kasaai, M. R., Arul, J., & Charlet, G. Intrinsic Viscosity-molecular Weight Relationship for Chitosan. *J. Poly. Sci. B: Polym. Physics.* 38 (2000): 2591-2598.

[61] Kasaai, M. R. Calculation of Mark-Houwink-Sakurada (MHS) Equation Viscometric Constants for Chitosan in Any Solvent-temperature System Using Experimental Reported Viscometric Constants Data. *Carbohydrate Polymers.* 68 (2007): 477-488.

[62] Williams, A. T. R., Winfield, S. A., & Miller, J. N. Relative Fluorescence Quantum Yields Using a Computer-controlled Luminescence Spectrometer. *Analyst.* 108 (1983): 1067-1071.

[63] Scaiano, J. C. (1989) (Ed.) Handbook of Organic Photochemistry, CRC press.

[64] Turro, N. J. (1965) Molecular Photochemistry, Benjamin, London, 44.

[65] Bard, A. J., & Faulkner, L. R. (2001) Electrochemical Methods: Fundamentals and Applications, 2nd Ed, John Wiley & Sons, Inc. New York.

[66] Grimshaw, J. (2000) Electrochemical Reactions and Mechanisms in Organic Chemistry, Elsevier.

[67] Bredas, J. L., Silbey, R., Chance, R. R., & Boudreaux, D. S. Chain-length Dependence of Electronic and Electrochemical Properties of Conjugated Systems: Polyacetylene, Polyphenylene, Polythiophene, and Polypyrrole. *J. Am. Chem. Soc.* 105 (1983): 6555-6559.

[68] Peng, Z., Bao, Z., & Galvin, M. E. Polymers with Bipolar Carrier Transport Abilities for Light Emitting Diodes. *Chem. Mater.* 10 (1998): 2086-2090.

[69] Hink, M. A., Visser, N. V., Borst, J. W., Hoek, A. V., & Visser, A. J. W. G. Practical Use of Corrected Fluorescence Excitation and Emission Spectra of Fluorescent Proteins in Förster Resonance Energy Transfer (FRET) Studies. *Journal of Fluorescence.* 13 (2003): 185-188.

[70] Icil, H. Energy Transfer Studies with Perylene bis-Diimide Derivatives. *Spectroscopy Letters.* 31 (1998): 747-755.

[71] Stern, O., & Volmer, M. Über die Abklingzeit der Fluoreszenz. *Physik. Zeitschr.* 20 (1919): 183-188 as cited in Mehra and Rechenberg, Volume 1, Part 2, 2001, 849.

[72] Li, A. D. Q., Wang, W., & Wang, L. Q. Folding versus Self-assembling. *Chem, Eur. J.* 9 (2003): 4594-4601.

[73] Neuteboom, E. E., Janssen, R. A. J., & Meijer, E. W. Aggregation of Perylenebisimidpolytetrahydrofuran Copolymers. *Synthetic Metals.* 121 (2001): 1283-1284.

[74] Neuteboom, E. E., Meskers, S. C. J., Meijer, E. W., & Janssen, R. A. J. Photoluminescence of Self-organized Perylene Bisimide Polymers. *Macromol. Chem. Phys.* 205 (2004): 217-222.

CURRICULAM VITAE

Jagadeesh Babu Bodapati,
Department of Chemistry,
Faculty of Arts & Sciences,
Eastern Mediterranean University,
FAMAGUSTA, NORTH CYPRUS.
e-mail: jagadeesh.bodapati@emu.edu.tr

Career objective

To join a dynamic and reputed organization which can utilize the inherent talent to the maximum; so that, I can put in my share of contribution into its growth, resulting in a relationship of mutual benefit.

To handle a challenging, diverse and dynamic job with good ease and corresponding work responsibility.

Present Status

Postdoctoral fellowship at Eastern Mediterranean University, Famagusta, North Cyprus under the supervision of Prof. Dr. Huriye İcil.

Academic qualifications

- **Doctor of Philosophy (PhD)** in CHEMISTRY from Eastern Mediterranean University, North Cyprus
- **Master of Science (MS)** in CHEMISTRY from Eastern Mediterranean University, North Cyprus
- **Bachelor of Technology (B.Tech)** in CHEMICAL ENGINEERING from Jawaharlal Nehru Technological Univeristy (JNTU), Anantapur, Andhra Pradesh, INDIA with DISTINCTION.

Industrial Experience

- Three-month live research as a project work at Indian Institute of Chemical Technology (IICT), Hyderabad, Andhra Pradesh, INDIA.

- One month industrial training at Dr.Reddy's Laboratories, Hyderabad, Andhra Pradesh, INDIA.

Projects Accomplished

1. **Ongoing Research Project, Tübitak, TBAG-110T201 (Postdoctoral Fellowship).**

2. 2004-2007 Research project, Tübitak, TBAG-2371 (One of the members of scientific researchers).

3. Bachelor Degree Fullfillment Project, titled: "Desalination of Aqueous Solution of Sodium Benzoate by Electro Dialysis". *Description:* Sodium salts of benzoic acid are used as preservatives. To reach the requirements of utilization as preservatives they should be desalinated. The live research was carried out and explored the processes in detail.

4. Industrial Training Project, titled: "Manufacturing of Enalapril Maleate". *Description:* It is an Anti-Hypertensive drug. The synthesis was carried out and an overview has been given on various aspects such as implemented processes, utilities and material balance, etc.

Publications

1. **J. B. Bodapati**, H. Icil

   A new tunable light-emitting and π-stacked naphthalene oligomer: Synthesis, photophysics and electrochemical properties

   Photochemical and Photobiological Sciences (2011, *in print*).

2. **J. B. Bodapati**, H. Icil

   Highly soluble perylene diimide and oligomeric diimide dyes combining perylene and hexa(ethylene glycol) units: Synthesis, characterization, optical and electrochemical properties

   Dyes and Pigments 79 (2008) 224–235

Conferences

1. Bodapati, J.B., İcil, H., "New n-type Organic Semiconductors for High Efficient Solar Cells: Synthesis, Characterization, Optical and Electrochemical Properties", *David G. Whitten Symposium*, Albuquerque, New Mexico, USA, 19 – 20 August 2010.

2. Bodapati, J.B., İcil, H., "Electrically Active Organic Polymers for Future High Efficient Solar Cells: Their Synthesis and Characterization", *Frontiers in Polymer Science*, Mainz, Germany, 07 – 09 June 2009.

3. Bodapati, J.B., İcil, H., "Excimer Confirmation and Electrochemical Studies of a Polyimide Derived from Naphthalene Dianhydride and Hexa(ethylene glycol) Moieties", *XXII. National Chemistry Congress,* Famagusta, Cyprus, 06-10 October 2008.

4. Bodapati, J.B., İcil, H., "Highly Soluble Perylene Diimide and Oligomeric Diimide Dyes Combining Perylene and Hexa(ethylene glycol) Units: Synthesis, Characterization, Optical and Electrochemical Properties", *XXII. National Chemistry Congress,* Famagusta, Cyprus, 06-10 October 2008.

5. Abimbola O. Aleshinloye, Bodapati, J.B., İcil, H., "Novel Multichromophoric Supramolecular Architecture: Design, Synthesis and Characterization" *XXII. National Chemistry Congress,* Famagusta, Cyprus, 06-10 October 2008.

6. Mustafa E. Özser, Bodapati, J.B., İcil, H. "Synthesis, Photochemical, and Thermal Properties of Bis-N, N'-(3-(2-(2-(3-aminopropoxy)ethoxy)ethoxy)propyl) -1,4,5,8-Naphthalene Diimide and the Polymer Theirof" *XXII. National Chemistry Congress,* Famagusta, Cyprus, 06-10 October 2008.

7. Bodapati, J.B., İcil, H., "Förster (fluorescence) Resonance Energy Transfer with a Soluble Fluorescent Perylene Polymer", *International Conference on Organic Chemistry,* Erzurum, Turkey, 5-9 June 2007.

8. Bodapati, J.B., İcil, H., "Yeni Katlanabilir Naftalen Polimer: Absorpsiyon, Floresans ve Molekuler Birimler Arası İlişkiler", *XX. Ulusal Kimya Kongresi*, Kayseri, Turkey, 4-8 September 2006.

9. Bodapati, J.B., İcil, H., "Çözünür Perilen Diimid Ve Poliimid: Sentez, Karakterizasiyon, Fotofizikal Ve Elecktrokimyasal Özellikler", *XIX. Ulusal Kimya Kongresi*, Kuşadası, Turkey, 4th September 2005.

10. Bodapati, J.B., İcil, H., "Synthesis of soluble Poly(perylene carboximides)", *XVII. Ulusal Kimya Kongresi*, Kars, Turkey, 9th July 2004.

11. J. B. Bodapati, Bhaskar, "Polymers in Membrane and Separation Technology", National Level Student Paper Contest (under Chemical Engg. division), Vignan Engineering College, Vadlamudi, AP, INDIA.

12. J. B. Bodapati, "Recent Trends in Sugar Industry Using Reverse Osmosis", National Level Technical Symposium, CHEM QUEST, 2001 (under Chemical Engg. division), Chitanya Bharathi Institute of Technology, Hyderabad, AP, INDIA.

13. J. B. Bodapati, "Bio Polymers for Challenging Millenium", National Level Chemical Engineering Students Seminar, Siddaganga Institute of Technology, Tumkur, INDIA.

Organizations

1. Served as a member of organizing secretariat committee of prestigious XXII. National Chemistry Congress held at Famagusta, North Cyprus on 6-10 October, 2008.
2. Served as a president, vice-president and treasurer for Indian Society at EMU.
3. Served as a member of organizing committee of FUSION-2000, 2001; both are national level seminars conducted by Department of Chemical Engineering, JNTU, Anatapur, AP, INDIA.

Computer skills

1. Operating Systems   :   UNIX, Windows.
2. Languages   :   C and Data Structures, Pascal.
3. Packages   :   Ms-Office.

Extra Curricular Activities

1. Champion of 5K run at Eastern Mediterranean University for the year 2006.
2. Participated and rewarded in various sports at School, College and University level.

Profile

1. Creativity oriented work in duties and responsibilities.
2. Success oriented and outgoing with a positive attitude.
3. Strong sense of responsibility and self-motivation.
4. Ability to manage and prioritize multiple duties simultaneously.
5. Work well under pressure, diplomat, tactful, meet strict deadlines, and fast learner.
6. Good verbal and written communication skills in English, Telugu and moderate skills in Hindi and Turkish.

Personal Profile

Father's Name	:	Apparao.
Date of Birth	:	03-07-1980.
Sex	:	Male.
Marital status	:	Married, one child.
Nationality	:	Indian.
Religion	:	Hindu.
Passport No	:	H5172980.
Hobbies	:	Listening to music, Playing Chess, Painting.
Languages Known	:	Telugu, English, Turkish, and Hindi
Phone	:	+90-533-847-2037.
Office	:	+90-392-630-1026.
Fax	:	+90-392-365-1604.
e-mail	:	jagadeesh.bodapati@emu.edu.tr.